

**REDUCED DEGRADATION OF CH₃NH₃PBI₃ SOLAR CELLS BY
GRAPHENE ENCAPSULATION**

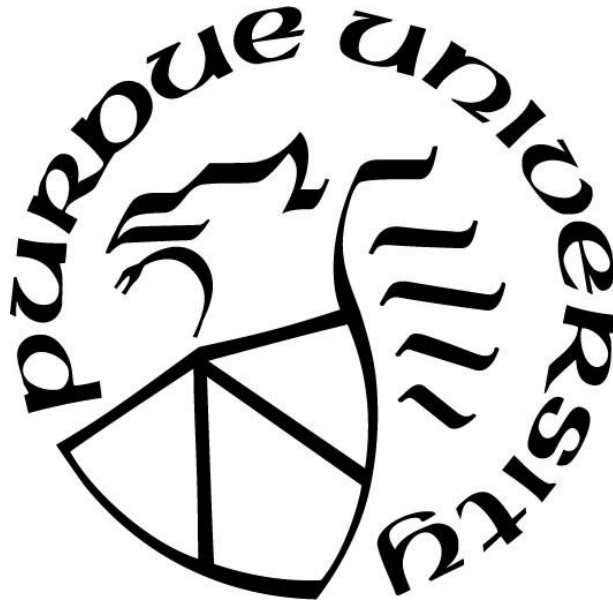
by
Kyle Reiter

A Thesis

Submitted to the Faculty of Purdue University

In Partial Fulfillment of the Requirements for the degree of

Master of Science



School of Engineering Technology

West Lafayette, Indiana

May 2019

THE PURDUE UNIVERSITY GRADUATE SCHOOL
STATEMENT OF COMMITTEE APPROVAL

Dr. Helen McNally, Chair

School of Engineering Technology

Dr. Letian Dou

School of Chemical Engineering

Prof. Paul McPherson

School of Engineering Technology

Approved by:

Dr. Duane Dunlap

Head of the Graduate Program

This thesis is dedicated to my mother who was the strongest person I knew, and my father who is the most supportive person I have ever known.

ACKNOWLEDGMENTS

I would like to acknowledge those who supported this research:

Dr. McNally for research guidance and use of the atomic force microscope,
Dr. Dou and Blake Finkenauer for guidance in the chemistry lab and use of the fluorescent
microscope,

And Professor McPherson for funding and general guidance.

TABLE OF CONTENTS

LIST OF FIGURES	viii
LIST OF TABLES	xii
LIST OF ABBREVIATIONS	xiii
GLOSSARY	xv
ABSTRACT	xvi
CHAPTER 1. INTRODUCTION	1
1.1 Statement of Problem	1
1.2 Research Question and Hypothesis	3
1.3 Scope	4
1.4 Significance	5
1.5 Definitions	6
1.6 Assumptions	7
1.7 Limitations	8
1.8 Delimitations	9
1.9 Chapter Summary	10
CHAPTER 2. REVIEW of LITERATURE	11
2.1 Perovskite Solar Cells and PL Measurements	12
2.2 Graphene	18
2.2.1 Graphene: Properties, Roll-to-Roll Production, and Limitations	18
2.2.2 Graphene and Perovskites	23
2.3 Graphene as a Gas Barrier	24
2.3.1 Graphene Used to Encapsulate Water Molecules	26
2.3.2 Graphene Covering Perovskite Simulation	27
2.3.3 Graphene and Polymer Encapsulations of Perovskite	28
2.4 Atomic Force Microscopy	32
2.5 Measurements Using Photoluminescence	34
2.6 Raman Spectroscopy and X-Ray Diffraction	37
2.7 Chapter Summary	39
CHAPTER 3. RESEARCH METHODOLOGY	40
3.1 Research Framework	40
3.1.1 Sampling Approach	41

3.1.2 Units of Measure	43
3.1.3 Variables.....	43
3.2 Instruments.....	44
3.2.1 Atomic Force Microscope: Topographical Measurements	44
3.2.2 Optical Microscope: Photoluminescence Measurements.....	48
3.2.3 Data Collection and Display Methods.....	50
3.2.4 Proposed Analysis of Data	50
3.3 Procedures.....	51
3.3.1 Preparation of Sample A: MAPbI ₃	51
3.3.2 Preparation of Graphene Solution	53
3.3.3 Preparation of Chemical Vapor Deposition Graphene.....	54
3.3.4 Preparation of Sample B: MAPbI ₃ With Graphene Solution Encapsulation	56
3.3.5 Preparation of Sample C: MAPbI ₃ With CVD Graphene Encapsulation	57
3.3.6 Photoluminescence Measurement Procedure	63
3.3.7 Atomic Force Microscope Measurement Procedure	64
3.4 Statistical Analysis.....	66
CHAPTER 4. RESULTS	68
4.1 Preliminary Trials Lessons Learned	68
4.1.1 Trial 1	68
4.1.2 Trial 2	72
4.1.3 Trial 3	73
4.2 Trial 4: Comparing Samples A and C.....	77
4.3 Trial 5 Comparing Samples A, B, and C	85
4.3.1 Raman Spectroscopy Characterization.....	86
4.3.2 Trial 5 Atomic Force Microscopy Data	89
4.3.3 Trial 5 Optical Images and Photoluminescence Data	113
4.4 Trial 6 Final Comparison of Sample A and C	123
4.4.1 Atomic Force Microscopy Data	124
4.4.2 Optical Images and Photoluminescence Data	140
4.4.3 X-Ray Diffraction Data.....	149
4.5 Data Analysis and Discussion.....	151
CHAPTER 5. SUMMARY, CONCLUSIONS, and RECOMMENDATIONS	162
5.1 Summary	162
5.2 Conclusions.....	164

5.3 Recommendations and Future Work 165
LIST OF REFERENCES 168

LIST OF FIGURES

Figure 1.1 MAPbI ₃ Fresh and Degraded Samples	2
Figure 1.2 MAPbI ₃ In Vacuum Jar and Petri Dish.....	2
Figure 2.1 Variety of Perovskites and PL Spectra.....	13
Figure 2.2 Varied Perovskite Spin-Coating Speeds and Colors	15
Figure 2.3 Slot-Die for R2R coating MAPbI ₃ Films.....	17
Figure 2.4 R2R set-up Diagram and Resulting Films.....	17
Figure 2.5 Graphene Carbon Honeycomb Lattice	20
Figure 2.6 R2R Schematic of Graphene Films	20
Figure 2.7 R2R Production of Graphene Films	21
Figure 2.8 Graphene Electrodes on Perovskite.....	24
Figure 2.9 TEM Image of Graphene Encapsulating Water Droplets.....	26
Figure 2.10 Chemical Schematic of Graphene/MAPbI ₃ Interface	27
Figure 2.11 Graphene/MAPbI ₃ Heterostructure Interface	28
Figure 2.12 Perovskite PL Intensity Over Time	29
Figure 2.13 PL Intensity MAPbI ₃ With and Without Graphene	30
Figure 2.14 PL Image Map of MAPbI ₃ With and Without Graphene	31
Figure 2.15 Normalized PL of Fresh and Aged MAPbI ₃	35
Figure 2.16 Fresh and Aged MAPbI ₃ Pin-Hole Growth	36
Figure 2.17 Raman Spectroscopy Peaks for Graphene.....	37
Figure 2.18 XRD Measurement of MAPbI ₃ Over Time	38
Figure 3.1 Sample Indicator Marks and Measurement Locations	42
Figure 3.2 Veeco Innova AFM Microscope Used	45
Figure 3.3 VEDA Simulation 5nm Wide Feature, 20nm Tip.....	46
Figure 3.4 MAPbI ₃ Sample in Putty on Magnetic Puck for AFM Scans	47
Figure 3.5 Olympus BX53M System Microscope, X-Cite Series 120, and Spectra Pro HRS – 300 Used	49
Figure 3.6 Pristine Graphene Flake Solution from Graphene Supermarket	54
Figure 3.7 CVD Graphene on PET Substrate From Graphene Supermarket	55

Figure 3.8 CVD Graphene on Copper Foil From Graphene Supermarket	55
Figure 3.9 UV Light Illuminating PET Substrate on MAPbI ₃	58
Figure 3.10 Liang et al. (2011) CVD Graphene on Cu Foil Transfer Method Process	59
Figure 3.11 Trial 3 Failed Graphene Transfer	60
Figure 3.12 Trial 4 Successful Graphene Transfer	60
Figure 3.13 CVD Graphene on Cu Foil PMMA Transfer Method to MAPbI ₃ Process	62
Figure 4.1 PET/Graphene Lamination on MAPbI ₃	73
Figure 4.2 Trial 3 Failed Graphene Transfer	74
Figure 4.3 Consistent MAPbI ₃ Samples in Trial 3	75
Figure 4.4 Diagram of Marking Indicators	78
Figure 4.5 Successful PMMA Graphene Transfer.....	78
Figure 4.6 Trial 4 Samples A and C Before Humidity Exposure	79
Figure 4.7 Trial 4 Averaged Photoluminescence Spectra for Sample A	82
Figure 4.8 Trial 4 Averaged Photoluminescence Spectra for Sample C	83
Figure 4.9 Raman Spectroscopy Characterization of MAPbI ₃	87
Figure 4.10 Raman Spectroscopy Characterization of PGF in Ethyl Alcohol Solution.....	87
Figure 4.11 First Raman Spectroscopy Characterization of PMMA/Graphene/MAPbI ₃	88
Figure 4.12 Second Raman Spectroscopy Characterization of PMMA/Graphene/MAPbI ₃	88
Figure 4.13 50 x 50 AFM Scan of Sample A at 0 Hours of 80% Humidity	91
Figure 4.14 Watershed Analysis of 50 x 50 AFM Scan of Sample A at 0 Hours of 80% Humidity	92
Figure 4.15 20 x 20 AFM Scan of Sample A at 0 Hours of 80% Humidity.....	93
Figure 4.16 Profile Path of AFM Scan of Sample A at 0 Hours of 80% Humidity	93
Figure 4.17 3D 20 x 20 AFM Image of Sample A at 0 Hours of 80% Humidity.....	94
Figure 4.18 5 x 5 AFM Image of Sample A at 0 Hours of 80% Humidity.....	95
Figure 4.19 3D 5 x 5 AFM Image of Sample A at 0 Hours of 80% Humidity.....	95
Figure 4.20 20 x 20 AFM Scan of Sample C at 0 Hours of 80% Humidity	97
Figure 4.21 Profile Path of AFM Scan of Sample C at 0 Hours of 80% Humidity.....	97
Figure 4.22 AFM Scans of Sample A at 12 Hours of 80% Humidity	98
Figure 4.23 20 x 20 AFM Scans of Sample A at 24 and 36 Hours of 80% Humidity	99

Figure 4.24 50 x 50 AFM Scan of Sample A at 48 Hours of 80% Humidity	99
Figure 4.25 3D 50 x 50 AFM Scan of Sample A at 48 Hours of 80% Humidity	100
Figure 4.26 AFM Scans of Sample A at 48 Hours of 80% Humidity	100
Figure 4.27 50 x 50 AFM Scan of Sample A at 48 Hours of 80% Humidity	101
Figure 4.28 3D 50 x 50 AFM Scan of Sample A at 48 Hours of 80% Humidity	102
Figure 4.29 20 x 20 AFM Scan of Sample A at 48 Hours of 80% Humidity	103
Figure 4.30 Profile Path of AFM Scan of Sample A at 48 Hours of 80% Humidity	103
Figure 4.31 20 x 20 3D AFM Image of Sample A at 48 Hours of 80% Humidity	104
Figure 4.32 AFM Scans of Sample A at 144 Hours of 80% Humidity	105
Figure 4.32 AFM Scan of Sample A at 216 Hours of 80% Humidity	106
Figure 4.34 Profile Path of AFM Scan of Sample A at 216 Hours of 80% Humidity	106
Figure 4.35 3D AFM Image of Sample A at 216 Hours of 80% Humidity	107
Figure 4.36 Decreasing Number of Peaks During Degradation Sample A	108
Figure 4.37 20 x 20 AFM Scan of Sample C at 216 Hours of 80% Humidity	109
Figure 4.38 Profile Path of AFM Scan of Sample C at 216 Hours of 80% Humidity	109
Figure 4.39 Trial 5 Surface Roughness Average of Sample A and C	110
Figure 4.40 Trial 5 Scan Height Range of Sample A and C	111
Figure 4.41 Trial 5 First Sign of Degradation of Sample A at 48 Hours of 80% Humidity	118
Figure 4.42 Trial 5 Average Peak PL Intensity Xbar Chart	119
Figure 4.43 Trial 5 Range PL Intensity Rbar Chart	121
Figure 4.44 20 x 20 AFM Scans of Sample A and C at 0 Hours of 80% Humidity	124
Figure 4.45 20 x 20 AFM Scan of Sample A at 0 Hours of 80% Humidity	125
Figure 4.46 Profile Path of AFM Scan of Sample A at 0 Hours of 80% Humidity	125
Figure 4.47 20 x 20 AFM Scan of Sample A at 0 Hours of 80% Humidity	126
Figure 4.48 Profile Path of AFM Scan of Sample C at 0 Hours of 80% Humidity	126
Figure 4.49 3D 20 x 20 AFM Image of Sample A at 0 Hours of 80% Humidity	127
Figure 4.50 3D 20 x 20 AFM image of Sample C at 0 Hours of 80% Humidity	127
Figure 4.51 20 x 20 AFM Scan of Sample A at 48 Hours of 80% Humidity	128
Figure 4.52 Profile Path of AFM Scan of Sample A at 48 Hours of 80% Humidity	129
Figure 4.53 20 x 20 AFM Scan of Sample C at 48 Hours of 80% Humidity	130

Figure 4.54 Profile Path of AFM Scan of Sample C at 48 Hours of 80% Humidity.....	130
Figure 4.55 20 x 20 AFM Scan of Sample A at 144 Hours of 80% Humidity.....	131
Figure 4.56 Profile Path of AFM Scan of Sample A at 144 Hours of 80% Humidity	131
Figure 4.57 20 x 20 AFM Scan of Sample C at 144 Hours of 80% Humidity	132
Figure 4.58 Profile Path of AFM Scan of Sample C at 144 Hours of 80% Humidity.....	133
Figure 4.59 20 x 20 AFM Scan of Sample A at 216 Hours of 80% Humidity.....	134
Figure 4.60 Profile Path of AFM Scan of Sample A at 216 Hours of 80% Humidity	134
Figure 4.61 20 x 20 AFM Scan of Sample C at 216 Hours of 80% Humidity	135
Figure 4.62 Profile Path of AFM Scan of Sample C at 216 Hours of 80% Humidity.....	135
Figure 4.63 20 x 20 Degraded AFM Scan of Sample C at 216 Hours of 80% Humidity	136
Figure 4.64 Trial 6 Decreasing Number of Peaks During Degradation Sample A and C	137
Figure 4.65 Trial 6 Surface Roughness During Degradation Sample A and C.	138
Figure 4.66 Trial 6 Scan Height Range During Degradation Sample A and C.	139
Figure 4.67 Trial 6 Average Peak PL Intensity Xbar Chart	146
Figure 4.68 Trial 6 Range PL Intensity Rbar Chart.....	148
Figure 4.69 XRD Scan of Sample A at 96 Hours of 80% Humidity	150
Figure 4.70 XRD Scan of Sample C at 96 Hours of 80% Humidity	151
Figure 4.71 Surface Roughness Comparison Trial 5 and 6.	152
Figure 4.72 Number of Peaks in 20 x 20 Scan While Degrading.....	153
Figure 4.73 Average Scan Height Range Comparison Trial 5 and 6.....	154
Figure 4.74 Average Peak PL Intensity Vs. Number of Peaks.....	155
Figure 4.75 Average Peak PL Intensity Vs. Average Scan Height Range	156
Figure 4.76 PL Regression Plot Trial 6 Data.....	158
Figure 4.77 AFM Number of Peaks Regression Plot	159
Figure 4.78 AFM Scan Height Regression Plot.....	160
Figure 4.79 AFM Surface Roughness Regression Plot	161

LIST OF TABLES

Table 1.1 Sample definitions for samples created, analyzed, and compared	3
Table 3.1 Sample definitions for samples to be created, analyzed, and compared.....	40
Table 3.2– Sample Group A1: MAPbI ₃	57
Table 3.3 – Sample Group B1: MAPbI ₃ & Pristine Graphene Flakes in Ethyl Alcohol	57
Table 4.1 Trial 1 bright field and PL images scale bars are 20 μm	69
Table 4.2 Trial 1 PL Intensity Peak Values and Degradation Ratios	72
Table 4.3 Trial 3 bright field and PL images scale bars are 20 μm	75
Table 4.5 Trial 4 peak PL intensity measurements.....	83
Table 4.7 Trial 5 bright field images scale bars are 20 μm	114
Table 4.8 Trial 5 bright field images and PL Peaks sample A 120 Hrs of 80% Humidity.....	122
Table 4.9 Trial 6 bright field images scale bars are 20 μm	141
Table 4.10 Regression Model Treatment Factor Levels.....	154
Table 4.11 Parameter Estimates for Average PL Peak Intensity Regression Model.....	159
Table 4.12 Parameter Estimates for Number of Peaks Regression Model.....	159
Table 4.13 Parameter Estimates for Scan Height Regression Model	160
Table 4.14 Parameter Estimates for Surface Roughness Regression Model	161

LIST OF ABBREVIATIONS

2D	Two Dimensional
3D	Three Dimensional
AFM	Atomic Force Microscopy
BADC	Blow Assisted Drop Casting
CB	Chlorobenzene
CCD	Charged Coupled Device
CH ₃ NH ₃	Methylammonium
CVD	Chemical Vapor Deposition
Cu	Copper
DI	Deionized Water
DMF	Dimethylformamide
DMSO	Dimethylsulfoxide
DSSC	Die Sensitized Solar Cells
EL	Electroluminescence
FD	Force Displacement
FTO	Fluorine Tin Oxide
FF	Full Field
FeCl ₃	Iron Chloride
h-BN	Hexagonal Boron Nitride
HCL	Hydrochloric Acid
HI	Hydroiodic Acid
H ₂ O	Water
H ₂ O ₂	Peroxide
HTL	Hole Transport Layer
IPA	Isopropyl Alcohol
ISO	Film Speed
ITO	Indium Tin Oxide
IV	Current Voltage

J _{sc}	Short Circuit Current
LED	Light Emitting Diode
MAI	Methylammonium Iodide
MAPbI ₃	Methylammonium Lead Triiodide
MoS ₂	Molybdenum Disulfide
NH ₄ Cl	Ammonium Chloride
NH ₄ OH	Ammonium Hydroxide
O ₂	Oxygen
PbI ₂	Lead Iodide
PCE	Photoconversion Efficiency
PEDOT:PSS	Poly(3,4-Ethylenedioxythiophene) Polystyrene Sulfonate
PET	Polyethylene Terephthalate
PGF	Pristine Graphene Flakes
PL	Photoluminescence
PMMA	Poly(methyl methacrylate)
PVA	Polyvinyl Alcohol
PVP	Polyvinylpyrrolidone
R2R	Roll-to-roll
RH	Relative Humidity
RPM	Rotations Per Minute
SEM	Scanning Electron Microscopy
Spiro-OMETAD	N ² ,N ² ,N ^{2'} ,N ^{2'} ,N ⁷ ,N ⁷ ,N ^{7'} ,N ^{7'} -octakis(4-methoxyphenyl)-9,9'-spirobi[9H-fluorene]-2,2',7,7'-tetramine
TEM	Transmission Electron Microscopy
UV	Ultraviolet
V _{oc}	Open Circuit Voltage
XRD	X-Ray Diffraction

GLOSSARY

Atomic Force Microscope (AFM): Method of measuring surface topography at a nanometer scale

Degradation Rate: Opposite of stability; Rate at which a material loses the ability to convert photons into electrons; When MAPbI₃ no longer can create electrons from photons; the decomposition of MAPbI₃ into PbI₂

Graphene: 2D Material; Carbon honeycomb structure; Hypothetical electrode contact

Halide Perovskite: Cell of the makeup ABX₃ (A = organic ammonium cation, Cs⁺; B = Pb²⁺; X = Cl⁻, Br⁻, I⁻)

ITO: Indium Tin Oxide; Typical electrode contact

MAPbI₃: Methylammonium Lead Triiodide, Most common perovskite composition; Control Sample; Sample A

Perovskite: Material of the crystal structure A¹⁺B²⁺X⁻¹₃

Photoluminescence (PL): Measurement taken of re-emitted photons by semiconducting material; photoconversion rate

Power Conversion Efficiency (PCE): Percentage of photons converted into usable electricity

Solar Cell: Device that converts light into electricity

Stability: $S = PL/t = PCE/t$; Power Conversion Efficiency over time; Ability to continue converting photons into electrons; Ability for MAPbI₃ to remain as a semiconducting material with a band-gap of approximately 1.6 eV (775nm peak PL intensity).

ABSTRACT

Author: Reiter, Kyle, J. MS

Institution: Purdue University

Degree Received: May 2019

Title: Reduction of Degradation of $\text{CH}_3\text{NH}_3\text{PbI}_3$ Solar Cells with Graphene Encapsulation.

Committee Chair: Helen McNally

Organic-inorganic halide perovskite solar cells have increased efficiencies substantially (from 3% to > 22%), within a few years. However, these solar cells degrade very rapidly due to humidity and no longer are capable of converting photons into electrons. Methylammonium Lead Triiodide ($\text{CH}_3\text{NH}_3\text{PbI}_3$ or MAPbI_3) is the most common type of halide perovskite solar cell and is the crystal studied in this thesis. Graphene is an effective encapsulation method of MAPbI_3 perovskite to reduce degradation, while also being advantageous because of its excellent optical and conductive properties. Using a PMMA transfer method graphene was chemical vapor deposition (CVD) grown graphene was transferred onto MAPbI_3 and reduced the MAPbI_3 degradation rate by over 400%. The PMMA transfer method in this study is scalable for roll-to-roll manufacturing with fewer cracks, impurities, and folds improving upon dry transfer methods. To characterize degradation a fluorescent microscope was used to capture photoluminescence data at initial creation of the samples up to 528 hours of 80% humidity exposure. Atomic force microscopy was used to characterize topographical changes during degradation. The study proves that CVD graphene is an effective encapsulation method for reducing degradation of MAPbI_3 due to humidity and retained 95.3% of its initial PL intensity after 384 hours of 80% humidity exposure. Furthermore, after 216 hours of 80% humidity exposure CVD graphene encapsulated MAPbI_3 retained 80.2% of its initial number of peaks, and only saw a 35.1% increase in surface height. Comparatively, pristine MAPbI_3 only retained 16% of its initial number of peaks and saw a 159% increase in surface height.

CHAPTER 1. INTRODUCTION

This chapter of the thesis study introduces the statement of the problem, hypothesis and general background of halide perovskite solar cells and their encapsulation with graphene. It states the purpose and significance of using graphene in conjunction with perovskite solar cells, as well as further explains the assumptions, limitations, and delimitations of the experiments and research evaluating degradation of perovskite samples.

1.1 Statement of Problem

Labs around the world are composing solar cells from a profusion of chemical compositions with photo conversion rates that compete with their silicon counterparts. The first three generations of solar cells are: crystalline silicon, metallic, and organic. However, arguably a fourth and exciting generation of organic-inorganic hybrid solar cells, also known as perovskites, are becoming a focus of research labs. Perovskites have received undivided attention and have undergone remarkable development with a power conversion efficiency that has improved from a 3.8% in 2009 to a 23.2% in 2018 (Yuan et al., 2018). The focus of this thesis is on methylammonium lead triiodide ($\text{CH}_3\text{NH}_3\text{PbI}_3$ or MAPbI_3) perovskite solar cells.

Concurrently, new applications of the 2D carbon material, graphene are being found and used across a wide array of electronics. Graphene has many applications and special properties that make it a very unique two-dimensional material (Geim, 2009). There is much research on using nanolayers of graphene for front and back contacts of solar cells of all types (Selopal, 2015). Currently, perovskite solar cells are unable to maintain efficiency in atmospheric conditions due to humidity (Yang, Siempelkamp, Liu, & Kelly, 2015). Recent research has also shown that graphene has an ability to be impenetrable to water molecules (Jiao et al., 2015). An atomic

simulation created by Jiao et al. (2015) shows that a graphene coating will protect MAPbI₃ from reaction with water. Without any protection MAPbI₃ degrades into PbI₂ within days up to months dependent upon the humidity as shown in figure 1.1. Figure 1.2 shows MAPbI₃ that were made at the same time, but one group was stored in air, and the other group was stored in a vacuum sealed jar indicating that preventing humidity and oxidation reduces degradation.

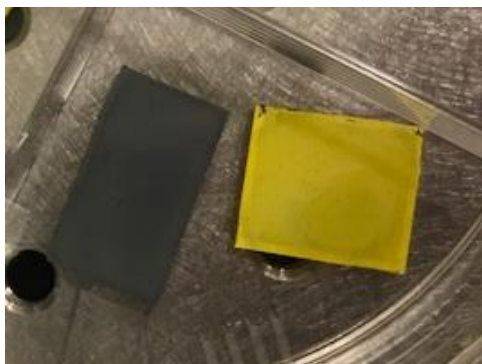


Figure 1.1 MAPbI₃ fresh (black) and MAPbI₃ degraded into PbI₂ (yellow) samples

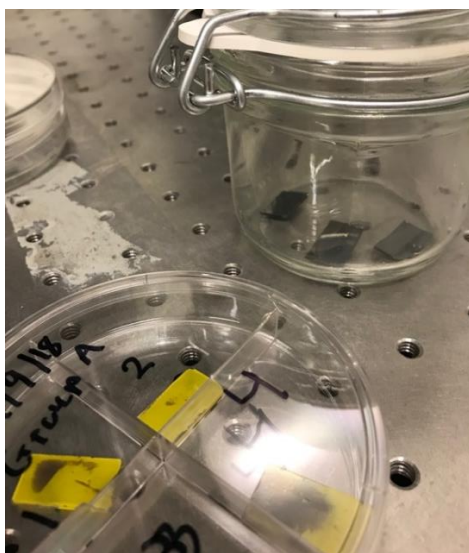


Figure 1.2 MAPbI₃ pristine (black) stored in Vacuum Sealed Jar for 40 days and MAPbI₃ degraded into PbI₂ (yellow) stored in ambient environment for 40 days

Only recently, one research group out of Australia laminated MAPbI₃ with graphene as a method of encapsulation to analyze degradation rates and proved that graphene does reduce the degradation of MAPbI₃ (Wang et al. 2018). This thesis research tested a wet PMMA transfer

method and degradation in a controlled environment of 80% humidity to expand on the work of Wang et al. (2018) and characterized the surface topography and optical properties during degradation of MAPbI₃ on its own and MAPbI₃ with graphene encapsulation. There were three types of samples, referred to as samples A, B, and C created and evaluated in this study and compared are defined below in Table 1.1.

Table 1.1 Sample definitions for samples created, analyzed, and compared

Sample A	MAPbI ₃ (Control Sample)
Sample B	MAPbI ₃ with Pristine Graphene Flakes in Ethyl Alcohol Spin-Coated on Top
Sample C	MAPbI ₃ with CVD Grown Monolayer Graphene Laminated on Top

To get organic-inorganic hybrid solar cells from a research lab into the competitive market of energy generation, improvements to the degradation rates are essential. By using materials provided by Dr. Dou's research group both MAPbI₃ perovskite cells with and without graphene were researched using photoluminescence (PL) and atomic force microscopy (AFM). With the use of the atomic force microscope (AFM) MAPbI₃ with and without graphene was analyzed by measuring and comparing the samples' surface topography during degradation characterized by the reduction in the number of peaks on a sample and the crystal surface height. Degradation rates were also measured using Dr. Dou's research group's fluorescent optical microscope, by measuring photoluminescence (PL) over time exposed to humidity.

1.2 Research Question and Hypothesis

Will the use of graphene encapsulation around a perovskite solar cell reduce degradation rates?

What are the degradation rates of Sample A, Sample B, and Sample C as defined in table 1.1 from PL measurements?

How does the MAPbI₃ surface topography change during degradation?

The hypothesis is that graphene encapsulation will allow the MAPbI₃ semiconducting crystal to maintain long-term stability (ability to convert photons into electrons) by providing a protective layer from H₂O.

1.3 Scope

Much research has been done on different applications of graphene as well as numerous compositions of perovskite solar cells. The application of graphene contacts on perovskite has significant literature and research as shown in section 2.2. Most of these papers measure the optoelectronic properties of the solar cell and the graphene. Until Wang et al. (2018) a missing component to the literature was the use of graphene as an encapsulation tool to reduce degradation and how well the graphene conforms to the MAPbI₃ surface. The research described in this paper will attempt to measure the degradation rate and topography of perovskite cells both with and without graphene contacts as a source of encapsulation. As defined in table 1.1 sample A will be the control sample of pristine MAPbI₃, and samples b, and c will be experimental samples.

Perovskite solar cells can be made of numerous different chemical compositions. This study only focused on one type of chemical composition for a perovskite: methylammonium lead triiodide (MAPbI₃). Humidity in the air is the main cause perovskites degrade quickly. MAPbI₃ reacts with water molecules to form hydrates and degrade into PbI₂, which results in a photoconversion efficiency (PCE) of 0% (Yang, Siempelkamp, Liu, and Kelly, 2015). To improve the stability of MAPbI₃ a layer of graphene should be applied to encapsulate the perovskite cell from harmful water molecules in the air. PL measurements were analyzed to compare degradation rates of the samples. AFM topographical measurements were taken to

analyze the surface roughness of each sample to draw conclusions on how well the encapsulation methods were conforming to the surface of the MAPbI₃ and how the surface changes during degradation.

This paper is less concerned with the composition of the perovskite and more interested in the effect graphene has on the perovskite. Therefore, the main components of the paper use MAPbI₃ as a control to the experiment, to be compared with MAPbI₃ with graphene encapsulation. All sample groups were then analyzed using subsequent measurements to give insight on the hypothesis that graphene improves stability. By comparing the PL and AFM measurements of each of the sample groups a general correlation was made with the use of graphene encapsulation and MAPbI₃ stability.

1.4 Significance

For solar energy to compete with fossil fuels, the prices of solar panels need to drop significantly. Currently, crystalline silicon is capable of 26% photoconversion efficiency, but silicon wafers are expensive to fabricate. Cheaper materials such as organic compounds can be used as solar cells, but have photoconversion efficiencies less than 10%. Furthermore, organic solar cells are not stable enough to convert photons to electricity for nearly as long as silicon solar cells. Crystalline silicon solar cells can be functional for over 20 years, while organic solar cells can degrade within a day. (Yang, Siempelkamp, Liu, and Kelly, 2015) Dr. Dou explained how these cells are instable, mostly due to humidity and oxidation, and that “stabilizing the materials and devices is critically important for the 2D halide perovskites” (Dou, 2017, pg. 11172). Being able to stabilize the cell will bring perovskites closer to commercialization. Reduced prices for perovskite solar panels would then compete with existing solar panels in use today, as well as other methods of energy generation.

Tan et al. (2016) applied graphene contacts on the perovskite cell inside a graphene encasing and subsequently saw improvements in degradation rate against water and acetone. Graphene can provide a protective layer to perovskites, but only few have characterized the measurements of stability, degradation rate, and surface topography. Applied measurements will fortify the theory that graphene improves MAPbI₃ stability; however, more measurements and composition techniques are necessary to bring graphene-perovskite solar cell technology to the commercial market.

1.5 Definitions

- Solar Cell: Device that converts light into electricity
- Perovskite: Material of the crystal structure $A^{1+}B^{2+}X^{-1}_3$
- Halide Perovskite: Cell of the makeup ABX_3 (A = organic ammonium cation, Cs⁺; B = Pb²⁺; X = Cl⁻, Br⁻, I⁻)
- Graphene: 2D Material; Carbon honeycomb structure; Hypothetical electrode contact
- ITO: Indium Tin Oxide; Typical electrode contact
- MAPbI₃: Methylammonium Lead Triiodide, Most common perovskite composition; Control Sample; Sample A
- Photoluminescence (PL): Measurement taken of re-emitted photons by semiconducting material; photoconversion rate
- Atomic Force Microscope (AFM): Method of measuring surface topography at a nanometer scale
- Power Conversion Efficiency (PCE): Percentage of photons converted into usable electricity

- Stability: $S = PL/t = PCE/t$; Power Conversion Efficiency over time; Ability to continue converting photons into electrons; Ability for MAPbI₃ to remain as a semiconducting material with a band-gap of approximately 1.6 eV (775nm peak PL intensity).
- Degradation Rate: Opposite of stability; Rate at which a material loses the ability to convert photons into electrons; When MAPbI₃ no longer can create electrons from photons; the decomposition of MAPbI₃ into PbI₂
- Interlayer Heterojunction Relationship: How well two different surfaces conform to one another at a nanoscale

1.6 Assumptions

Having formulized a hypothesis and scope for the study, the limitations, delimitations and assumptions can now be explained. There are many assumptions being made in this study. Sample-to-sample variation is nearly impossible to eliminate completely and therefore one of the largest assumptions will be that the average of all samples A, B and C can be generalized to represent the whole. For example, for sample A, the MAPbI₃ film may be produced with a refined and repeatable process, but each time, even while taking the same steps, samples may be affected by the surrounding environment, such as cleanliness, temperature, and humidity. To minimize the effects of sample-to-sample variation MAPbI₃ samples were produced at the same time ensuring the same temperature and humidity during conception; however, even while the procedure takes extensive care for cleanliness, micro sized and nanosized dust particles may still land on the samples effecting measurements. Furthermore, even when using the finest tuned procedures and instruments there will be innate variations due to human error for how each MAPbI₃ sample is prepared, such as exact chemical composition ratios, spin-coating times, and time on each hot plate, etc. While human error and the environment can influence the preparation

of graphene, the graphene used in this paper was prepared by Graphene Supermarket and therefore has a professional quality (graphene coverage approximately 95%) and consistent repeatability so human error for this procedure is negligible.

Numerous, uncontrollable effects can change the results of the experiment. While, many steps will be taken to reduce outside influence, error is inevitable. Many assumptions will be made while taking measurements using the AFM. One major assumption that must be made is that variances in the environment during AFM measurements will be noise that can be subtracted out of the signal. To optimize accurate measurement using the AFM, the lab space must be kept as clean as possible, mechanical vibration will be minimized, temperature and humidity must remain as consistent as possible, and electromagnetic radiation must be minimized. All four of these environmental situations can adversely affect the measurements. Environmental effects during the sample's creation and measurement will have an adverse effect on the results; however, by carefully mitigating as much environmental effects as possible and by increasing the number of samples measured, error will be minimalized.

The PL measurements will be assumed to be at the exact same settings, for each measurement taken. Therefore, any changes in the bulb intensity or other inner instrumental components were assumed to remain unchanged. However, any tunable dials or adjustable settings on the instrument or software was the exact same for each measurement. Lastly, all PL measurements were assumed to be within the calibrated range of error of $\pm 0.112\text{nm}$ of each wavelength value calibrated within every 6 months.

1.7 Limitations

The study was limited to the comparison of PL measurements and AFM measurements of samples A, B, and C as defined in table 1.1. To provide more accurate insight to generalize the

results to represent the whole, data of samples A, B, and C were averaged. More measurements on each sample and more samples of each type improved findings. Nine measurement points were used across the samples to find a general characterization for the sample as a whole. Measuring more samples improved statistics to be more representative of the whole and have more authority. However, this implied that the preparation of the MAPbI₃ films always went through the same procedure to be synthesized. The assumptions section clarifies that the procedure should be as repeatable as possible, but due to human error and an inability to completely control the surrounding environment sample-to-sample variations was inevitable. The chemical composition of the samples remained the same but weighed values of MAI and PbI₂ may have varied minutely. Furthermore, measurements were taken on the same instruments, but environmental factors such as temperature, humidity, and mechanical vibration varied minutely. As explained in the definitions, degradation rate was measured by PL intensity over time using an optical microscope and a UV beam of light. PL intensity data was limited to comparing peak values to compute ratios over time. Furthermore, PL data was taken at nine locations for each sample at a location directly to the right of a mark on the sample. PL data was only measured once at each location for each day measured. AFM measurements were limited to contact mode and only topography data was extracted. Lastly, AFM was analyzed at fewer locations than PL due to time constraints to represent the whole.

1.8 Delimitations

While knowing what is included in the experiment and the analysis of the results is important, it is also imperative to be completely clear what the study is not. There was no analysis of other properties, procedures, or issues of MAPbI₃. Furthermore, the study only focused on the PL and AFM topography measurements; therefore, there were no calculations for

common solar cell measurements such as full field (FF), short-circuit current (J_{sc}), and open circuit voltage (V_{oc}). These common solar cell measurements are important for full devices, but for the purpose of this study PL measurements were sufficient to demonstrate that a band gap still exists, thus the MAPbI₃ is still a semiconductor and has not degraded into an insulator.

The graphene, similar to the perovskite underwent a closely repeatable process to minimize sample-to-sample variations, but perfect repeatability is impossible. There was no experimentation on molar ratios in the preparation of the MAPbI₃. Lastly, the transfer of graphene to the MAPbI₃ perovskite was a subsidiary goal of this study; however, incorporation of graphene into an entire solar cell device was not studied.

1.9 Chapter Summary

This chapter gives an overview of the research in this paper, stated the research question, defines the scope, and significance of this study. Chapter 1 also provides the definition of technical terms used in this paper, as well as assumptions, limitations and delimitations of the research presented. The second chapter of the paper will review literature and research on MAPbI₃ and graphene. The third chapter will explain the experimental method to synthesize the three groups of samples, measurement procedures, and the equipment it was taken on. The fourth chapter will present the data taken and cross analyze the sample group measurement results to provide insight on the hypothesis. Finally, the fifth chapter will present an analysis of the data to either reject or fail to reject the hypothesis that graphene encapsulation improves the stability of MAPbI₃ cells.

CHAPTER 2. REVIEW OF LITERATURE

This chapter provides a literature review for background information for this thesis divided into four parts. The first part describes perovskite solar cells including a general background, issues with degradation, and the laboratory procedure that was followed closely for the experimental samples used in this study. The second part is an overview of graphene for use as electrode contacts and builds as a reference for the motivation to use graphene as not only an optimal encapsulation material, but also efficient for the solar cell device architecture. The third part of the literature review explains graphene as a material with the potential benefit for encapsulation around a perovskite and a similar study accomplished during this study that proved graphene reduces degradation of MAPbI₃. The fourth part will describe the tools used for measurement of the solar cells including the fluorescent microscope and measurements using an atomic force microscope (AFM). This chapter aims to explain general background information, new research, the progression of perovskite solar cells, and use of the 2D material graphene.

Before diving into the overview of recent literature, it is important to note that all of the different studies' experimental results in this literature review were accomplished in different environments with unique processes. Consequently, not all findings are completely repeatable. Furthermore, there are inherent limitations of each study's equipment, and human error is always a factor. Lastly, all literature found for this literature review was completed through the online Purdue University library for access to numerous scientific journals with a focus on research conducted in the past few years.

2.1 Perovskite Solar Cells and PL Measurements

Perovskite solar cells are a new material that is gaining traction in the scientific community. In as few as five years perovskites have increased their efficiency from 3.8 to 22.1% (Jiang et al. 2017). A perovskite is an inorganic-organic hybrid semiconducting material that can consist of many different compositions. Most importantly of these varying materials is that perovskites “exhibit strong light absorption, small exciton binding energies, high charge carrier mobilities, as well as long and balanced charge diffusion lengths” (Bai, Yuan, and Gao, 2016, 3898). In short, these perovskite materials can be used for a variety of devices such as solar cells, LEDs, lasers, photodetectors, and transistors since the band gaps are tunable based on the chemical composition. Another characteristic advantage of a perovskite is that they have excellent photoluminescence (PL) properties, which can be manipulated for lighting and display technologies. Bai, Yuan, and Gao (2016) were able to characterize a variety of cesium-based perovskites exhibiting that the many compositions are capable of a wide range of excitation energies represented by different colors and PL intensities with respect to wavelength as shown in figure 2.1 a and b.

Photoluminescence is an excellent method for characterizing bandgap materials. The variation of color in figure 2.1 a is due to the materials having varying PL emissions. The perovskites are put under ultraviolet (UV) light. High-energy UV photons penetrate into the material and are absorbed. If the light has a greater amount of energy than the material’s band gap an electron can be excited from the valence band to the conduction band. If there is no electrode to collect or use excited electrons then they will eventually relax and recombine with the hole created in the valence band. During this recombination a photon will be re-emitted, which is what PL is measuring (Nishikawa and Isu, 1999). Figure 2.1 shows the spectrum of re-

emitted photons from the wide variety of materials used in Bai, Yuan, and Gao's (2016) research.

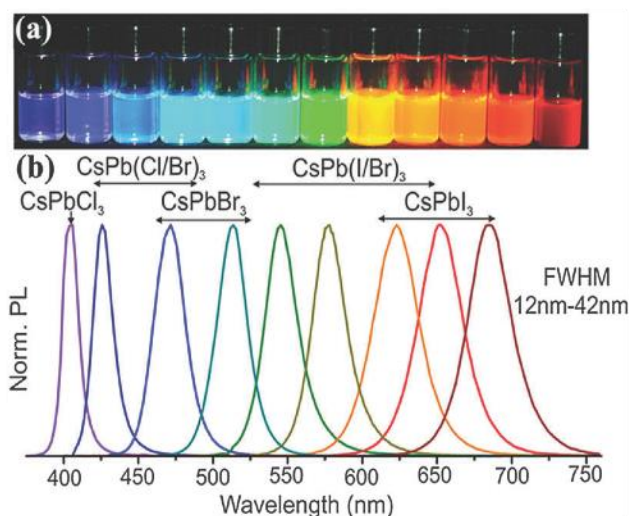


Figure 2.1 Bai, Yuan, and Gao, (2016) a) Image of variety of Cesium based Perovskites under 365nm UV lamp b) the representative PL spectra excited by UV light

It is important to understand what PL measurements represent and the information that can be derived from it. Soufiani et al. (2016) describes PL imaging as the detection of photons generated by radiative recombination of the photo-generated electron-hole pairs. PL data can give insight of the material band gap by comparing the PL intensity peak value to its correlating wavelength. This peak wavelength can easily be translated into photon energy by $E=hc/\lambda$ and used as an estimate of the band gap of the material. However, the PL intensity has arbitrary units of counts that relate to the UV source and CCD chip sensor of the optical microscope. PL intensity holds no real quantitative meaning unless major considerations of the bulb, and power being applied to the sample are considered. What is important to understand is the ratio of UV light illuminating the surface (in candelas) from the optical microscope in comparison with the returned value of intensity (counts in electric pulses), can give insight into the quantum yield of the material (Nishikawa and Isu, 1999). Quantum yield is a more quantifiable measurement, because it is standardized and examines the efficiency of the solar cell. However, there are a

host of standards and calibrations that are necessary for measurements of photoluminescence quantum yields that are beyond the scope of this study (Crosby and Demas, 1971). Furthermore, the scope of this study is to prove that the material still has a band gap, and that the intensity peak value remains as close to the original value after many days while using the same instrument settings.

Purdue's Dr. Dou and his Research Group (2017) research organic-inorganic hybrid solar cells of the makeup ABX_3 ($A = \text{organic ammonium}$, $B = \text{Pb}^{2+}$, $X = \text{Cl}^-$, Br^- , and I^-), which are common halide perovskite solar cell materials. The name halide-perovskite simply means it is an organic-inorganic hybrid solar cell with an ABX_3 crystalline makeup, where X is a halogen (Cl^- , Br^- , and I^-). It is important to note that the physics of how a perovskite converts photons into electrons is the same as its silicon counterparts; only the crystalline intrinsic properties vary. Another important aspect is that perovskite solar cells convert photons into electron hole pairs and then electrodes transport electrons to a drain that is connected to a battery or other methods of energy storage for use. Dou (2017) reports up to a "20% quantum efficiency" for lead based perovskites, which is promising for hybrid solar cell types compared to 26% for silicon (Dou, 2017, pg. 11169). Since this research will be more concerned about the effect that graphene has on the solar cell, the perovskite sample will remain the same composition of Methylammonium Lead Iodide ($\text{MAPbI}_3 = \text{CH}_3\text{NH}_3\text{PbI}_3$).

Why perovskites then? It is quite simple. These hybrid solar cells provide a cheaper and less rigid alternative to silicon solar cells with a wide variety of potential applications. Since perovskites have tunable band gaps, devices can be intricately designed to accomplish exactly what is intended. Furthermore, perovskites are solution processable at low temperatures, and by varying the thickness unique colors can be achieved and if thin enough transparent. Transparent

cells only have electrons excited by ultraviolet radiation and therefore still can collect energy, while being see-through. A collaboration between NREL and Brown University by Zhou et al. (2015) displayed that a variety of colors of the same perovskite can be achieved by changing the thickness of the film by varying the spin-coating speeds as shown in figure 2.2. Therefore, the applications for perovskite solar cells could be much greater than rigid, silicon solar panels.



Figure 2.2 Zhou et al. (2015) Varying perovskite spin coating speeds can control color

Dr. Dou's research group provided the chemicals, processes, and protocols to create perovskite samples and therefore is the driving factor for the solar cell preparation methods. The materials to construct the samples and processes used were based on a procedure by Ahn et al. (2015) because of the article's results of high PCE samples and repeatability. Minute changes from the procedure presented by Ahn et al. (2015) occurred to improve upon the outcome as described in chapter 3. Since the procedure from Ahn et al. was replicated to create the control sample A and the active layer of samples B and C, this paper will have the greatest effect on the experimental procedure. Additionally, the research lab had experience with graphene, but did not actively create graphene, therefore various types of graphene were attained from the third-party

Graphene Supermarket. The procedure and methodology to create the graphene perovskite heterostructure was unique to this study. The replicable procedure is given in detail in the methodology section.

Research on solar cells involves a wide gamut of chemical compositions and types. While silicon, or first-generation solar cells, provides the greatest efficiencies, the materials are the most expensive, and rigid. Second generation solar cells are metallic, such as CdTe or other thin film chalcogenides. Third generation solar cells are organic perovskite or dye sensitized solar cells (DSSCs). The third-generation solar cells on average have been the least efficient, but are the least expensive, and therefore much research is being done to improve their solar cell PCE to match that of their first-generation counterparts. Perovskites, or organic-inorganic hybrid solar cells have been argued as ground breaking for third-generation solar cells due to their improvement from 3% to 22% PCE within five years. Some even consider perovskites a fourth-generation solar cell (Ahn et al, 2015).

One last major consideration that can make perovskite solar cells optimal and advantageous over silicon solar panels is the capability for these materials to be produced in roll-to-roll manufacturing methods. Zuo, Vak, Angmo, Ding, and Gao (2018) created roll-to-roll (R2R) processing of perovskite solar cells to bring perovskites closer to being on the market. R2R manufacturing methods promote an ultra-low-cost and high throughput production. Using a blowing-assisted-drop-casting (BADC) method MAPbI_3 was capable of being prepared and was optimized by adding NH_4Cl and reported a 19.48% PCE. By applying the solution through a slot-die coating process a fairly homogeneous film that resulted in minimal hysteresis for forward and reverse current-voltage scans was achieved as indicated in figures 2.3 a and b (Zuo, Vak, Angmo, Ding, and Gao, 2018).

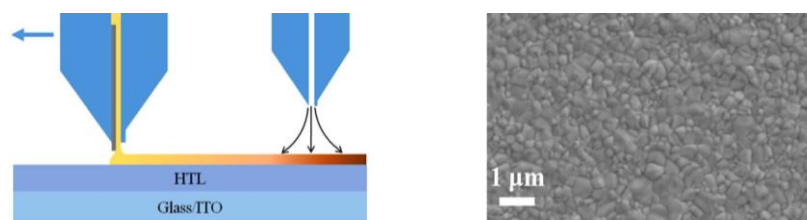


Figure 2.3 Zuo, Vak, Angmo, Ding, and Gao (2018) a) Slot-Die coating process diagram for MAPbI₃ films b) SEM image of slot-die coated MAPbI₃ films

The R2R processing of MAPbI₃ by Zuo, Vak, Angmo, Ding, and Gao (2018) is certainly a breakthrough. First, a PET substrate was coated with PEDOT:PSS, or a hole transport layer (HTL) with speed of production at 0.2m/min with a flow rate of 20 μL/min and then passed by a hot plate at 130°F to anneal. The film was then rolled back to the starting point in the R2R apparatus to coat the MAPbI₃ with an NH₄Cl additive at a speed of .6m/min with a flow rate of 25μL/min with two hot plates afterward, the first at 60°F and the second at 100°F as shown in figure 2.4 a and b. (Zuo, Vak, Angmo, Ding, and Gao, 2018).

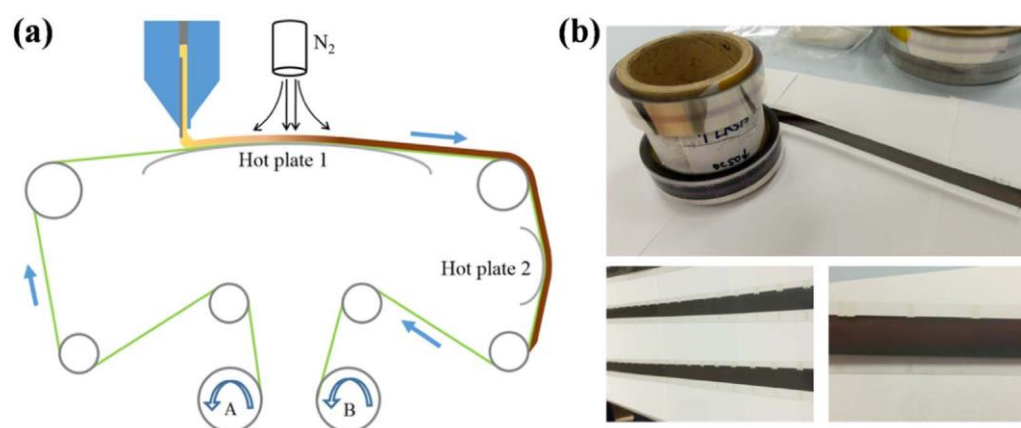


Figure 2.4 Zuo, Vak, Angmo, Ding, and Gao (2018) a) R2R set-up diagram for continuous production of MAPbI₃ film b) Resulting MAPbI₃ films prepared

Clearly the production of perovskites is becoming closer and closer to the market and will have a demanding influence on the electronics and solar cell industry. As R2R production of

MAPbI₃ becomes common place and typical machines are being created flexible solar cell devices will make their way to the market changing the solar industry. With background knowledge on perovskites, PL measurements, and the potential for R2R process manufacturing now the encapsulating material of this study needs to be analyzed.

2.2 Graphene

Graphene has been a promising material for numerous applications with much research being done in the last decade. While graphene will not be used as an electrode in this study for a device, this section of the literature review provides background on graphene as electrode contacts to warrant the use of graphene as encapsulation method, which could be multifunctional as an electrode. Furthermore, much more research has been done using graphene as an electrode rather than as an encapsulation material, therefore this literature review will provide a greater extent of background on graphene used in solar cell devices.

This literature review will first focus on what graphene is and advancements in roll-to-roll manufacturing. Then graphene applications in thin film solar cells will be reviewed as background knowledge for the incorporation of graphene contacts on perovskite solar cells as well as potential encapsulation methods. This section of the review will build a case for using graphene as an encapsulation material compared to other, more rudimentary encapsulating methods.

2.2.1 Graphene: Properties, Roll-to-Roll Production, and Limitations

Within the last decade graphene has been filling up electronic journal articles and press releases. Graphene's original conception was by Andre Geim and Konstantin Novoselov in 2004 by applying scotch tape to a piece of graphite to discover the 2D material. In 2010 both Geim

and Novoselov were awarded the Nobel prize in physics for groundbreaking experiments regarding the two-dimensional material graphene. Millions of dollars of investment into graphene has been rumored for the tech giants such as Apple, Samsung, and Google. According to the Graphene and 2D Materials Investment Report (2018) graphene is now the most widely researched and developed 2D nanomaterial. Currently, over 200 companies are either producing graphene or developing applications (Graphene and 2D Materials Investment Report, 2018). Other 2D materials have also been introduced as alternatives to graphene that contain a bandgap such as “molybdenum disulfide, MoS₂, hexagonal boron nitride (h-bN) and phosphorene,” because they contain many of the same property characteristics as graphene such as “high electrical conductivity, high thermal conductivity, high mechanical strength, gas diffusion barriers, high chemical stability, and radiation shielding” (Graphene and 2D Materials Investment Report, 2018, abstract).

Graphene is a single-atomic layer sheet of carbon, oriented in a honeycomb lattice (Geim, 2009) as shown in figure 2.5 Since graphene is one atomic layer of carbon the material is considered two dimensional, and is a strong material that can be transparent and very conductive. Banszerus et al. (2016) reported finding chemical vapor deposition (CVD) grown graphene to have over 28 μm of ballistic transport. The mechanical, electromagnetic, optical, and thermal properties of graphene is what makes it so attractive for use as a contact for electronics.

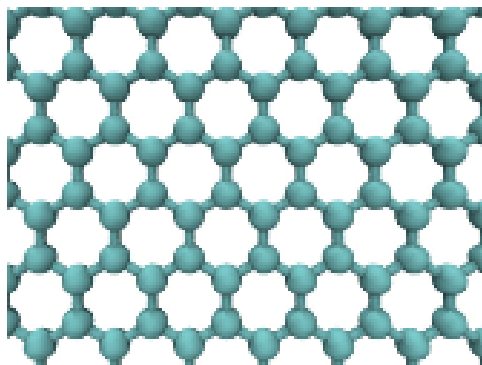


Figure 2.5 Geim, A., (2010) Schematic of graphene honeycomb, carbon lattice

Another important aspect of graphene is that it can be produced in a roll-to-roll manufacturing fashion as shown in figure 2.6. When implemented with roll-to-roll manufacturing of perovskite solar cells entire devices of thin-film solar cell rolls could be quickly produced, for a low cost, and easily adhere to surfaces. Using transparent graphene contacts and transparent perovskite solar cells, rolls of entirely transparent solar cell devices can hypothetically be developed to be put on windows, such as skyscrapers to add power to the grid, onto electric cars, or handheld devices to be constantly charging when in the sun. Even by 2010 graphene was being produced roll-by-roll. Bae et al. (2010) successfully created 30-inch graphene films for transparent electrodes as shown in figure 2.7.

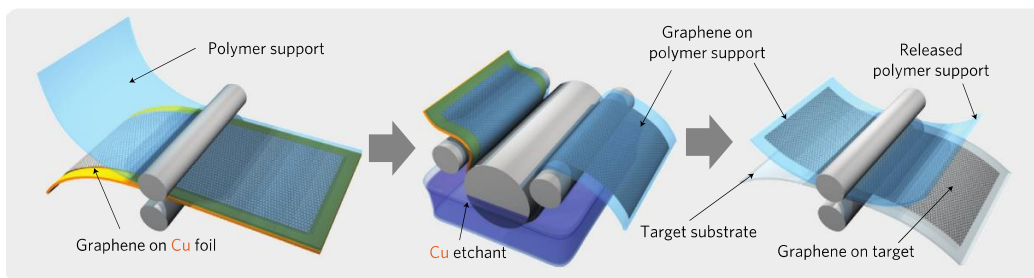


Figure 2.6 Bae et al. (2010) Schematic of roll base production of graphene films grown on copper

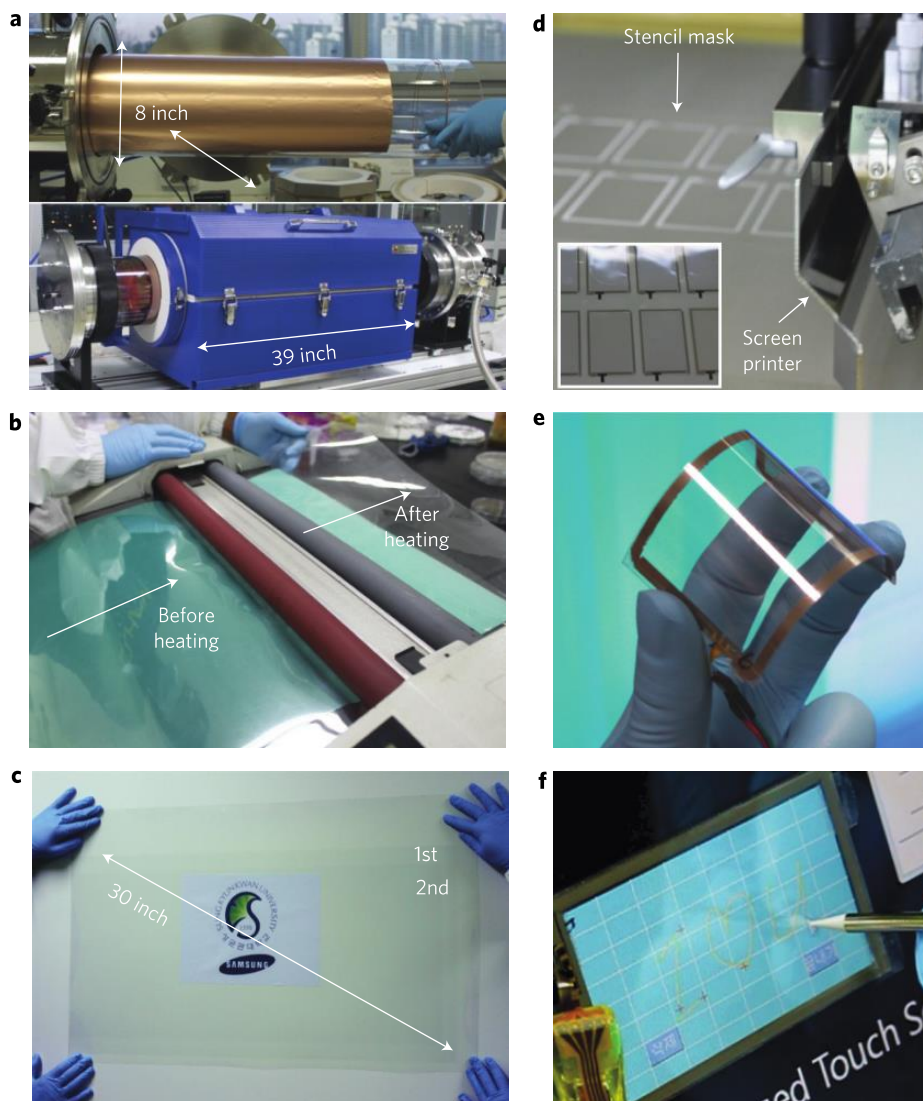


Figure 2.7 Bae et al. (2010) photographs of roll-based production of graphene films

The rolls produced by Bae et al. (2010) were created using a tubular quartz reactor for a CVD system synthesizing a monolayer graphene film, which resulted with 97.5% optical transparency and a sheet resistance of $\sim 125 \Omega \square^{-1}$. When four sheets of graphene were stacked on each other the optical transparency dropped to 90%, but the sheet resistance dropped to $\sim 30 \Omega \square^{-1}$, which indicates it would be worth stacking the graphene layers to optimize electrode conductivity (Bae et al., 2010). In comparison typical touch sensors and flat panel displays use

indium tin oxide (ITO) which has a sheet resistance of $100\Omega\text{□}^{-1}$ therefore graphene provides an advantageous alternative for transparent electrodes. The roll-to-roll production of graphene presented by Bae et al. (2010) makes use of a polymer support, such as polymethyl methacrylate (PMMA), which is the same polymer used to for the transfer procedure in this study; however, Bae et al. used a heat transfer tape, which explained later can result in more cracks to the graphene film.

Throughout the last decade CVD machines have been researched to improve roll-to-roll manufacturing of graphene with success. Polsen, McNerny, Viswanath, Pattinson, and Hart, (2015) created a concentric tube chemical vapor deposition (CTCVD) reactor for roll-to-roll production of graphene capable of creating 500mm/min. However, at faster speeds the quality of the graphene was compromised. At slower speeds such as 25mm/min the graphene had fewer gaps; however, the Cu foil grains were a limiting factor for the quality of graphene.

Purdue's own Alrefae et al. (2017) presents an article on process optimization of graphene growth in a roll-to-roll plasma CVD system. Using a statistical approach and a design of experiments (DOE) methodology found that the graphene quality is heavily influenced by the gas pressure, nitrogen, oxygen, and plasma power (Alrefae et al., 2017). Furthermore, the study presented by Alrefae et al. (2017) concluded that any presence of Ar^+ , C_2 , H_α , CN, and O led to defects and the plasma limits the quality of the graphene, but by optimizing the inputs for the plasma CVD rates can be raised up to 1000mm/min of high-quality graphene production.

As improvements to the CVD machines that make graphene are implemented and techniques optimized graphene is becoming closer to being in typical devices such as smartphones, laptops, televisions, and solar cells. Mohan, Lau, Hui and Bhattacharyya (2018) touch on how graphene production has been improving but is still bottlenecked by mass

production. Even with issues of mass production in the last decade the “production of graphene is becoming more and more inexpensive and available in large quantity,” but there still remain issues with yield making graphene oxide a common alternative (Mohan, Lau, Hui and Bhattacharyya, 2018, 207). Mohan, Lau, Hui and Bhattacharyya (2018) specifically mention that graphene is an excellent option as transparent and flexible electrodes for solar cells. While graphene production still has significant room for improvement and alternative materials are being developed it should still be considered a material with the greatest potential for use as a transparent electrode on solar cells.

2.2.2 Graphene and Perovskites

Many of the experiments synthesizing the use of graphene and solar cells have shown a better optical transmission rate than typical contacts and better current carrier concentration suggesting graphene has more capability than just an encapsulation material. Furthermore, there are numerous advantages of using perovskites than the second-generation solar cells. Ning, Dou, and Yang (2017) researched third-generation solar cells specifically using CsPbBr_3 and measured a band gap between 1.8 and 3.0eV, which is an optimal range for photodetectors because wavelengths of visible light have enough energy to be excited from the valence band to the conduction band. Sun et al. (2017) used a different third-generation composition and focused on the use of organic solvents, such as ethanol, methanol, and acetone, as an environmentally friendly, repeatable, and scalable method for placing graphene-oxide onto various substrates rather than heating methods. Tan et al. (2016) constructed a perovskite solar cell with graphene electrodes of a width of 100nm using electron beam lithography (EBL) and plasma etching as shown in figure 2.8 a and a scanning electron microscopy (SEM) image of the actual fabricated device in figure 2.8 b. Transparent graphene electrodes run across an active layer of perovskite

material, which converts photons into electrons. The graphene contacts serve as a conductive, strong material to collect and move electrons, or current, between a source and drain. Gaps of 100nm between graphene electrodes improved effective carrier concentration compared to wider gaps. More current may occur, because excited electrons in the perovskite layer may not travel far before recombining, therefore by applying smaller electrode gaps the excited electrons are more likely to reach the conductive electrodes and contribute to collected current (Tan et al, 2016). In the future these gaps may shrink, further improving the current collection from the photoelectric conversion region.

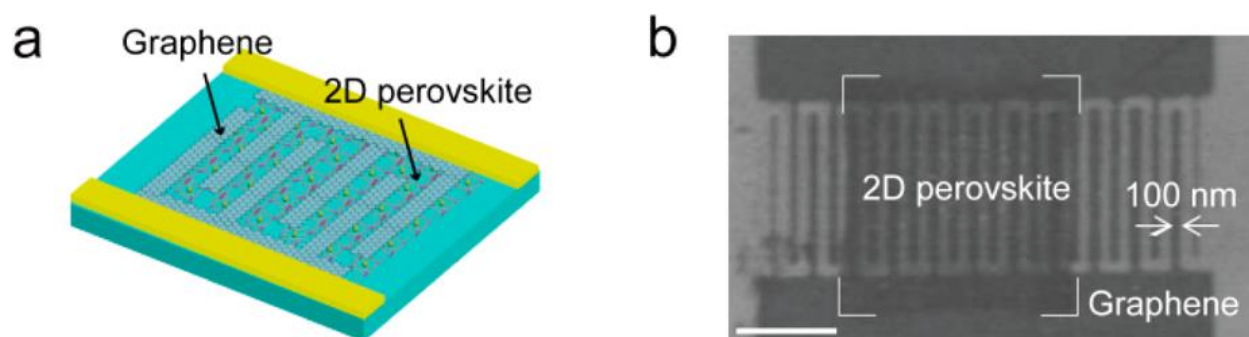


Figure 2.8 Tan et al. (2016) (a) Illustration of electrodes, (b) SEM image of device

The new transparent electrode geometry provided by Tan et al. (2016) is a groundbreaking step for improving organic solar cells. Current work by many researchers is how to make consistent production of graphene electrodes for perovskites and improvements of degradation rates (Dou, 2017). The use of graphene with perovskites is typically for advantages of electronic properties in a device, but can also be used as a gas barrier and encapsulation device to reduce degradation.

2.3 Graphene as a Gas Barrier

An essential aspect for perovskite solar cells to compete in a modern-day market place is improving the degradation rate. Currently, perovskite solar cells are not stable at room

temperature and degrade rapidly due to water molecules in the air (Dou, 2017). One hypothetical method of improving the perovskite solar cells is through encapsulation of the cell in graphene (Tan et. al, 2016). The carbon-carbon bond lengths in graphene are approximately 1.42Å, and comparatively the molecular size of H₂O is 2.75Å and O₂ is 1.52Å. Therefore, the major molecules that cause degradation of a perovskite are too large to permeate through graphene. Applying a graphene encapsulation around perovskite can potentially improve the degradation rate by preventing water molecules from coming in contact with the active perovskite layer.

For the purpose of this experiment the graphene used cannot allow water molecules to interact with the perovskite material. Kim et al. (2017) used a composition of graphene as an encapsulation method to create a gas-barrier for a silicon solar cell and witnessed long-term stability. Both transparent graphene electrodes and a protection layer of graphene were applied on a silicon solar cell. Twenty solar cells were studied with a varied amount of silver nanowire (Ag NW) dopants to find that .1 wt.% (weight percentage) returned the best results. Ag NW/graphene contacts and graphene/Ag NW/graphene contacts and encapsulation were compared over a 30-day period to compare losses over time in photoconversion efficiencies (PCE) at 25°C and 50% humidity. The solar cell with the encapsulation lost 6.4% of its original PCE value after 30 days (from 3.51% to 3.28%) compared to the non-encapsulated solar cell, which lost 25.8% of its original PCE value (from 3.31 to 2.45%) (Kim et. al, 2017, pg. 1140). The results from Kim et al. (2017) show that the degradation rate of silicon solar cells decreased nearly 20% by using a graphene encapsulation. However, the improvement in this case was contributed to a lower rate of oxidization of the electrode contacts. On the contrary, the degradation rate of perovskite solar cells is more contributed to water molecules rather than oxidation. Another

study proved the ability for graphene to also be a barrier for water molecules, but not to keep water molecules out, rather to trap water molecules in a graphene sandwich.

2.3.1 Graphene Used to Encapsulate Water Molecules

Another study from Sasaki, Kituara, Yuk, Zettl, and Shinohara (2016) used a graphene sandwich device to encapsulate a water molecule. While the purpose of this study was using transmission electron microscopy to understand the effects on a water molecule, the use of two graphene sheets to encapsulate a liquid exclaims the impermeability of graphene by H₂O. Figure 2.9 shows TEM images over time of a graphene sandwich around water molecules, where the white dot in the center is an air bubble.

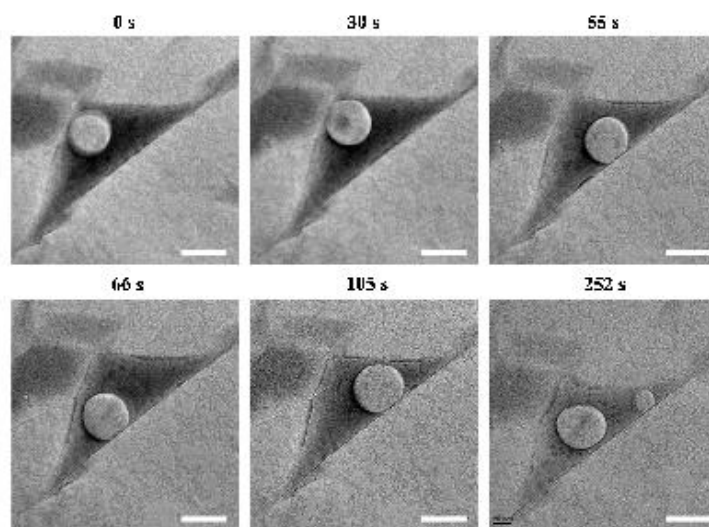


Figure 2.9 Sasaki, Kituara, Yuk, Zettl, and Shinohara (2016) TEM images of graphene water encapsulation with scale bar of 50nm.

However, Harris, Elias and Chung (2016) emphasize that the quality of graphene must be very high, to have a tight-knit lattice spacing, which makes reproducibility difficult. Sasaki, Kituara, Yuk, Zettl, and Shinohara (2016) suggest a different tweak than the preparation method introduced by Aghigh et al. (2015) with a preliminary step by using a hydrogen gas on the copper foils for the CVD grown graphene to create smaller lattice spacing disallowing any water

molecule to pass through. The method for creating tight-knit graphene by Sasaki, Kituara, Yuk, Zettl, and Shinohara (2016) should be a major consideration for graphene that is used for perovskite encapsulation.

2.3.2 Graphene Covering Perovskite Simulation

Jiao et al. (2015) used a complex simulation program “based on density functional theory (DFT) by using plane wave basis Vienna ab initio simulation package (VASP) code, implementing the projector augment wave (PAW) method” for the atomic calculation of graphene on top of MAPbI₃ for atomic geometry, electronic, and optical properties (Jiao et al., 2015, pg. 82347). Figure 2.10 shows the atomic geometry of graphene on MAPbI₃, as well as the side views of graphene on MAI and PbI₂ for a better understanding of the atomic level geometries and interactions with MAPbI₃.

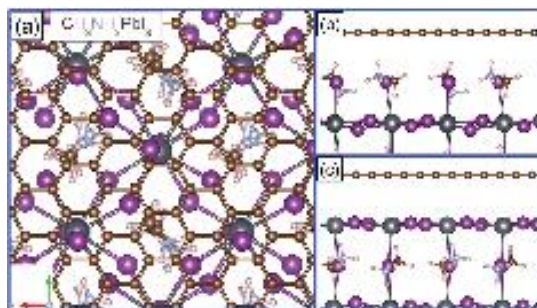


Figure 2.10 Jiao et al. (2017). (a) Top view and (b) side view of graphene/MAI interface; (c) side view of graphene/PbI₂ interface. Brown, black, silver, violet and light pink balls represent C, Pb, N, I and H atoms, respectively.

The simulation also gives good estimations on many characterizations of the two materials. The equilibrium distance between the graphene and MAI/PbI₂ surface was found to be 2.8/3.8 angstroms, the interface binding energy was found to be -1.52 eV and -1.79eV respectively, which indicates a high structural stability. Furthermore, the band gap of MAPbI₃ was found to be 1.58 eV, which is in agreement with experiments. The simulation also showed that electron accumulation occurred on the iodine molecules on MAI and depletion occurred

around the CH_3NH_3 molecules. Another advantage presented by the use of graphene on MAPbI_3 is that the dielectric function simulation suggests enhanced light absorption compared to pristine MAPbI_3 .

The most relevant finding from the simulation that supports the work of this paper was simulating graphene/ MAPbI_3 in a water environment. AIMD simulations were undertaken to put 36 water molecules placed on top of a graphene layer that sandwiched a MAPbI_3 . Most importantly, the simulation concluded, “No water molecule was able to reach the perovskite surface and bond with the Pb cations (Jiao et al., 2015, pg. 82349).” Furthermore, Jiao et al. (2015) concluded, “the stability of methylammonium lead triiodide in a water environment can be maintained via the graphene-coated strategy (Jiao et al., 2015, pg. 82349).” Lastly, there were no experiments that had supported this simulation’s findings until very recently.

2.3.3 Graphene and Polymer Encapsulations of Perovskite

During the course of this study a research group collaboration between Australia and China successfully proved that graphene on MAPbI_3 reduces degradation. As was the original goal of this study graphene encapsulation does act as a gas barrier to ambient humidity. Wang et al. (2018) transferred graphene developed from Graphene Supermarket to MAPbI_3 using a gel film to create the heterostructure as depicted in figure 2.11.

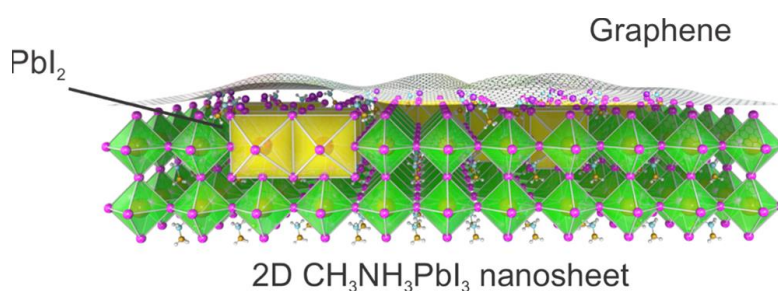


Figure 2.11 Wang et al. (2018) Schematic of graphene/ MAPbI_3 heterostructure

In the groundbreaking study presented by Wang et al. (2018) a two-dimensional crystal of MAPbI₃ was formed by CVD. Graphene was then applied to part of the sample and individual locations of the sample with and without graphene were analyzed using photoluminescence (PL). Wang et al. (2018) also provides insight on the degradation process of MAPbI₃, where humidity and the ambient environment is mainly caused by cation evaporation leading to reduced PL intensities and consequently lower PCEs. Figure 2.12 shows 3 consecutive days of PL measurements when stored in ambient conditions (RH ≈ 30%), where by the third day there was no detectable PL signal. Degradation was then confirmed by using Raman measurements where after two days in ambient conditions where the spectral bands of MAPbI₃ were no longer prevalent, but rather the spectral band of PbI₂ crystals were present (Wang et al., 2018).

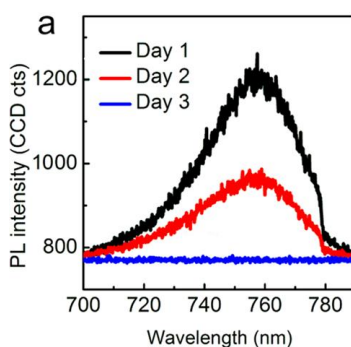


Figure 2.12 Wang et al. (2018) Perovskite PL intensity as a function of time in ambient conditions

Figure 2.12 indicates the quickly decreasing PL intensity of MAPbI₃ without graphene encapsulation. The graph shown in Figure 2.12 will be very similar to the data displayed in this report and a prime example of how to prove degradation is occurring. However, Wang et al. (2018) did not measure a 2D perovskite with graphene encapsulation during ambient degradation to see how well graphene compares. Instead Wang et al. (2018) compared degradation of a single sample of 2D perovskite with graphene during heat treatment at 150°C for 20min. Figures 2.13 a

and b below show the PL measurement comparison of the area of the sample that was covered with graphene and the area that was not.

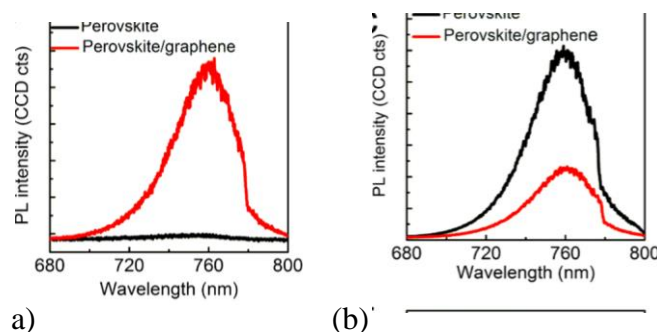


Figure 2.13 Wang et al. (2018) PL intensity graphs of MAPbI₃ with and without graphene (a) Initial PL reading (b) PL reading after 20 min of 150 °C heat treatment

Figure 2.13 a and b indicate that while the initial reading of PL intensity for the graphene laminated MAPbI₃ was lower than the unlaminated section of the sample, after twenty minutes of heat treatment the perovskite without graphene no longer had any PL intensity, whereas the graphene laminated section still had a sensible PL reading. The graphs shown in figures 2.13 will also be an essential method for comparing samples in this study, however the results of this study will be like the combination of figures 2.12 and 2.13. That is, the results in this study will be taking PL measurements of both graphene covered and pristine perovskite crystals over the course of several days in a controlled humidity environment. Figure 2.14 shows the comparison in ambient conditions over the course of 28 days to exclaim how graphene covered MAPbI₃ degrades much slower where after 30 days 35% of the original PL intensity was retained likely due to the graphene on MAPbI₃ entrapping evaporated cations. (Wang et al. 2018).

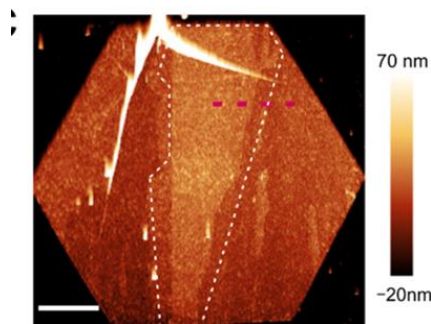


Figure 2.14 Wang et al. (2018) PL intensity ratio graphs of MAPbI₃ with and without graphene over 30 days

While this article proved what this study had intended to prove there will still be merit in this study by controlling input parameters, diversifying the data results, and studying the surface topography of the graphene/MAPbI₃ heterostructure. The full procedure is described in detail in chapter 3; however, it is important to summarize how this study will expand and differentiate from the study presented by Wang et al. (2018). The synthesis of the MAPbI₃ will be quite different in this study and will not be using CVD methods to create a two-dimensional crystal, but rather a three-dimensional MAPbI₃ film. While this study will also use PL intensity as the major indicator of degradation, the samples will be stored in a controlled humidity environment rather than uncontrolled ambient conditions. The most important difference in this study from the study presented by Wang et al. (2018) is the transfer process of graphene to MAPbI₃. Wang et al. (2018) reported using a gel film and a dry transfer process to laminate graphene on the 2D MAPbI₃ crystal. This study will make use of a wet PMMA transfer method that reduces cracks and improves conformity compared to dry transfer methods as explained in section 3.3.5 and is an improvement to the method presented by Wang et al. (2018). AFM surface topography will also, be studied in depth to compare surface degradation between sample A and C. Furthermore, this study will make use of multiple samples, that are either fully encapsulated by graphene or

are not at all. By using multiple samples, the statistical power should improve upon the data results presented by Wang et al. (2018).

While graphene is certainly an effective and useful material to encapsulate perovskites, there are other methods that can be useful. Wang et al. (2018) suggests that h-BN may be another useful gas barrier. Messegee, Mamun, Ava, Namkoong, and Abdel-Fattah (2019) studied the effects of encapsulation of numerous different polymers to increase the stability of MAPbI₃ including polymethyl methacrylate (PMMA), polyvinyl alcohol (PVA), polyvinylpyrrolidone (PVP), and sodium polyacrylate (NaPA). Using X-ray diffraction (XRD) it was found that PMMA was the most effective polymer studied to reduce degradation when kept in a controlled environment of approximately 40% relative humidity for 0 hours, 48 hours, and 72 hours. Larger pin-holes in NaPA and PVA films were the main issues with those polymers whereas PVP exhibited smaller and less pin-holes. PMMA showed that no pin-holes were present. Finally, surface degradation of each sample was conducted to find that PMMA coatings resulted in little to no surface degradation compared to 15.67% for PVP, 30.68% for PVA, and 35.93% for NaPA (Messegee, Mamun, Ava, Namkoong, and Abdel-Fattah, 2019). Of all the potential materials that can be used for encapsulation, however, graphene remains an optimal material because of its intrinsic properties and capability of being used as conductive, transparent electrodes as well.

2.4 Atomic Force Microscopy

Up to this point the literature review has focused on explaining what perovskite solar cells are, using graphene electrodes on solar cells, and graphene encapsulation theory and methodology. This section will describe the atomic force microscope and what it will measure. AFM will be used to characterize the surface topography during degradation. By analyzing nanoscale topography of MAPbI₃ with and without graphene an understanding of how well the

graphene is able to conform to the MAPbI₃ surface can be found. A more conformal contact will provide less air gaps reducing electrical resistance and degradation. AFM will also be used to investigate how the surface topography of MAPbI₃ changes during degradation. The remainder of the literature review will examine conceptual understanding of the AFM, instrumental methodology, and applicable analysis techniques of surface topography for a better understanding of samples A, B, and C. The exact instrument settings, tips used, scan settings, and post processing will be explained in the AFM methodology section.

Since its invention, the AFM has been an extremely accurate method using a nanoscale sized tip controlled by a piezoelectric to define nanoscale surface geometry (Binnig and Quate, 1986). AFM has a wide range of applications. Dr. McNally used AFM to apply nano/micro-punctures to neuron membranes and in-situ imaging of the dying neurons (McNally and Borgens, 2004). McNally's study is a paramount example of how AFM can both manipulate and measure samples. AFM tips were used to provide nanoscale measurements and imaging of surface topographies as well as to interact with the cell by physically cutting the membrane, thus damaging the neuron. The study provides real time images of the death of the neuron cell body after nanoscale damage (McNally and Borgens, 2004). The AFM successfully provided precise quantitative measurements of distance, surface area, and volume, which will be the main use of the AFM in this study for measuring samples A, B, and C.

To measure surface topographies an Innova scanning probe microscope (Veeco Digital Instruments, Santa Barbara, CA) will be used with a Bruker DNP silicon nitride tip. Contact mode will be used to take measurements. Kollak and McNally (2013) used AFM contact mode surface topography measurements on polycrystalline silicon solar panels and an organic solar cell from a conductive polymer. The organic solar cells prepared were P3HT:PC3M with and

without a PEDOT:PSS transport layer (Kollak and McNally, 2013). However, scans in this study were done using a dynamic-mode, oscillating cantilever. Kollak and McNally (2013) measured depths, widths and surface topographies to determine the surface area available to collect energy for each sample. Surface areas of a flat image and of a projected image can be created in the Nanoscope software and compared to find the surface area difference and how much surface area will be contacted by photons (Kollak and McNally, 2013).

The AFM uses a set point voltage of X to be translated into a force on the sample by using a laser that bounces off the back of a cantilever and into a photodiode. A set point voltage (i.e. 2.5 volts) is a way to know how much force is between the tip and sample surface by indicating how much the cantilever is bent thus how far the laser has been shifted from the center of the photodiode. The z -height of the piezoelectric then determines the height changes of the sample. AFM uses a nanoscale tip connected to a cantilever, or metal rod of a known spring constant to determine the Z direction distance by using Hook's law: $F = -kd$. As the cantilever bends the laser moves off center of the photodiode changing the voltage. There are many different types of tips, which have a large effect on how the topography is measured, also known as sample-tip geometry; however, the AFM provides surface topography with atomic resolution.

2.5 Measurements Using Photoluminescence

Photoluminescence is a method used in conjunction with an optical microscope to measure many organic and semiconducting materials. The measurement of photoluminescence occurs by shining UV light on a semiconducting material, which will excite an electron from the valence band to the conduction band. After a short time, the electron will relax back into the valence band and recombine with the hole where photons will be re-radiated and captured by the optical microscope. Being able to detect re-emitted photons proves that the material has a band

gap (Soufiani et al., 2016). Very early in the conception of fluorescence it was understood that there was a group of materials where light can excite a material to glow or emit out photon radiation that has a shorter wavelength than the light that was used to excite the material (Flourescence, 1926). Later on, with a better understanding of quantum mechanics, it was understood that the absorbed energy from the UV light is typically greater than the reemitted light due to recombination, which is known as Stokes' shift (Aoki, 2006).

Photoluminescence (PL) has been an increasingly useful and nondestructive method to identify electronic characteristics for many materials. Aoki (2006) describes the uses of PL spectroscopy as a “sensitive tool for investigating both intrinsic electronic transitions between energy bands and extrinsic electronic transitions at impurities and defects of organic molecules, semiconductors and insulators (Aoki, 2006, pg 76).” Soufiani et al. reports that PL is a paramount tool for measuring MAPbI₃ and used PL imaging to understand degradation of MAPbI₃ when fresh and after being stored in a dark glove box for two months. They found a peak intensity wavelength at approximately 773 nm as shown in figure 2.15 Furthermore, Soufiani et al. (2016) found that after two months in the dark glove box the open circuit voltage (V_{oc}) had barely changed as indicated by the same PL peak occurring near the same wavelength of 773 nm.

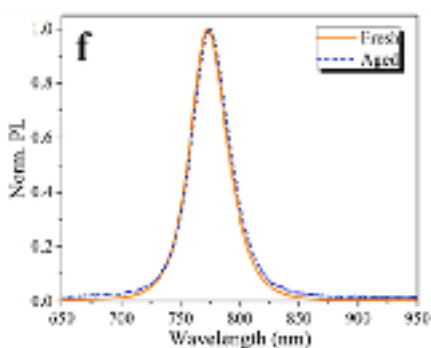


Figure 2.15 Soufiani et al. (2016) Normalized PL of fresh and aged MAPbI₃

It is important to understand that the PL intensity values were normalized so the peak intensity values were likely not the same, but used PL to show there was no shift in wavelength where the peak occurs. Soufiani et al. (2016) used electroluminescence (EL) imaging of the fresh and aged MAPbI₃ samples to show degradation occurred indicated by growing pin-holes as shown in Figure 2.16. While EL will not be used in this study AFM can be used to indicate pin-hole sizes.

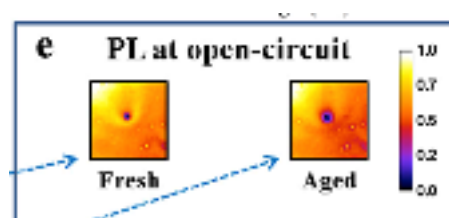


Figure 2.16 Soufiani et al. (2016) Fresh and Aged MAPbI₃ pin-hole growth

PL intensity data are the primary measurement in this study to indicate degradation. Soufiani et al. (2016) did confirm that the aged MAPbI₃ had reduced values of J_{sc}, FF, and PCE, which were indicated by I-V curves; however, with the exact same parameters, PL intensity lowering also indicates a lowering in PCE. Crosby and Demas (1971) describe the ability of finding quantum yields from PL measurements. However, Crosby and Demas describe finding the total relative photon output of a material to be difficult, tedious, “time consuming and introduce substantial sources of error” (Crosby and Demas, 1971, pg. 1011). Rather than having to consider the grating, photodiode, UV light, and many other PL components to calculate a total photon count, PL measurements will retain the exact same settings for each measurement and compare the ratio of PL intensity, which has a direct correlation to PCE.

2.6 Raman Spectroscopy and X-Ray Diffraction

Additional measurements that were useful in the study was Raman spectroscopy to analyze the presence of graphene on the samples and X-ray diffraction (XRD) to analyze the crystallinity of the MAPbI_3 and to speculate about the presence of PbI_2 and potential hydrates. Raman spectroscopy measures the difference between the wavelength of incident light on a sample and the reflected light off of that sample to indicate the sample's composition. Bischoff et al. (2011) showed that graphene has characteristic peaks for Raman spectroscopy measurements. Three bands are present for the Raman shift of graphene: The D band, the G band, and the 2D band with peaks appearing at 1340 cm^{-1} , 1590 cm^{-1} , and 2680 cm^{-1} respectively. Bischoff et al. (2011) specifically took Raman spectroscopy measurements on graphene nanoribbons of different widths as shown in figure 2.17 below.

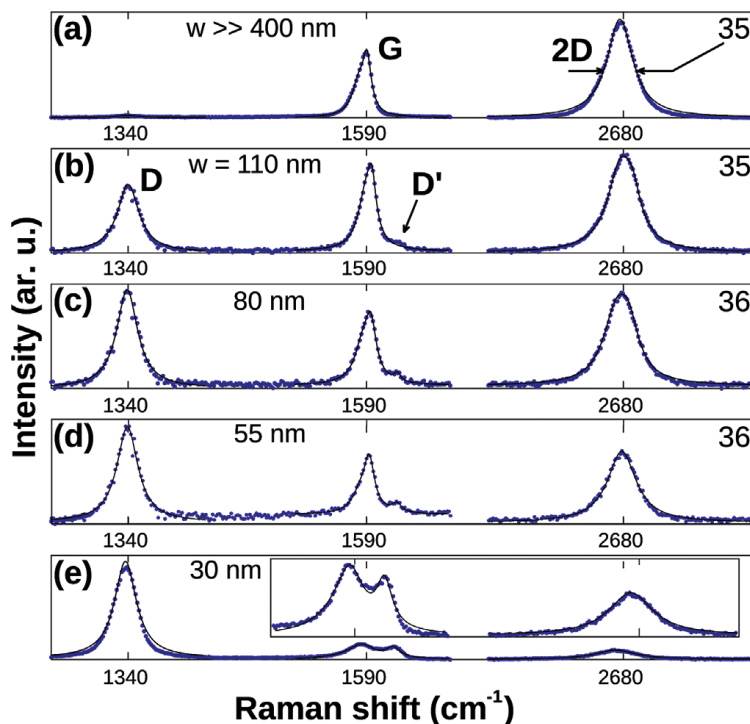


Figure 2.17 Bischoff et al. (2011) Raman Spectroscopy Peaks for Graphene

X-ray diffraction is a characterization tool to understand crystal structures and compositions by scattering x-rays in regularly spaced atoms according to Bragg's law. Wang and

Chen (2016) was used as a reference for XRD measurements. Like Raman spectroscopy XRD analysis depends on where peaks occur on the x-axis. However, while Raman spectroscopy uses green or red lasers, XRD uses x-rays and Bragg's law to understand crystallinity and can identify the crystal chemical composition. Wang and Chen (2016) studied the decomposition of MAPbI₃ and measured XRD for samples over time as shown below in figure 2.18.

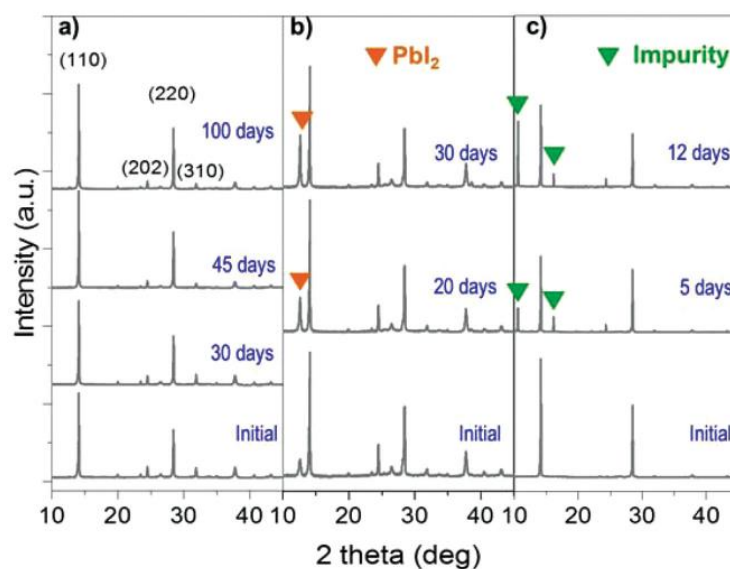


Figure 2.18 Wang and Chen (2016) XRD Measurement of MAPbI₃ Over Time

Figure 2.18 above is a reference for where peak intensities occur for MAPbI₃ and its degraded form PbI₂. Wang and Chen (2016) explain that diffraction peaks at approximately 14.1° is MAPbI₃ in a (110) lattice plane and peaks at 28.4° is typical of MAPbI₃ in the (220) lattice plane. Diffraction peaks occurring at 12.6° are typical of PbI₂ or the degraded form of MAPbI₃ (Wang and Chen, 2016). Lastly, peaks have been documented at approximately 8.7°, 10.6°, and 11.6° and are contributed to hydrates of the form CH₃NH₃PbI₃·H₂O and (CH₃NH₃)₄(PbI₆)·2H₂O (Leguy et al. 2015). Lu et al. (2017) describes peaks that occur at 28.4°, and 31.8° are assigned to the (220) and (310) MAPbI₃ lattice planes.

2.7 Chapter Summary

The encapsulation of MAPbI₃ with graphene should improve the halide perovskite solar cells to be closer to a marketable device. This chapter reviewed four major areas that are relevant for this research. It discussed background on perovskites and R2R manufacturing, graphene as an encapsulating layer, instruments, and measurements used in this study.

CHAPTER 3. RESEARCH METHODOLOGY

Having a comprehensive background on all the topics in this thesis study now the methodology can be explained. This chapter of the thesis will explain the experimental method and procedure that was used to provide insight on the hypothesis with the results displayed in chapter 4. Within this chapter the research framework, instruments, procedures, and statistical analysis plan will be explained.

3.1 Research Framework

The goal of this research study is to compare degradation rates and surface topography of three different groups of samples as indicated in table 1.1. This section of the study will define how the samples are prepared and what instruments and measurements will be necessary for the sample groups to be evaluated. Table 1.1 is repeated again below for reference.

Table 3.1 Sample definitions for samples to be created, analyzed, and compared

Sample A	MAPbI ₃ (Control Sample)
Sample B	MAPbI ₃ with Pristine Graphene Flakes in Ethyl Alcohol Spin-Coated on Top
Sample C	MAPbI ₃ with CVD Grown Monolayer Graphene Laminated on Top

The research framework evolved through a series of trials of experiments. The first three experimental trials were used to improve the preparation of the samples and measurement techniques so that the data displayed had minimal error and was appropriate to draw conclusions about the hypothesis. Through the first three trials many procedural changes occurred. First, the creation of MAPbI₃ evolved to be a more homogenous crystal film and graphene encapsulation methods were improved. Adjustments of the sampling approach were applied to improve statistics and reduce material use. Improvements to measurement procedures were applied to

optimize photoluminescence (PL) measurements and reduce error. Lastly, calibration of the AFM and improved optimization techniques were applied to reduce error and make the data more representative of the sample. Trials 4 and 5 were then designed to optimize the experimental procedure by learning from the faults of the first three trials. Issues with dissolving the PMMA graphene transfer material created small, but important changes to sample C so that trial 6 went through the exact steps as indicated throughout the methodology section described here.

Once the MAPbI₃ preparation for all three sample groups, and graphene applications of sample groups B and C were optimized the degradation rates and surface topography of the sample groups were then measured. After all the data was collected and displayed the data then was compared and analyzed to either fail to reject or reject the hypothesis. With the goals clearly understood, the experimental steps were as follows, according to sample definitions from table 1.1:

1. Create Samples A, B, C
2. Measure/Record PL/AFM Measurements
3. Put samples in humidity cabinet for allotted time at 80% humidity
5. Repeat steps 2 and 3 up to 528 hours of 80% humidity
6. Graph PL Data, Calculate Peak Intensity Values
7. Analyze AFM Surface Topography Data
8. Cross-Analysis of PL/AFM Data

3.1.1 Sampling Approach

Accurate statistics relies on the measurement of numerous samples. The sampling approach evolved from creating many samples to making many measurements on each sample to

reduce cost and waste of materials. There are three sample groups as shown in table 1.1. Each sample had 9 measurements to improve the statistical authority. Starting with trial 4 there were 9 spots used to indicate where measurements were to be made directly to the right of each marking and averaged over the sample. Below is a diagram of examples of how samples for trials 4, 5 and 6 were measured. The named locations such as A1 references the 1st measurement for sample A and so on. In the diagram where the A1 is written is approximately where the measurement was taken and so on for A1-A9 and C1-C9. It is important to note while the general location of each measurement was the same the exact location varied. Figure 3.1 shows a diagram of how samples in trial 4 were measured, which was then repeated for the samples in trial 5 and 6.

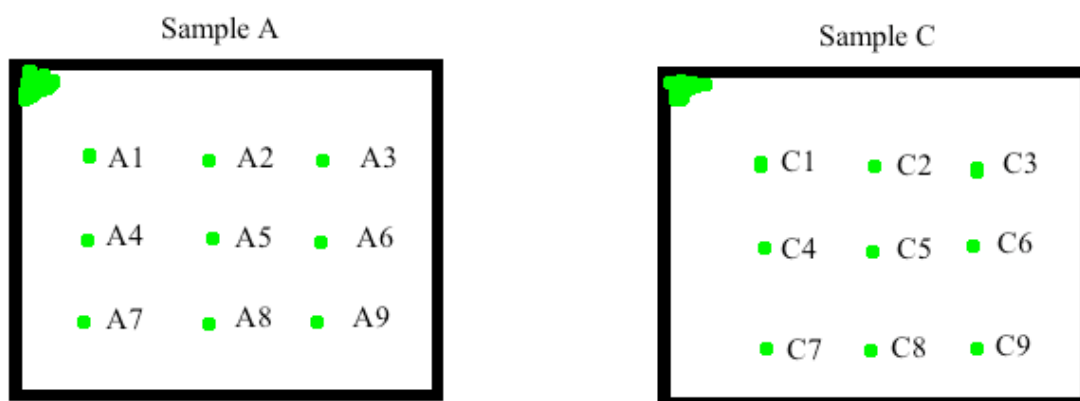


Figure 3.1 Sample Indicator Marks and Measurement Locations

MAPbI₃ solar cells degrade very quickly in a high humidity environment. To improve accuracy of measurements the samples were measured within hours of their initial creation. Due to the complex and expensive nature of creating a CVD graphene encapsulation the number of samples for sample type C was the limiting factor in the number of samples created.

3.1.2 Units of Measure

- Degradation Rate – Photoluminescence intensity over time, graphed in relation to wavelength (nm)
- Peak Intensity – Maximum photoluminescence intensity in arbitrary units or counts of electron pulses based on the CCD sensor chip in the optical microscope.
- Surface Topography – Measured dimensions of length, width and height in micrometers or nanometers
- Surface Roughness – Difference between a flat scan area (SA) and the projected surface area (PSA) presented as a percentage ($1-(PSA/SA)$)
- Scan Height Range – Measured maximum height range of an AFM scan area in micrometers
- Number of Peaks – Number of peaks in an AFM scan area
- Time for the degradation rate will be measured in hours
- Humidity measured as a percentage.

3.1.3 Variables

While the experiments were in an environment with as much control as is available, there was some variation between the creation and measurement of samples. To minimize the effect of the environment on the samples and the measurements there was an acute awareness to optimize cleanliness, reduce mechanical vibration, reduce electromagnetic radiation, and control temperature and humidity. These four variables did have an effect on the samples and measurements, but this effect was minimalized. Another variable that adversely affected the sample preparation, and measurements was human error caused by minute differences in the

weighed amounts of MAI and PbI_2 , therefore minimal variance of the chemical make-up. Small differences of times during bath washing steps and hot plates steps also may have caused small variations; however, longer times than necessary on these steps should not adversely affect error. Error was quantified by error bars in graphs based on standard deviations of the multiple measurements taken per sample. In between original conception and measurements humidity in the air was different based on the time of year and weather. Typical environmental humidity between conception and measurements varied from 10 to 33%.

3.2 Instruments

Multiple instruments were used throughout this research. The atomic force microscope was used to determine surface topography for understanding of how well the encapsulation material conforms to the perovskite. The fluorescent optical microscope was used to measure photoluminescence intensity over time correlating to degradation.

3.2.1 Atomic Force Microscope: Topographical Measurements

To measure surface topographies an Innova scanning probe microscope (Veeco Digital Instruments, Plainview, NY) was used with a Bruker DNP-20 silicon nitride tip with a spring constant of 0.58N/m and a tip radius of 20nm. The Innova AFM provided a surface resolution of 1/10 nanometer in the Z direction and 1/2 nanometer in the (X,Y) direction. Figure 3.2 shows the AFM used for this study.



Figure 3.2. Veeco Innova AFM Microscope Used

The tools used in this research had a direct effect on the data returned and therefore it is important to describe the error and assumptions being made. It is important to understand the sample-tip geometry and how the tip path can be misleading to the actual surface topography. Figure 3.3 shows a VEDA simulation tip-sample geometry relation between a sample feature of 5 nm wide 10nm in height and a 20 nm tip. The VEDA program is an AFM simulation software used to examine contact mode sample-tip geometry. While the height of the feature is accurate, the width is not. Understanding how the width of a feature may be augmented is an insight into the error of the topographical data seen in the results section of this report.

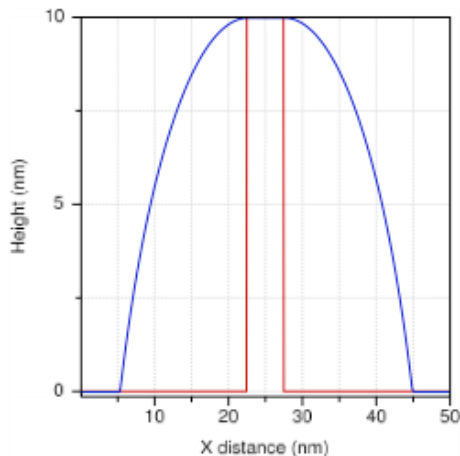


Figure 3.3 VEDA Simulation 5nm Wide Feature, 20nm Tip

The programs used in conjunction with the AFM to get the resulting data were Nanodrive 8.01 from Nanoscope for the AFM data acquisition and Gwyddion from the Department of Nanometrology at the Czech Metrology Institute for the visualization of the data. Nanodrive 8.01 is software that controls the Innova AFM and the microcontroller in real-time. The program has six parameters that are used to optimize the data results to be as accurate as possible. The six parameters are image size, rotation angle; scan rate, samples per line, set point voltage, and PID gains. To optimize the parameters the tip will trace and retrace the same profile of the sample to compare the two paths until the tip paths are as close as possible. To optimize the parameters the rotation angle should be perpendicular to the feature, the slower the scan rate often results in better resolution, but consequently lengthening the total scan time. More samples per line will also improve the resolution, but again sacrificing the scanning speed. The set point voltage and PID gains are the main parameters to optimize the trace and retrace paths to be as close as possible. The set point voltage indicates how much force the tip is having with the surface of the sample. PID stands for proportional, integral, and differential gains. In general, the proportional gain should be 2 to 10 times the value of the integral gain, but the values can vary over orders of

magnitude. Differential gain was left as a value of 0 throughout the procedure of the lab experiment because it had a negligible effect on optimization of scan parameters.

Gwyddion was the software used to report the data for analysis and final three-dimensional graphical imaging. Gwyddion image post processing was also used before reporting the display of AFM images for the image to more accurately reflect the sample. The post-production corrections applied to the data were leveling the data by mean plane subtraction so that any consistent slopes appear flat. Any 2nd degree polynomial background profiles were removed in the x-direction due to any bowing error from the AFM scan movement. Scratches were removed using a feature in Gwyddion that correct horizontal scars or strokes and rows were aligned using a median of differences algorithm. Lastly, the minimum data value of the scan was shifted to be equal to 0.

All samples analyzed under the AFM were securely fastened to the AFM sample holder using a magnetic puck and putty as shown in figure 3.4 below. Having the samples securely fastened is imperative for accurate data. The tip is in contact mode and therefore is creating a lateral force on the sample, which could potentially move the sample if not securely fastened. Lastly, the AFM was calibrated for X, Y, and Z axes.

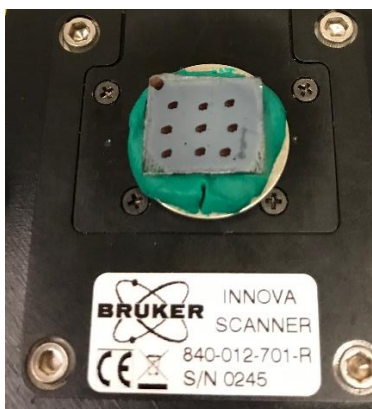


Figure 3.4 MAPbI₃ Sample in Putty on Magnetic Puck for AFM Scans

3.2.2 Optical Microscope: Photoluminescence Measurements

PL measurements in this report are used to identify the ability for the MAPbI₃ to convert photons into electrons. An optical microscope was used to take PL measurements using a focused UV light. The photons emitted from the optical microscope are absorbed into the material exciting electrons from the valence band into the conduction band. If there is no functional device with electrodes connected to the active region, excited electrons are not captured so they will relax, eventually recombine, and emit photons. The reemitted photons, from the electron-hole pair recombining in the active layer were the measured PL intensity values.

Bright field images are taken with just white light and were used to show where PL measurements were taken as well as how the crystal is changing throughout degradation. PL images were used to visually inspect the crystal morphology formed and the relation of the morphology with the ability to excite electrons to the conduction band. For PL images a brighter image indicates more electrons excited to the conduction band. The color of the image indicates the wavelength of the light reemitted. Graphs of the PL intensity vs. wavelength also were used to analyze the intensity of light across the visible spectrum. Graphs numerically compare sample PL intensities as well as variations over time. PL measurements are used to examine the degradation of the active layer of a solar cell. An initial PL intensity for a MAPbI₃ cell is not retained over time. Losses in PL intensity counts to eventually reach 0 expresses the inability of the MAPbI₃ to convert photons into excited electrons and are considered the indication of degradation in this report (Soufiani et al., 2016). The goal of this study was to create a method to retain peak PL intensity measurements over time for MAPbI₃ that are consistent with the initial PL intensity. It is important to understand that in order to have accurate results the settings of the fluorescent microscope were exactly the same through the course of the study. Any different

settings such as filters, exposure times, or brightness would lead to measurements that cannot be compared. Only when using the exact same settings are the PL intensity values able to be compared and the degradation of the perovskite to be characterized.

The exact tools used in this study was an Olympus BX53M System Microscope with an X-cite Series 120 fluorescent excitation lamp from Excelitas Technologies, and a Spectra Pro HRS-300 triple grating imaging spectrometer as shown in figure 3.5. The lens used to record all the crystal morphology images and PL intensity graphs was a MPlanFL N 100x FN26.5 lens (Olympus America Inc., 2010). The software to record the images taken of the crystal morphology was Olympus Start Stream. PL graphical data was collected with the software Lightfield and exported as .csv files to be analyzed with excel spreadsheets.



Figure 3.5 Olympus BX53M System Microscope, X-Cite Series 120, and Spectra Pro HRS - 300

3.2.3 Data Collection and Display Methods

All AFM surface height data files, PL crystal morphology images, and PL intensity graph data were recorded and saved on the computer instantly after being measured. Raw AFM data files were exported from Nanodrive 8.01, then were post processed and analyzed in Gwyddion as explained in section 3.2.1. PL crystal morphology images were ready for display instantly after being exported as PNG image files from Olympus Start Stream. Lastly, the PL intensity data sets were instantly collected by Lightfield and exported as a .csv file that was imported into excel spreadsheets to be displayed in graphical form. Degraded samples also had PL intensity data sets collected from Lightfield, exported as a .csv file, and imported into the same excel spreadsheets for the entire trial.

3.2.4 Proposed Analysis of Data

Sample group A was the control group, to be compared with sample groups B, and C as defined in table 1.1. For each sample, measurements of photoluminescence over set time periods were compared. Similarly, each type of sample had AFM surface topography measurements for analysis of surface roughness of the encapsulating and active layers. By comparing the surface roughness of MAPbI₃ with and without graphene encapsulating layers the conformability of graphene to the MAPbI₃ surface was able to be analyzed and better understood. With sample groups A, B, and C being stored in the same conditions degradation rates can be cross-analyzed. Plotting PL intensity data curves with the exact same settings overtime gave insight to general degradation trends and the ratio of a fresh sample's PL intensity peak to aged samples PL intensity peaks indicated the degradation rates. Sample group data values were averaged across the many measurements taken on each sample to create a general characteristic of the sample as

a whole. Then, averaged values of each sample group were compared to draw conclusions about the hypothesis.

3.3 Procedures

This section will describe the scientific procedures for the preparation for each of the sample groups as defined in table 1.1. Since MAPbI₃ was the control sample, and was in all sample groups, the method of preparation will only be described for sample A; however, the preparation method of MAPbI₃ for samples B, and C are the same. The preparation of graphene and the methods to cover the perovskite have different procedures. A monolayer graphene solution in ethyl alcohol was used for the preparation of sample B, and a chemical vapor deposition (CVD) grown graphene on both a PET substrate and a copper foil substrate was used for the preparation of sample C. Both methods were purchased from the third-party Graphene Supermarket for high-quality, reproducible graphene encapsulating methods.

3.3.1 Preparation of Sample A: MAPbI₃

The first sample analyzed is a Methylammonium Lead Triiodide (MAPbI₃) solar cell. MAPbI₃ is an organic-inorganic halide perovskite or a subset of organic solar cells. The procedure for preparing the MAPbI₃ is fairly simple and repeatable in the lab. Ahn et al. (2015) created replicable MAPbI₃ perovskite film samples with an average power conversion efficiency rate of 18.3%. The procedure in this study closely followed that of Ahn et al. (2015). Three main sections are required to prepare the MAPbI₃. First, the solutes and solvents are added in a vial and mixed. Second, glass substrates are cleaned and prepared. Third, the solution is put on the glass substrate, spin coated, and placed on hot plates.

To prepare the sample, 69 mg of Methylammonium Iodide MAI was mixed with 200 mg of Lead Iodide PbI_2 in a vile. The solvents are then added: 278 μL DMF, 30.8 μL DMSO, and 30 μL of HI. A stir bar is then added to the vile. The MAPbI_3 vile is then put in an ultrasonic bath to mix the solution using vibration for about one minute. The vile is then often put on a hot plate at room temperature and mixed at 200 rpm for 10 to 20 minutes.

Cleanliness is imperative throughout the lab procedure. All materials are cleaned with ethanol and KIMTECH wipes. The glass slides are cut to approximately 1 cm x 1 cm squares. Numerous slides were prepared throughout this study. The glass is then cleaned with IPA and placed in the oven to ensure full evaporation. Marks are placed on the bottom of the slide to indicate the bottom side. The glass slides are then placed face up in UV Model 30 ozone plasma for 10 minutes to make the surface more hydrophilic to improve the spin coating process.

Once the glass substrates are ready the solution is spin-coated onto the glass. From trial and error Ahn et al (2015) found that a two-step spin-coating process returned the best results. A glass substrate is put on the spin coater and held in place using a vacuum pump. The MAPbI_3 solution is added to the glass substrate, enough to cover the entire surface, but not directly measured. Ahn et al. (2015) described their process as the glass is then spun at 4000 rpm, with as fast a ramp up speed as possible, for 25 seconds. During these 25 seconds 400 μL of diethyl ether is prepared. Once the glass is done spinning, it is instantly spun for another 25 seconds, while dripping diethyl ether on the substrate. During the first three trials the recipe evolved to create crystals that were more homogenous and consistent. First, a spin-coating speed of 3000 became more optimal for reducing sample variation. Furthermore, dripping diethyl ether became too inconsistent so instead samples were prepared by spraying 250 μL of Chlorobenzene (CB) at the 7th second of the second spin-coating step. These procedural changes reduced sample-to-sample

variation and promoted the full evaporation of DMF. After the second spin coating step the glass is then immediately placed onto a hot plate at 65°C for 1 minute, then placed on a second hot plate at 100°C for 2 minutes. The series of hot plate steps fully evaporates the DMSO. The film changes from a transparent color to a brown, or dark color, which indicates that only MAPbI₃ is left as intended. The change of color is key for the creation of the MAPbI₃ and indicates that there is no longer DMF or DMSO in the MAPbI₃ sample. The procedure to create the MAPbI₃ was used for all sample groups, but sample groups B and C had additional steps for encapsulation methods. Next the encapsulation materials and procedures will be described.

3.3.2 Preparation of Graphene Solution

The preparation of an electrochemically-exfoliated graphene gave insight into the differences in quality of graphene preparation methods. Exfoliated graphene is much cheaper to produce than chemical vapor deposition techniques. Furthermore, exfoliated graphene results in graphene flakes or a powder, which when put into DMF can be used as conductive ink. Electro-chemical exfoliation of graphite is a fairly simple procedure as described by Parvez et al. (2014), and many graphite powders and flakes are cheap to purchase. Parvez et al. (2014) also painted the conductive inks onto commercial sheets of paper and returned very low sheet resistances ($\sim 11\Omega/\text{sq}$) with .74mg of DMF/graphene solution per cm^2 . Many trials of conductive inks were created and tested in lab using both graphite flakes and graphite powder; however, the resulting conductive ink was always dark and not the clear as is necessary for a solar cell. Due to the inability to create a transparent solution a third party was used. Graphene Supermarket has a clear, monolayer solution available on the market as shown in figure 3.6. Since the solar cell needs a clear encapsulation for light absorption, the graphene conductive inks made in lab were

not adequate for use. Subsequently, 50 mL of pristine graphene monolayer flakes in ethyl alcohol were purchased and used for the encapsulation method of sample B.



Figure 3.6 Pristine Graphene Flake Solution from Graphene Supermarket

3.3.3 Preparation of Chemical Vapor Deposition Graphene

There are many ways to prepare chemical vapor deposition (CVD) graphene. Similarly, to the graphene solution, CVD grown graphene was cheaper and had better quality if purchased from a third-party. Graphene Supermarket was again used for the purchase of a CVD grown monolayer graphene 1" x 1" sample on a PET substrate as shown in figure 3.7 a and b. After trial and error from the first three trials it was found that CVD graphene on PET substrate was incapable of being transferred onto the MAPbI₃ samples. Therefore, for trials 4, 5, and 6 a 2" x 2" sample of CVD graphene grown on a copper foil was purchased from graphene supermarket as shown in figure 3.8 a and b. The CVD grown graphene on copper foil originally is produced with graphene on both sides of the foil and therefore the vendor used O₂ plasma etching to remove graphene from one side of the copper foil.



Figure 3.7 – CVD Graphene on PET substrate used in Trials 1-3 and incapable of being transferred to MAPBI₃; (a) CVD graphene from Graphene Supermarket in original encasement, (b) CVD monolayer graphene on PET substrate (face up)



Figure 3.8 – CVD Graphene on copper foil used in Trials 4 – 6 successfully transferred to MAPBI₃; (a) CVD graphene from Graphene Supermarket in original encasement, (b) CVD monolayer graphene on Cu foil (face up)

3.3.4 Preparation of Sample B: MAPbI₃ With Graphene Solution Encapsulation

Two methods of encapsulating the perovskite with graphene were tested. The first method used the graphene monolayer solution as shown in figure 3.6. After, failed attempts of transferring graphene from PET shown in figure 3.7 the second tested method used the CVD grown monolayer graphene on copper foil as shown in figure 3.8. Samples prepared using the graphene solution method will be referred to as sample B and samples prepared using the CVD grown graphene will be referred to as sample C.

To attempt to encapsulate the MAPbI₃ perovskites only one additional step is required after the creation of Sample A. After sample A is prepared the glass slide is then placed again on the spin-coater with the MAPbI₃ facing up so that 50-75 μ L of the pristine monolayer graphene flakes in ethyl alcohol solution can be place on top. With the solution on top the glass slide is spin-coated at 3000 RPM. The sample is then placed on a 65°C hot plate for 2 minutes to ensure the full evaporation of the ethyl alcohol leaving only the graphene monolayer flakes dispersed on top of the MAPbI₃.

The early trial 1 used variant spin-coating speeds. 16 samples were created in the first trial as shown in tables 3.3.4.1 and 3.3.4.2, comparing sample group A to sample group B. These samples in trial 1 gave insight to better techniques of preparation of MAPbI₃, the solution encapsulation procedure, and measurement methods. The resulting data was inconclusive for trial 1, but the lessons learned were applied in trial 5. Through trial and error, it was concluded to be more useful to measure multiple locations of a sample rather than multiple samples. Therefore trial 5 only used one sample of type B with optimized techniques of spin-coating at 3000 rpm and annealing at 65°C for 2 minutes. The data collected from trial 1 of the samples described in table 3.2 and 3.3 will be summarized in chapter 4 and the optimized results from trial 5 will be displayed and analyzed.

Table 3.2– Sample Group A1: MAPbI₃

Sample Group A	
Sample 1	MAPbI ₃
Sample 2	MAPbI ₃
Sample 3	MAPbI ₃
Sample 4	MAPbI ₃
Sample 5	MAPbI ₃
Sample 6	MAPbI ₃

Table 3.3 – Sample Group B1: MAPbI₃ & Pristine Graphene Flakes in Ethyl Alcohol

Sample Group B	
Sample 1	MAPbI ₃ & Graphene Solution 4000 RPM
Sample 2	MAPbI ₃ & Graphene Solution 4000 RPM
Sample 3	MAPbI ₃ & Graphene Solution Single Drop
Sample 4	MAPbI ₃ & Graphene Solution 1000 RPM
Sample 5	MAPbI ₃ & Graphene Solution 4000 RPM
Sample 6	MAPbI ₃ & Graphene Solution 4000 RPM

3.3.5 Preparation of Sample C: MAPbI₃ With CVD Graphene Encapsulation

In trial 2 a 1” x 1” sample of graphene on a PET substrate was purchased to attempt to transfer the graphene onto MAPbI₃. Two methods to dissolve the PET substrate failed. The first method submersed the CVD graphene on PET in DMSO with a .1g/10mL ratio for up to 1 week. The second method submersed the CVD graphene on PET in chlorobenzene (CB) with a .1g/10mL ratio for up to 1 week. Both methods used ultrasonic vibration before removing the sample from the solution. Unfortunately, both methods failed to dissolve the PET substrate and left a visible thickness of PET connected to the graphene. If only graphene were on the MAPbI₃ it would not be visible to the eye since graphene has an atomic thickness. After laminating the MAPbI₃ with both the CVD grown graphene on PET submersed in DMSO and CB PL measurements were incapable of being taken. When putting light, either bright field or UV, on the sample the entire PET substrate illuminated creating noise that completely saturated the

image thus making any measurement of the crystal morphology impossible as shown in figure 3.9. Resulting images of the CVD graphene on PET lamination attempts are summarized in chapter 4.



Figure 3.9 UV Light Illuminating PET Substrate on MAPbI₃

Due to the inability to transfer CVD grown graphene from a PET substrate to the MAPbI₃ samples a different substrate and transfer method was then attempted for trial 3. A more typical method of CVD grown graphene transfer uses a copper foil substrate. Graphene transfer methods are well documented in journal article literature. Li et al. (2009) describes a preliminary method of graphene transfer; however, this method often results in cracks and non-continuous films of graphene, which would not be optimal for this study. Liang et al. (2011) then introduced an improved method of graphene transfer. Figure 3.10 is a flow chart that describes the steps of the graphene transfer method from a copper foil. In trial 3 the steps shown in figure 3.10 were followed exactly, but issues resulting in an optimization of the transfer process.

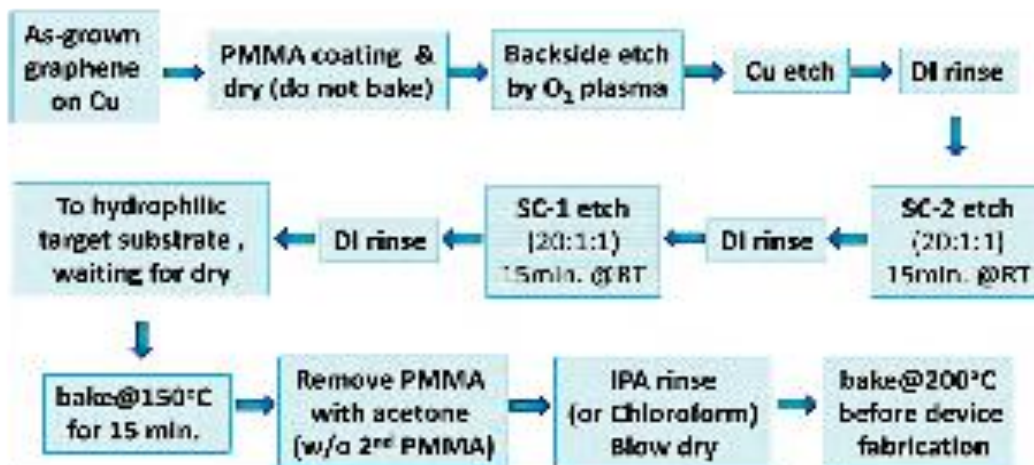


Figure 3.10 Liang et al. (2011) CVD Graphene on Cu Foil Transfer Method Process

Not all of the steps in figure 3.10 were used for the optimized transfer method used in trials 4 through 6. Backside etching of the Cu foil using O₂ plasma was accomplished by Graphene Supermarket, and therefore was not part of the transfer process. There were also some other issues that occurred when following the procedure presented by Liang et al. (2011). Changes to the initial PMMA spin coating step, Cu etchant, baking temperature, and IPA rinse step were necessary for a successful transfer in trials 4 through 6.

A major issue found in trial 3 was that a single spin-coating of PMMA on top of the CVD graphene on Cu foil resulted in a film too thin to handle that would crumple up on itself due to Van Der Waal forces too easily during the transfers of the many baths steps resulting in an unusable film. To make the film thicker in trial 4 PMMA was spin coated on top of the graphene on Cu foil at 800 RPM, annealed at 80° C for 10 minutes, and cooled at room temperature for 5 minutes, then repeated 4 more times. The resulting film in trial 4 was stiffer and easy to transfer from bath to bath and then eventually hung to air dry. Figures 3.11 a, b and c show the film before and after the copper foil was etched away with only one PMMA spin coating. Figures

3.12 a, b, and c show the film before and after the copper foil was etched away with five repetitions of the PMMA spin coating steps.



Figure 3.11 Single PMMA spin coat on graphene before and after Cu etch (a) PMMA on graphene on Cu when first put in Cu etchant, (b) Single PMMA coat on graphene after Cu etch, (c) Handling film resulted in it crumpling up on itself making incapable of transfer

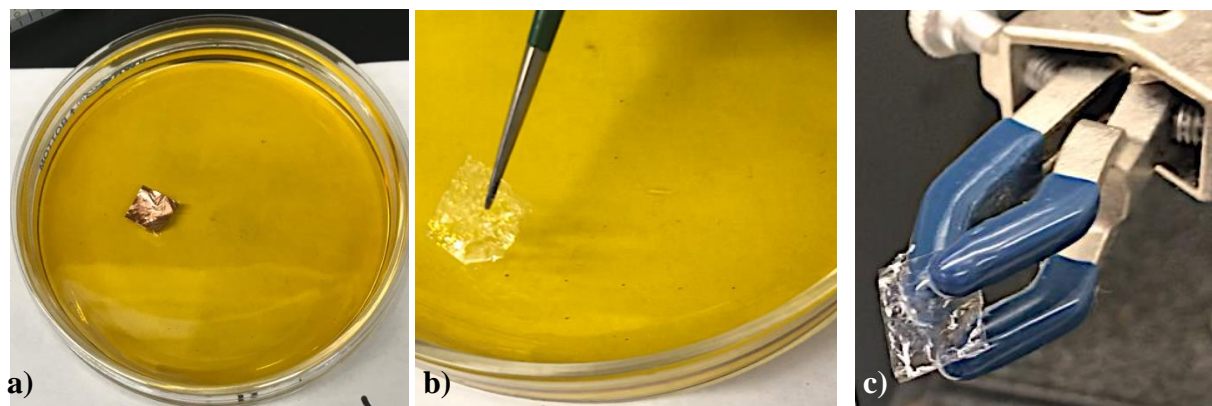


Figure 3.12 Five PMMA spin coats on graphene before and after Cu etch (a) PMMA on graphene on Cu when first put in Cu etchant, (b) Five PMMA coats on graphene after Cu etch, easy to handle, (c) Air drying PMMA and graphene film

The copper etchant that is used by Liang et al. (2011) is iron nitrate ($\text{Fe}(\text{NO}_3)_3$) and is placed in the bath for 15 minutes; however, in our lab ferric chloride was available and according to Ayerst, G. (1966) ferric chloride is an excellent etchant for copper. Approximately 16.2 grams of ferric chloride (FeCl_3) was used with 7.5mL of concentrated HCL, or 0.1 mol HCl and 92.5 mL of water. The copper etchant solution was then vacuum filtered to remove any impurities. To ensure the copper was fully etched the PMMA on graphene on copper foil remained in the bath

overnight. Liang et al. (2011) describes the SC-2 and SC-1 baths as a “modified RCA” cleaning method. SC-1 is a 20:1:1 ratio of H₂O/H₂O₂/NH₄OH bath and is used to remove insoluble organic contaminants. SC-2 is a 20:1:1 ratio of H₂O/H₂O₂/HCl and is used to remove ionic and heavy metal contaminants (Liang et al. 2011). Another change that had to be implemented was the final baking steps. Unfortunately, temperatures above 120° C are destructive to the MAPbI₃ film and therefore the baking steps were modified to a temperature of 100° C. Lastly, to fully dissolve the PMMA took much longer than expected. Trial 4 only used a few drops of CB to dissolve the PMMA, which was too little. Trial 5 submersed sample C with PMMA in a CB bath for five minutes, which was too short of a time. Finally, in trial 6 all of the PMMA was able to be fully dissolved by submersing sample C with the PMMA into a CB bath for two hours. With all the necessary changes in mind a transfer procedure specifically for graphene to MAPbI₃ was formulated and is outlined in the flow chart depicted in figure 3.13.

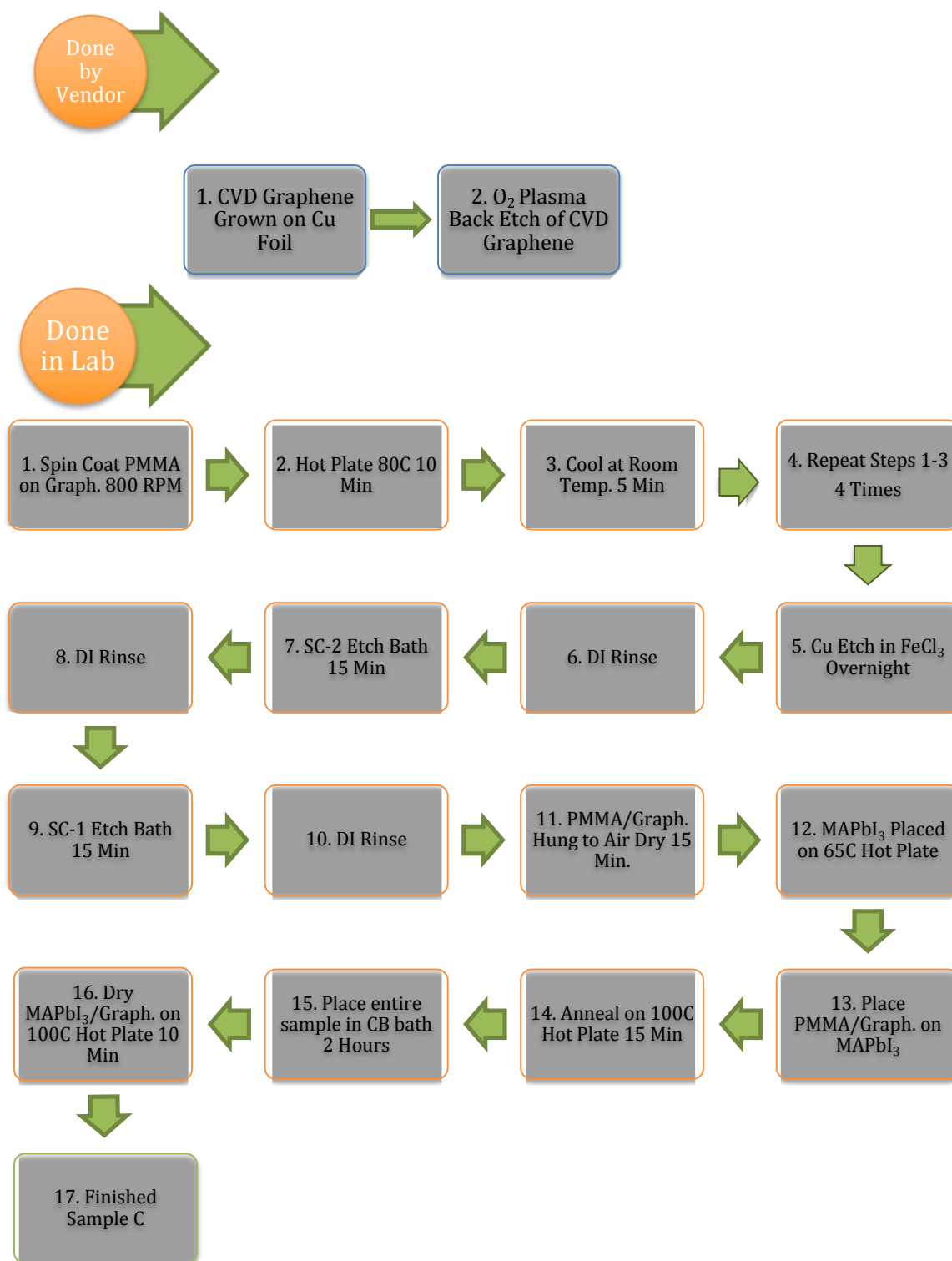


Figure 3.13 CVD Graphene on Cu Foil PMMA Transfer Method to MAPbI₃ Process

3.3.6 Photoluminescence Measurement Procedure

To take PL measurements a very specific order of steps was followed with specific instrument and software settings to ensure that each sample's measurement would be consistent. First, both the Lightfield and Start Stream software were opened and all instruments turned on. An experiment with a template of the specific settings needed for these measurements was opened within the Lightfield software.

The first sample to be measured was then placed on a glass slide and under the microscope. The 100x magnification lens was selected for viewing. The microscope was set to the bright field setting for white light to be shined on the sample. A live view of the crystal morphology was seen on a computer monitor under the bright field settings on the optical microscope and is brought into focus by moving the microscope platform up or down in the z direction. By moving the stage of the optical microscope in the x and y directions the location directly to the right of each location indicator was selected for data analysis. Once a location was chosen a picture of the live view was taken with a 16.6 ms exposure and an ISO of 400 and the X-Cite iris 1/8th open for the bright field images. The images were then saved as a .png image file to a folder correlating with the sample and the time taken. Without moving the sample, the microscope was then changed to PL imaging mode, where ultraviolet light was shined on the same location of the sample. PL intensity data was then taken for graphical analysis. Any PL images were taken after taking PL data to avoid photobleaching the location being measured. PL images were taken with a 4 second exposure with an ISO of 400 and the X-Cite iris 1/2 open.

When recording PL data, the Lightfield software was opened to record PL intensity vs. wavelength graphs. A specific experiment template was used for all measurements with the defined settings of a 500ms exposure, a grating of 300g/mm, with a center wavelength of 750nm and X-Cite iris that is 1/8th open. A live view of the data was shown, and an extract button was

selected to pick one 500ms exposure data result. However, when UV light was first applied the PL intensity counts start to grow. For trial 5 PL data was not taken until the PL intensity counts would reach an equilibrium and no longer grow. However, it could take up to 3 minutes for the PL spectrum to reach equilibrium and could cause photobleaching. For trial 6 PL measurements were taken after 10 seconds of UV illumination on the spot indicated by the optical image. Once the extract button was selected and the data exported as a .csv file and was placed in the same folder as the Start Stream image for that specific sample location at that specific time. The microscope stage was then moved again to find the next location indicator and measurements were taken directly to the right of the indicator for all nine locations on the sample. Once all nine locations were measured and imaged the sample was taken away from the microscope, off the glass slide, and placed back in a Petri dish where it was stored. The next sample was then analyzed, and the procedure repeated for all samples measured.

3.3.7 Atomic Force Microscope Measurement Procedure

For AFM measurements first, the computer was turned on, then the microcontroller, then the Nanodrive 8.01 software was opened. A contact mode experiment template was opened in the software. Using the optical microscope on the AFM the laser was centered on the triangle of the cantilever to result in the largest sum voltage possible as indicated by the photodiodes. A mirror was then adjusted so that the laser reflected off the cantilever to be centered on the photodiode. At this point the instrument was left for approximately an hour for the entire system to warm up and stabilize.

After an hour the optics had drifted and the mirror was readjusted again to center the laser reflected off the cantilever to the center of the photodiode. The sample to be measured was placed in putty on a magnetic puck then under the AFM head on the scanning platform. The

cantilever and tip were then brought down towards the surface of the sample, first by using motors. By analyzing the sample with the optical microscope, a general location of the sample was chosen by moving the sample platform in the x and y direction. When close to the surface, the engage tip button was selected and the AFM used the piezoelectric until the surface was found, indicated by changes to the photodiode. Once the tip was on the surface a scan was started. After about 1/5th of the scan had occurred the scan was stopped to begin an optimization process.

To optimize a scan a line was drawn over the taken image to indicate where the tip scans and a repeat function was applied so that the tip continuously scans over the indicated line. A profile path window in the software was then used. The tip trace and retrace profiles were displayed and the set point voltage, scan rate, samples per line, and PID parameters were manipulated until the trace and retrace profiles were as similar as possible. Once the parameters had been optimized a full scan was taken.

First, a large scan of 50 μm was taken and the raw topographical data was saved to a folder for the specific sample for that specific time. Based on the first image smaller scans of 20 μm and 5 μm were taken. Trial 6 only made use of 20 μm scans. These subsequent topographical data sets were then saved to the same folder. Once data measurements were taken the tip on the cantilever was lifted off of the surface. The sample was then removed from the scanning platform and another sample was placed on the platform to be measured. To keep consistent comparisons of surface roughness, scan height, and the number of peaks in a scan 20 μm scans were the most common.

The most common set point voltage used was 2.0 volts; however, sometimes lower values such as 1.5 volts or 1.0 volts was used. Typical PID values was 8.0 for the proportional

gain and 1.0 for the integral gain. The differential gain was left at 0 for the entire study. Other PID values include 10.0 for proportional gain and 2.0 for integral gain. The scan rate was most commonly 0.70 hertz and each image had 512 samples per line. Since the scans were 50 μm x 50 μm , 20 μm x 20 μm , and 5 μm x 5 μm with 512 samples per line the resolution for each are 98 nm, 39 nm, and 9.8 nm respectively.

3.4 Statistical Analysis

The PL and AFM data collected used different statistical analysis methods. For the PL data the statistical analysis was comprised of Xbar and Rbar charts to evaluate the average of nine locations for PL peak measurements. Xbar charts are the equivalent to the average of the nine measurements taken for each sample at each time of degradation in hours. The Rbar chart is the range of the nine PL peak measurements and gives an idea of how large a change of peak intensities occurred across the nine measurements. However, error bars in the Xbar chart were based on standard deviations of the nine measurements and their magnitudes correlate directly with the Rbar chart values. Differences between samples in PL peak intensities during degradation gave a conclusion to either reject the null hypothesis or fail to reject the null hypothesis.

AFM data analysis used similar statistics. AFM data was comprised of surface roughness, height range of scans, and number of peaks per scan to be compared across samples. Averages of the scans data of each scan size was then used to compare samples. These averages were used to construct Xbar charts that had error bars that were ± 1 standard deviation. Comparing sample averages for the surface roughness, height range of scans, and number of peaks per scan was then used to either reject the null hypothesis or a fail to reject the null hypothesis.

Finally, cross analysis of PL data and AFM data was used to correlate the measurements that indicate degradation of PL peaks and degradation of the surface topography. Lastly, a linear regression model of a full factorial design was analyzed to find parameter estimates and statistically calculate the probability value, or p-value. The linear regression models used the PL and AFM data with the treatment factor of graphene encapsulation to understand the significance of the correlation of the data results and the treatment factors using the software JMP 13.

CHAPTER 4. RESULTS

Having fully explained the experimental methodology and having a comprehensive background of knowledge the results of the experiment will be displayed with discussion. The first section of chapter 4 will display the preliminary results of trial 1, 2, and 3, discuss the issues that occurred, and the evolution of the experimental procedure. By building on the results from trials 1 through 3 more insightful data results from trials 4, 5 and 6 are displayed and discussed to provide insight on the hypothesis and research questions.

4.1 Preliminary Trials Lessons Learned

The preliminary trials in this study were used to gather initial information and better understand the characteristics of MAPbI₃ and graphene. Throughout the first three trials numerous different approaches were attempted and instrumentation procedures were optimized. Trial 1 resulted in major issues of MAPbI₃ inconsistency. After trial 1 changes to the procedure of the preparation of MAPbI₃ led to more homogenous films. Trial 2 had issues with how photoluminescence data was being collected and therefore honed the instrumental measurement procedures. By trial 3 the crystal morphology was consistent, and the instrumentation procedure had been improved. Trial 3 failed to transfer graphene to MAPbI₃ and continued to improve measurement procedures. This section discusses some early, failed experimental results and describes how the experiment evolved to be successful in later trials.

4.1.1 Trial 1

In the first trial the crystal did not fully form and the preparation of MAPbI₃ needed to be improved. However, trial 1 introduced the process and an introduction to PL measurements. In

trial 1 only samples A and B were prepared and measured. Table 4.1 shows the resulting crystal morphologies of samples A and B for both bright field and PL (red) images. Images were taken at 0 hours and after 4 days exposed to air of approximately 50% relative humidity.

Table 4.1 Trial 1 bright field and PL images scale bars are 20 μm

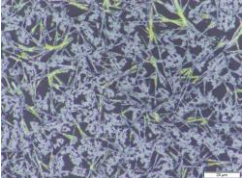
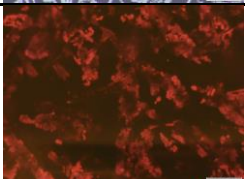
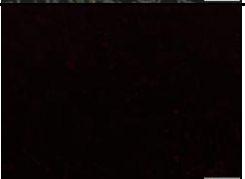
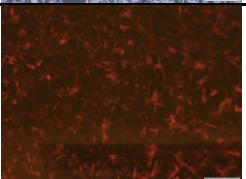
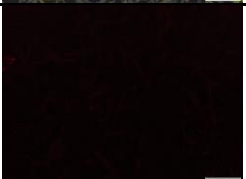
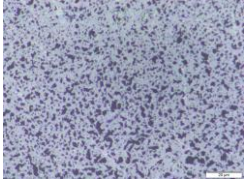
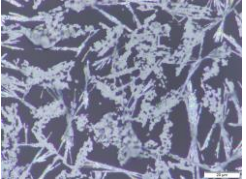
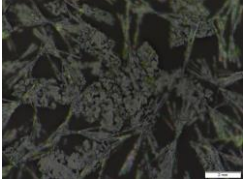
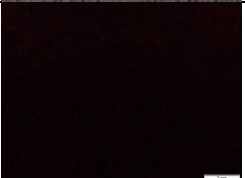
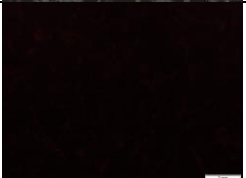
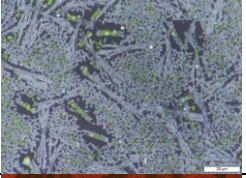
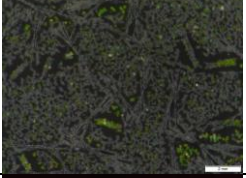
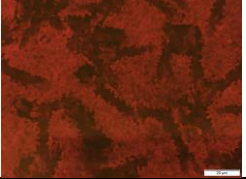
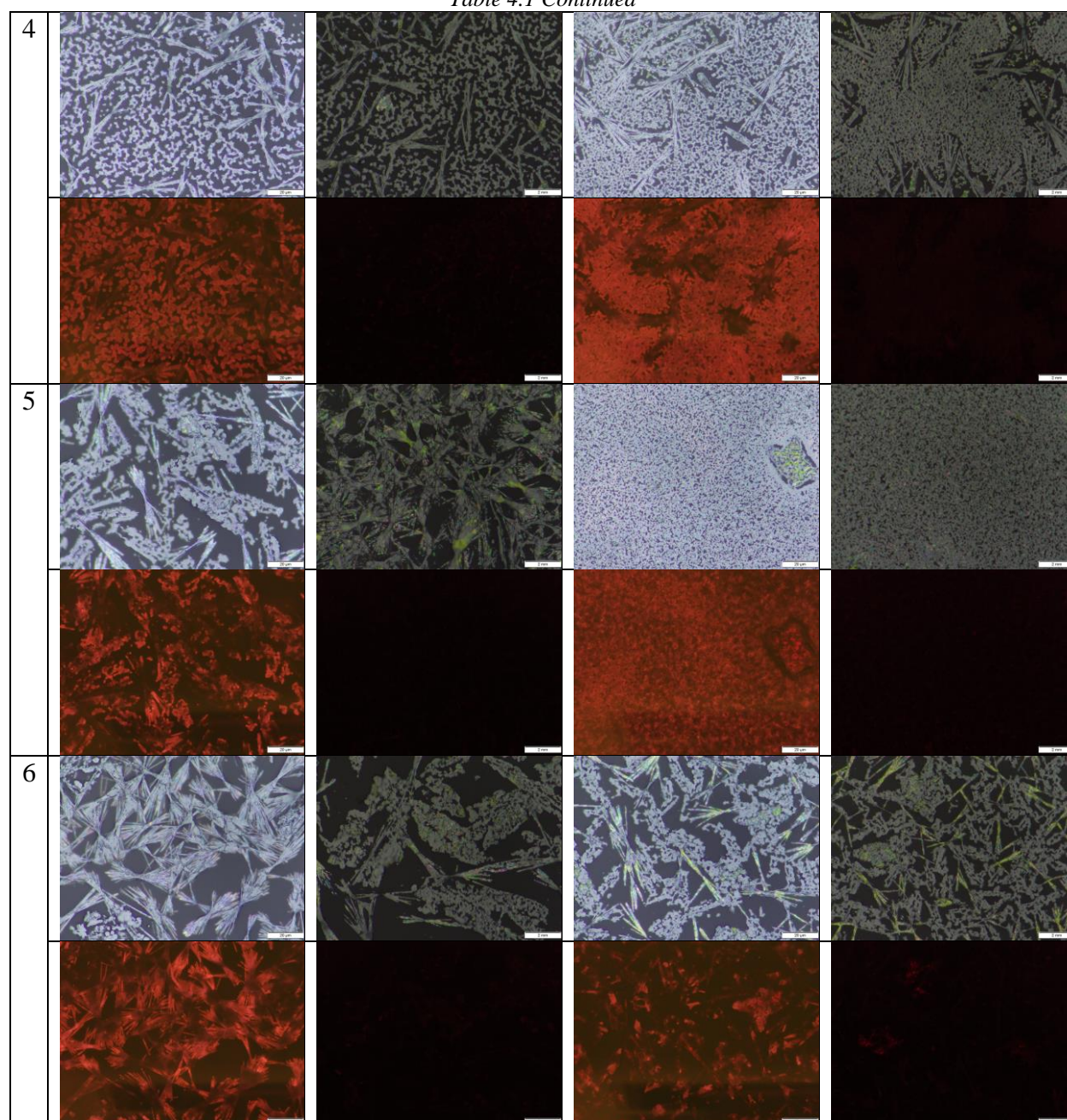
#	Sample A Images		Sample B Images	
	Day 1	Day 4	Day 1	Day 4
1				
				
2				
				
3				
				

Table 4.1 Continued



There are some key takeaways from the data presented in Table 4.1. First, the crystal morphology is not consistent between samples and within each individual sample itself. The goal was to have as homogenous of a film as possible, therefore sample B5 was the best prepared sample of trial 1. Because of the major inconsistency of the crystal morphology modifications to

the preparation of MAPbI₃ were employed. The spin-coating speed was dropped from 4000 RPM to 3000 RPM and 400 μ L of diethyl ether was replaced with 250 μ L of chlorobenzene during the second spin-coating step.

Another major issue that is indicated in the data shown in table 4.1 is that bright field images are not the same brightness on day 1 as day 4. There was clearly a discrepancy in the optical microscope settings to retrieve the PL data from days 1 and 4. The issue that occurred was that the ISO value for the images was set at 400 for day 1 and at 200 for day 4; however, these discrepancies gave insight into how important it is to have exactly the same settings for the PL measurements. Later trials made sure that the exact same settings were used for PL measurements.

One last observation that can be seen in table 4.1 is that the solution ethyl alcohol that contains the pristine graphene flakes (PGF) is destructive to MAPbI₃. Yellow tinting of the crystal indicated the effect ethyl alcohol had on MAPbI₃. For sample B5 the yellow rectangle on the right side of the image is the cause of ethyl alcohol causing larger grain boundaries than the rest of the film. A variety of spin-coating speeds were used to create a layer of PGF on the top of the MAPbI₃. When the PGF in ethyl alcohol was spin-coated at higher speeds the ethyl alcohol had less of an effect on the perovskite. Therefore, another conclusion from trial 1 is that spin-coating speeds of 4000 RPM are effective for spreading the PGF solution without being destructive to the perovskite.

PL intensity data was also collected and analyzed. Even if the days 1 and 4 may not have had the exact settings, the same settings between samples A and B for both days still allow for insight if PGF in ethyl alcohol coated on top of MAPbI₃ reduces degradation. Unfortunately, since the crystal morphologies were so inconsistent PL measurements seemed to be more

dependent on how homogenous the film was. The more homogenous the film the higher the PL intensity. Table 4.2 shows the results of the peak PL intensities for the initial sample and the degraded sample left in ambient conditions for 4 days.

Table 4.2 Trial 1 PL Intensity Peak Values and Degradation Ratios

#	Sample A Images			Sample B Images		
	PL Peak Day 1 (Counts)	PL Peak Day 4 (Counts)	Ratio %	PL Peak Day 1 (Counts)	Peak PL Day 4 (Counts)	Ratio %
1	16680	1272	7.6%	12389	1070	8.6%
2	65535	3859	5.9%	36263	868	2.4%
3	25427	3894	15.3%	43472	1635	3.8%
4	10127	2220	21.9%	63858	4139	6.5%
5	15978	1088	6.8%	65535	3087	4.7%
6	13079	1079	8.2%	45896	1265	2.8%
Ave	24,471	2,235	10.95%	44,568	2,011	4.8%

There is little insight that can be concluded from the Trial 1 data. Inconsistencies in the crystal morphology correlated with huge differences in the peak value. Sample group A had a wide range of initial Peak PL values from 10,127 to 65,535 (CCD sensor maximum) and sample B varied from 12,389 to 65,535 (CCD sensor maximum). The wide range of results then can only be attributed to the inconsistency in the ability to make the MAPbI₃. Furthermore, the maximum value of 65,535 counts was occurring too often and therefore PL settings needed to be lowered so that the PL measurements can stay within the CCD sensor's range. Trial 1 certainly had a multitude of issues, but with all the problems came many learning opportunities.

4.1.2 Trial 2

After both the chemical and measurement processes were re-evaluated and reconstructed trial 2 attempted to improve the crystal morphology to have homogeneous films. Furthermore, in trial 2 a CVD graphene was attempted to be transferred to MAPbI₃ from a PET substrate and

ultimately failed. Other methods of polymer encapsulation were experimented with as a method to start characterizing lamination techniques and PL measurements.

The greatest lesson learned in trial 2 is that CVD graphene on PET cannot be transferred to MAPbI₃. Attempts to dissolve the PET substrate failed using both chlorobenzene and DMSO for a week. Resulting films were too thick when laminated on MAPbI₃ films. When trying to take a PL image of the laminated region of the sample the noise level was so excessive that the crystal morphology was unable to be seen and PL data unable to be taken as shown in figures 4.1 a, b and c.



Figure 4.1 PET/Graphene Lamination on MAPbI₃, scale bars are 100 μ m (a) Brightfield image of edge of PET/Graphene on MAPbI₃ (b) Entire sample during PL imaging; UV light illuminates PET substrate (c) PL image at edge of PET/Graphene on MAPbI₃

Figure 4.1 indicate how PL data was able to be obtained because the light would illuminate the PET substrate creating excessive noise and no visible image of the MAPbI₃. Due to the excessive noise no PL data was taken. The major lesson learned from trial 2 was that sample C could not be prepared with CVD graphene on a PET substrate. To learn from trial 2 the subsequent trial made use of CVD graphene on a copper foil, which is much more common. Yet, the general crystal morphology was improving as the sample A preparation was being honed.

4.1.3 Trial 3

Trial 3 was the last of the preliminary trials where the results did not give concrete evidence towards the hypothesis or research hypothesis. Unfortunately, the first attempt of

graphene lamination using a PMMA transfer resulted in a film that was too thin to handle as was shown in the methodology section figure 3.10 and repeated below in figure 4.2



Figure 4.2 Single PMMA spin coat on graphene before and after Cu etch (a) PMMA on graphene on Cu when first put in Cu etchant, (b) Single PMMA coat on graphene after Cu etch, (c) Handling film resulted in it crumpling up on itself making incapable of transfer

Trial 3 showed that the copper etchant worked effectively, but took longer than originally expected. Furthermore, thicker film needed to be developed to be handled, therefore lowering the initial PMMA spin-coating speeds and repeating the step 5 times to make the film more rigid was employed to ensure a graphene transfer would be possible in trial 4.

On the contrary, one of the most successful aspects of trial 3 was that the MAPbI_3 preparation was significantly more consistent than the previous two trials. In trial 3 chlorobenzene was used during the second spin-coating step when preparing the MAPbI_3 instead of diethyl ether. Furthermore, spin-coating speeds were lowered from 4000 RPM to 3000 RPM to further ensure the film was completely covering the glass substrate. The resulting films prepared for sample A were much more consistent throughout each sample and from sample to sample as shown in figure 4.3.

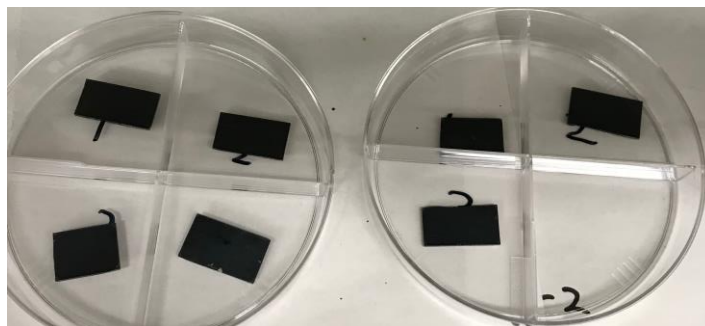


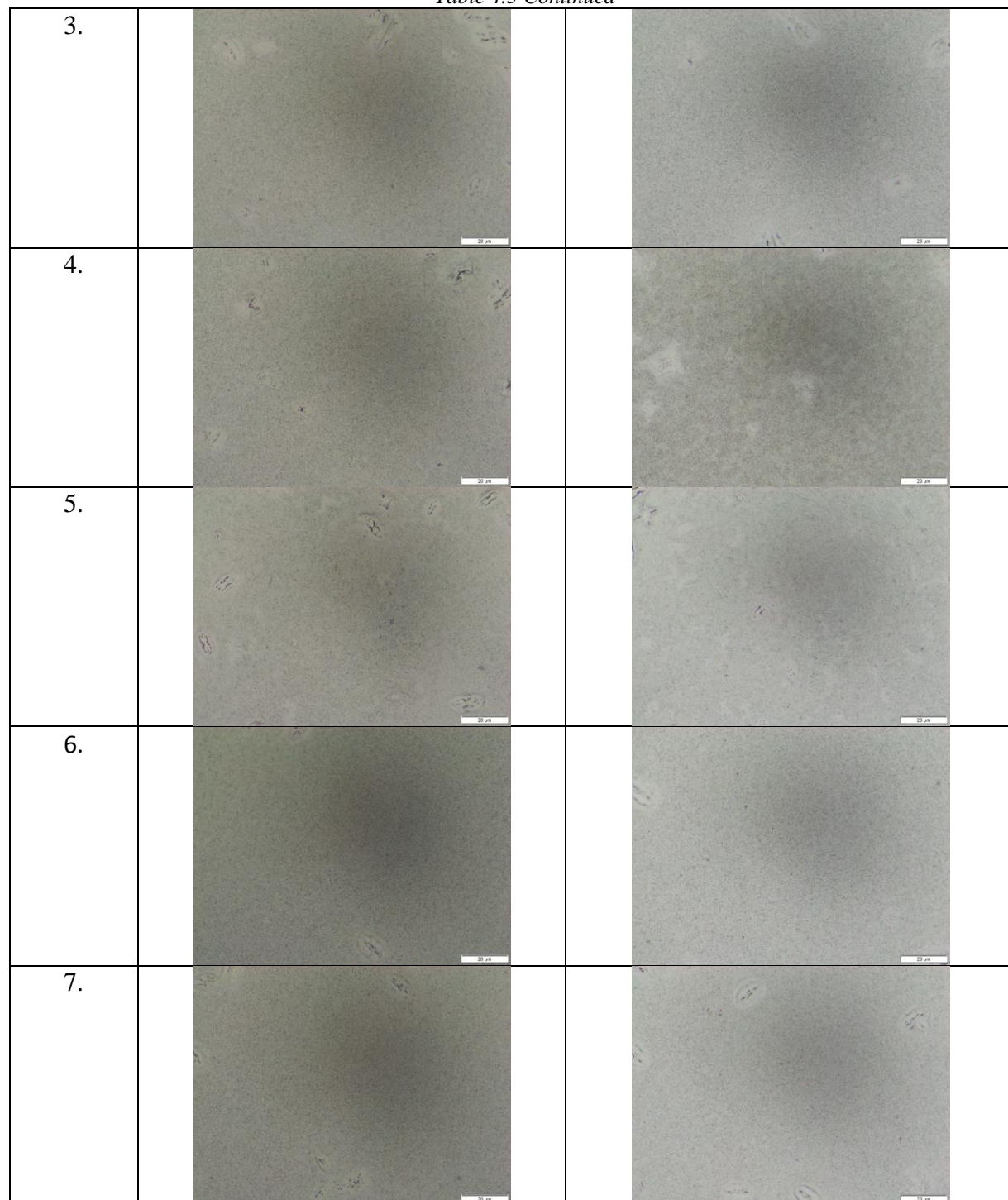
Figure 4.3 Consistent MAPbI₃ Samples in Trial 3

Figure 4.3 shows seven resulting sample A films with the improved processes for preparation. Visual inspection alone indicates the samples were more consistent. Bright field images were taken of each sample as shown in Table 4.3. However, at this point in the year humidity was much lower than during trial 1. Humidity during trial 1 was approximately 50% and for trial 3 the ambient humidity was approximately 15%, therefore the degradation time was increased significantly to 17 days. Only sample type A was created, and all scale bars are 20 μm .

Table 4.3 Trial 3 bright field and PL images scale bars are 20 μm

Sample #	Sample A Images	
	Day 1	Day 17
1.		
2.		

Table 4.3 Continued



The brightfield images shown in table 4.3 indicate two things: improved crystal morphology and the degradation was not occurring due to low humidity. Trial 3 was useful for

the improvement of the crystal morphology of sample type A, which had been optimized and was highly repeatable resulting in homogenous MAPbI₃ samples. Since the ambient environment had a reduced humidity from trial 1 it was decided that a controlled humidity cabinet would be best to control the degradation of the samples. Therefore trial 4 implemented the use of a humidity cabinet where samples were stored in 80% humidity for 12 to 24 hours at a time.

Two other improvements occurred because of trial 3. First, was an updated PL measurement process to reduce photobleaching error. Taking PL images that had 4 second exposures with the X-Cite iris ½ open was causing photobleaching errors during measurements of PL intensity graphs. Subsequently, the PL measurement procedure was updated so that PL data would be taken after the bright field image and PL image mapping was rid of, because it did not provide useful quantitative information for the hypothesis. The second change was a choice to start taking 9 measurements on each sample and calculate sample averages rather than taking one measurement on numerous different samples to improve the statistics and get a better idea of the samples as a whole.

4.2 Trial 4: Comparing Samples A and C

Trial 4 only compared samples A and C and was the first trial to make use of a 3x3 array of spot indicators to take measurements at similar locations for each time measured. The top left corner was also marked so that orientation of the sample could be indicated. Measurements were made directly to the right of each dotted indicator. Figure 4.4 below depicts how the samples were marked using a green marker. It is important to understand that while each measurement was in the same general location of the sample, it was not possible to measure the exact same location for each measurement.

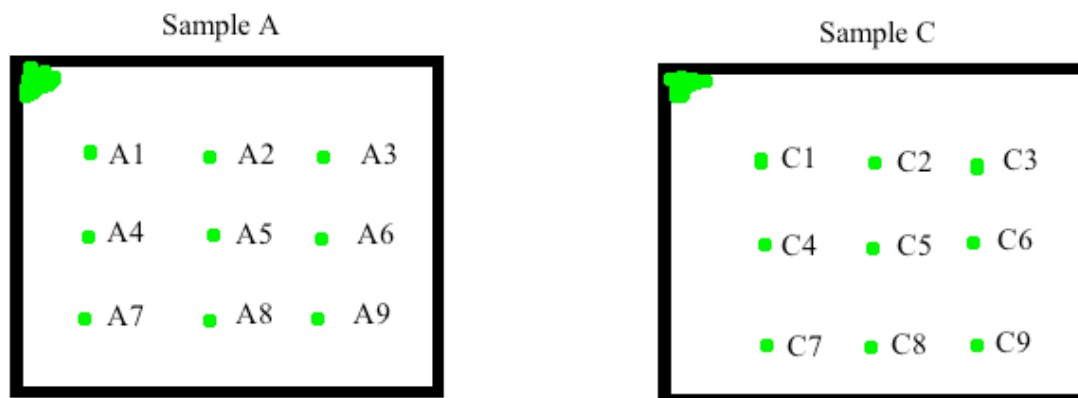


Figure 4.4 Diagram of marking indicators for samples A and C

Figure 4.4 describes the marking indicators, orientation, and labeling of each measurement. Measurements were taken approximately where each label in figure 4.4 is located. Trial 4 was the first successful PMMA transfer of graphene to sample C. PMMA was spin-coated 5 times at 800 rpm on the graphene while still on the copper foil. The resulting film was thick enough to be transferred from the FeCl_3 copper etchant bath to the SC-1 and SC-2 cleaning baths with DI rinses in between. The graphene/PMMA was hung and air-dried before being laminated during the annealing of MAPbI_3 . Chlorobenzene (CB) was then dripped on top of the laminated sample to dissolve the PMMA; however, not enough to fully dissolve the PMMA. Figures 4.5 a, b, and c show the stiffer film capable of being transferred and air dried.

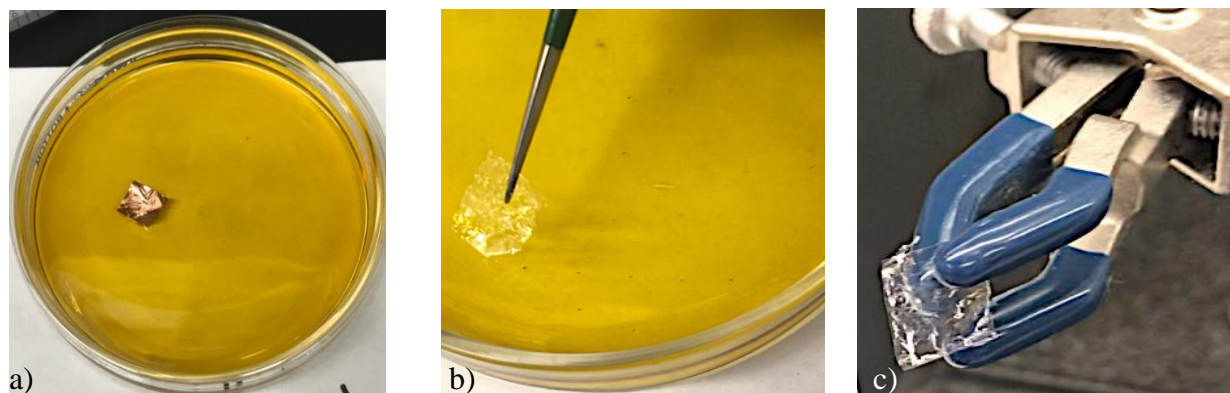


Figure 4.5 Five PMMA spin coats on graphene before and after Cu etch (a) PMMA on graphene on Cu when first put in Cu etchant, (b) Five PMMA coats on graphene after Cu etch able to be handled, (c) Stiff film was able to be air dried for transfer process to sample C

The resulting samples A and C with the measurement indicators are shown below in figure 4.6 a and b.

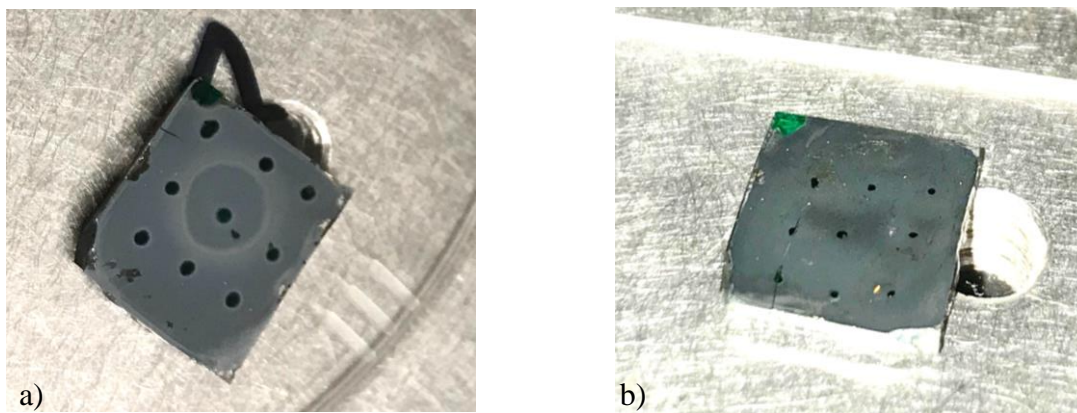
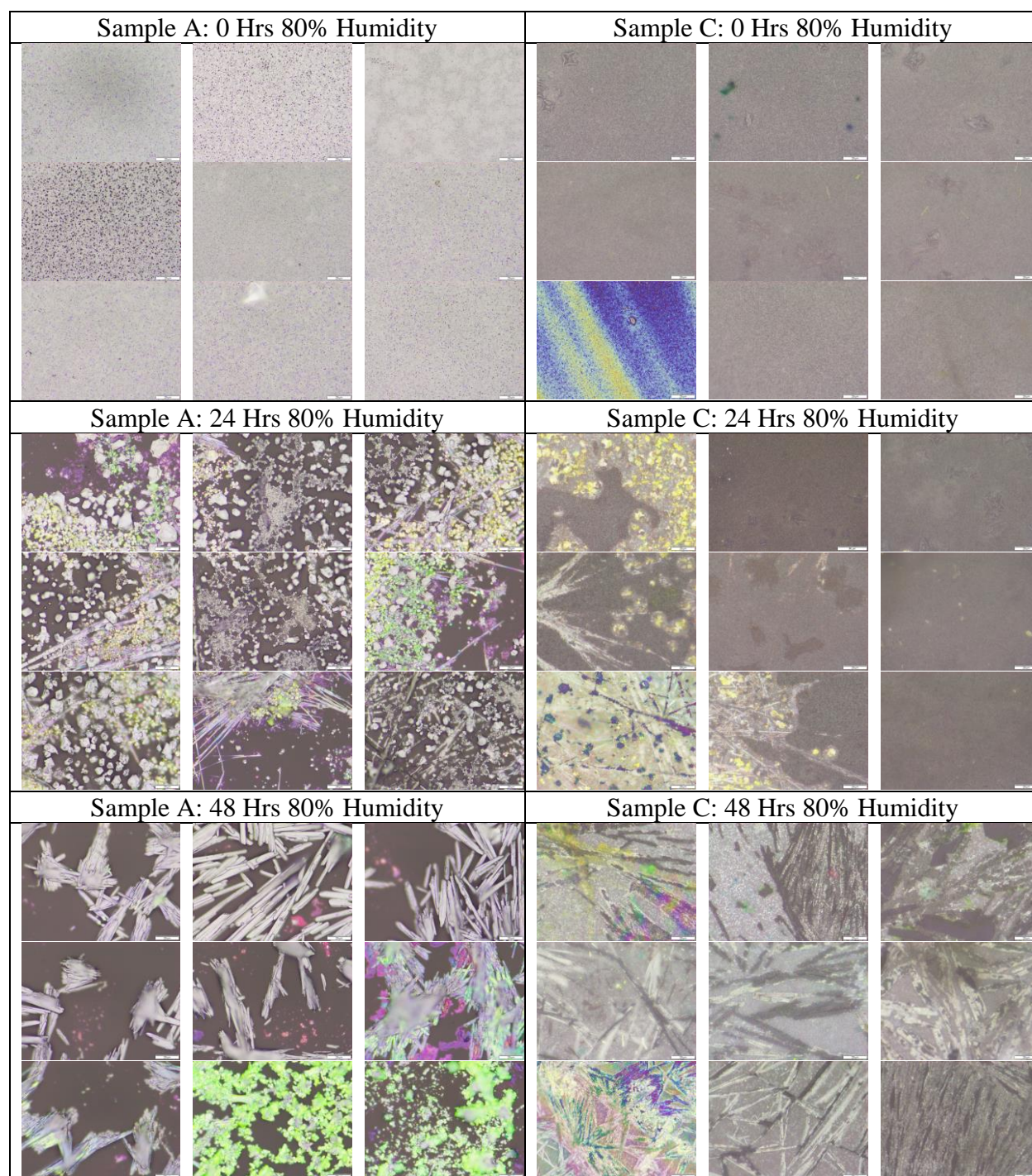


Figure 4.6 Trial 4 samples A and C before any exposure to humidity (a) Sample A: MAPbI_3 with 3x3 array of measurement indicators and orientation marking in the top left corner (b) Sample C: MAPbI_3 with graphene/PMMA lamination with 3x3 array of measurement indicators and orientation marking in the top left corner

The two samples for trial 4 then had the nine locations measured for optical images and PL measurements for 0, 24, and 48 hours of 80% humidity. There was some inconsistency, however in the storage of the samples. The samples were left in the humidity cabinet in a petri dish. Initially the petri dish lid was left on, for 30 minutes of the first 24 hours the petri dish lid was taken off so that the humidity mist would directly contact the samples causing the degradation to occur much faster. From 24 to 48 hours the petri dish lid again was left off for 30 minutes exacerbating the degradation process. While both samples went through equivalent conditions consistency in keeping the petri dish lid on for the full time was improved in subsequent trials. Table 4.4 below is the collected optical images comparing samples A and C for 0, 24, and 48 hours of 80% humidity exposure in the 3x3 array as indicated in figure 4.6.

Table 4.4 Trial 4 bright field images scale bars of 20 μm



The optical images of samples A and C clearly show that the crystal morphology of sample A is more effected by the humidity than sample C. Initial images of sample A and C at 0 hours of humidity shows that the crystal morphology is similar; however, sample C images seem

dimmer than sample A, which is occurring because the PMMA has not been fully dissolved. A layer of PMMA will reduce the optical brightness and PL intensity because some of the light is absorbed into the material. Furthermore, sample C1-7, or the bottom left corner has a blue and yellow color that also can be attributed to the PMMA. PMMA can have iridescence that is changing the color of the optical images. Optical images for C1-7 for 24 and 48 hours also have the same iridescent appearance indicating that the PMMA was not fully dissolved as intended. Future trials made use of a CB bath rather than just dripping CB on top of the PMMA to dissolve the transfer material.

Comparing the crystal morphology of sample A to sample C and its reaction to humidity sample A has a more drastic change in crystal morphology than in A. At 24 hours of 80% humidity exposure all nine locations of sample A imaged show a decomposition of the film that had been present before humidity exposure. Degradation is indicated by loss of material due to the cation evaporating, change from a homogenous film to islands of crystals separated by the now exposed glass substrate below, purple fiber-like structures, and yellowing of the crystal indicating a change from MAPbI_3 to PbI_2 . Any green tints were due to the marker indicator bleeding and was subsequently changed to a red sharpie in later trials. While all nine of the image locations of sample A showed degradation at 24 hours of exposure, only four of the nine locations showed significant signs of degradation for sample C. Images C1, C4, C7, and C8 show significant yellowing of the crystal suggesting humidity was entering underneath the graphene and PMMA lamination from the left side of the sample. Minute yellowing is visible in images C5 and C6 for 24 hours of exposure, and no yellowing is visible for images C2, C3, and C9.

At 48 hours of 80% humidity exposure sample A shows no resemblance to its original form and sample C had also become quite degraded. Sample A's crystal morphology has changed to mostly fiber-like islands, with A8 and A9 being green due to the bleeding of the green marker. Sample C's crystal morphology at 48 hours shows some sparse areas of its original form, but overwhelmingly is becoming fibrous like sample A. Degradation is certainly occurring in both samples but is occurring in sample A faster. While, it can be said that sample C is having a slowed rate of degradation the indication that PMMA is still present muddles whether the reduced degradation is occurring because of the graphene or the PMMA layer.

Below figures 4.7 and 4.8 are the resulting average PL spectrums during the degradation of samples A and C. PL data was collected containing 1024 equally spaced wavelength points between 612 nm to 885 nm. Each image in table 4.4 indicates where the PL data was taken after 0, 24, and 48 hours of 80% humidity exposure. Each of the nine measurement locations were then averaged for all 1024 wavelength points to create an estimate of the PL intensity that represents the entire sample as indicated in the graphs below.

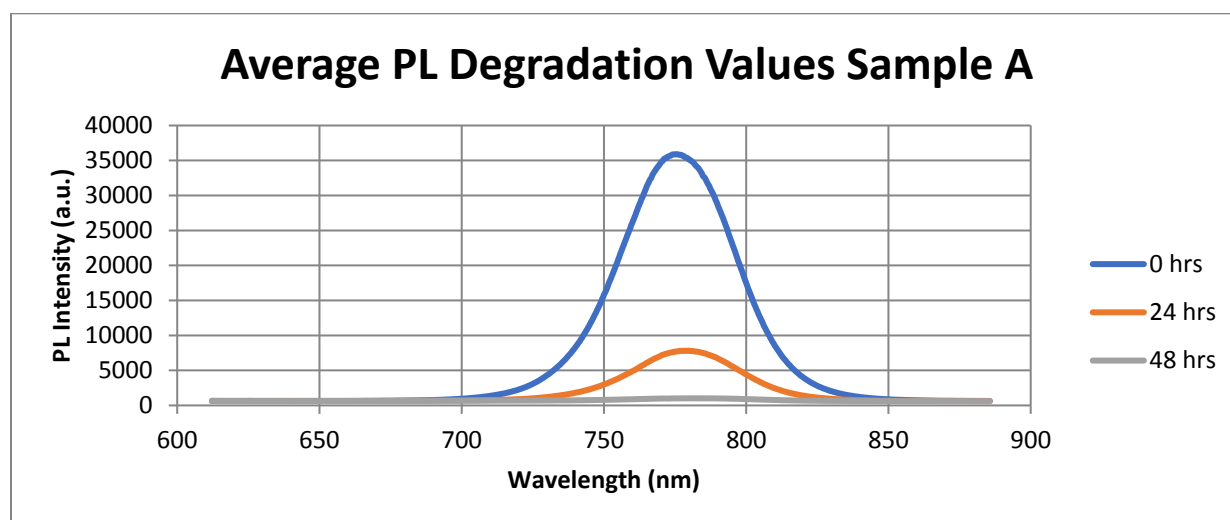


Figure 4.7 Trial 4 averaged photoluminescence spectra for sample A

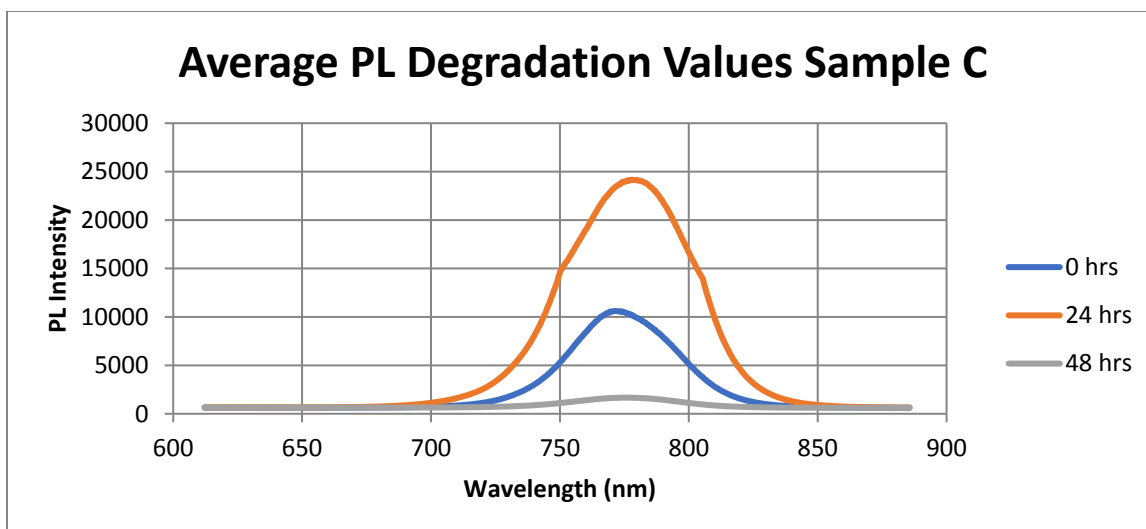


Figure 4.8 Trial 4 averaged photoluminescence spectra for sample C

The PL peak intensity measurements for each of the nine locations and their averages are provided in table 4.5 below.

Table 4.5 Trial 4 peak PL intensity measurements

Sample A Maximum PL Intensity Values			
	0 Hrs	24 Hrs	48 Hrs
A1	38004	1001	777
A2	35828	38760	830
A3	34844	1400	642
A4	35059	3599	924
A5	30236	2406	1580
A6	40590	826	638
A7	31355	1625	1361
A8	31818	726	1495
A9	47103	22247	1392
Ave.	36093	8066	1071

Ratio After 24 Hrs	22.35%
Ratio After 48 Hrs	2.97%

Sample C Maximum PL Intensity Values			
	0 Hrs	24 Hrs	48 Hrs
C1	11133	23775	652
C2	7081	4686	1672
C3	5595	12018	5969
C4	6130	30510	1749
C5	8270	65535	1137
C6	8402	6517	1141
C7	36523	7841	896
C8	6874	11887	894
C9	6099	59601	1130
Ave.	10679	24708	1693

Ratio After 24 Hrs	231.48%
Ratio After 48 Hrs	15.86%

From figures 4.7 and 4.8 and table 4.5 there are some key takeaways from trial 4. First, and most importantly is that the ratio of the peak PL intensity for sample C after 48 hours of 80% humidity exposure is greater than the ratio of sample A, which provides support to the hypothesis

that sample C will degrade less than sample A. Sample C attained approximately 16% of its original PL intensity after 48 hours of 80% humidity exposure while sample A only attained approximately 3% of its original PL intensity.

Another major takeaway is that sample C had a 231% increase in PL intensity after 24 hours of humidity as indicated in table 4.5 and shown graphically in figure 4.8. Sample A however did not indicate any increase in PL intensity and had only 22% of its original PL intensity after 24 hours of 80% humidity exposure.

The results of trial four also indicate that the PL intensity for sample A at 0 hours was significantly higher than sample C. Sample A had an average peak intensity of approximately 36,000 counts at 0 hours while sample C had an average peak intensity of approximately 11,000 counts at 0 hours. Sample C had a much lower initial PL intensity than sample A because the PMMA coating was blocking some light from hitting the MAPbI_3 through both absorption and reflection and again was blocking reemitted photons that were leaving the MAPbI_3 reducing the total counts detected by the photodetector. The PL spectra curve of sample C as shown in figure 4.8 also is not as gaussian as the PL spectra curve for sample A in figure 4.7 also because of the effect due to PMMA reflection and absorption.

Overall trial 4 was an important step towards the final goal of the study by successfully transferring graphene to the surface of MAPbI_3 and measuring a reduction in degradation; however, several improvements were made when moving to subsequent trials. First, the green marker indicator was changed to a red sharpie. Second, the petri dish lid needs to be left on for the full time of the humidity exposure. Third, the PMMA needs to be fully dissolved to ensure that the graphene is responsible for the reduction in degradation and not the PMMA. Furthermore, Raman spectroscopy was suggested to characterize sample C to ensure that

graphene is in fact on the sample. Fourth, AFM measurements need to be taken to characterize the surface topography of the samples as they degrade, see if PMMA is still on the surface, and compare sample C with sample A to get a general idea of how well graphene conforms to the surface of MAPbI₃. Fifth, sample C still saw significant degradation likely due to cracks in the film or pockets that allowed humidity to seep in from the left side of sample C. Trial 5 attempted to improve upon the issues of trial 4 and included sample B again for degradation rates of all three samples to be compared.

4.3 Trial 5 Comparing Samples A, B, and C

Trial 5 was the most comprehensive trial of this study, but still had faults. In trial 5 one sample of A, B, and C were created and compared with the optical microscope, PL data, and AFM data. Raman spectroscopy was also taken on the samples to indicate whether graphene was on the surface. Each of the samples were then exposed to 80% humidity for up to 240 hours with the petri dish lid left on. With the petri dish on the samples were not directly contacted by the mist from the humidifier, but the petri dish is not air tight. Because the mist could not fall directly onto the samples the degradation rate was much slower than what was observed for trial 4. However, again each of the samples went through the exact same environmental conditions throughout the trial. Sample B seemed to have the exact same characteristics as sample A. After taking Raman spectroscopy measurements it was found that the pristine graphene flakes in ethyl alcohol provided a negligible amount of graphene to the surface of the MAPbI₃ and therefore sample B was dismissed as an ineffective method to encapsulate the perovskite. No optical or AFM images of sample B are provided due to its dismissal as a method of encapsulation during this trial; however, the final PL peak intensity averages and ranges will include sample B to show its inability to reduce degradation.

Another issue that occurred during trial 5 was a malfunction of the spin coater when applying the PMMA coats for the graphene transfer. The spin coater stopped working after only 4 PMMA coats at 810 RPM so resulting films after the Cu etch were difficult to handle and transfer from bath to bath. Unwanted folds and tears occurred before laminating the PMMA/graphene on the MAPbI₃ leading to the potential of cracks in the laminating film allowing for degradation of sample C.

4.3.1 Raman Spectroscopy Characterization

The Raman spectroscopy data is presented first for the dismissal of sample B. Figure 4.9 shows the Raman characterization of MAPbI₃ alone. Figure 4.10 shows the Raman characterization of the pristine graphene flakes in ethyl alcohol alone. Figures 4.11 and 4.12 are the results of the Raman characterization of the lamination of PMMA/Graphene on MAPbI₃ and indicate that graphene is present. For all the Raman spectroscopy a laser wavelength of 633 nm was used.

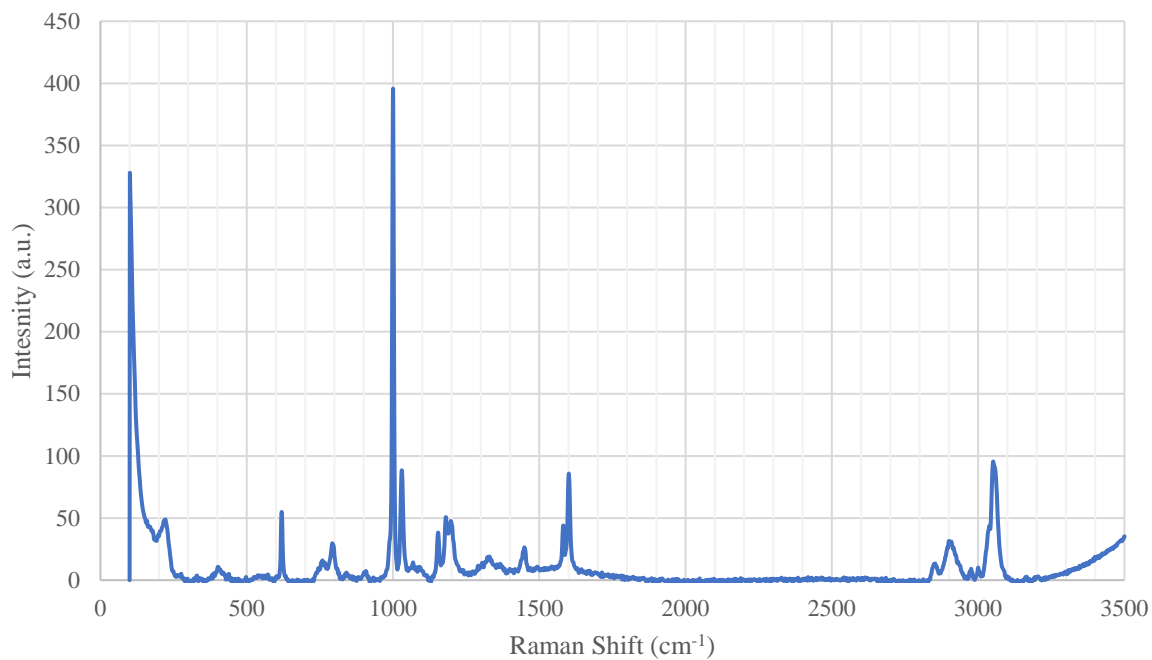
RAMAN Of MAPbI₃ (Sample A)

Figure 4.9 Raman Spectroscopy Characterization of MAPbI₃

RAMAN PGF in Ethyl Alcohol

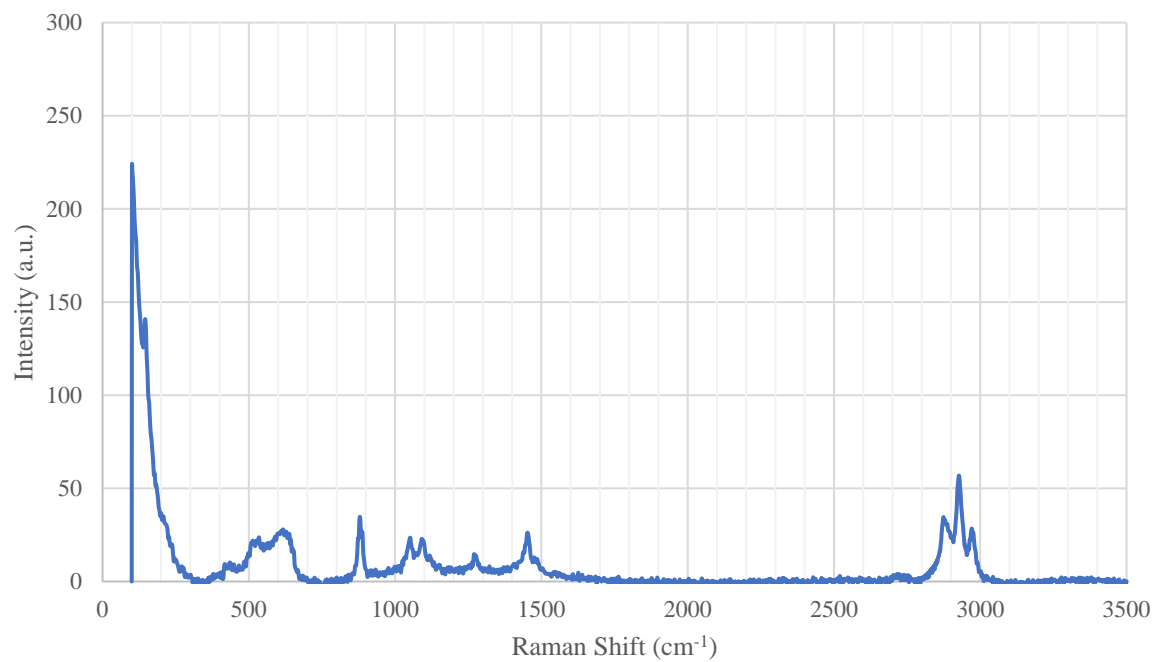


Figure 4.10 Raman Spectroscopy Characterization of Pristine Graphene Flakes in Ethyl Alcohol Solution

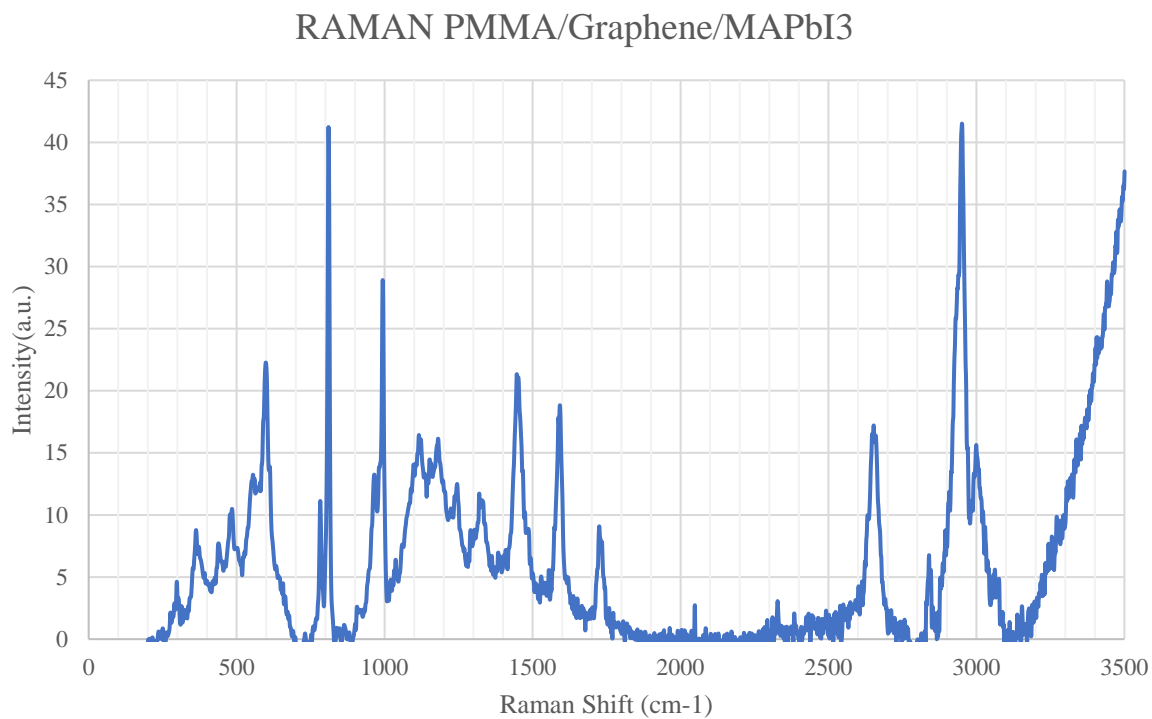


Figure 4.11 First Raman Spectroscopy Characterization of PMMA/Graphene/MAPbI₃

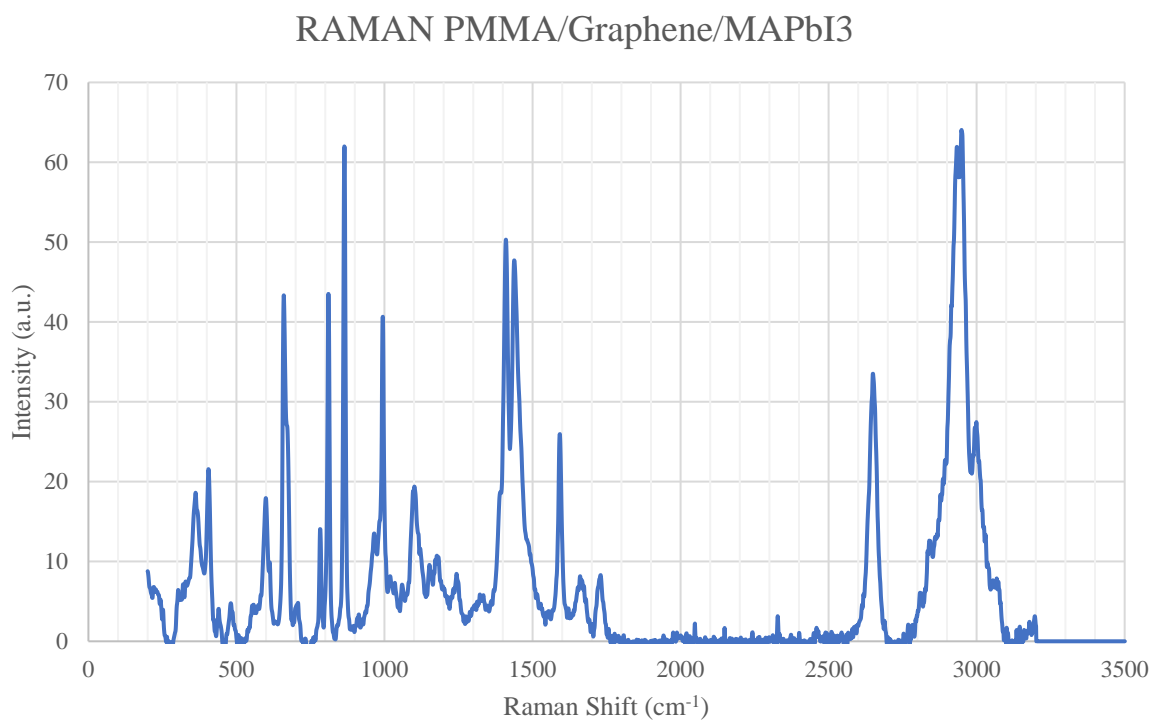


Figure 4.12 Second Raman Spectroscopy Characterization of PMMA/Graphene/MAPbI₃

The main purpose for the Raman spectroscopy measurements was to see if graphene was present on the samples. Figure 4.9 gives a background of the Raman characterization of just MAPbI₃ and can be used as a reference for figures 4.11 and 4.12. Figure 4.10 of the graphene flakes in ethyl alcohol shows no indication that graphene is present. As was described in the literature review Bischoff et al. (2011) explains that the peaks of graphene should occur at approximately a Raman shift of 1340 cm⁻¹, 1580 cm⁻¹ and 2680 cm⁻¹. The Raman characterization of the graphene flakes in ethyl alcohol solution showed none of the essential peaks that indicate the presence of graphene and was the main reason why sample B was dismissed. Upon further analysis the degradation of sample B also happened to behave very similarly to sample A because there were negligible differences between the samples.

Figures 4.11 and 4.12, however did indicate that graphene was present. In both figures' peaks are visible at approximately 1400 cm⁻¹, 1600 cm⁻¹ and 2650 cm⁻¹ indicating that graphene is present for sample C. Furthermore, the dual peak at 1400 cm⁻¹ in figure 4.12 is also common for graphene and provides further evidence that graphene is present for sample C. The Raman spectroscopy data was useful for understanding the presence of graphene and is one of the only ways of indicating that graphene is indeed there.

4.3.2 Trial 5 Atomic Force Microscopy Data

The atomic force microscopy (AFM) data provided essential information about the samples for trial 5. Specifically, for sample C the AFM distinguished that the PMMA had not been fully dissolved and therefore a longer Chlorobenzene (CB) bath was necessary. For trial 5 the PMMA/graphene/MAPbI₃ sample was submersed in the CB bath for only five minutes. Since numerous coats of PMMA was spin coated on the original graphene/Cu foil sheet the CB bath time needed to be substantially longer.

Trial 5 was used as an in-depth analysis for the surface topography during degradation of sample A. The data presented in this section will be the most comprehensive of all the AFM data for sample A degradation as well as the analysis. Trial 6 also took AFM data but focused on only 20 μm x 20 μm scans for consistency for surface roughness, height, and peak data. The data presented in this section will cover different sized scans and analysis on certain features.

Initially the surface of MAPbI_3 appears as a hilly or “bubbly” surface with numerous peaks that are evenly spaced and homogenous. After degradation the “bubbly” features conform into a ridge and the fibers seen previously in optical images. Each AFM image went through a series of post-production corrections to make the image more accurately represent the sample. The post-production corrections applied to the data were leveling the data by mean plane subtraction so that any consistent slopes appear flat. Any 2nd degree polynomial background profiles were removed in the x-direction due to any bowing error from the AFM scan movement. Scratches were removed using a feature in Gwyddion that correct horizontal scars or strokes. Rows were aligned using a median of differences algorithm. And lastly the minimum data value of the scan was shifted to be equal to 0. Figure 4.13 is an AFM scan for sample A before any exposure to humidity of the size 50 μm x 50 μm .

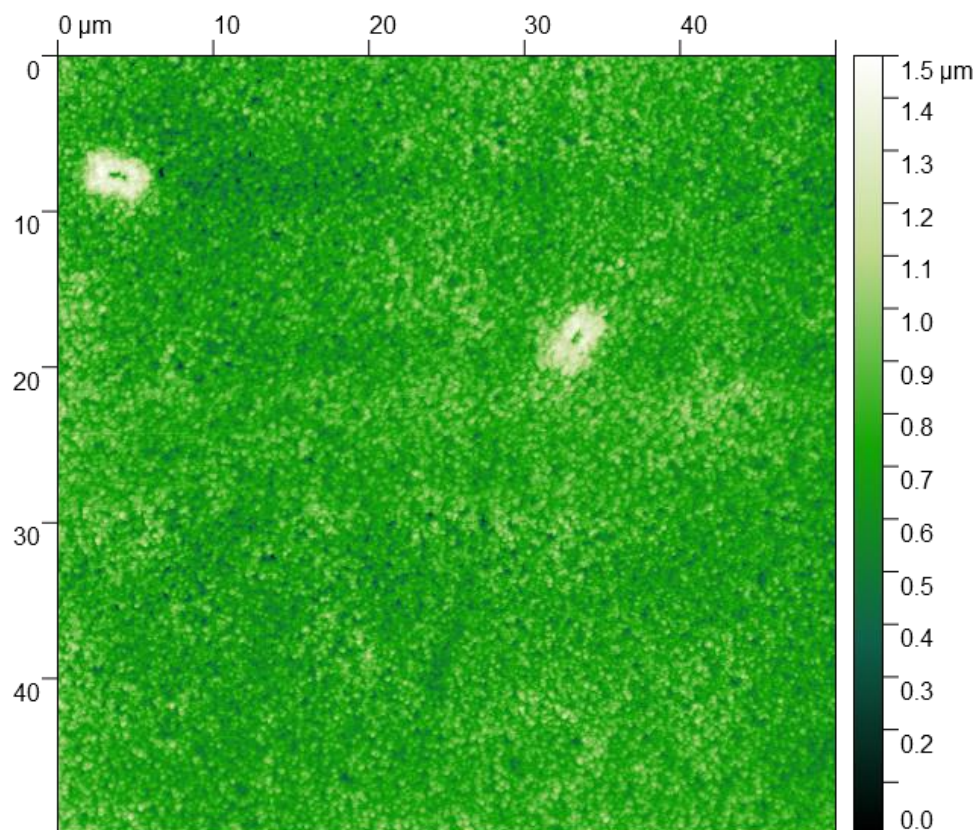


Figure 4.13 50 x 50 AFM scan of Sample A (MAPbI₃) at 0 Hours of 80% Humidity

The number of peaks was found using the watershed feature in Gwyddion with grain location settings of 2 steps, a 5% drop size, and a threshold of 1, and segmentation settings of 100 steps and a drop size of 5%. These settings were used for each of the scans analyzed for the number of peaks. The resulting image using the watershed tool is shown in figure 4.14, where the red is the mask that is separating out the grains, or peaks and is analogous to water drops creating lakes at each of the minima of the scan.

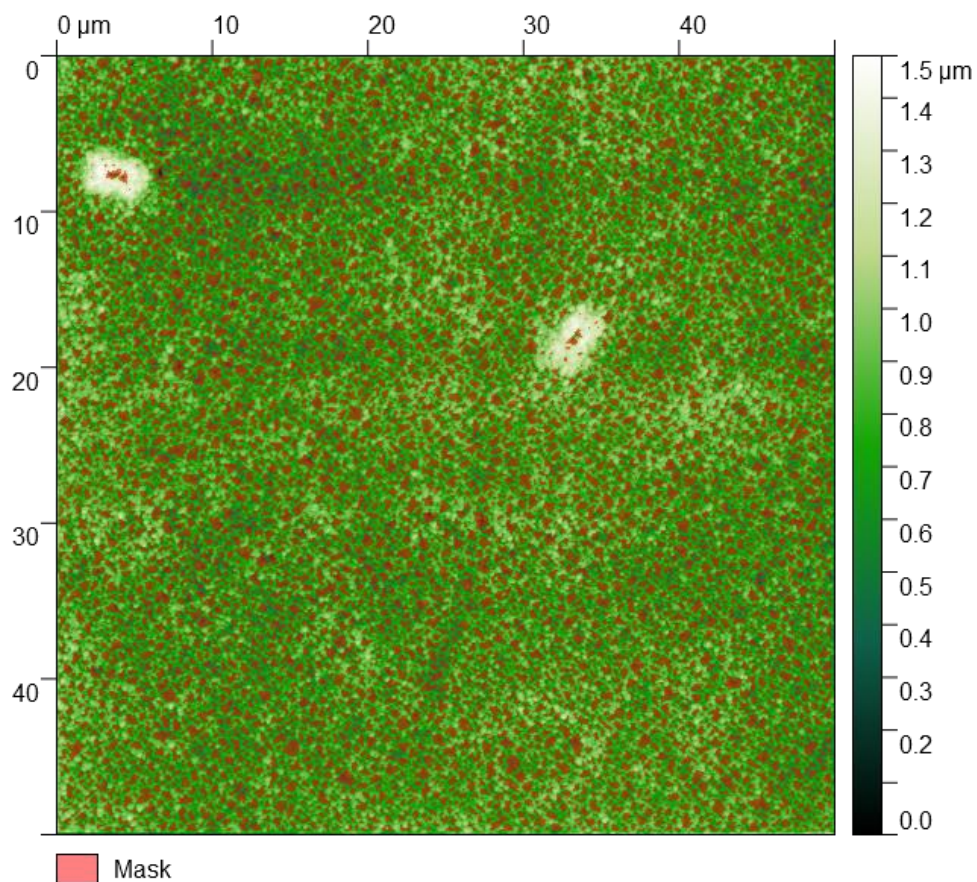


Figure 4.14 Watershed analysis of 50 x 50 AFM scan of Sample A (MAPbI₃) at 0 Hours of 80% Humidity

8,771 peaks were identified in figure 4.14. Peak values were recorded for all the scans and will be graphically represented at the end of this section. Figure 4.15 is the same area as figure 4.13 but a 20 μm x 20 μm scan zoomed directly in the middle of figure 4.13 with profile line 1 drawn across the image.

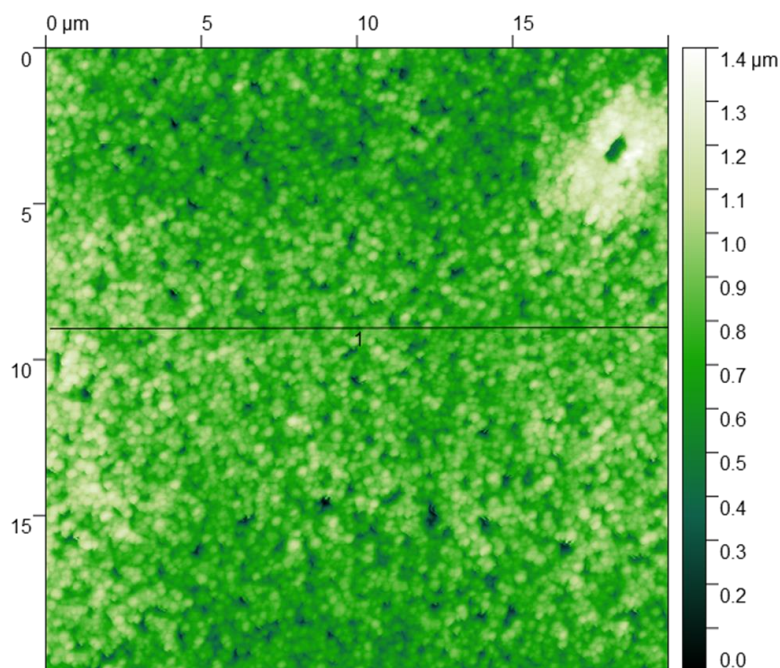


Figure 4.15 20 x 20 AFM Scan of Sample A (MAPbI_3) at 0 Hours of 80% Humidity

3754 peaks were found in figure 4.15, which is obviously less than the $50\ \mu\text{m} \times 50\ \mu\text{m}$ scan. The profile height data of the profile path indicated in the above AFM scan figure 4.15 is shown in figure 4.16 with measured distances between the purple indicator bars and the intersection of the profile path on the right with measurements between each indicator bar going from left to right.

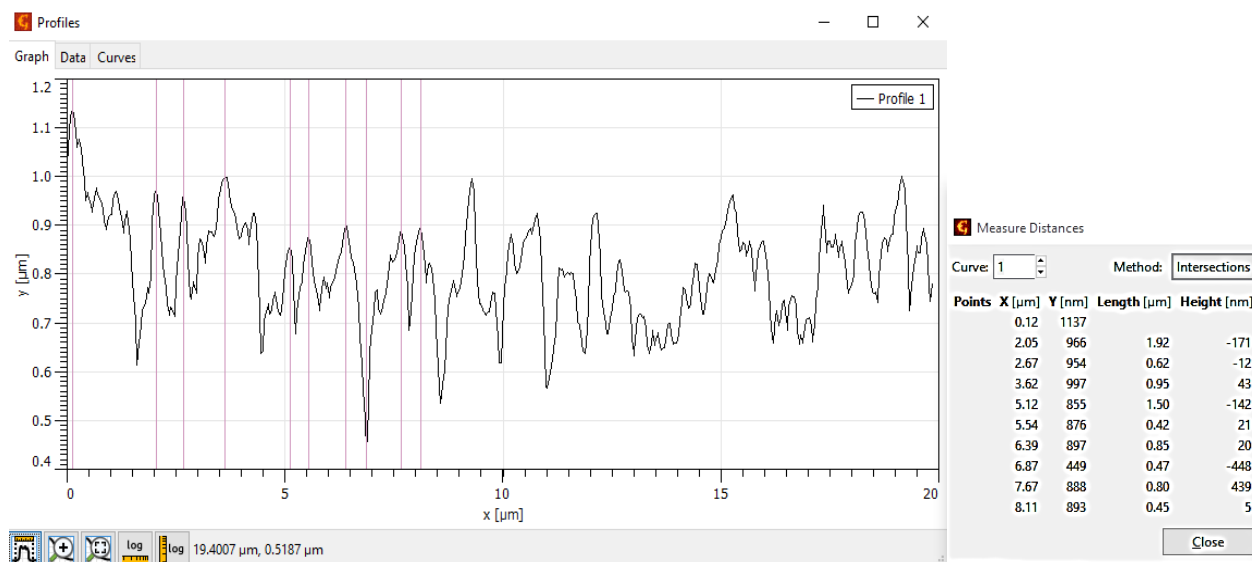


Figure 4.16 Profile Path of AFM Scan of Sample A (MAPbI_3) at 0 Hours of 80% Humidity

The profile path shown in figure 4.16 shows that MAPbI₃ begins with many peaks often within a micrometer from one another. Heights of the peaks vary, but larger ranges from the bottom of the valley to the peak are approximately 450 nm. Figure 4.17 below shows a three-dimensional (3D) rendition of the two-dimensional (2D) image shown in figure 4.15.

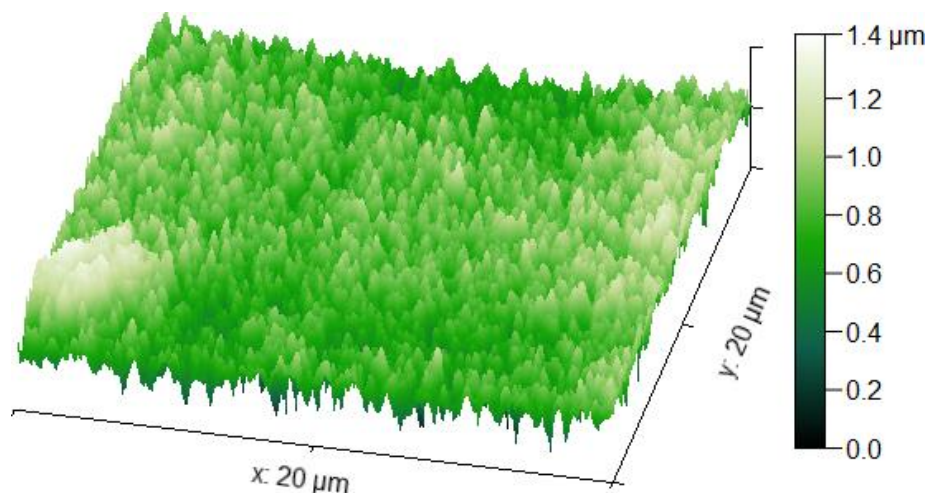


Figure 4.17 3D 20 x 20 AFM Image of Sample A (MAPbI₃) at 0 Hours of 80% Humidity

Figure 4.17 gives a better visual representation of the topography of MAPbI₃ before any humidity exposure. The surface has a sort of “bubbly” quality with a maximum height range of 1.4 μm , or Z value, in a 20 μm x 20 μm scan for the X and Y values. Each of the AFM scans evaluated for surface roughness and height range for trial 5 and 6 were 20 μm x 20 μm for consistency to trend the topography characteristics throughout degradation. Figure 4.18 below is a 5 μm x 5 μm scan that zoomed in further into the center of the 20 μm x 20 μm and 50 μm x 50 μm scan directly into the middle of the scan area. Figure 4.19 is the 3D visualization of the AFM scan in figure 4.18.

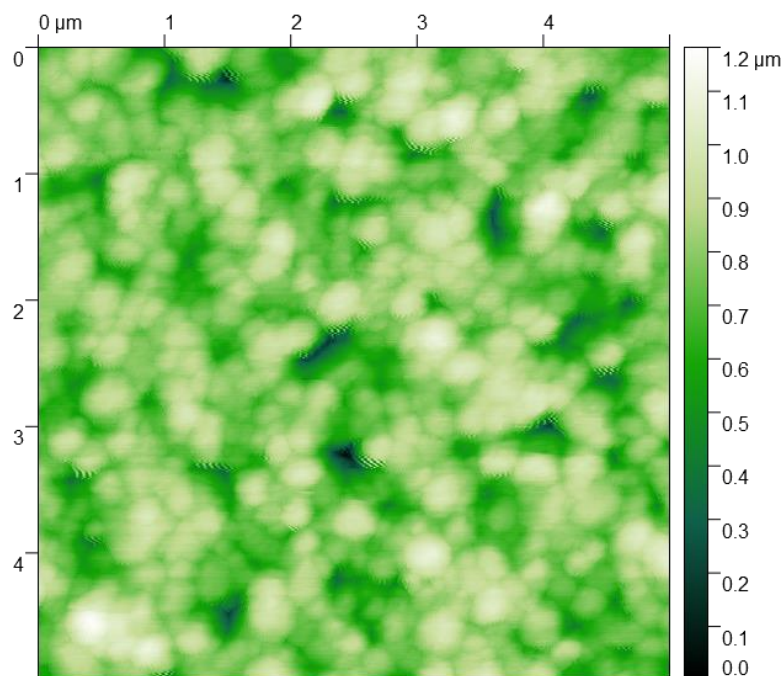


Figure 4.18 5 x 5 AFM Image of Sample A (MAPbI₃) at 0 Hours of 80% Humidity

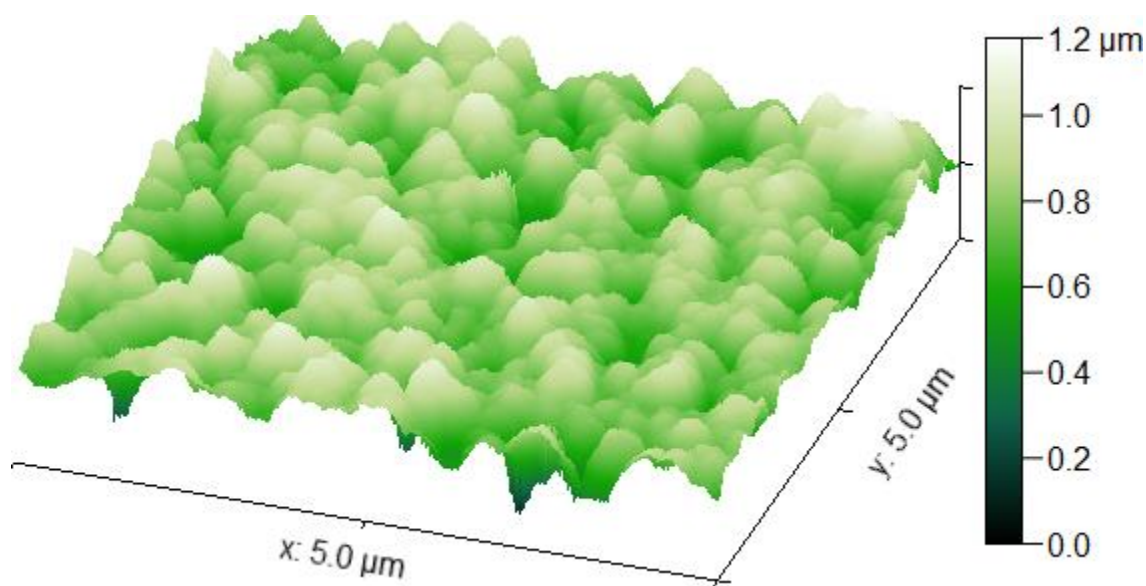


Figure 4.19 3D 5 x 5 AFM Image of Sample A (MAPbI₃) at 0 Hours of 80% Humidity

For the 5 μm x 5 μm scan shown in figures 4.18 and 4.19 545 peaks were found, expressing that as the scan zoom in further and further smaller peaks will become apparent.

Based on the ratio of 545 peaks in a $25 \mu\text{m}^2$ area the $20 \mu\text{m} \times 20 \mu\text{m}$ scan, or $400 \mu\text{m}^2$ is 16 times larger and should have over 8000 (compared to the 3754 calculated) and even greater for the $50 \mu\text{m} \times 50 \mu\text{m}$ scan. The peak finding watershed tool in Gwyddion uses a steepest decent algorithm and has exit criteria that is subject to the user and a threshold input that affects the capability of what peaks will be detected. The $5 \mu\text{m} \times 5 \mu\text{m}$ scan works as a good estimate for accurate peak finding, because within a $1 \mu\text{m} \times 1 \mu\text{m}$ area of the scan the visible peaks can be physically counted and averaged to be about 22 peaks. This average multiplied by 25 then gives a total estimate of 550 peaks. While smaller peaks may be below the detection of the algorithm for the $20 \mu\text{m} \times 20 \mu\text{m}$ scan, by keeping the same input values for the watershed tool and using the same scan area over time insight on the number of peaks during degradation was accomplished.

In comparison the surface of sample C in trial 5 was extraordinarily smooth indicating that PMMA was still present and had not been fully dissolved. Figure 4.20 below shows the AFM scan of sample C at 0 hours of 80% humidity exposure with a profile line traversing the scan to graphically represent the height data.

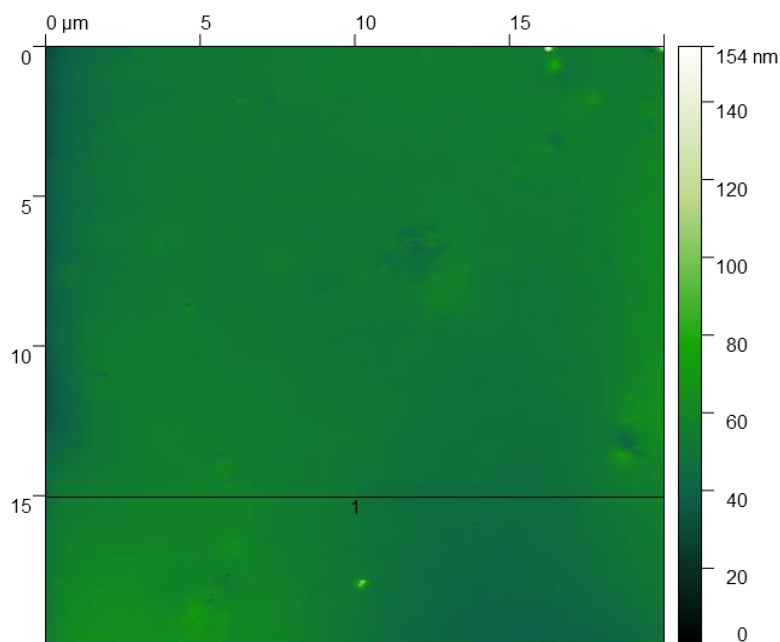


Figure 4.20 AFM Scan of Sample C ($\text{MAPbI}_3/\text{Graphene}/\text{PMMA}$) at 0 Hours of 80% Humidity

The profile path in the AFM scan of sample C shown in figure 4.20 above is then graphically displayed in figure 4.21 below with the intersection measurements to the right.

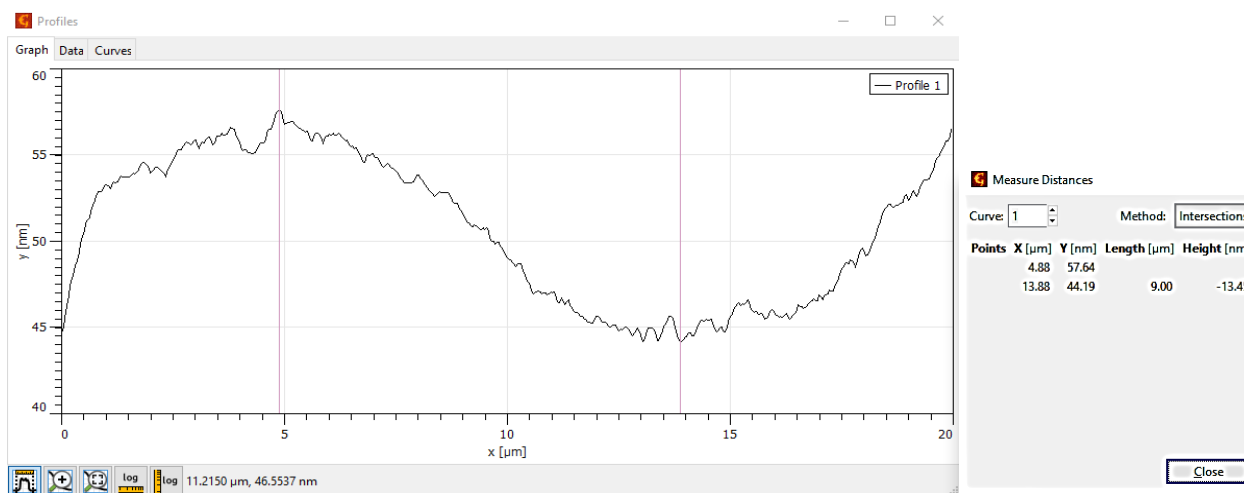


Figure 4.21 Profile Path of AFM Scan of Sample C ($\text{MAPbI}_3/\text{Graphene}/\text{PMMA}$) at 0 Hours of 80% Humidity

While the profile path in Figure 4.21 may look like a large sinusoidal wave the measurement indicators show that there is only an approximate change of 13.5 nm in height in a 20 μm long path. When comparing the profile path of sample C (figure 4.21) to sample A (figure

4.16) sample C is orders of magnitude flatter and smoother. Furthermore, only 37 peaks were found using the watershed analysis. For trial 5 any measurements of degradation for sample C were affected by the layer of PMMA coating the surface disallowing accurate conclusions on the hypothesis; however, an understanding of the degradation of sample A can still be concluded from trial 5. No changes to the surface topography occurred to sample C during the degradation as can be seen later in figure 4.37 and figure 4.38.

AFM measurements of sample A were then taken at 12 hours, 24 hours, 36 hours and 48 hours of 80% humidity exposure. Figure 4.22 a, b, and c below show a $50\ \mu\text{m} \times 50\ \mu\text{m}$, $20\ \mu\text{m} \times 20\ \mu\text{m}$ and $5\ \mu\text{m} \times 5\ \mu\text{m}$ scan at 12 hours of 80% humidity exposure, with no visible affects to the surface topography, however, the number of peaks were decreasing.

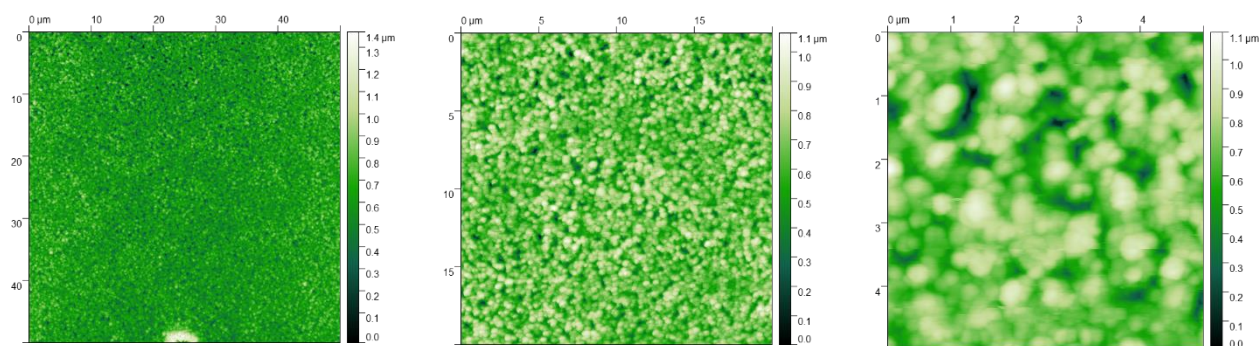


Figure 4.22 AFM Scans of Sample A (MAPbI_3) at 12 Hours of 80% Humidity a) 50×50 , b) 20×20 , c) 5×5

While the topography looks very similar, the statistics changed. Each of the scans in figure 4.22 had a reduction in the number of peaks compared to 0 hours of humidity exposure. The $50\ \mu\text{m} \times 50\ \mu\text{m}$ scan dropped from 8,771 peaks to 7,602, the $20\ \mu\text{m} \times 20\ \mu\text{m}$ scan dropped from 3,754 peaks to 3,289 peaks, and the $5\ \mu\text{m} \times 5\ \mu\text{m}$ scan dropped from 545 peaks to 344 peaks. For 24 and 36 hours of humidity exposure there was a focus on the $20\ \mu\text{m} \times 20\ \mu\text{m}$ scans. Figure 4.23 a and b below show the $20\ \mu\text{m} \times 20\ \mu\text{m}$ AFM scans for sample A at 24 and 36 hours of humidity exposure respectively.

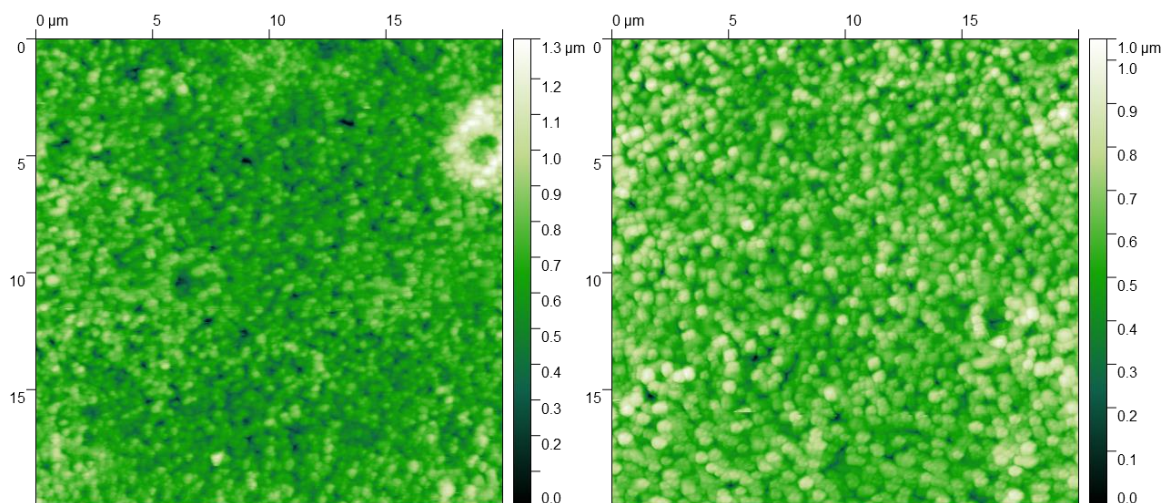


Figure 4.23 20 x 20 AFM Scans of Sample A (MAPbI_3), a) 24 Hours of 80% Humidity b) 36 Hours of 80% Humidity

The trend of peaks reducing during exposure to humidity continued. For 24 hours of 80% humidity, figure 4.23 a, had 2,528 peaks, down from 3,289 at 12 hours. At 36 hours of 80% humidity exposure, figure 4.23 b, had 2,313 peaks. There was a consistent decrease in peaks.

After 48 hours of 80% humidity exposure to sample A there were clear, visible changes to the crystal morphology and sample topography. Figure 4.24 is a 50 μm x 50 μm scan of the edge state between the homogenous, “bubbly” film and the beginning of a fibrous structure.

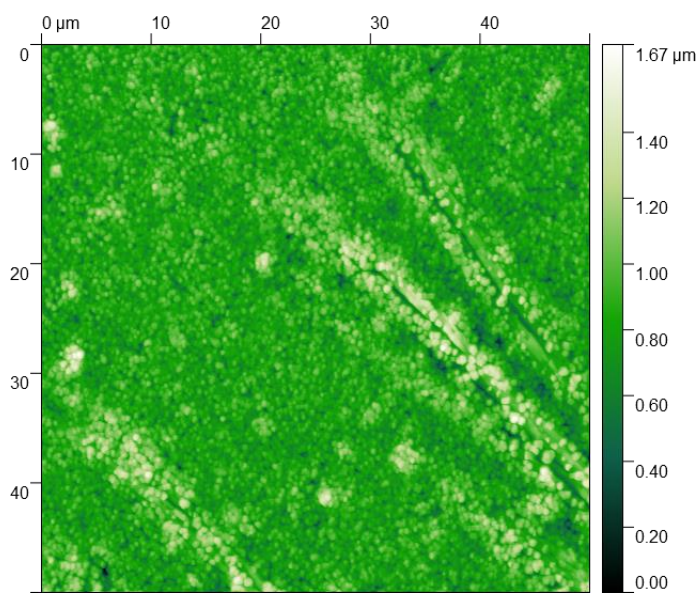


Figure 4.24 50 x 50 AFM Scan of Sample A (MAPbI_3) at 48 Hours of 80% Humidity

Figure 4.24 is a prime example of the very first signs of a fibrous structure emerging from the original film. The number of peaks continues to decrease. Figure 4.24 had 5,606 peaks, down from 7,602 at 12 hours of humidity exposure. Figure 4.25 is the 3D image of figure 4.24 and shows that the height of these fibers increases the total range of the sample.

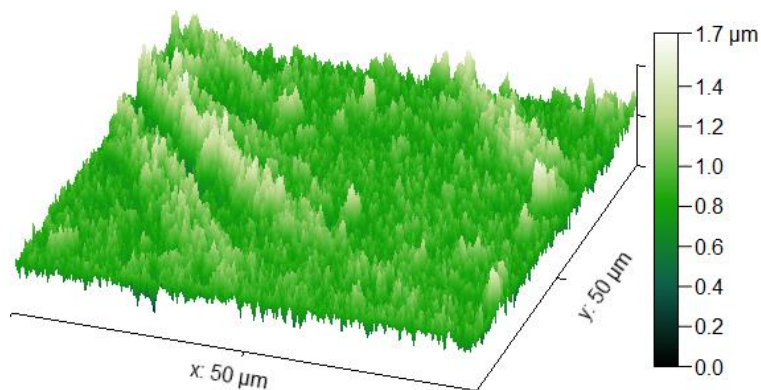


Figure 4.25 3D 50 x 50 AFM Image of Sample A (MAPbI_3) at 48 Hours of 80% Humidity

Note that the height range of 1.67 μm in figure 4.24 is the greatest range yet recorded for all the scans of sample A. The general trend of these ridges increasing in height and number of peaks decreasing continues and is amplified throughout the degradation process. Other areas of the sample had more prolific fibers that had emerged. Figure 4.26 a, b, and c is a 50 μm x 50 μm , 20 μm x 20 μm scan, and 5 μm x 5 μm scan of some more defined fibers.

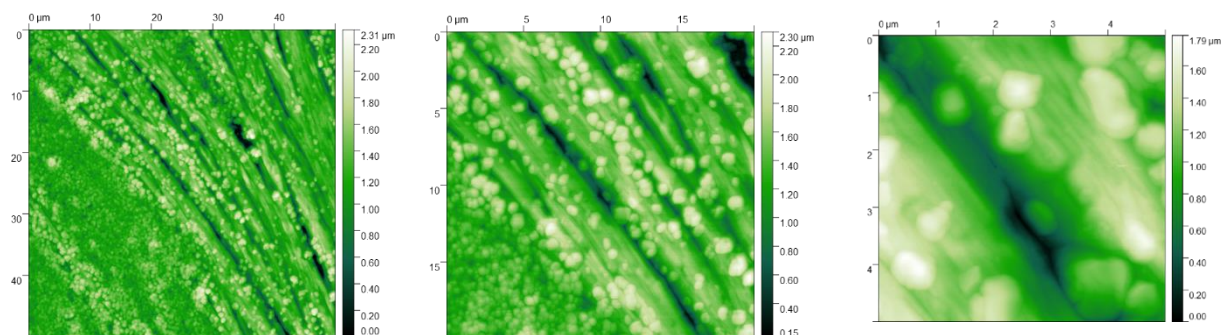


Figure 4.26 AFM Scans of Sample A (MAPbI_3) at 48 Hours of 80% Humidity a) 50 x 50, b) 20 x 20, c) 5 x 5

Figure 4.26 further illustrates fibers expanding through the original film. The 50 μm x 50 μm image shows that the fibers run nearly parallel while the original “bubbly” film is still present in the bottom left corner. Again, the height range is greater than any previous scan of sample A with the 20 μm x 20 μm being 2.30 μm . The trend of decreasing peaks has also continued this 50 μm x 50 μm scan contained 4,308, which is substantially less than the area that had just the first signs of fibers. The 20 μm x 20 μm scan contained 1,803 peaks, down from 2,313 at 36 hours of humidity exposure. Lastly, the 5 μm x 5 μm scan peaks can essentially be counted by hand and only contains 39 peaks.

48 hours of 80% humidity exposure was the first obvious sign of degradation for sample A. Figure 4.27 is a 50 μm x 50 μm scan that was taken at what appeared to be the center and the source of the fiber. Figure 4.41 in section 4.3.3 shows a bright field optical image of the entire formation and geometry of these fibers indicating degradation and should be used as a reference to better understand the meaning of the “center” or “source” of the fiber structure.

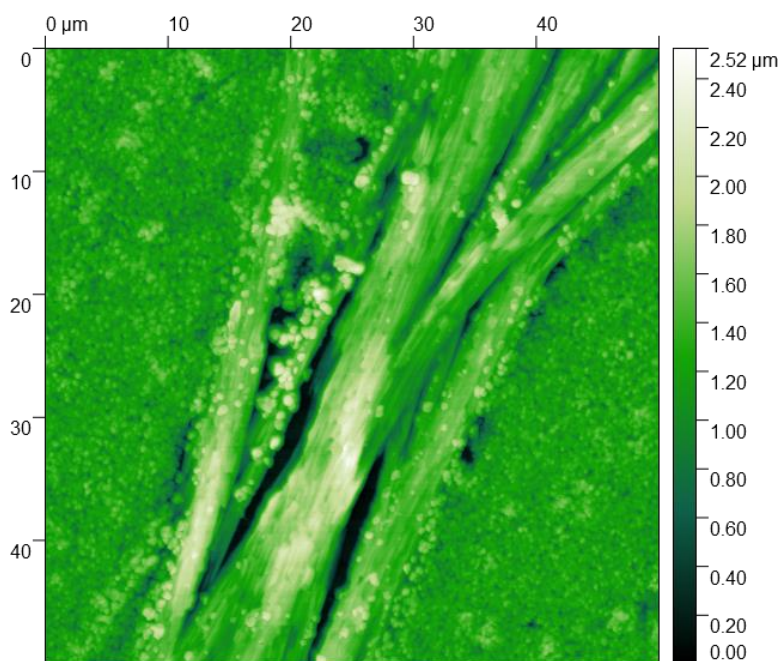


Figure 4.27 50 x 50 AFM Scan of Sample A (MAPbI_3) at 48 Hours of 80% Humidity

Figure 4.27 is where the convergence of many fibers come to a center and reaches its highest point of $2.52\ \mu\text{m}$. The $50\ \mu\text{m} \times 50\ \mu\text{m}$ scan above also showed a significant decrease in the number of peaks from the original value of 8,771 to 4,703. Figure 4.28 below is the 3D image of figure 4.27 and indicates the sharp contrast between the side of the fibers and the original homogenous film.

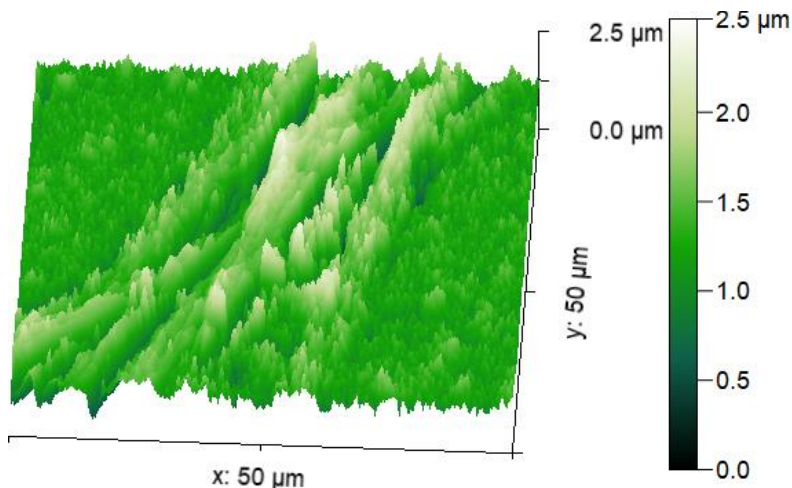


Figure 4.28 3D 50 x 50 AFM Scan of Sample A (MAPbI₃) at 48 Hours of 80% Humidity

Figure 4.29 below shows the zoomed in AFM scan of figure 4.26 with a profile path crossing perpendicularly to the newly formed fibrous features. The graphical representation of the profile path's height data and the measured distances are shown in figure 4.30.

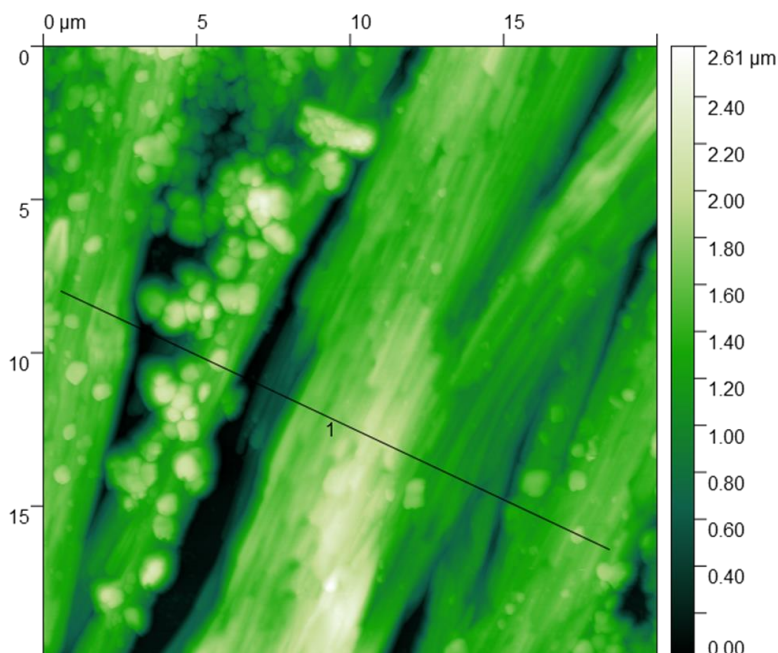


Figure 4.29 20 x 20 AFM Scan of Sample A (MAPbI_3) at 48 Hours of 80% Humidity

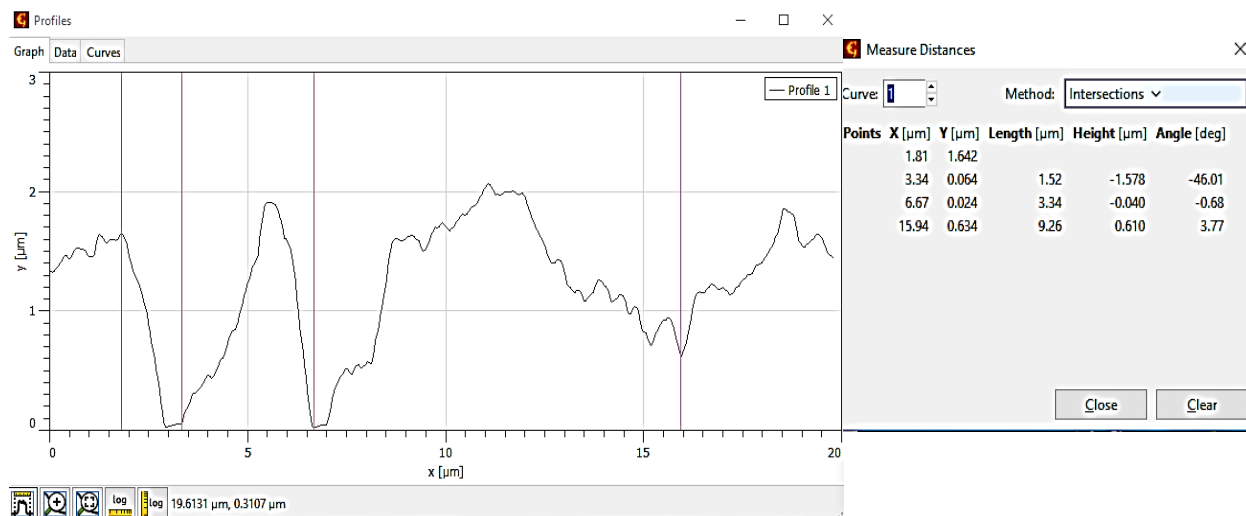


Figure 4.30 Profile Path of AFM Scan of Sample A (MAPbI_3) at 48 Hours of 80% Humidity

The profile path also concludes that as humidity degrades the MAPbI_3 into PbI_2 by evaporating MAI cations the surface of the 3D perovskite transforms from a bubbly surface to a fibrous surface where the many different smaller peaks begin to conform and congregate into larger more defined peaks and valleys between them. The profile path of figure 4.30 indicates

that there is a significantly less jagged profile than the pristine MAPbI₃ profile shown in figure 4.16. Furthermore, the height differences from the bottom of the valley to the conforming peak in figure 4.30 has jumped to values of up to 2 μm compared to the 450 nm in profile 4.16. Figure 4.31 below is the 3D imaging of the 2D AFM scan shown in figure 4.29 and a zoomed in version of figure 4.28.

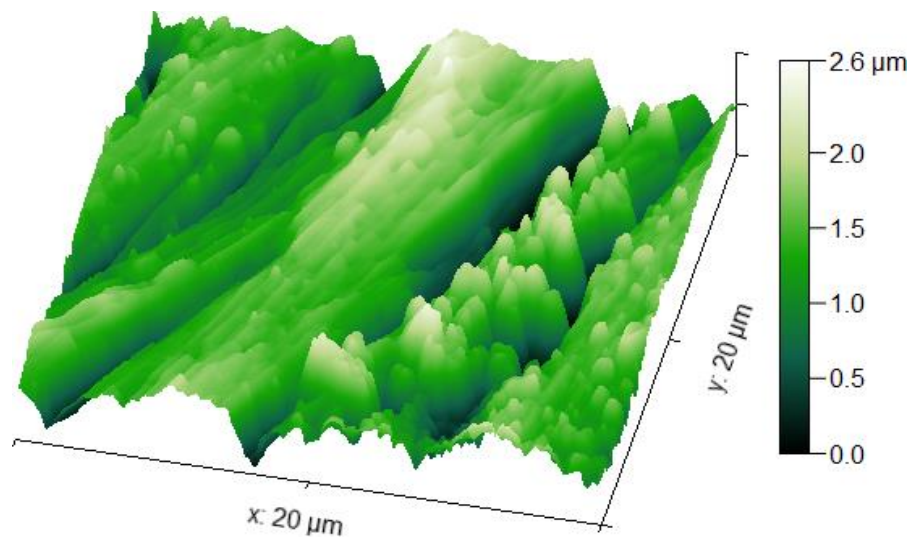


Figure 4.31 20 x 20 3D AFM Image of Sample A (MAPbI₃) at 48 Hours of 80% Humidity

It is also noteworthy that the height range of the entire 20 μm x 20 μm scan for sample A increased from 1.4 μm in figure 4.17 to 2.6 μm in figure 4.31. This concludes the in-depth AFM analysis at the first signs of fibers on the surface, which correlates with the first signs of degradation. As humidity exposure continued the first areas of fibers became taller and more defined and the outer reaches of the fiber began spreading to all areas of the homogenous, “bubbly” film.

Figure 4.32 a and b below are a 50 μm x 50 μm scan and a 20 μm x 20 μm scan at 144 hours of 80% humidity exposure.

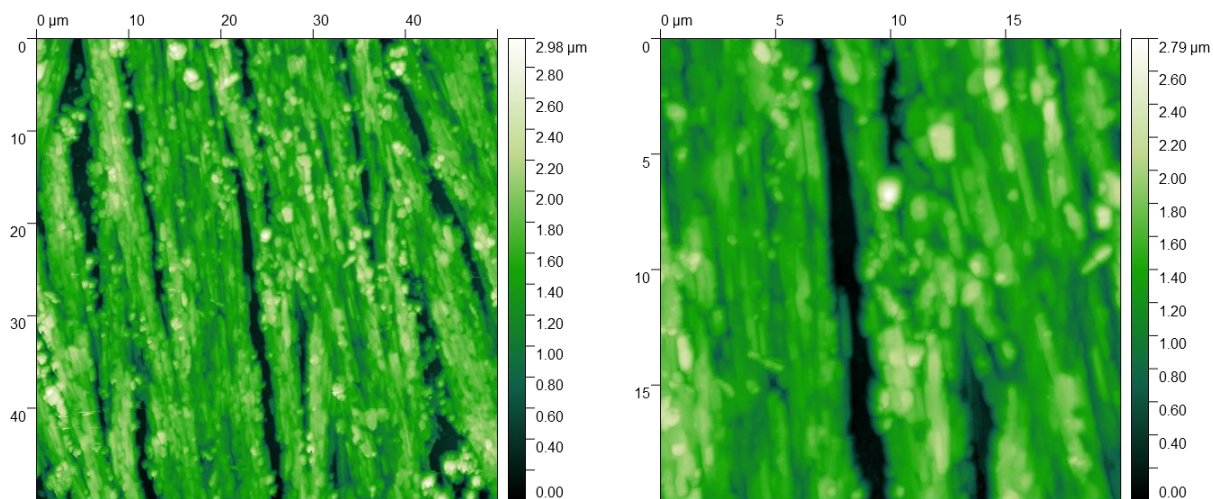


Figure 4.32 AFM Scans of Sample A (MAPbI_3) at 144 Hours of 80% Humidity a) 50 x 50, b) 20 x 20

Figure 4.32 displays how valleys between fibers are widening and the height range has increased to $2.98 \mu\text{m}$. Additionally, the fibers have now fully encompassed the originating “bubbly” film. The trend of the number of peaks decreasing also continued. The $50 \mu\text{m} \times 50 \mu\text{m}$ scan had 2,660 peaks, down from 4,958 at 48 hours, and the $20 \mu\text{m} \times 20 \mu\text{m}$ scan had 1,127 peaks, down from 1,723 at 48 hours.

Further accentuating the degradation and drastic change in the surface topography is shown below in figure 4.33, which is the AFM scan of sample A taken after 216 hours of 80% humidity exposure with the profile line perpendicular to the fibrous features and graphically represented with measurements in figure 4.34.

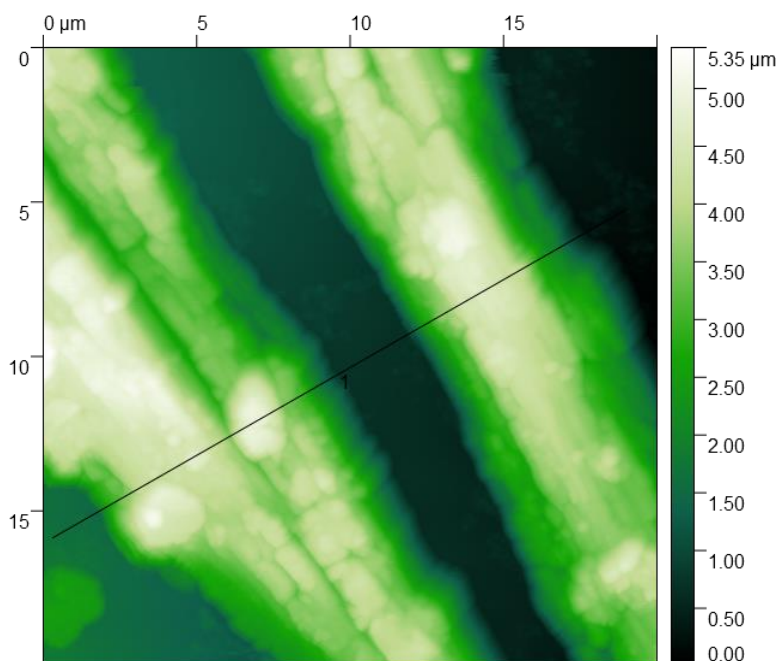


Figure 4.33 AFM Scan of Sample A (MAPbI_3) at 216 Hours of 80% Humidity

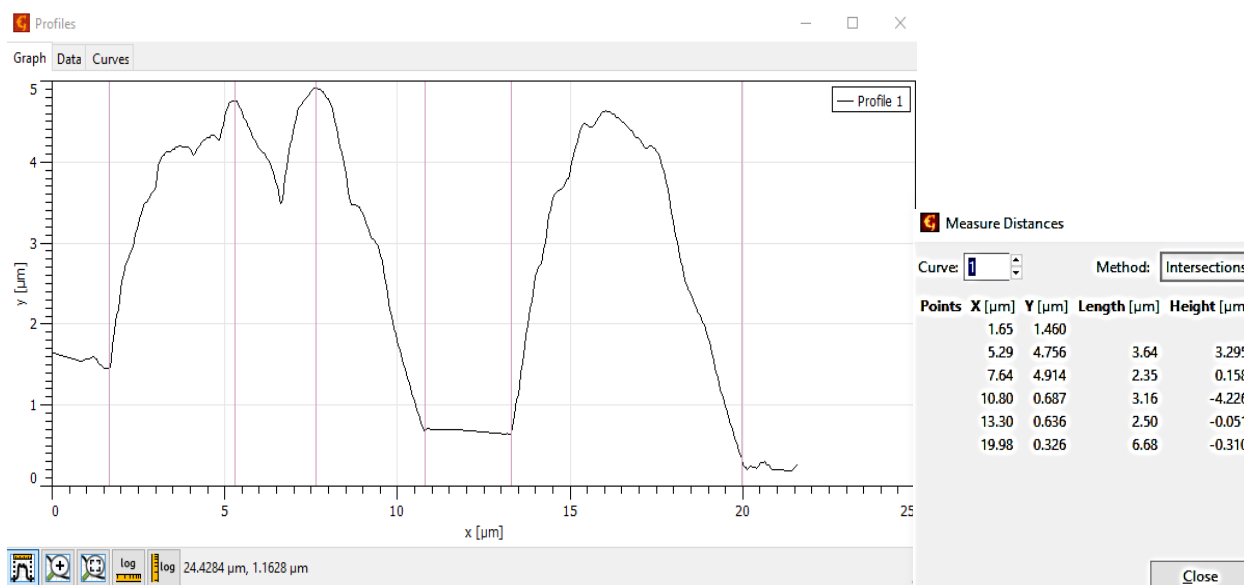


Figure 4.34 Profile Path of AFM Scan of Sample A (MAPbI_3) at 216 Hours of 80% Humidity

The profile path now very clearly indicates a reduction from the numerous peaks of a 20 μm profile to only three major peaks as shown in figure 4.34. The heights of these peaks have increased substantially to values greater than 4 μm . The rightmost fiber-like feature in this scan

had a width greater than $6.5\ \mu\text{m}$ with $2.5\ \mu\text{m}$ between features, where the surface between the features was the exposed glass below. Figure 4.35 below is the 3D image of the AFM scan in figure 4.33 and exemplifies the mountains and valleys of the degraded MAPbI₃ topography that is not representative of the original surface shown in figures 4.15 and 4.17.

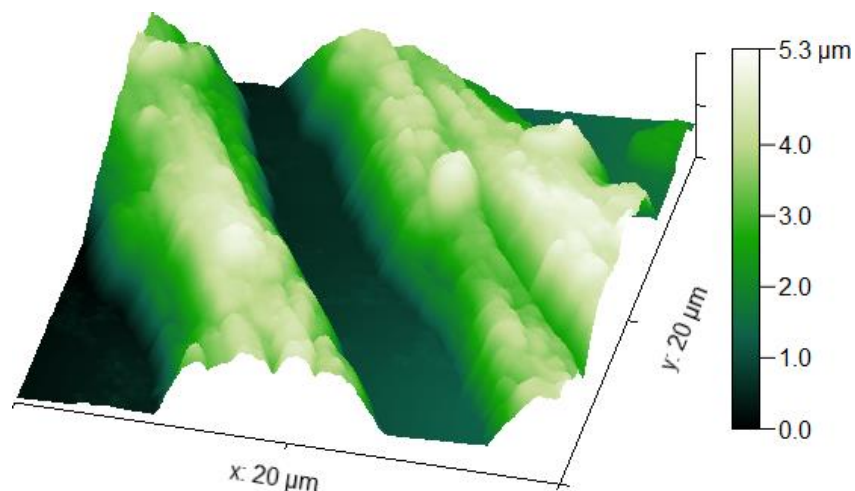


Figure 4.35 3D AFM Image of Sample A (MAPbI₃) at 216 Hours of 80% Humidity

It is noteworthy that at this point the height range of the $20\ \mu\text{m} \times 20\ \mu\text{m}$ scan was $5.3\ \mu\text{m}$ and had further increased from 48 hours of 80% humidity exposure and substantially from sample A's initial conception. Moreover, the number of peaks decreased substantially, the $20\ \mu\text{m} \times 20\ \mu\text{m}$ scan had only 566 calculated peaks. Figure 4.36 below graphically displays the decrease in the number of peaks in relation to hours exposed to 80% humidity.

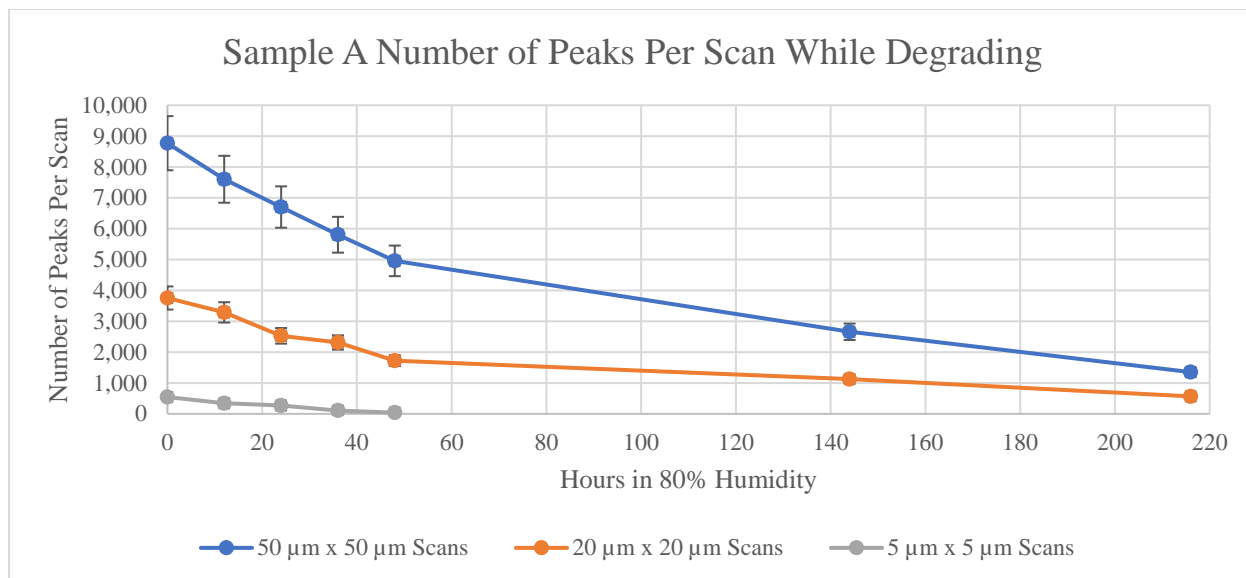


Figure 4.36 Decreasing number of peaks during degradation of sample A, error bars of ± 1 standard deviation

Figure 4.36 is the graphical image that had been explained throughout the degradation process that the number of peaks for sample A were decreasing as time in 80% humidity increased. AFM scans of sample C for trial 5, however, was unable to characterize degradation.

While AFM scans clearly showed the degradation of the surface of sample A the PMMA coating that encased sample C showed no signs of change throughout the degradation process. While, the optical images and PL data shown later clearly indicated that sample C was degrading there was virtually no change in the surface topography exclaiming that the PMMA was unaffected by the humidity as expected for a plastic. Figure 4.37 below shows an AFM scan of sample C after 216 hours of 80% humidity exposure while a profile path running across the sample. Figure 4.38 is the graphical representation of the profile path's height data along the path indicated in figure 4.37.

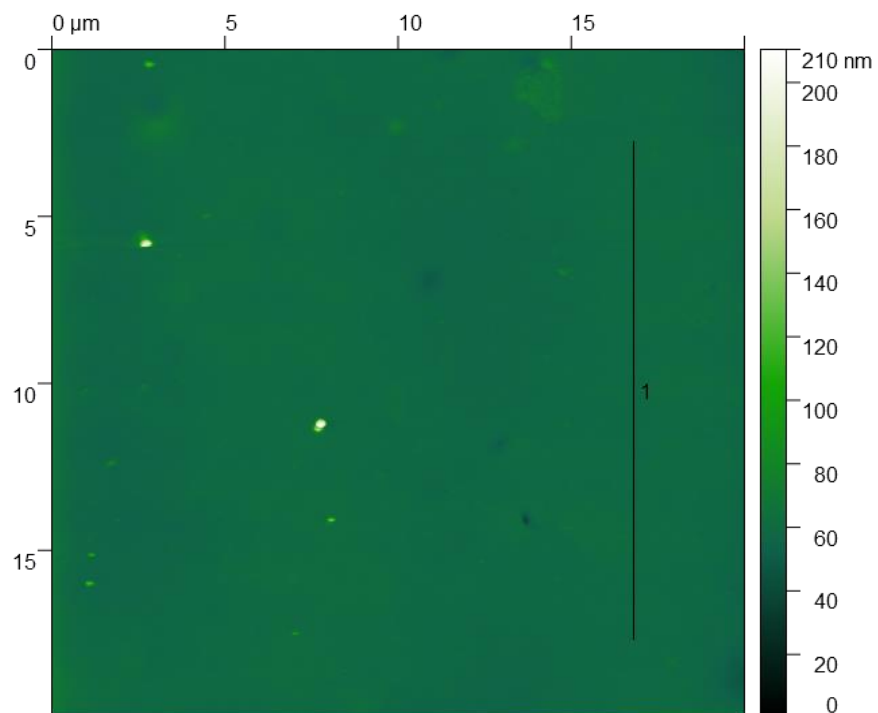


Figure 4.37 AFM Scan of Sample C (MAPbI₃/Graphene/PMMA) at 216 Hours of 80% Humidity

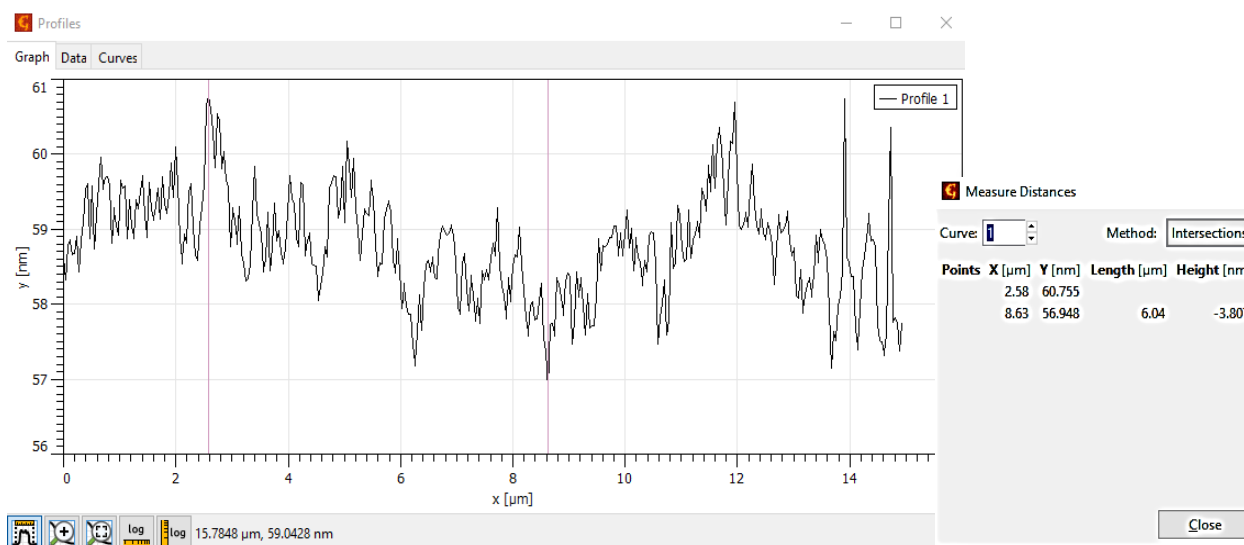


Figure 4.38 Profile Path of AFM Scan of Sample C (MAPbI₃/Graphene/PMMA) at 216 Hours of 80% Humidity

Again, the profile at first sight may seem very jagged with many peaks; however, all of these changes are occurring within a range of a few nanometers and therefore the surface is exceptionally smooth. The difference in height from the highest point in the profile path and the

lowest is less than 4 nm and therefore the surface of sample C shows no resemblance of sample A again indicating that the PMMA was not fully dissolved in the CB bath.

To create a larger picture of the AFM data surface roughness and height range was recorded for each scan of both samples A and C during the degradation process. For each time scans were taken the surface roughness data and height ranges were averaged for both samples A and C respectively. For each time slot four $20\ \mu\text{m} \times 20\ \mu\text{m}$ scans were taken and averaged for each sample. Figure 4.39 below shows the graphical representation of the surface roughness average comparison between samples A and C over time and figure 4.40 shows the average height range of the scans over time. The error bars are ± 1 standard deviation for both figures 4.39 and 4.40.

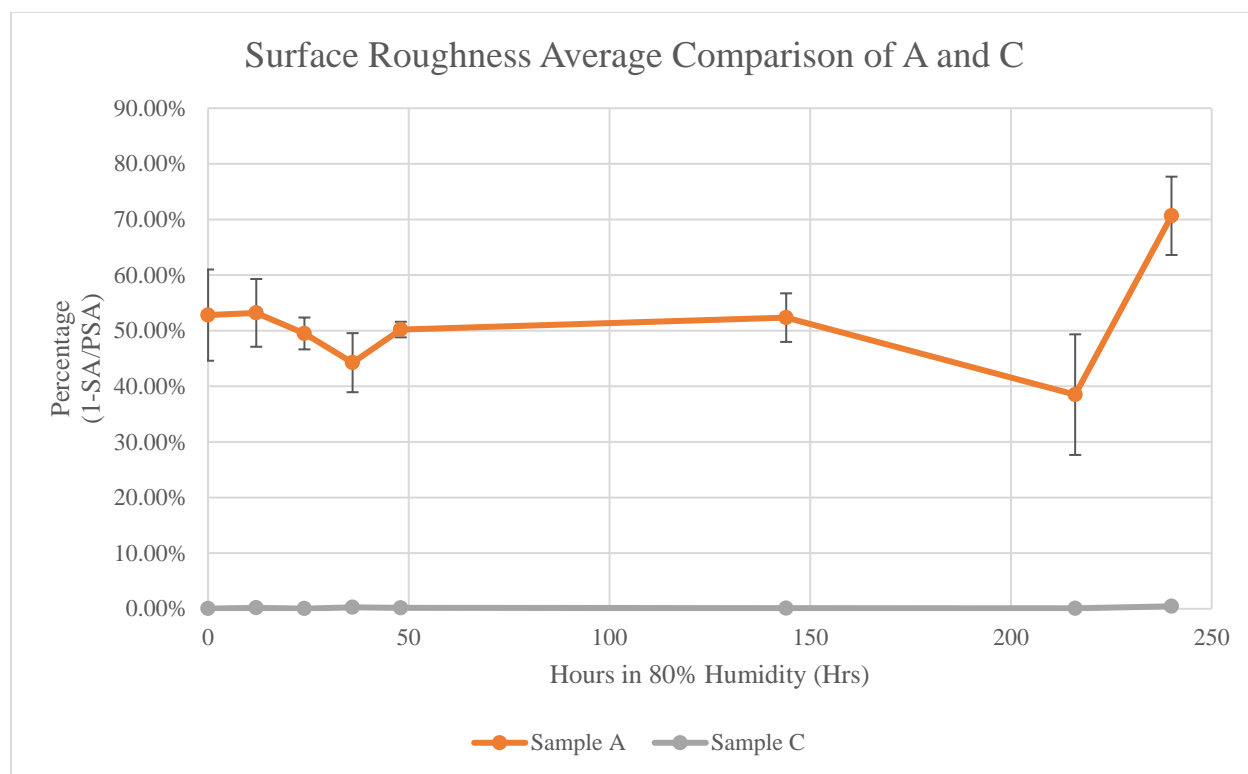


Figure 4.39 Trial 5 surface roughness average of Sample A and C with error bars of ± 1 standard deviation

The surface roughness comparison between samples A and C for trial 5 follows the trend seen from the AFM images that the PMMA left on sample C has made the surface extraordinarily smooth. The expectation when all the PMMA is dissolved is to see comparable surface roughness' between samples A and C. Another interesting aspect is that even during large changes in surface topography of sample A the overall surface roughness stays relatively the same.

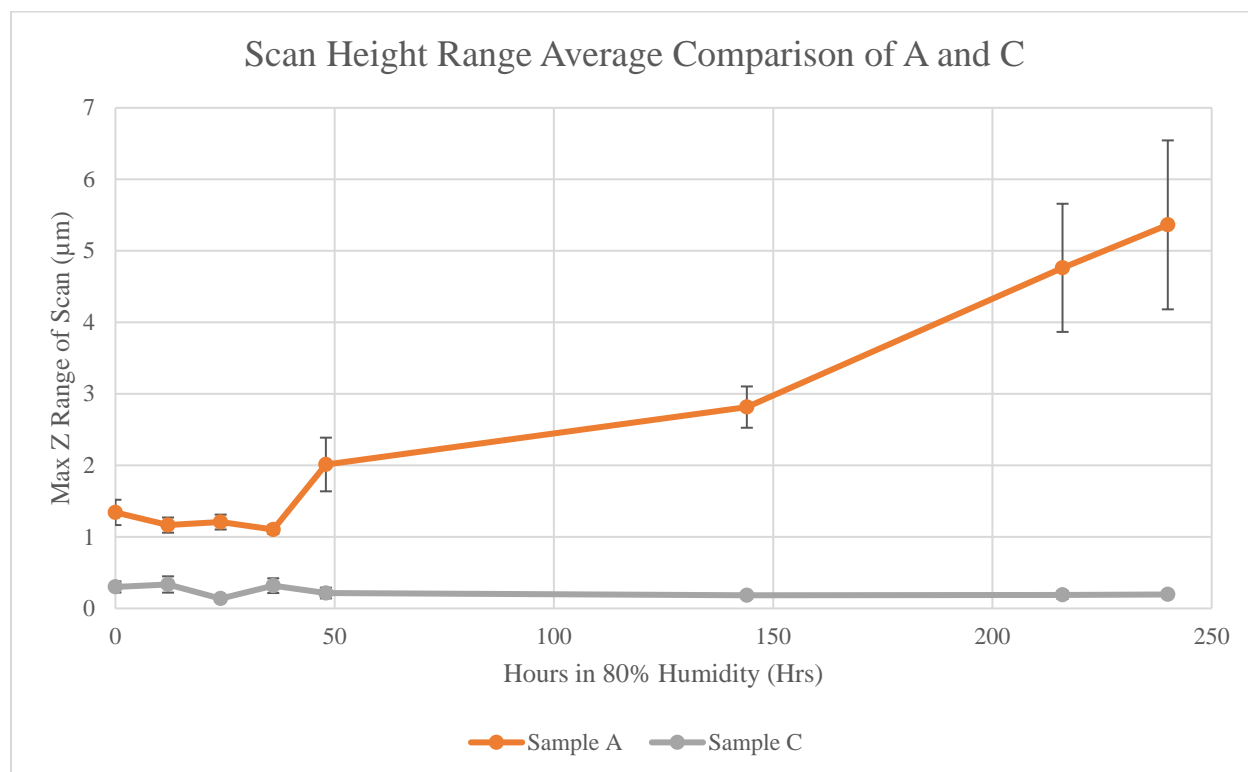


Figure 4.40 Trial 5 Scan height range averages of sample A and C with error bars of ± 1 standard deviation

The average scan height range comparison between samples A and C also follows the trend seen in the AFM images. As sample A degrades the typical height range of the scan increases. Initially sample A had scan height ranges around 1.2 µm. At 48 hours of humidity exposure fibrous features began to emerge and there is a large jump in the scan height range. There seems to be a threshold of humidity exposure that leads to a quick change in the surface

from a “bubbly” more homogenous film to fibrous features that root and branch out from a center point amongst the homogenous film. As time of 80% humidity exposure further increased the scan height range also increased. By 240 hours of 80% humidity exposure the average range of the height of a 20 μm x 20 μm scan was greater than 5 μm . On the other hand, the surface of PMMA on sample C had a very low height range that seemed to be completely unchanged during the degradation process. Initially the scan height range averages of sample C began around 300 nm and stayed consistent up to 240 hours of 80% humidity exposure. Table 4.6 below indicates the standard deviations for the N = 4 scan that were used as the error bars shown in figures 4.39 and 4.40.

Table 4.6 Trial 5 Standard Deviations for Surface Roughness and Scan Height Range Data for Samples A and C

N = 4	Hrs	SD SA Diff A	SD Rmax A	SD SA Diff C	SD Rmax C
	0	8.20%	0.177	0.02%	0.078
	12	6.09%	0.106	0.07%	0.114
	24	2.87%	0.104	0.01%	0.013
	36	5.31%	0.060	0.08%	0.103
	48	1.40%	0.375	0.03%	0.075
	144	4.37%	0.289	0.01%	0.019
	216	10.84%	0.896	0.02%	0.055
	240	7.04%	1.181	0.04%	0.032

The standard deviation table exemplifies how little of change there was from scan to scan for sample C for both surface roughness and scan height ranges compared to sample A. The AFM data compiled in trial 5 was useful to understand the characteristics of how sample A degrades and how the surface topography changes. Unfortunately, sample C for trial 5 failed to highlight any conclusions directly toward the hypothesis but helps further understand the importance of the transfer procedure and the need to fully dissolve the PMMA transfer material when laminated onto MAPbI₃. Lessons learned from trial 5 were directly implemented to the

more successful trial 6 and AFM data used from this trial were directly compared to results in trial 6. The optical images and photoluminescence data gathered in trial 5 further conclude characteristics of degradation for sample A and that PMMA was not fully dissolved for sample C.

4.3.3 Trial 5 Optical Images and Photoluminescence Data

The bright field optical images are a way to qualitatively visualize the changes to the crystal morphology as degradation occurs over time. As was shown in section 4.2 and table 4.4 sample A and C will be compared side by side with time indications of 80% humidity exposure. Both samples A and C had a 3 x 3 array of indicator points for reference to measure similar areas as degradation continued. The 3 x 3 array of points are indicated in the same fashion for the optical images and are precisely where photoluminescence intensity data was taken. Again, while sample B was also analyzed using the same techniques the optical images have been omitted, because sample B has been dismissed as an ineffective method for encapsulating MAPbI₃. Table 4.7 below shows the full array of images of sample A and C for degradation intervals from 0 hours to 240 hours of 80% humidity exposure. As before all optical images shown in table 4.7 have scale bars of 20 μm.

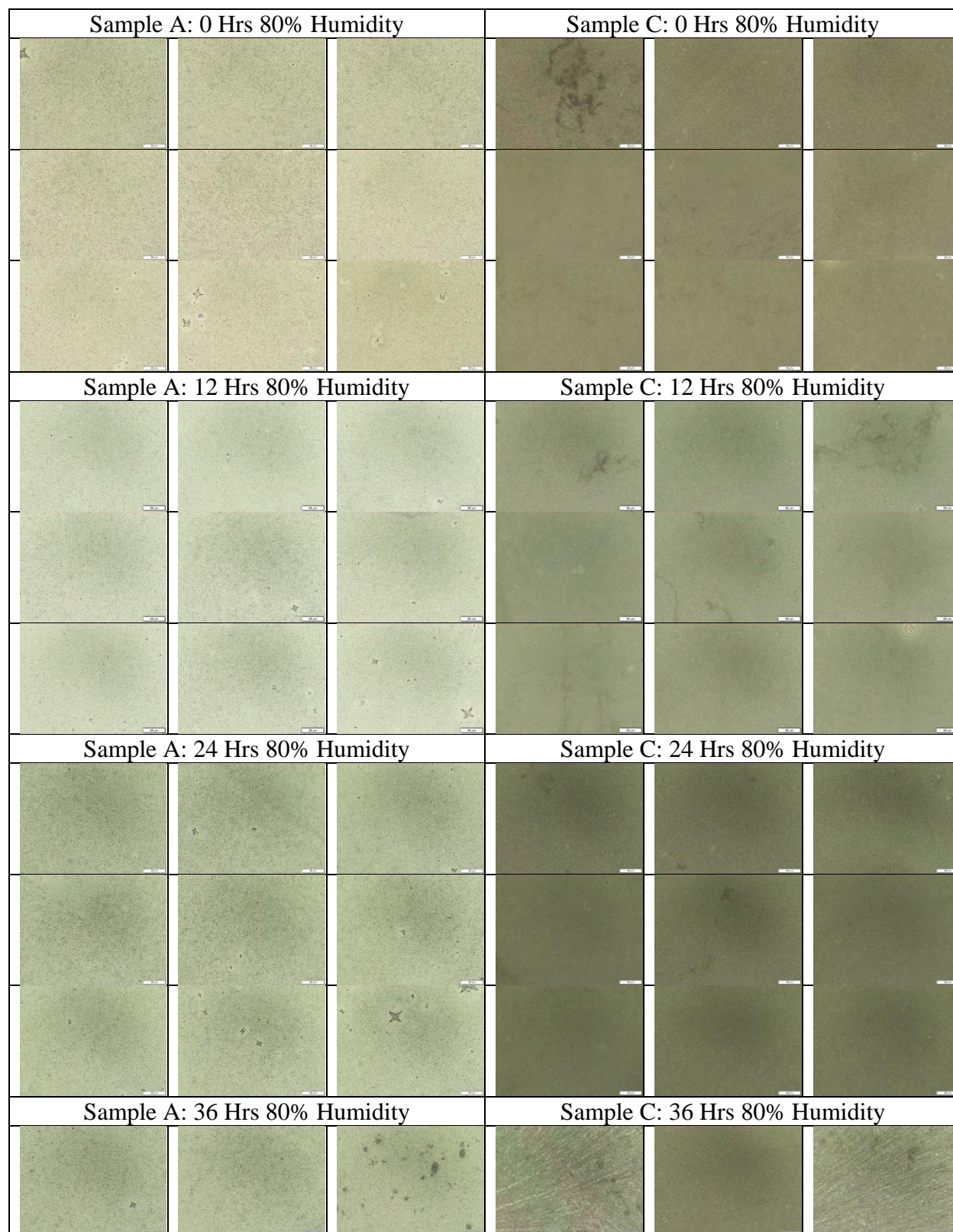
Table 4.7 Trial 5 bright field images scale bars are 20 μm 

Table 4.7 Continued

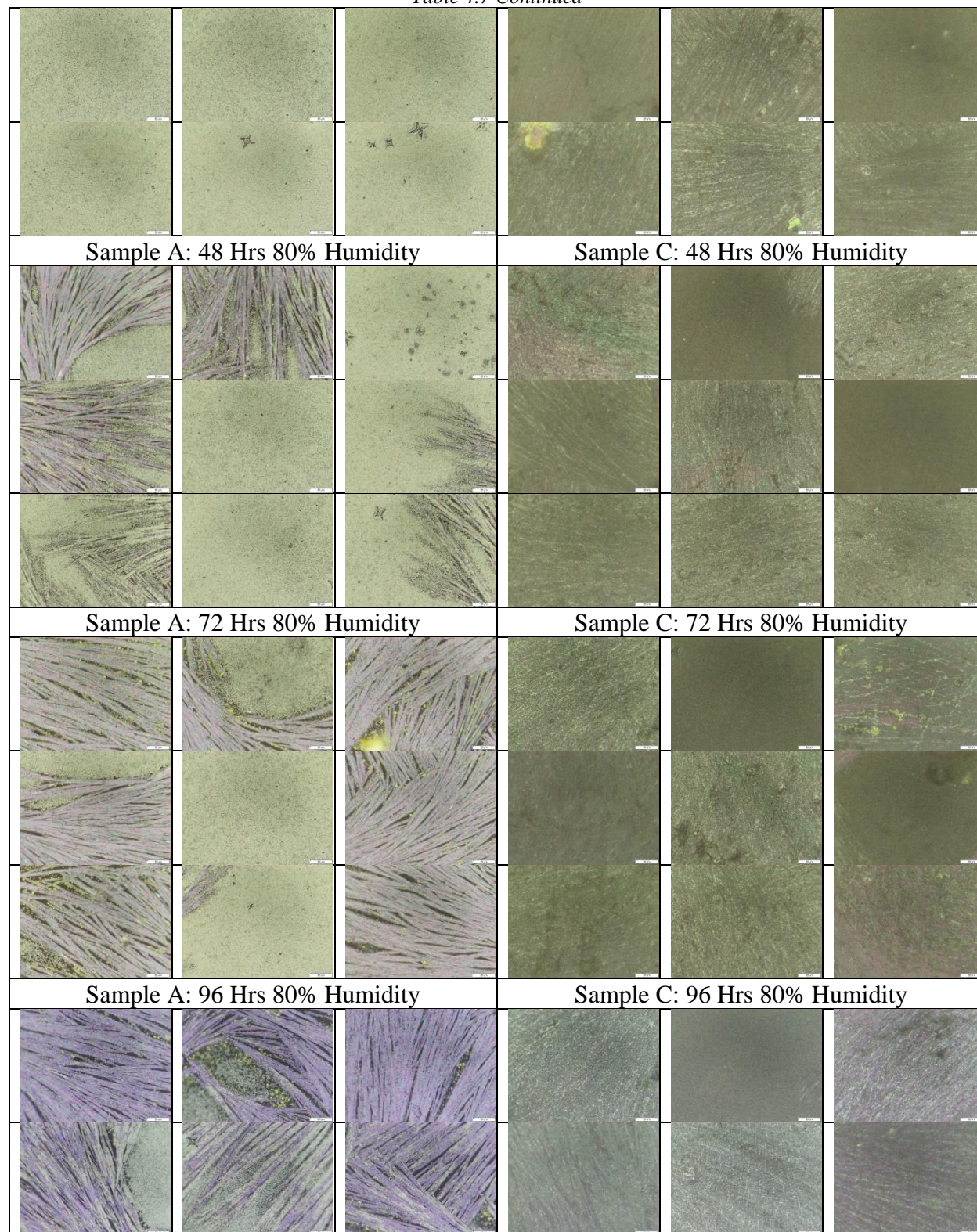


Table 4.7 Continued

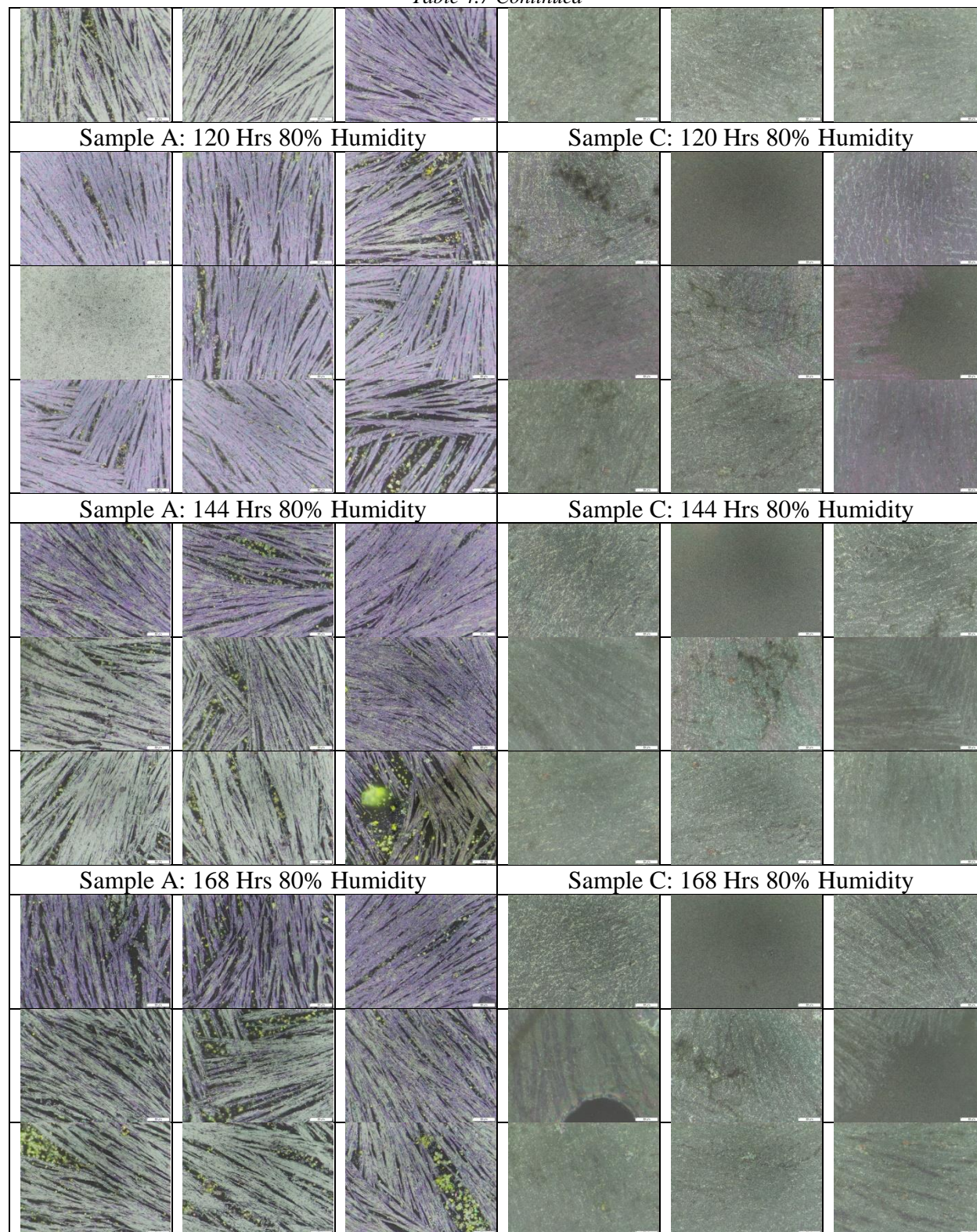
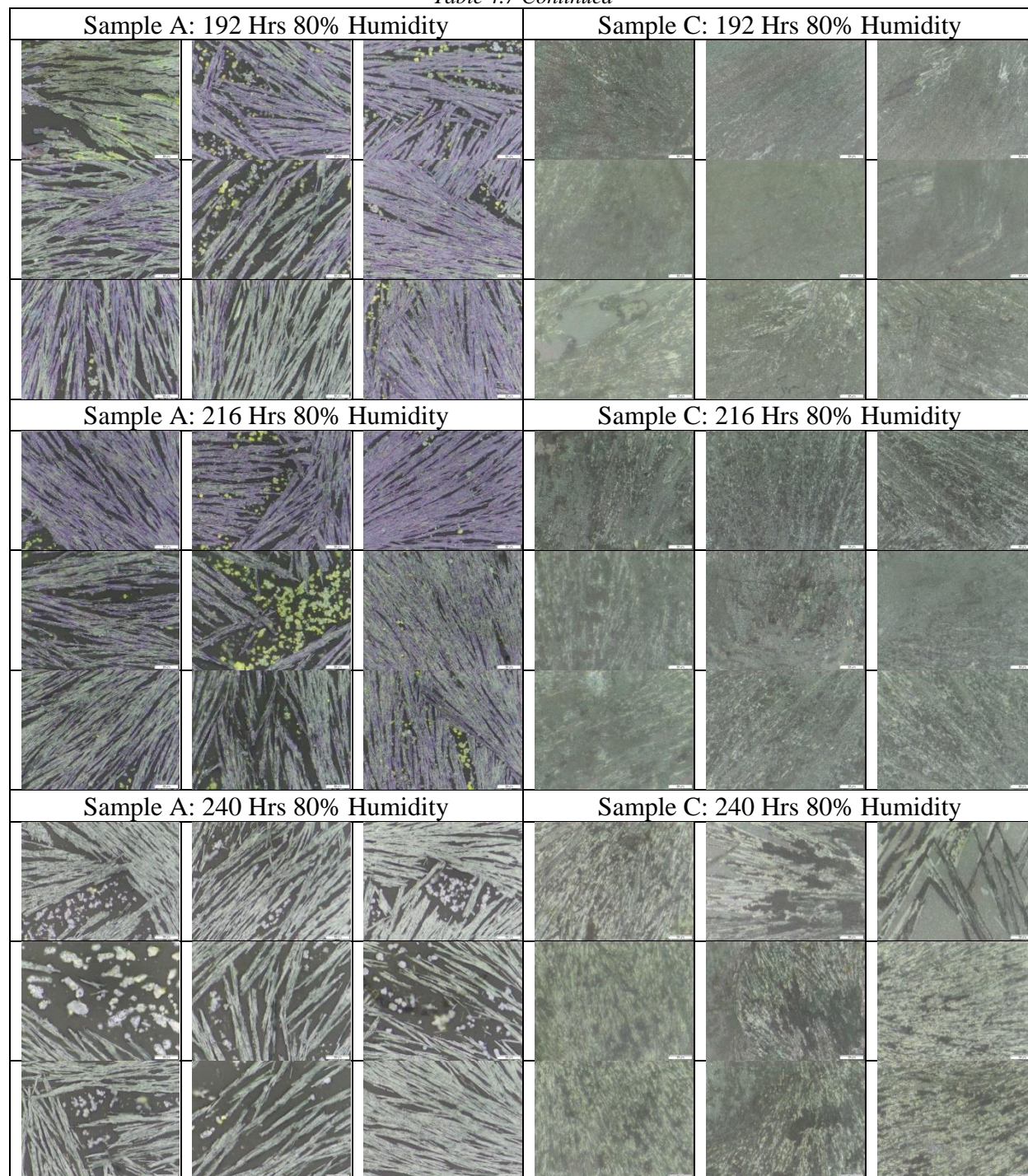


Table 4.7 Continued



Many conclusions can be drawn from the optical images shown in table 4.7. First, from the initial images it is clear that sample A shows up as brighter than sample C, because the PMMA is absorbing some of the light that should be captured by the charge-coupled device

(CCD) detector in the optical microscope. Another initial observation that can be seen is that the films are both initially very homogenous with minimal pinholes and contaminants. At 36 hours of 80% humidity exposure sample C shows the first signs of the crystal morphing from a bubbly homogenous film into fibers. Not until 48 hours of 80% humidity exposure does sample A show signs of the change to fibrous characteristics as indicated in the AFM analysis. It is likely that cracks, air pockets, or imperfect lamination lead to humidity entering between graphene/PMMA and the MAPbI_3 surface leading to sample C degrading before sample A. To get a clear idea of how degradation forms and spreads figure 4.41 below was taken at the first sign of fibrous morphing of sample A at 48 hours of humidity exposure with a scale bar of 100 μm .



Figure 4.41 Trial 5 first sign of degradation of sample A at 48 hours of 80% humidity exposure

Figure 4.41 indicates that the fibrous growth, which is correlated with the degradation of MAPbI_3 , begins from a center and expands outward like roots or branches. The root-like structure begins vertically extending from the center then branches out radially. The change in the crystal structure seems extreme; however, even with the major change in the crystal structure photoluminescence is still captured.

Some other conclusions can be drawn from table 4.7. By 240 hours of 80% humidity exposure sample A is beginning to have larger separations between fibers and more of the glass underneath is being exposed. Sample C on the other hand does not show major indications that fibers are separating immensely enough to expose the glass beneath. While humidity may have been trapped underneath the surface of the graphene and PMMA it seems that evaporating MAI also is trapped and rebinds with PbI_2 . While the optical images on their own are useful when combined with PL intensity data many more interpretations can be made. Figure 4.42 below is the averages of all the peak intensities across the nine locations imaged as seen in table 4.7 including sample B and is known as an Xbar chart. The average peak PL intensities indicate how well that measured location can convert photons into electrons where lower PL peaks correlate with a lower photoconversion efficiency (PCE).

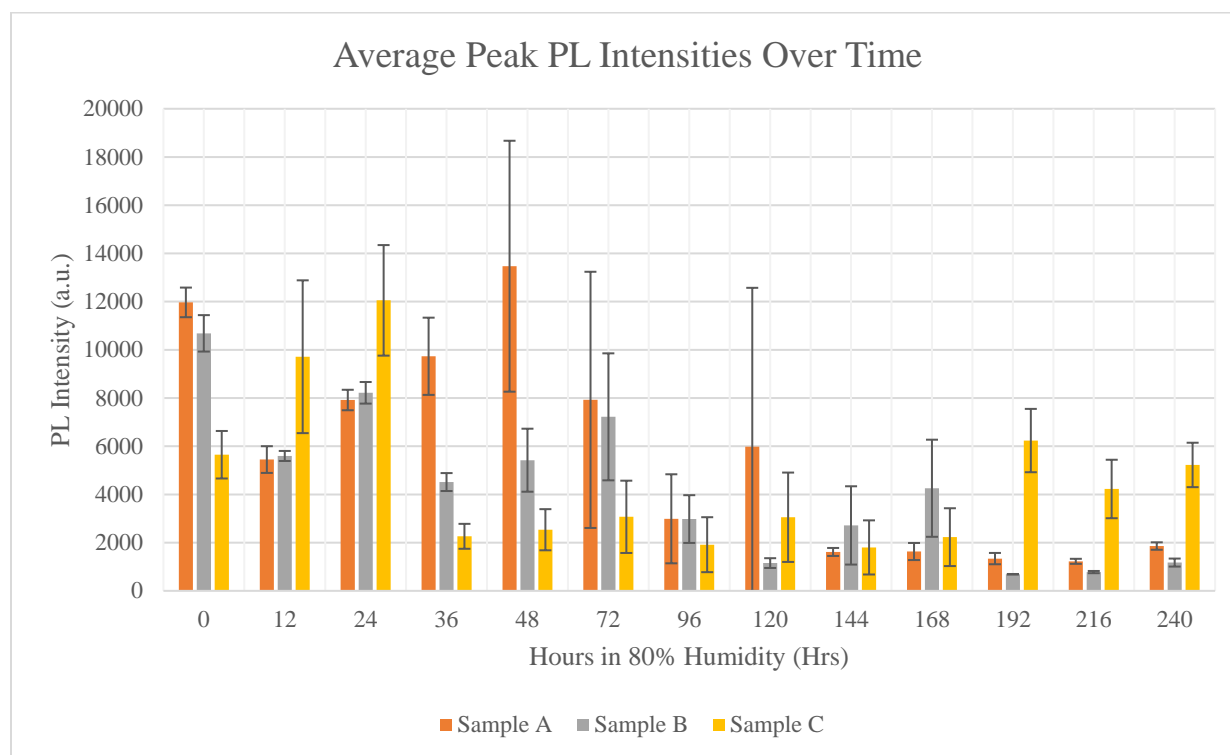


Figure 4.42 Trial 5 Xbar Chart for average peak PL intensity across 9 measurement locations for samples A, B and C over time exposed to 80% humidity with error bars of ± 1 standard deviation

The Xbar chart shown in figure 4.42 is the most succinct use of data with the greatest insight for the hypothesis yet. Peak PL intensity measurement averages for times 192, 216, and 240 hours are results that indicate that sample C does degrade slower than sample A proving the hypothesis correct; however, because PMMA is still present on the sample the reduction of degradation cannot be directly attributed to the graphene for trial 5 and therefore is inconclusive. There were some inconsistencies with the PL measurements taken in trial 5. Initially, when taking PL data, the UV bulb would be left on the sample area for approximately 3 minutes until the PL peak would stop increasing and reach an equilibrium; however, applying the UV bulb on the sample for that long could cause photobleaching. By the end of trial 5 and all of trial 6 PL data was taken with only 10 seconds of UV exposure to avoid photobleaching. Figure 4.42 is an Xbar chart however for proper analysis a Rbar chart should also be considered, which is the range of the values across all nine measurements that computed the average shown in the Xbar chart. The Rbar chart for the trial 5 PL data is shown below in figure 4.43. It is noteworthy that the ranges are correlated with the error bars 4.42. The larger the range the larger the error. No error bars are included in the Rbar chart because standard deviation cannot be calculated from a range of values.

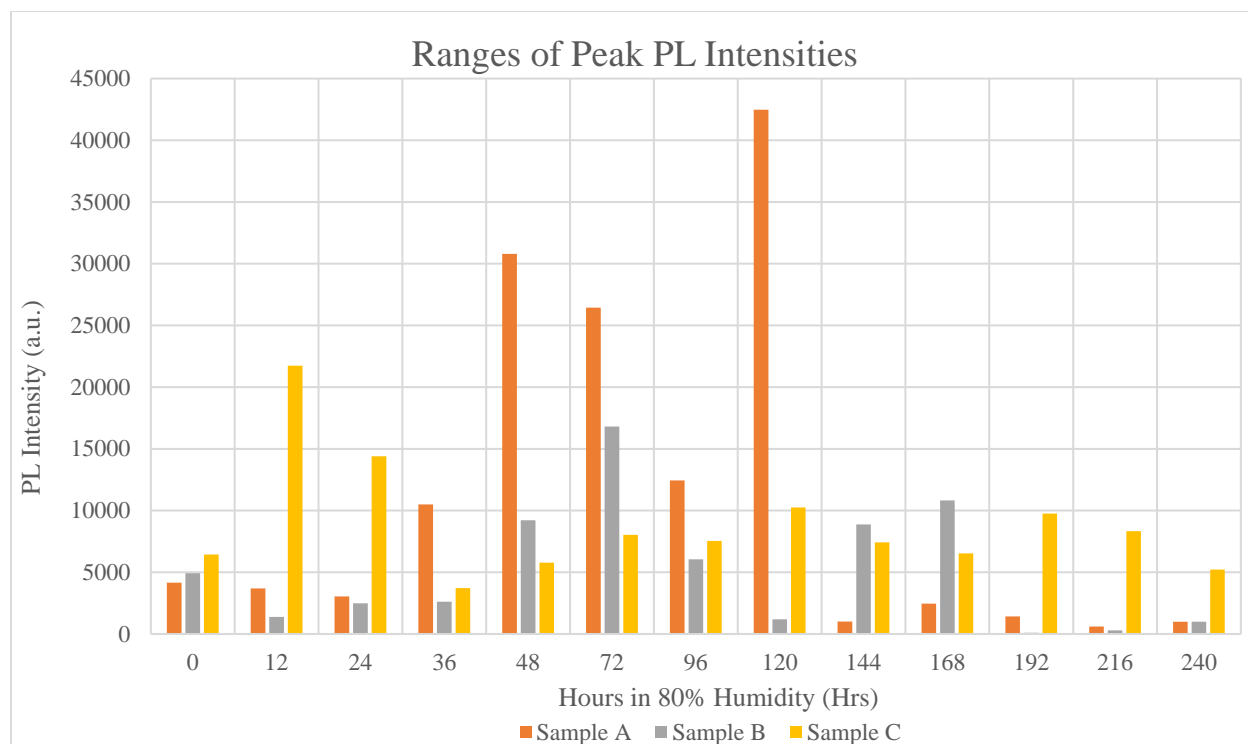
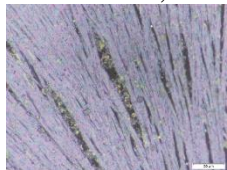
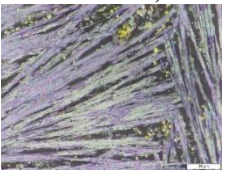
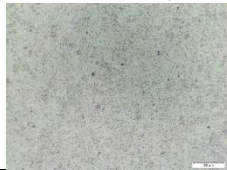
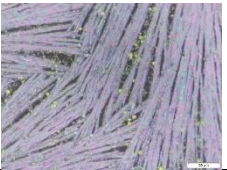
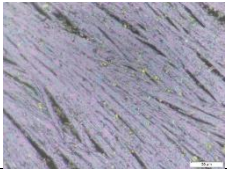
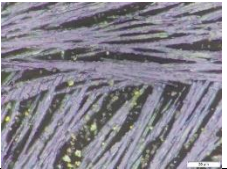


Figure 4.43 Trial 5 Rbar Chart for peak PL intensity ranges among 9 measurement locations for samples A, B and C over time exposed to 80% humidity

The Xbar and Rbar chart when combined gives great amounts of information and detail about the characteristics of the PL peaks. First, it is important to note that the initial ranges of all three samples are relatively small and that the ranges are smaller than the averages. At 48 hours when the first sign of degradation occurs for sample A the range becomes much larger. A trend occurs at the threshold between a homogenous “bubbly” film and the emergence of fibers there is a spike in the average PL peak and the range. At 48 hours of humidity exposure sample A saw its highest PL peak average above 12,000 and a range greater than 30,000. The peak average then began to decrease, but the range was still above 25,000 for 72 hours. At 96 hours of humidity exposure it appeared that sample A’s PL intensity was beginning to taper off, but at 120 hours of humidity exposure the most exceptional case of PL intensity occurred. The 9 optical images for sample A at 120 hours of 80% humidity exposure shows that 8 of the 9 measurement locations were completely composed of fibers. Section A-4 was the one optical image that had

the original appearance of a “bubbly” homogenous film and had an exceptionally high PL intensity. Table 4.8 indicates the 9 optical images and their peak PL intensities.

Table 4.8 Trial 5 bright field images and PL Peaks sample A 120 Hrs of 80% Humidity

Sample A: 120 Hrs 80% Humidity		
PL Peak: 1,497 	PL Peak: 707 	PL Peak: 1,881 
PL Peak: 43,173 	PL Peak: 707 	PL Peak: 713 
PL Peak: 703 	PL Peak: 698 	PL Peak: 3746 

From table 4.8 it appears that A1-4 may be an outlier, but there is an important phenomenon occurring when MAPbI_3 is on the threshold of degrading into a fibrous structure a large spike in PL intensity occurs. The average PL peak intensity at 120 hours of humidity is 5,981; however, if the outlier A1-4 is excluded than the average drops to 1,331, which is much more comparable to the averages taken for sample A for hours 144 to 240 shown in figure 4.42. The main points that should be taken from the average PL peak data and range of PL peaks is that sample C ended with a consistently higher PL intensity than sample A and that the ranges were occurring from some sections of the sample being more degraded than other sections. Sample B did not have higher PL intensities than samples A and C other than at 168 hours. In general, the PL data of sample C in trial 5 is inconclusive because of the presence of PMMA.

The degradation of sample A, however, was controlled and is applicable to be compared to trial 6.

4.4 Trial 6 Final Comparison of Sample A and C

Trial 6 was the most successful trial of the entire study. Using all the lessons learned from the previous 5 trials and implementing new strategies lead to a successful transfer of graphene to the MAPbI₃ surface, the full dissolution of PMMA, AFM scan and measurements depicting graphene fully conformed to the MAPbI₃ surface, and sample C degrading significantly slower than sample A. The AFM data presented in trial 6 indicates that degradation of sample C was less than that of A through measurements of scan height ranges and number of peaks per scan. AFM data on surface roughness comparing sample A and C suggests that graphene is conforming to the surface of MAPbI₃. PL data presented in trial 6 indicates that degradation of sample C was less than that of A through PL peak intensities being greater than A through the entire trial.

For trial 6 sample A and sample C were left in the humidity cabinet at 80% humidity from 0 hours to over 500 hours of humidity exposure to see long term PL measurements of sample C. Samples A and C were left in the humidity cabinet in a petri dish with the petri dish left on. Again, the petri dish with the lid on is not air tight; however, a small experiment was run to test if the humidity inside the petri dish was the same as the humidity in the entire humidity cabinet. A humidity sensor was placed inside the petri dish overnight in the humidity cabinet at 80% humidity. The next morning the humidity sensor outside of the petri dish and inside the petri dish both read 80% humidity. Therefore, as expected, the relative humidity outside the petri dish was the same as the humidity inside the petri dish. To begin the analysis of trial 6 first the AFM data will be presented.

4.4.1 Atomic Force Microscopy Data

Because trial 5 went through an in-depth AFM analysis of sample A, and its degradation characteristics, trial 6 focused on the comparison of sample A and sample C during degradation. Data that was presented in trial 5 is compared with trial 6 in section 4.5 for comprehensive comparison. For trial 6 only $20\ \mu\text{m} \times 20\ \mu\text{m}$ scans were taken. For each time interval evaluated 4 scans were taken for each sample to evaluate surface roughness, height range of the scan, and number of peaks per scan. Figure 4.44 a and b below shows $20\ \mu\text{m} \times 20\ \mu\text{m}$ scans of both sample A and sample C at 0 hours of humidity exposure.

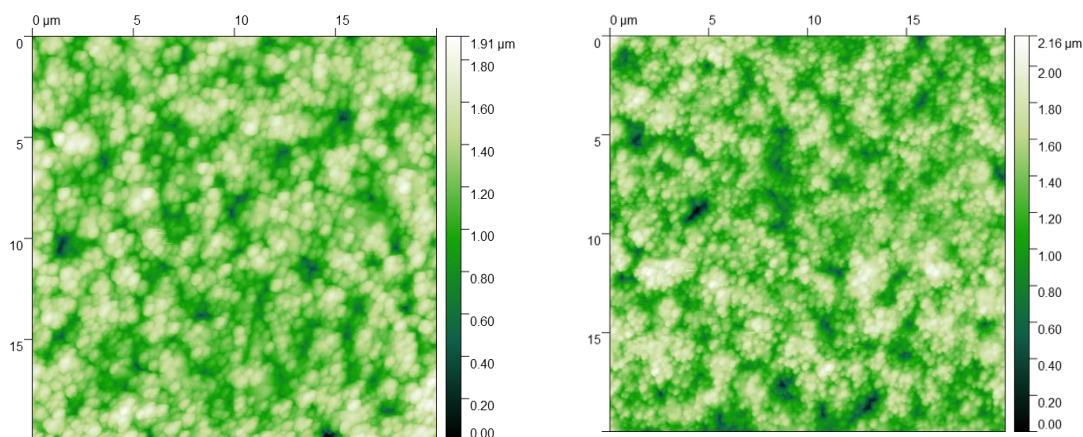


Figure 4.44 20×20 AFM Scans at 0 Hours of 80% Humidity a) Sample A (MAPbI_3) b) Sample C ($\text{MAPbI}_3/\text{Graphene}$)

From initial visual inspection the surfaces appear the same between sample A and sample C suggesting that not only had the PMMA been fully dissolved, but that the graphene is fully conforming to the MAPbI_3 surface. The maximum height range is also comparable, much more than in trial 5. Figure 4.45 is another $20\ \mu\text{m} \times 20\ \mu\text{m}$ scan of sample A with a profile path across the sample and figure 4.46 is the resulting profile graph with measurements.

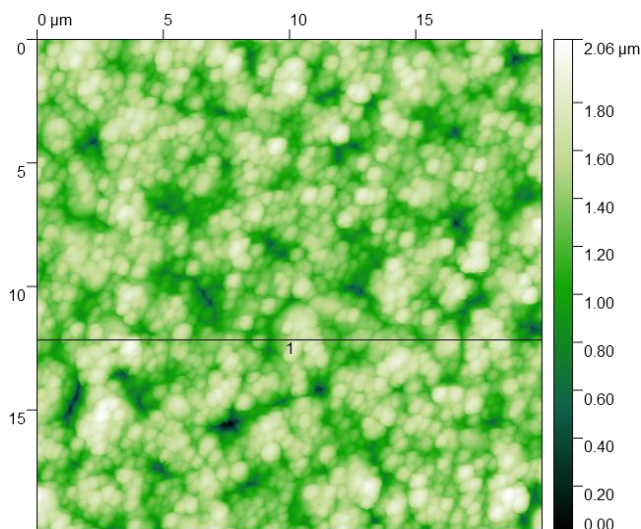


Figure 4.45 20 x 20 AFM Scan of Sample A (MAPbI₃) at 0 Hours of 80% Humidity

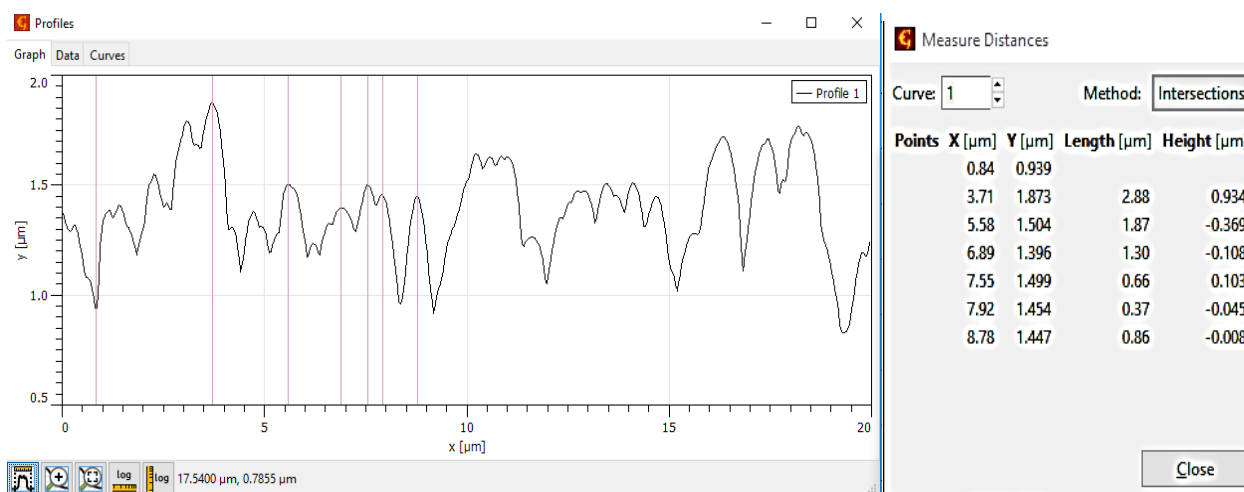


Figure 4.46 Profile Path of AFM Scan of Sample A (MAPbI₃) at 0 Hours of 80% Humidity

From the profile path of sample A there were many peaks often within a micron of each other and a maximum height difference between peaks and valleys of about a micron as well. Figures 4.47 below is another 20 μm x 20 μm scan of sample C with a profile path traversing across the scan with figure 4.48 being the resulting height profile graph.

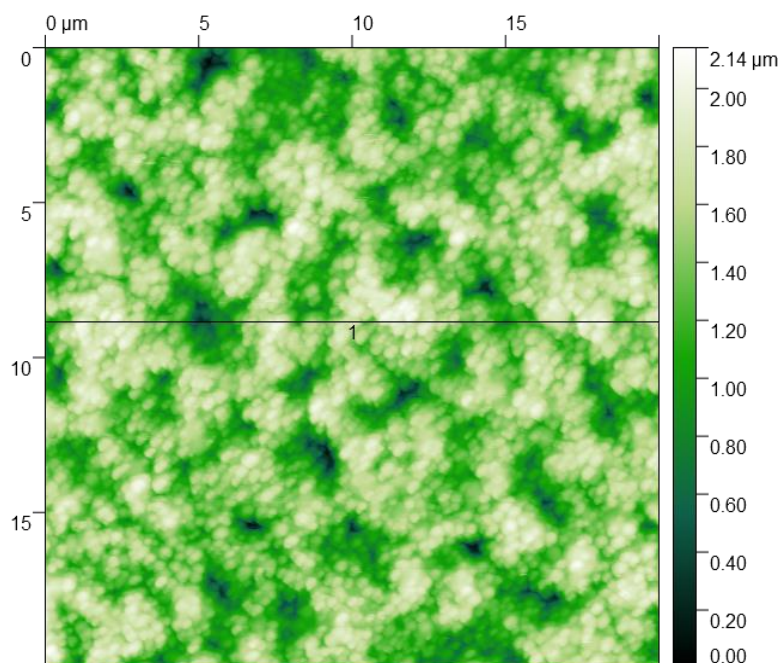


Figure 4.47 20 x 20 AFM Scan of Sample C ($\text{MAPbI}_3/\text{Graphene}$) at 0 Hours of 80% Humidity

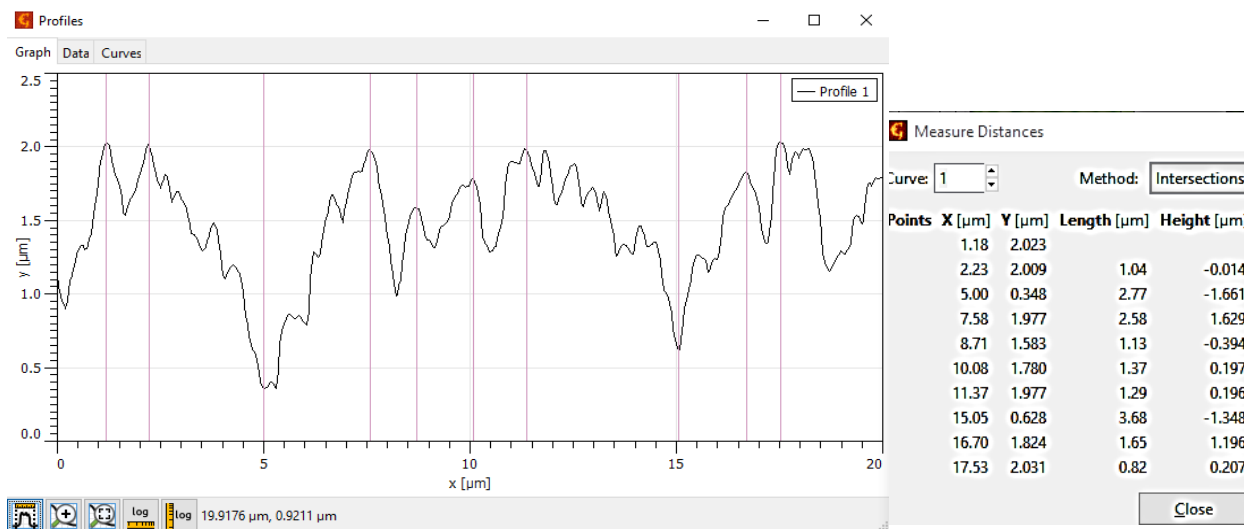


Figure 4.48 Profile Path of AFM Scan of Sample C ($\text{MAPbI}_3/\text{Graphene}$) at 0 Hours of 80% Humidity

The profile path measurements from figure 4.48 show that peaks were occurring a little over one micron away from one another with a maximum height range for peak to valley of about 1.7 micrometers. While there were some minute differences in the profile paths recorded between A and C they are much closer than trial 5 and any differences could be the result of random error. One last visualization to compare samples A and C at 0 hours of 80% humidity is

the 3D rendering of 20 μm x 20 μm scans with the profile paths of both samples A and C shown below in figures 4.49 and 4.50.

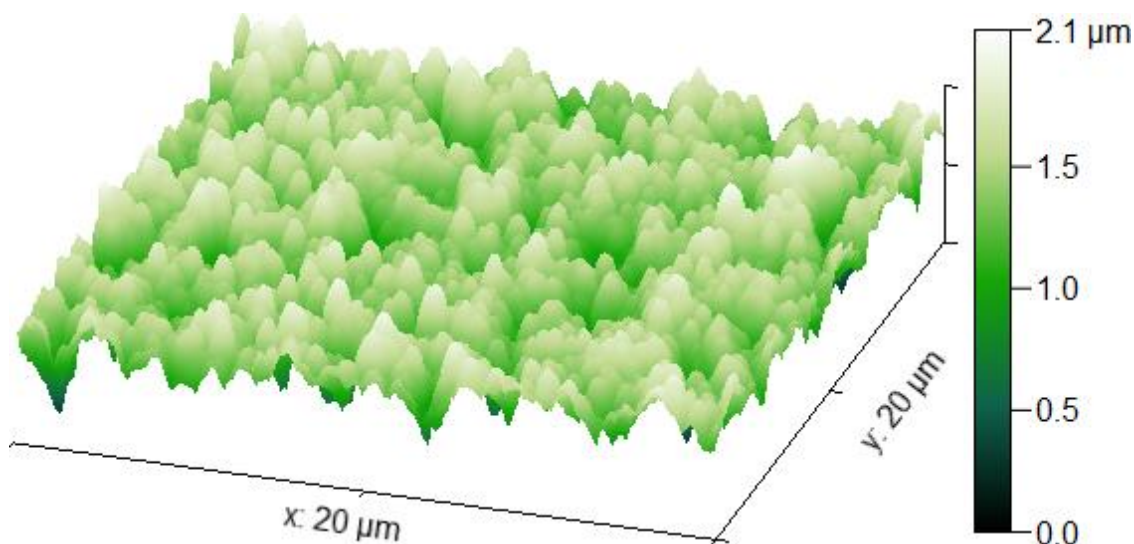


Figure 4.49 3D 20 x 20 AFM Image of Sample A (MAPbI₃) at 0 Hours of 80% Humidity

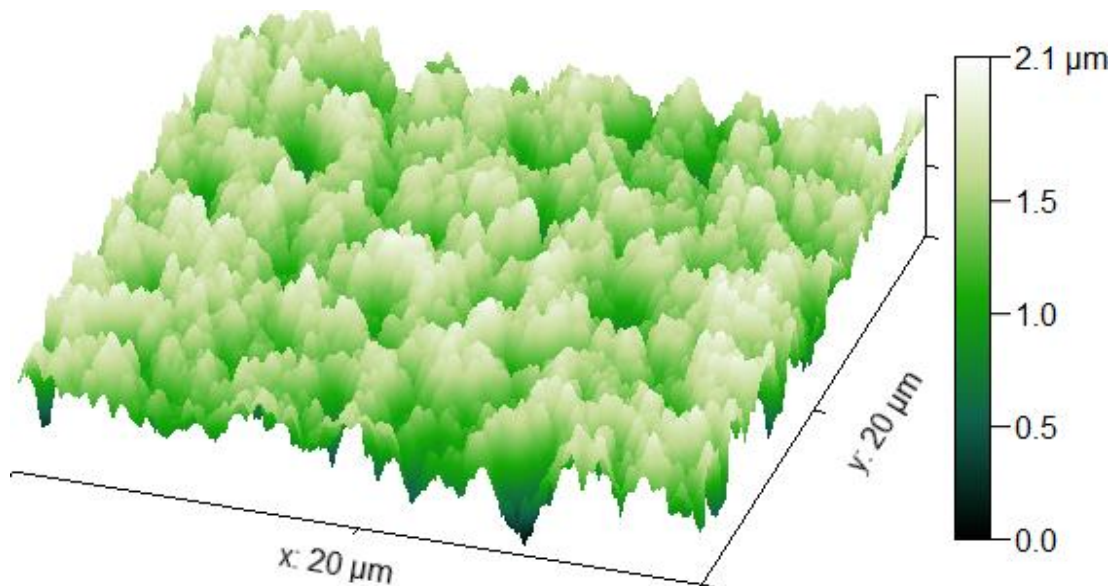


Figure 4.50 3D 20 x 20 AFM image of Sample C (MAPbI₃/Graphene) at 0 Hours of 80% Humidity

The comparison of figures 4.49 and 4.50 emphasizes how similar the surface topography of both samples was. The height range of the 3D images are also both 2.1 μm further emphasizing the similar topography. One potential difference is that sample C seems to have sharper peaks and sample A seems to have more “bubbly,” rolling peaks.

The average number of peaks for the four $20\ \mu\text{m} \times 20\ \mu\text{m}$ scans of sample A was 3121 and for the four $20\ \mu\text{m} \times 20\ \mu\text{m}$ scans of sample C was 3419, which is very comparable. Sample C may have had more peaks than sample A because to fully laminate the graphene on the MAPbI_3 a longer annealing time was required. For sample A only 2 minutes of annealing at 100°C occurred while for the lamination of graphene 15 minutes of annealing at 100°C occurred.

Over time exposed to 80% humidity sample A saw significant degradation to the sample topography, while sample C saw minimal changes to the topography. Figure 4.51 below shows a $20\ \mu\text{m}$ by $20\ \mu\text{m}$ scan of sample A after 48 hours of humidity exposure with a profile line across the sample and the profile height graph in figure 4.52.

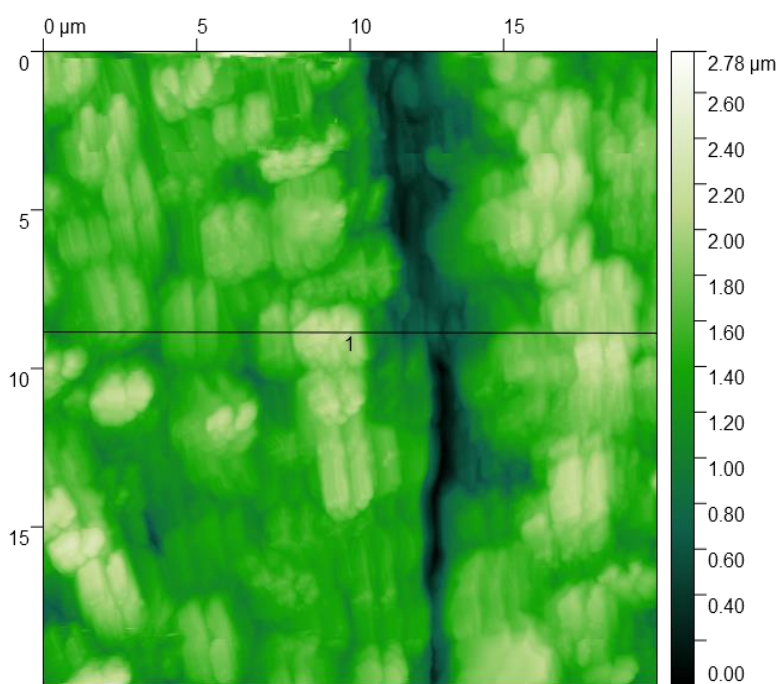


Figure 4.51 20 x 20 AFM Scan of Sample A (MAPbI_3) at 48 Hours of 80% Humidity

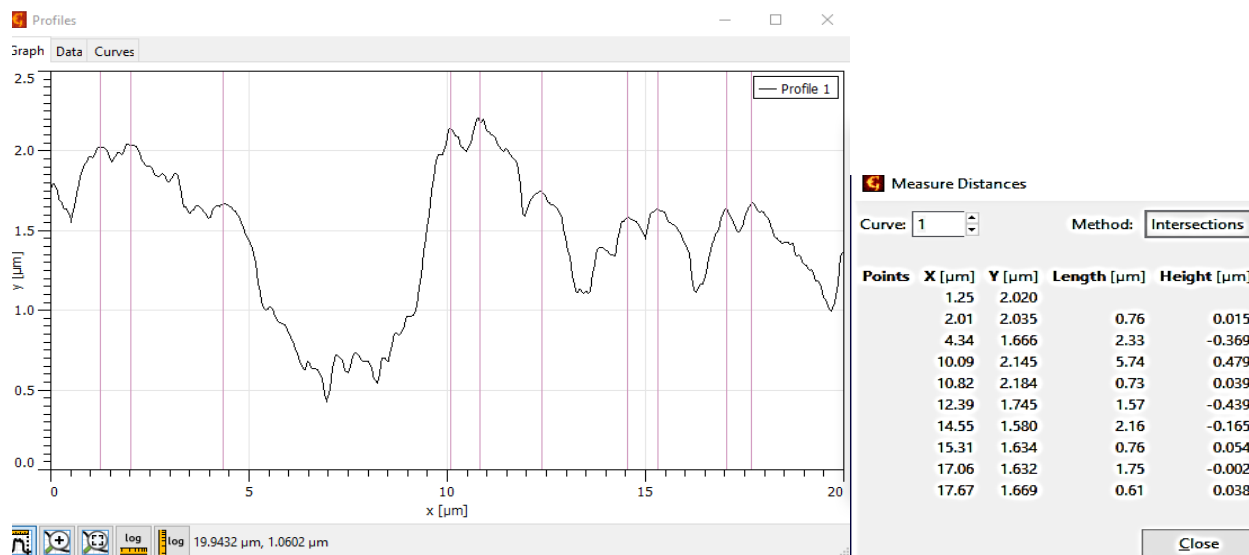


Figure 4.52 Profile Path of AFM Scan of Sample A (MAPbI_3) at 48 Hours of 80% Humidity

Figure 4.51 clearly shows a large valley where the separation of the homogenous film is beginning to transform into fibers and the once numerous peaks are conforming into fewer, but taller peaks. The profile path in figure 4.52 has lesser peaks than the original profile path in figure 4.45. The average distance between peaks is also increasing with the peaks on the opposite sides of the valley being over $2 \mu\text{m}$ away. The height range of the scan has also increased up to $2.78 \mu\text{m}$ from the original $2.06 \mu\text{m}$. Sample C, however, did not see as drastic of changes to the surface topography as shown below in figure 4.53 and the resulting profile path 4.54.

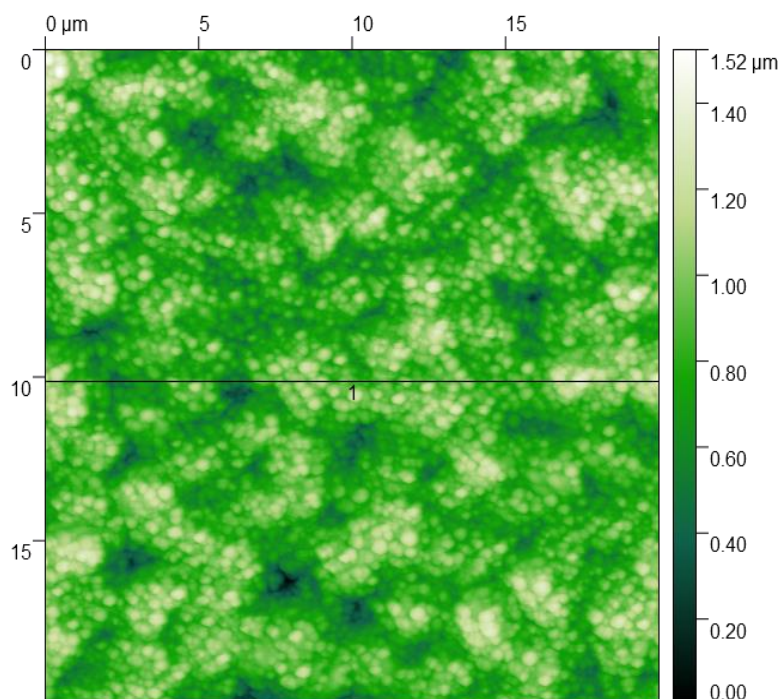


Figure 4.53 20 x 20 AFM Scan of Sample C (MAPbI₃/Graphene) at 48 Hours of 80% Humidity

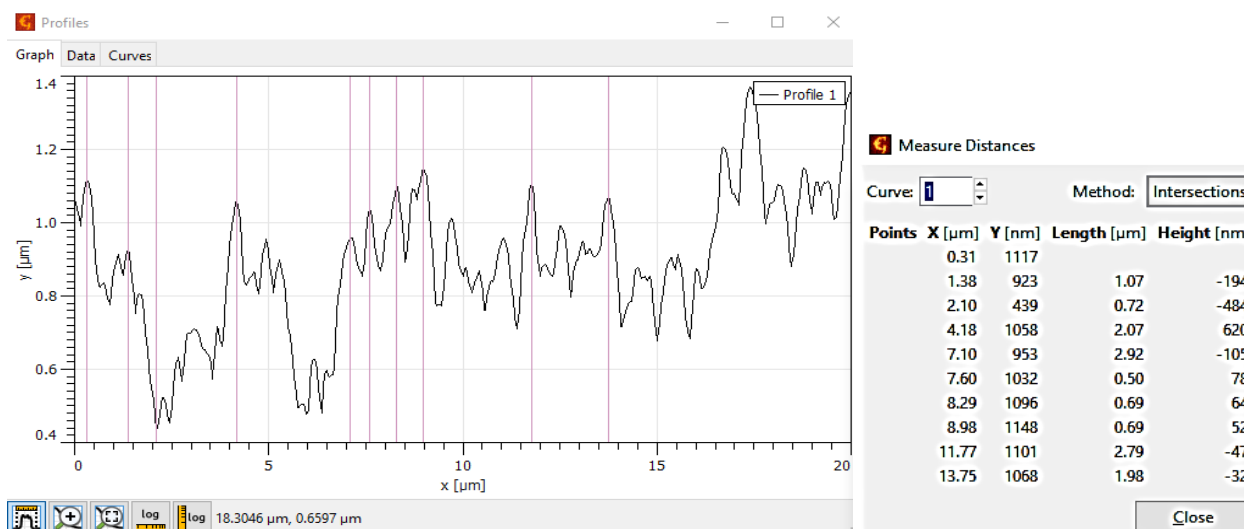


Figure 4.54 Profile Path of AFM Scan of Sample C (MAPbI₃/Graphene) at 48 Hours of 80% Humidity

Contrary to sample A, sample C shows a height profile that is very similar to its original form. There are numerous peaks across the 20 μm profile path with distances less than 1 μm between peaks and height differences less than 1 μm. The total height range of figure 4.53 is only 1.52 μm, which is significantly less than sample A, which was 2.78 μm.

As the sample were exposed longer to 80% humidity the variation of the topography between the two samples became more drastic. Figure 4.55 is an example of one of the four 20 μm x 20 μm AFM scans taken for sample A at 144 hours of 80% humidity exposure with a profile path perpendicular to the fibers shown graphically with measurements in figure 4.56.

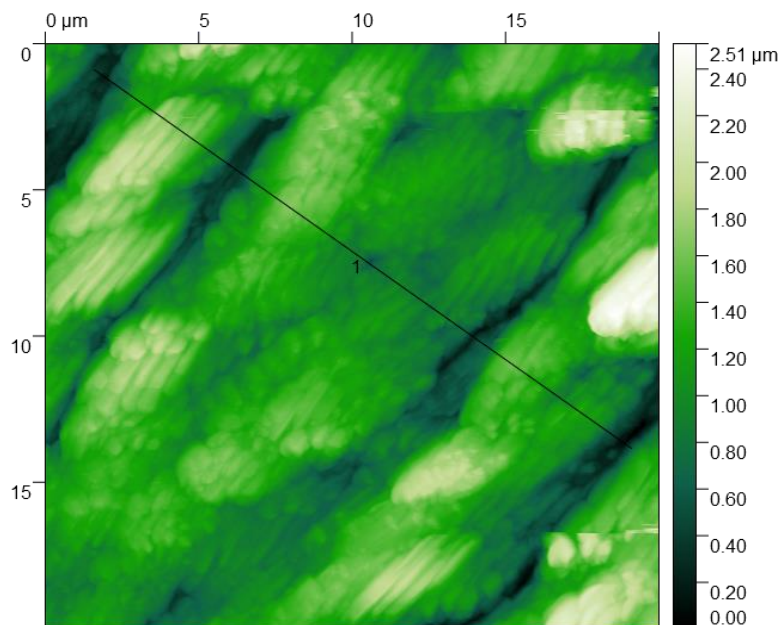


Figure 4.55 20 x 20 AFM Scan of Sample A (MAPbI_3) at 144 Hours of 80% Humidity

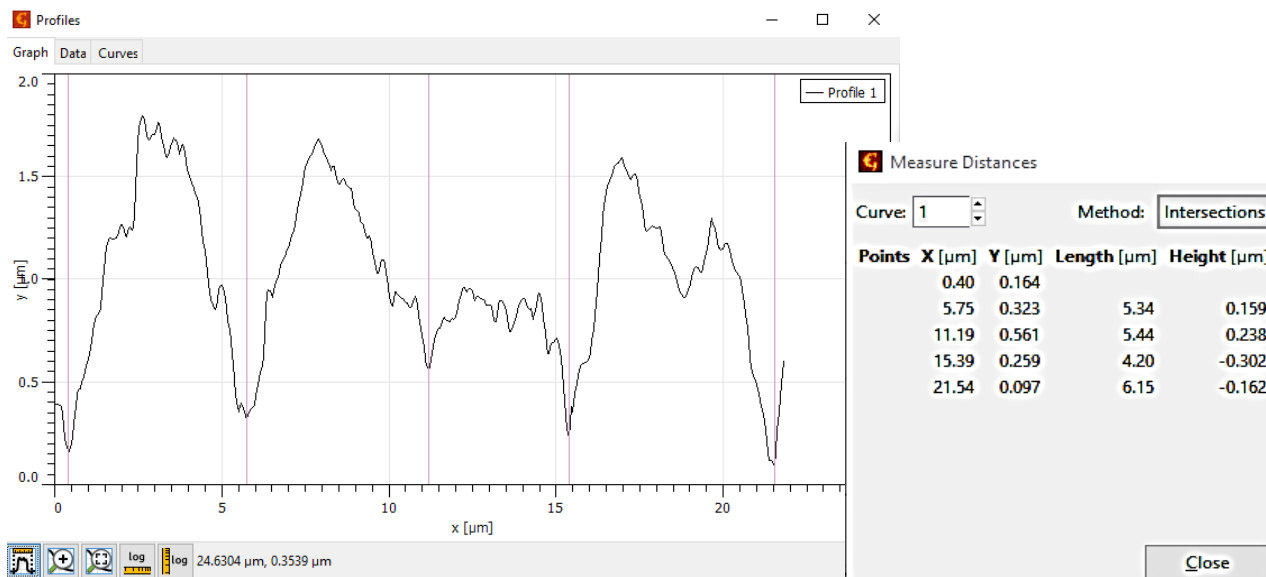


Figure 4.56 Profile Path of AFM Scan of Sample A (MAPbI_3) at 144 Hours of 80% Humidity

Distinct changes in sample A's topography are shown in the profile path in figure 4.56. Originally sample A had numerous peaks and at 144 hours of humidity exposure figure 4.56 shows a profile path of four major features with large valleys between them. The width of these features is approximately 5 μm and the total height range of the scan in figure 4.55 is 2.5 μm . While the height of this scan may not seem as drastic, the overall height range average of the four scans increased to over 3 μm . In contrast figure 4.57 shows one of the four 20 μm x 20 μm AFM scan for sample C at 144 hours of 80% humidity exposure and the resulting profile path graph in figure 4.58.

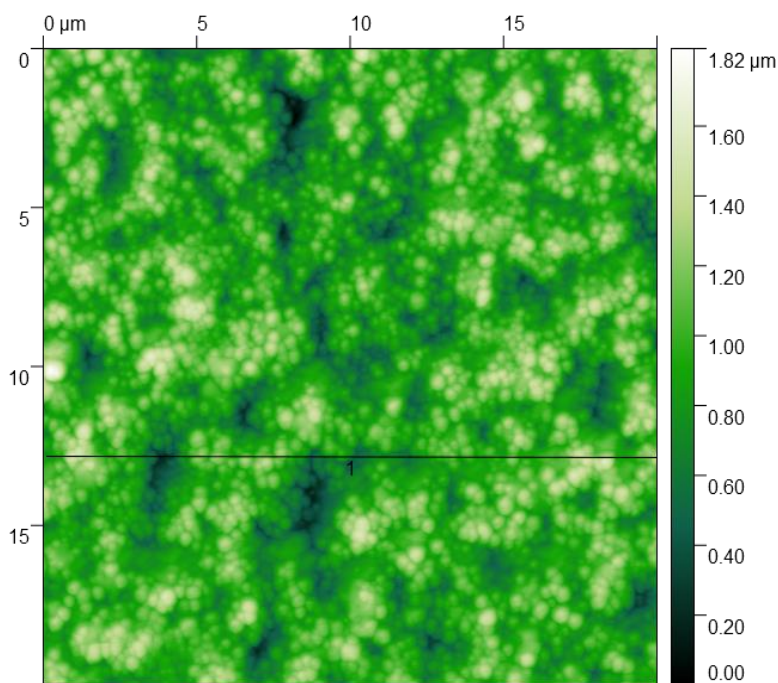


Figure 4.57 20 x 20 AFM Scan of Sample C (MAPbI₃/Graphene) at 144 Hours of 80% Humidity

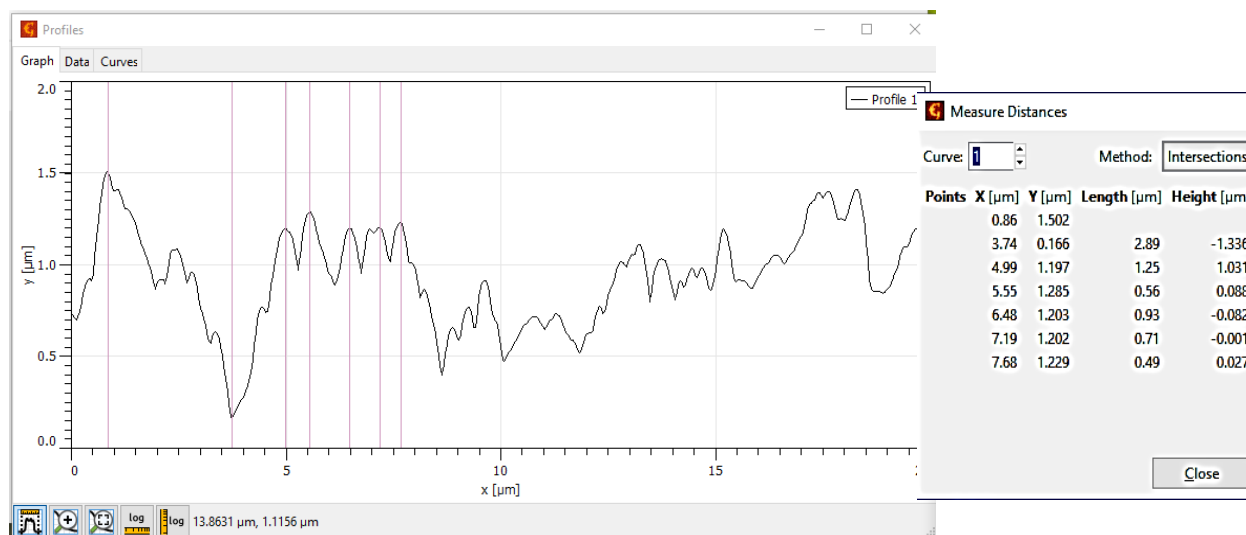


Figure 4.58 Profile Path of AFM Scan of Sample C (MAPbI₃/Graphene) at 144 Hours of 80% Humidity

Even at 144 hours of 80% humidity exposure sample C is not seeing detrimental degradation to the surface topography that was typical of sample A in both trial 5 and trial 6. The total height of the scan in figure 4.57 was 1.82 μm and was still less than sample A. Furthermore, the profile graph shown in figure 4.58 shows numerous peaks with minimal conformation into larger fiber-like features. Many peaks had less than 1 μm of length between them with one major valley that had a height difference from the nearest peaks of approximately 1.4 μm. Some mild forms of degradation may be occurring on sample C by 144 hours of humidity exposure that is further highlighted in the PL data analysis section. One final evaluation of the surface topography at 216 hours of 80% humidity exposure was taken to examine the comparison of degradation of sample A and C using the AFM.

Figure 4.59 below shows one of the four 20 μm x 20 μm scans of sample A at 216 hours of humidity exposure with a profile path running perpendicularly to the fiber-like features and graphically displayed in figure 4.60.

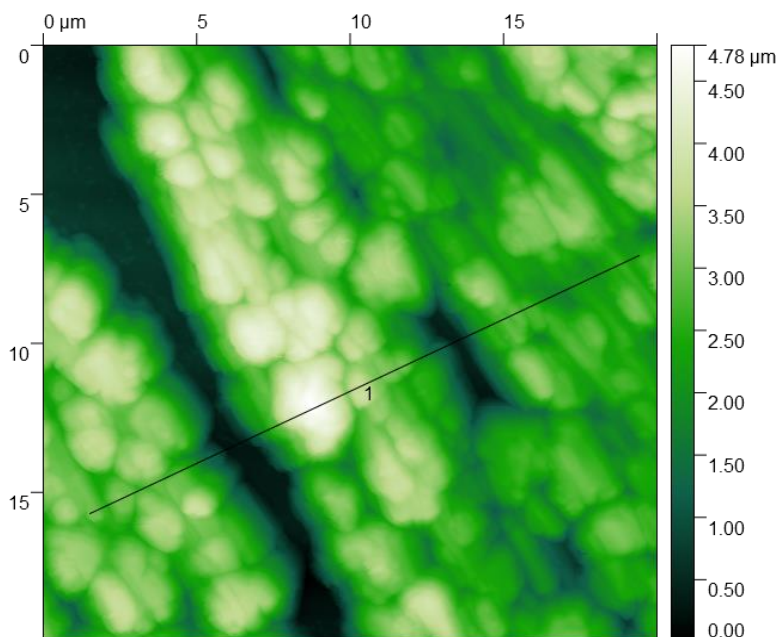


Figure 4.59 20 x 20 AFM Scan of Sample A (MAPbI_3) at 216 Hours of 80% Humidity

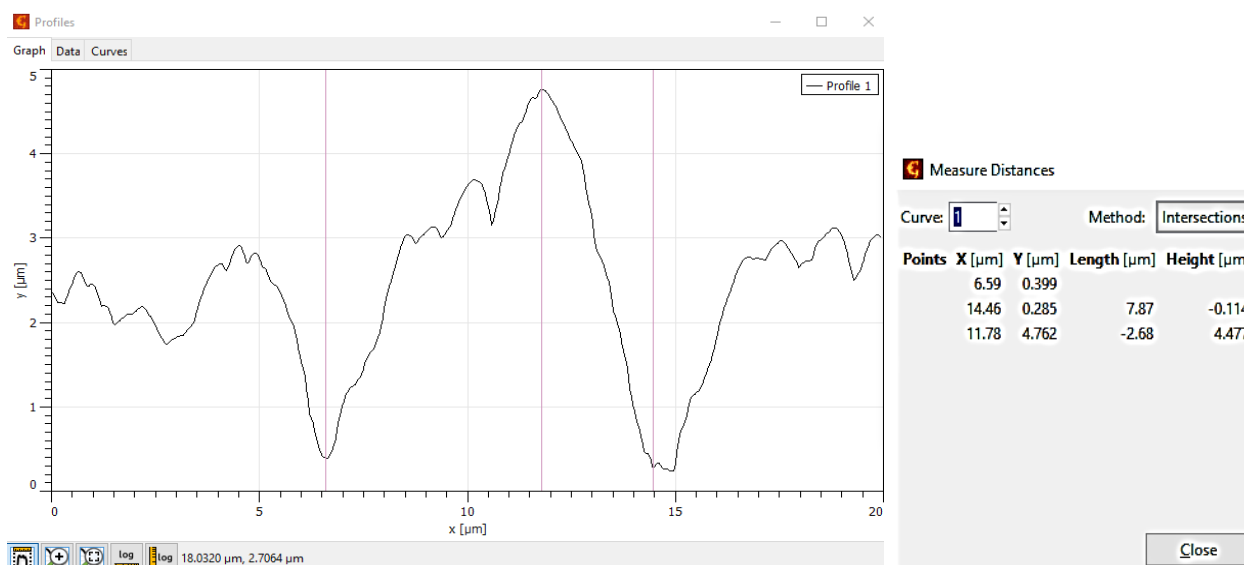


Figure 4.60 Profile Path of AFM Scan of Sample A (MAPbI_3) at 216 Hours of 80% Humidity

Sample A by 216 hours of humidity exposure had a significantly different surface topography compared to its original form. The once many peaks now had formed into three major sections with a much larger height. The large peak in the center of the profile shown in

figure 4.60 had a width of approximately 8 μm and a height of approximately 4.5 μm . The height range of figure 4.58 is 4.78 μm , which is significantly larger than the original height ranges of the homogenous film. Sample C, however, did not see as significant of changes occurring to the surface topography. Figure 4.61 is one of the four AFM scans taken for sample C at 216 hours with its profile path shown graphically in figure 4.62.

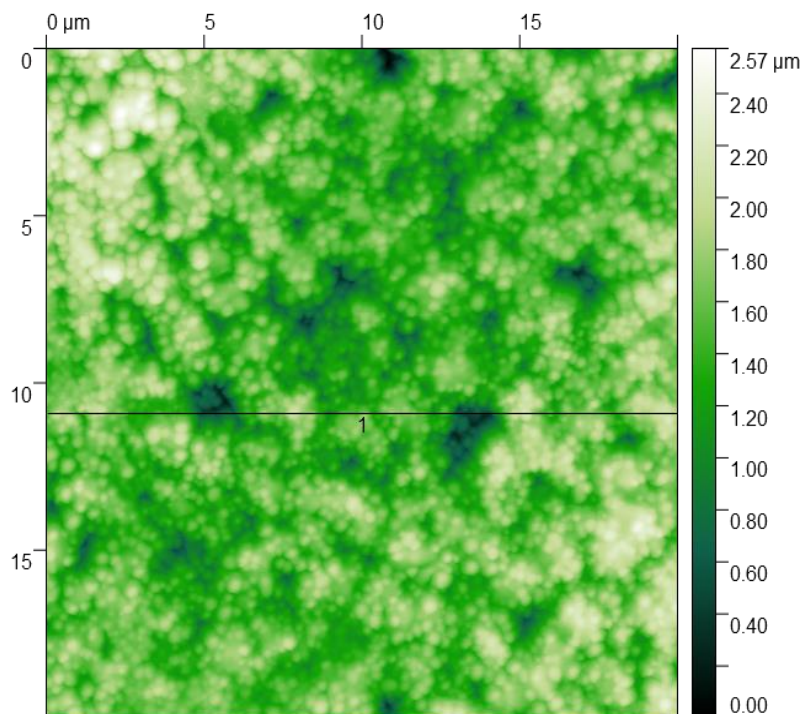


Figure 4.61 20 x 20 AFM Scan of Sample C ($\text{MAPbI}_3/\text{Graphene}$) at 216 Hours of 80% Humidity

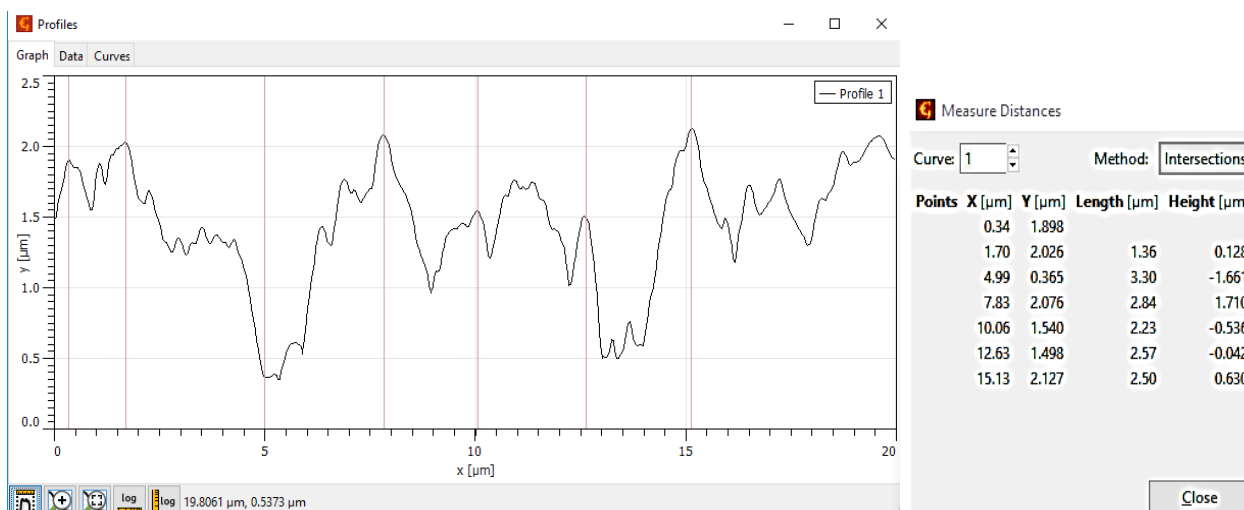


Figure 4.62 Profile Path of AFM Scan of Sample C ($\text{MAPbI}_3/\text{Graphene}$) at 216 Hours of 80% Humidity

Figure 4.62 shows that sample C may have some conforming of peaks into larger features. Where larger peak and valley differences had heights of $1.7\ \mu\text{m}$ and distances between peaks were widening from under $1\ \mu\text{m}$ to over $1\ \mu\text{m}$ up to $2.5\ \mu\text{m}$. By 216 hours sample C did begin seeing degradation to the surface topography, but not nearly the extent of sample A. The height range of figure 4.61 was the largest value for AFM scans of sample C of $2.57\ \mu\text{m}$. Some areas of sample C seemed untouched by humidity and were maintaining the original topography, but some areas such as the scan shown in figure 4.63 below were clearly degrading and comparable to sample A.

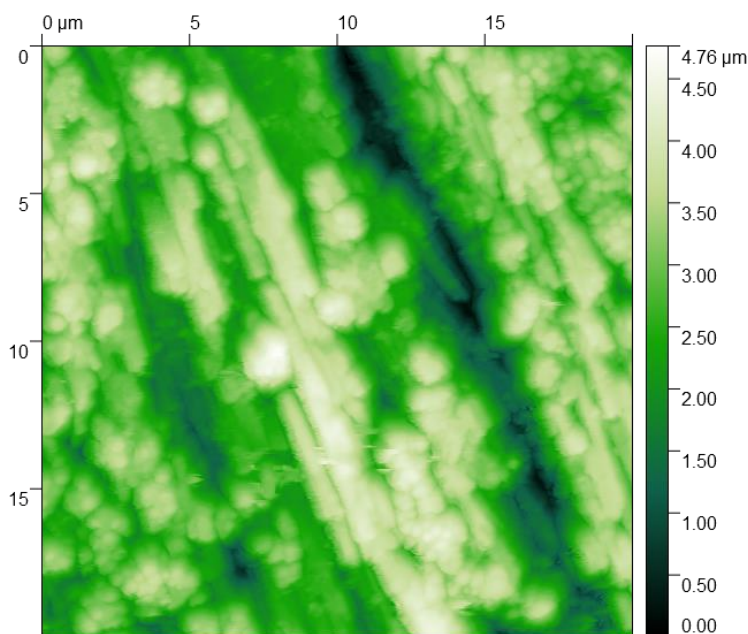


Figure 4.63 20 x 20 Degraded AFM Scan of Sample C ($\text{MAPbI}_3/\text{Graphene}$) at 216 Hours of 80% Humidity

Figure 4.63 exemplifies that not all regions of sample C were unaffected by the humidity. The scan height of $4.76\ \mu\text{m}$ is substantially greater than all previous AFM scans of sample C and the other three scans of sample C at 216 hours of humidity exposure. Potential cracks or pockets in the graphene encapsulation much have left passages for humidity to contact MAPbI_3 and begin degradation. While sample C certainly degraded slower than sample A degradation was still occurring. To potentially reduce degradation further multiple encapsulation layers of

graphene may be necessary, or an entire encapsulation of plastic around a finished solar cell device may fully mitigate degradation.

The three major measurements recorded during the degradation process was surface roughness, scan height range, and the number of peaks per scan. Surface roughness measurements suggests how well the graphene conformed to the MAPbI₃ surface. Whereas, scan height range and the number of peaks per scan indicate that sample C degraded less than sample A. Figure 4.64 below shows the decrease in the number of peaks on 20 μm x 20 μm scans for trial 6 during the degradation.

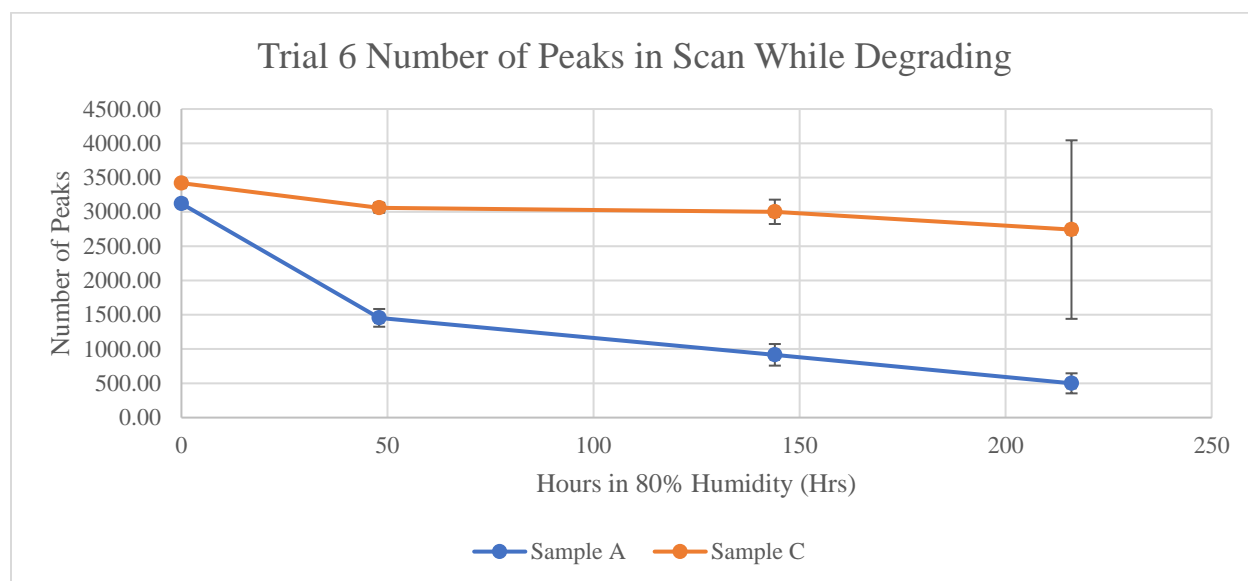


Figure 4.64 Trial 6 Number of Peaks in 20 x 20 AFM Scans During Degradation with error bars of ± 1 std dev.

Figure 4.64 exemplifies how the number of peaks on sample C is remaining quite consistent, while the number of peaks on sample A are decreasing substantially. The reduction in the number of peaks per 20 μm x 20 μm scan for sample A is an indication of degradation and the consistency of number of peaks per 20 μm x 20 μm scan for sample C indicates a reduction in degradation. The number of peaks for sample C did still decrease, but substantially less than sample A. The error bar for the last measurement of sample C is much larger than all the others

because one scan of sample C was thoroughly degraded with fiber-like features, while the other three scans were consistent with the original homogenous, “bubbly” film.

The first indication of the reduction of degradation and the comparison of rates can be found using figure 4.64. The initial average number of peaks for sample C was 3419.5 and at 216 hours it was 2741.75, which is 80.2% of its initial value. Conversely, sample A initially had an average of 3120.75 peaks and at 216 hours had 499.75, which is 16.0%. By comparing the change in the number of peaks the degradation rate of sample C is 501% slower than sample A.

The surface roughness measurements averaged across the four AFM scans per sample at each time interval are graphed in figure 4.65 below.

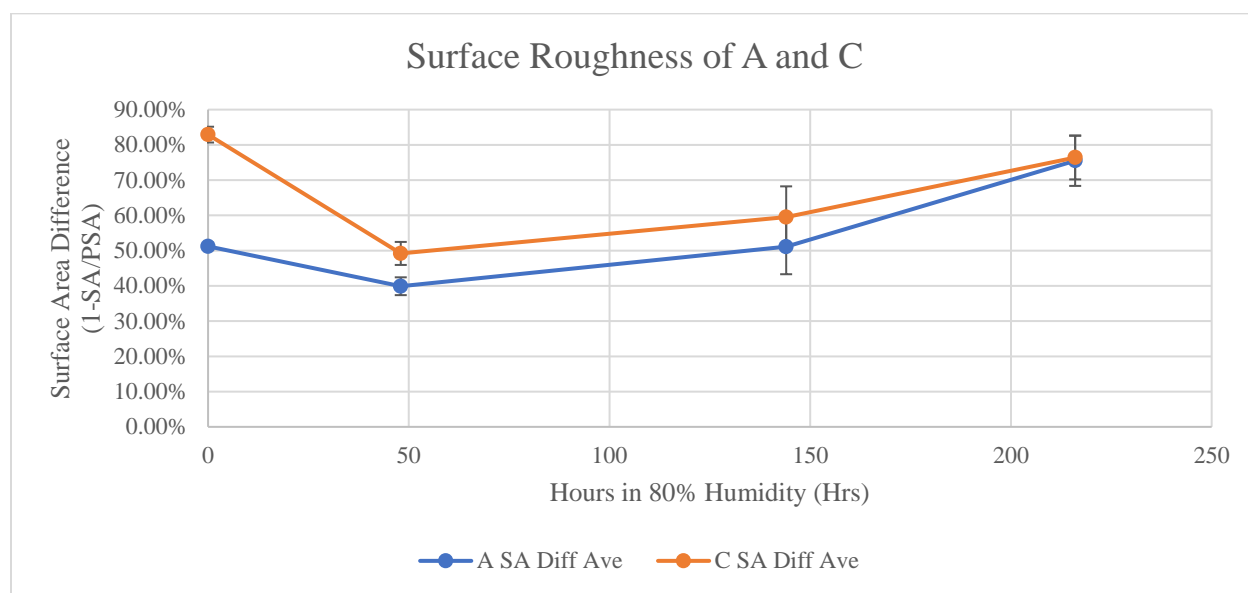


Figure 4.65 Trial 6 Surface Roughness Comparison of Sample A and Sample C with error bars of ± 1 std dev.

Figure 4.65 suggests that the graphene is conforming to the MAPbI₃ surface since the surface roughness of sample A and sample C are comparable and that all the PMMA had been dissolved in contrast to the results of trial 5. Sample C does have a rougher surface than sample A throughout the degradation process and is likely due to the sharper peaks seen in the profile graphs compared to the smoother, “bubbly” peaks of sample A. The graphene thus likely creates

sharper peaks above the smooth hills of MAPbI₃ and could possibly have nanoscale gaps between the sharp peak of graphene and the smoother peak of MAPbI₃.

The third measurement that was traced using the AFM was the scan height range during the degradation process. As the “bubbly” film transformed into fibrous structures the scan height ranges increased. Figure 4.66 below depicts the difference between the average scan height ranges of sample A and sample C.

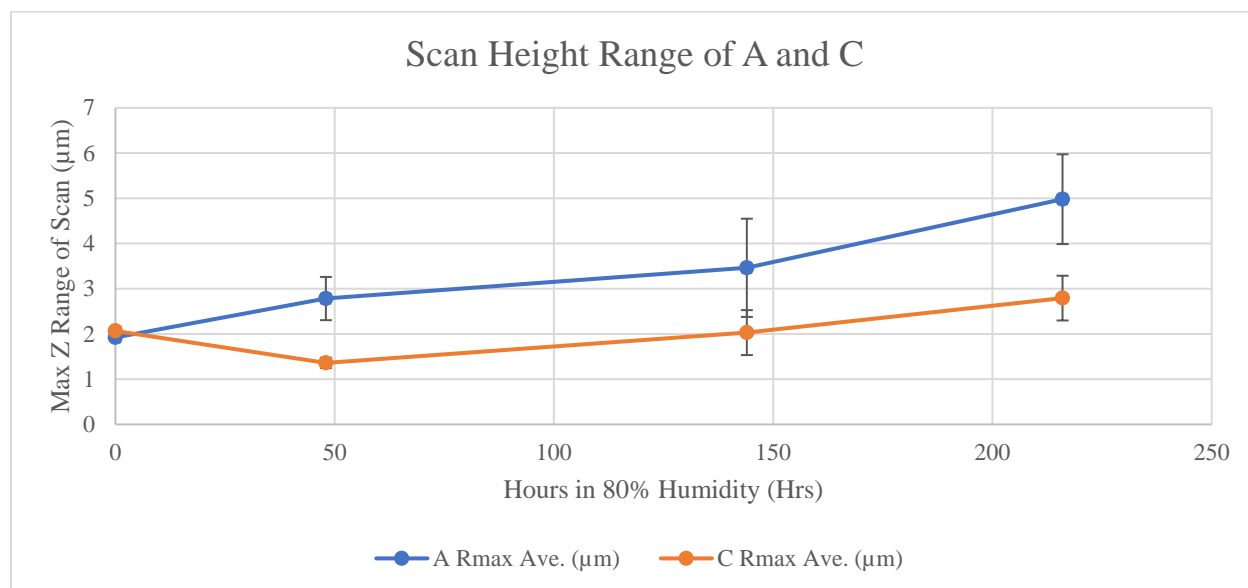


Figure 4.66 Trial 6 Scan Height Range Comparison of Sample A and Sample C with error bars of ± 1 std dev.

Figure 4.66 is also evidence that sample C is degrading less than sample A. Initially the scan height range of both sample A and sample C were approximately the same. As the samples were exposed to 80% humidity over time the features of sample A grew in height faster than the features of sample C. The scan height was an indication that the homogenous film was changing into fibrous features. As the fibers emerged the scan heights increased. As was seen in trial 5 (and is indicated in trial 6) the PL peak intensity decreased as fibers protruded through the film. The increase of height of sample A scans occurred more rapidly than sample C. By 216 hours of humidity exposure sample A had average height ranges of 5 µm with an increase of over 3 µm

from its original form. Sample C on the other hand had average height ranges of less than 3 μm by 216 hours of humidity exposure with an increase of less than 1 μm from its original form. All the AFM surface topography scan images and data analysis of trial 6 indicate that sample C is degrading less than sample A. The PL data presented in the next section also indicates a significant reduction in degradation by encapsulating MAPbI_3 with graphene.

Figure 4.66 also indicates the degradation rate comparison between sample A and sample C. The initial average scan height of sample C was 2.068 μm and at 216 hours the scan height was 2.793 μm , which is a 35.1% increase. Comparatively, sample A had an initial average scan height of 1.923 μm and at 216 hours the average scan height was 4.980 μm , which is a 159.0% increase. By comparison the scan heights of sample C degraded 453% slower than sample A.

4.4.2 Optical Images and Photoluminescence Data

The PL data presented for trial 6 is conclusive towards the hypothesis, because PMMA is no longer present on sample C any lasting PL intensities is due to the reduction of degradation from graphene encapsulation. Table 4.9 below shows the full array of images of sample A and C for degradation intervals from 0 hours to 240 hours of 80% humidity exposure the same as trial 5. As before all optical images shown in table 4.9 have scale bars of 20 μm .

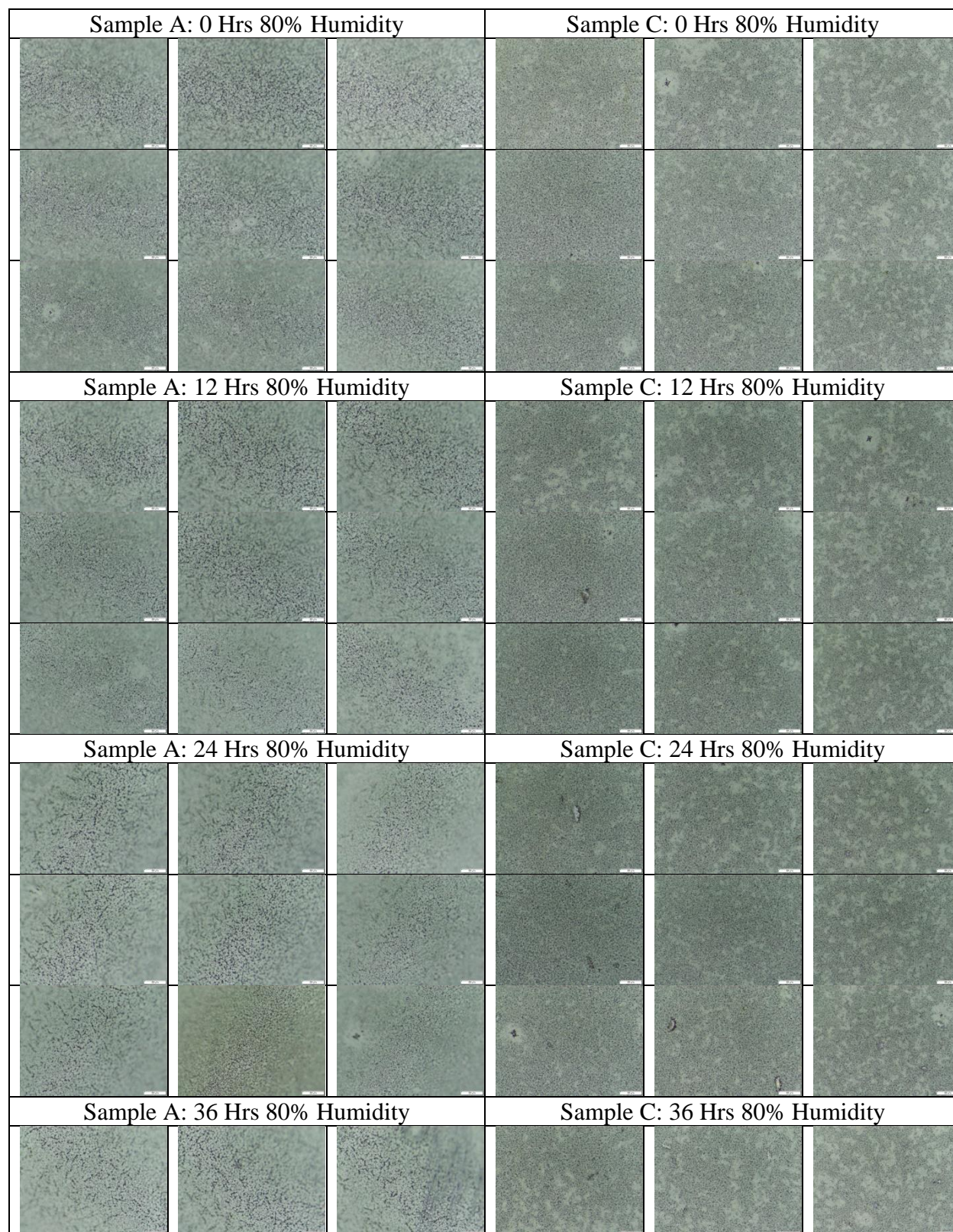
Table 4.9 Trial 6 bright field images scale bars are 20 μm 

Table 4.9 Continued

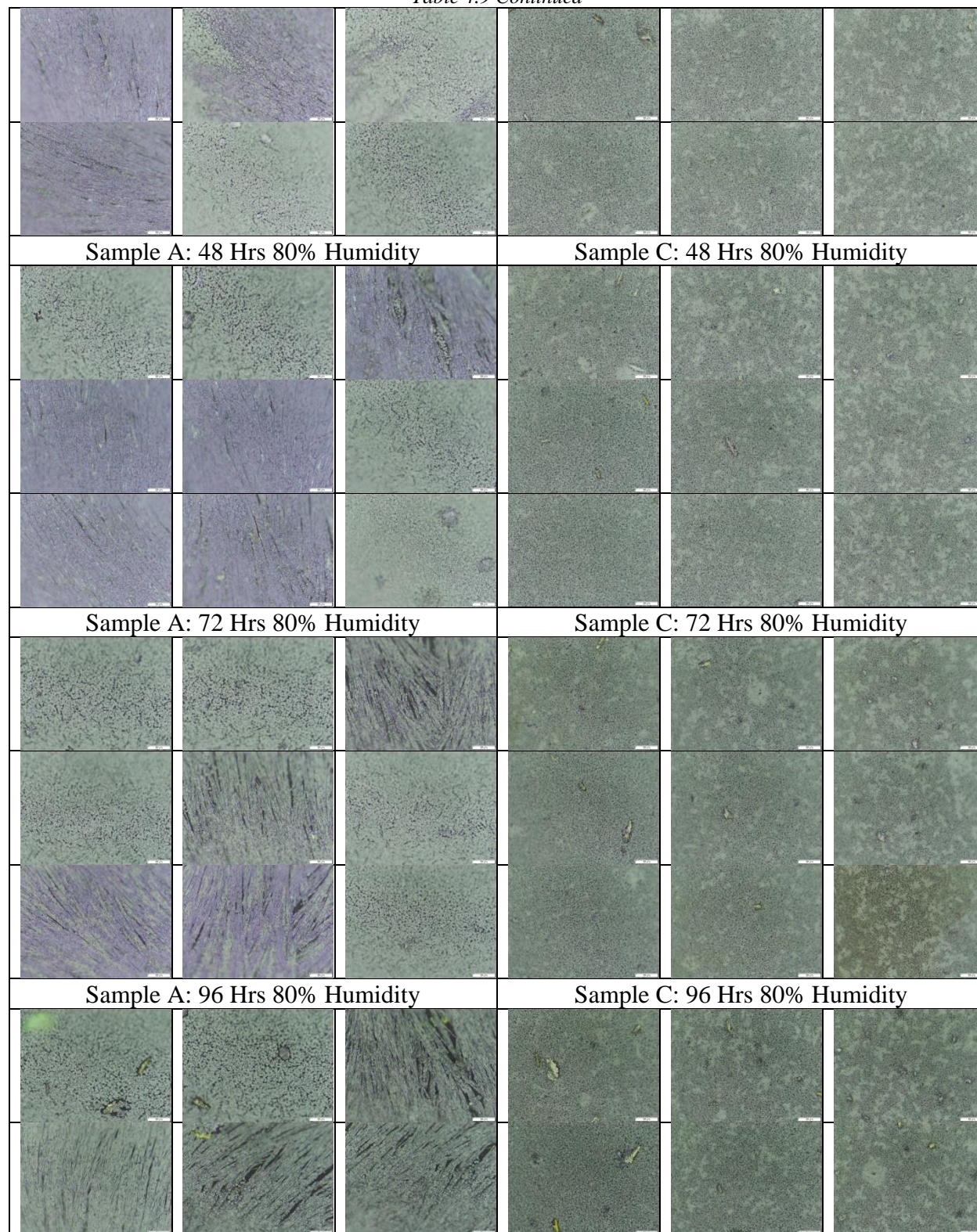


Table 4.9 Continued

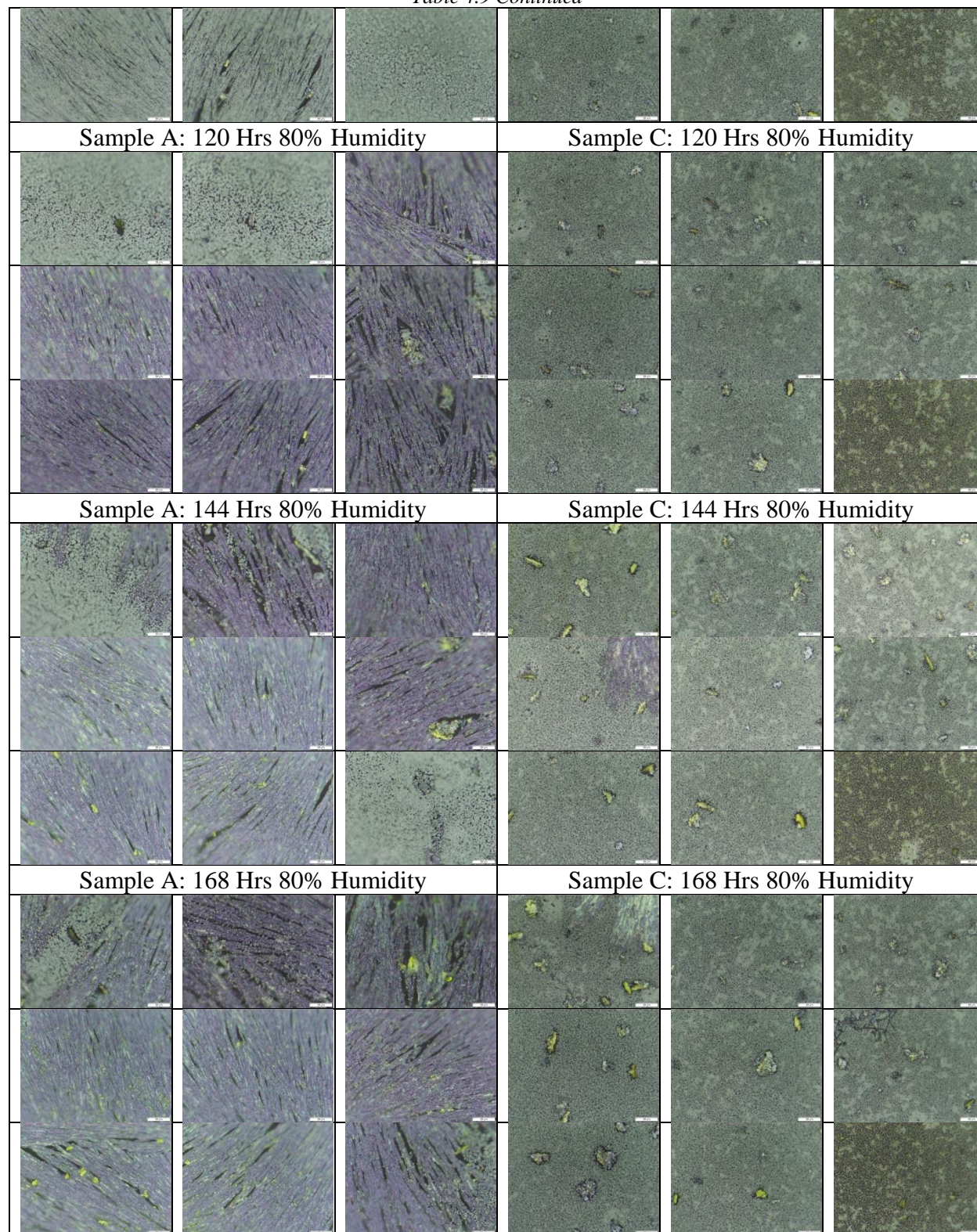
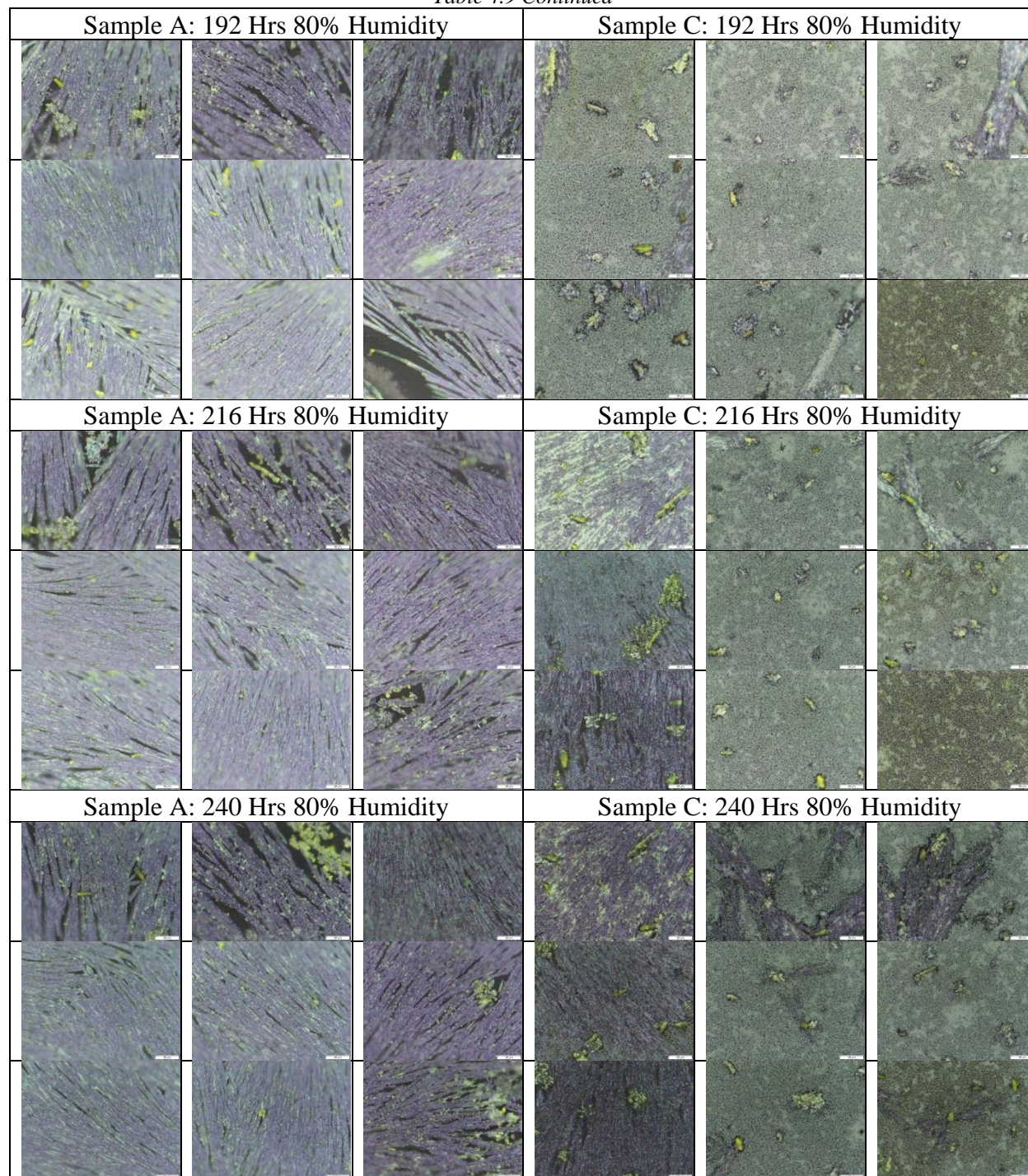


Table 4.9 Continued



Like trial 5 a series of optical images comparing sample A and C are shown above in table 4.9 and can then be compared with the Xbar chart of average PL peak intensities of the

areas indicated in the optical image array. During trial 6 long term PL intensities were recorded because sample C still had PL peaks occurring after 500 hours of 80% humidity exposure. Optical images of the PL measurement locations are only supplied up to 240 hours of 80% humidity exposure. The PL measurements were taken in 3 x 3 arrays on the sample. Locations of measurements were approximately the same each time, yet the exact location of each measurement differed for each time interval.

Many key qualitative observations can be made from table 4.9. First, and most importantly sample A shows purple fibrous growth at 36 hours of 80% humidity exposure. Comparatively sample C did not show any purple fibrous growth until 144 hours of 80% humidity exposure. According to the key sign of crystal morphological change from a homogenous film to fibers sample C degraded 400% slower at a minimum. Even so at 36 hours sample A showed 3 of the 9 optical images with purple fibers. Sample C did not have 3 of the 9 optical images containing purple fibers until 216 hours, therefore more accurately sample C degraded 600% slower than sample A by qualitative observation.

Other key observations from table 4.9 is that the brightness of both images is equivalent unlike in trial 5 for table 4.7, therefore another sign that the PMMA has been fully dissolved. The optical images, like the AFM analysis, does still show that sample C is degrading, yet significantly slower than sample A. To quantify the optical images in table 4.9 an Xbar chart of the average PL peak intensities over time is shown below in figure 4.67.

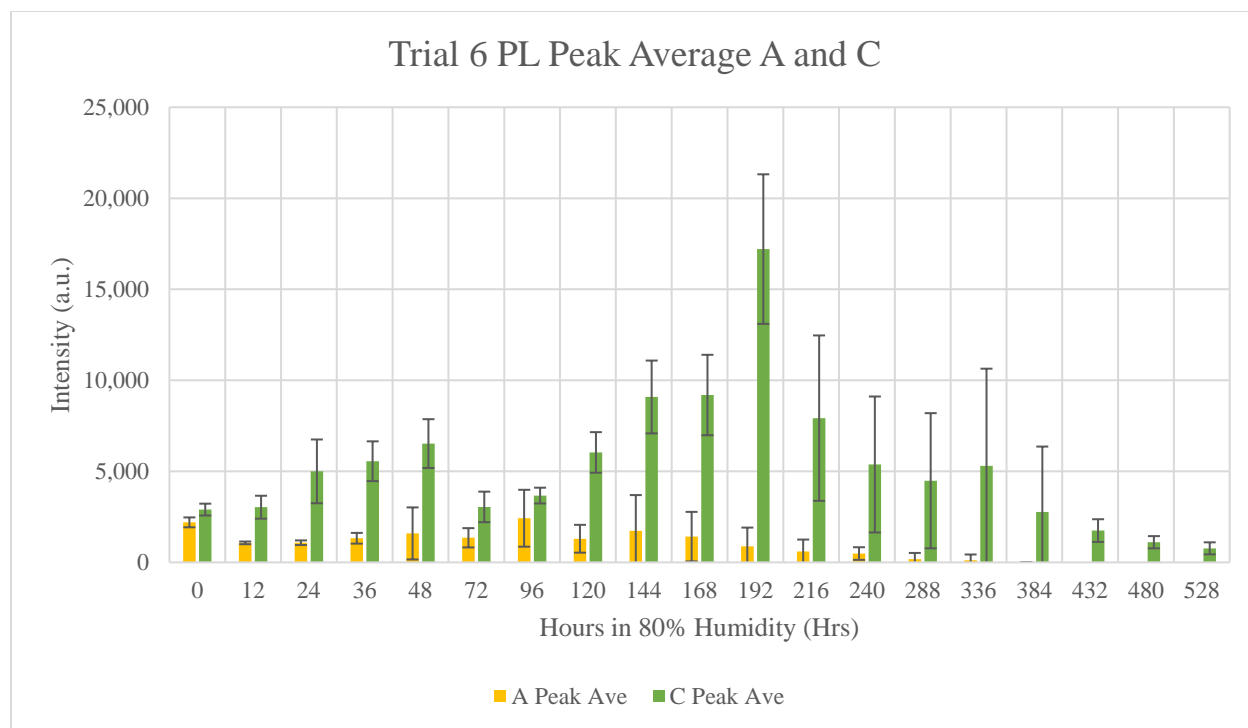


Figure 4.67 Trial 6 Xbar Chart for average peak PL intensity across 9 measurement locations for samples A and C over time exposed to 80% humidity with error bars of ± 1 standard deviation

Figure 4.67 is the most important chart of the entire thesis study. The PL peak intensity average across the 3 x 3 array for sample A and sample C are compared in figure 4.67 and clearly sample C not only has better PL performance, but also has a significantly longer lifetime. At 0 hours of humidity exposure sample C outperformed sample A by more than one standard deviation suggesting that graphene may improve the electronic properties. For all time intervals measured from 0 hours of 80% humidity exposure to 528 hours of humidity exposure sample C outperformed sample A's average PL peak intensity.

At initial conception sample C had an average PL peak intensity that was 31.8% greater than sample A. For 12 hours to 336 hours, where A had a non-zero average PL peak intensity, sample C had an average PL peak intensity that was on average 983% greater than sample A! At 384 hours of 80% humidity exposure sample C still had 95.4% of its initial average PL peak intensity. Even at 528 hours of 80% humidity exposure sample C had 26.6% of its initial PL

peak intensity. The PL degradation between sample A and sample C can also be used to better understand the comparative degradation rates. At 528 hours sample C had 26.6% of its initial PL intensity. Comparatively at 216 hours sample A had 26.8% of its initial PL intensity. Therefore, sample C was reaching 27% of its initial PL intensity 144% slower than sample A. However, other times and percentages of initial PL intensity may not agree. At 480 hours sample C had 38.2% of its initial PL intensity, which occurred at approximately 192 hours for sample A. So, sample C reached 38% of its initial PL intensity 150% slower than sample A. At 432 hours sample C had 60.2% of its initial PL intensity, which occurred at approximately 168 hours for sample A. Therefore, sample C reached 60% of its initial PL intensity 157% slower than sample A. Lastly, sample C reached 95.4% of its initial PL intensity at 384 hours, whereas sample A reached 95.4% of its initial PL intensity at approximately 100 hours suggesting sample C degraded 284% slower than sample A. As an average of all the different PL ratios degradation rates suggests that sample C degrades 184% slower than sample A.

According to Wang et al. (2018) applying graphene using a dry transfer method on a 2D CVD grown MAPbI₃ perovskite led to 35% of the PL peak intensity after 30 days in approximately 30% humidity exposure. At 480 hours, or 20 days of 80% humidity exposure sample C had 38.2% of its initial PL peak value. From preliminary trials 1-3 sample A seemed to degrade exponentially faster with increasing humidity. However, assuming a linear relation between humidity percentage and degradation time, that is at 40% humidity it would take twice the time to degrade MAPbI₃ as it would at 80% humidity, then sample C presented in this study would take approximately 1280 hours for sample C to be at 35% of its initial PL peak intensity ratio. That is, it would take approximately 54 days at 30% humidity to degrade the graphene encapsulated MAPbI₃ sample using the wet PMMA transfer method presented in this study to

35% of its initial PL peak intensity ratio. Therefore, the wet PMMA transfer method presented in this study improves the capability to reduce degradation by at least 80% compared to the dry gel film transfer presented by Wang et al. (2018). Assuming an exponential relationship between humidity percentage and degradation time would increase the improvement percentage to well over 100%.

While the error bars in figure 4.67 have a relation with the range of values of the 9 measurements taken to calculate the average peak PL intensity it is important to present a Rbar chart to accompany the Xbar chart. Figure 4.68 below is the Rbar chart, or the range of the 9 PL peak intensities for all time intervals during the degradation of samples A and C in trial 6. Again, the Rbar chart does not have error bars because standard deviation cannot be calculated from a range of values.

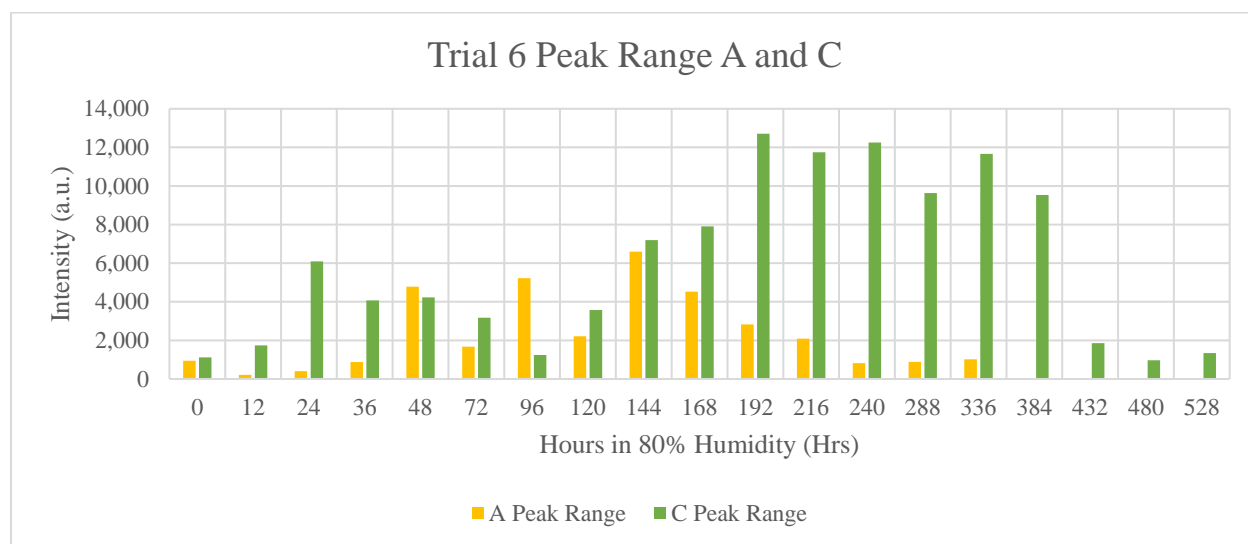


Figure 4.68 Trial 6 Rbar Chart for peak PL intensity ranges among 9 measurement locations for samples A and C over time exposed to 80% humidity

Figure 4.68 is useful to understand the variance of the measurements to calculate the averages in figure 4.67. Initial ranges were small and increased during the degradation time. While sample averages for sample C were larger so were the ranges of peak PL values. So, while

the average peak PL intensity of sample C was greater than A there was a larger variation throughout the sample. Another point to add is that as sample A degraded and eventually all peak PL intensities were at 0, therefore sample A has no ranges for 384 hours to 528 hours. Moreover, sample C saw a large jump in peak PL ranges when first showing signs of degradation and purple fibrous growth. The first sign of purple fiber degradation for sample C occurred at 144 hours, which saw a large jump in peak PL ranges. As more degradation occurred the ranges remained large because parts of sample C were degrading with fibers and other measurements had the original “bubbly,” homogenous film present. Lastly, the phenomenon of PL intensity increasing when on the threshold of degradation also occurred in trial 6 for sample C as was seen for sample A in trial 5 and sample C in trial 4. At this point it would be future work to investigate if PL intensity truly increases as it reaches the threshold of degradation.

4.4.3 X-Ray Diffraction Data

Although certainly not a focus of this study X-Ray Diffraction (XRD) data is commonly used to characterize perovskite solar cells. During trial 6 XRD data was taken at 96 hours of humidity exposure to compare sample A and sample C. XRD is especially useful for the degradation of MAPbI_3 to identify the crystal where as described in the literature review peaks near 12.6° are characteristic of PbI_2 and peaks near 14.1° are characteristic of MAPbI_3 . The relative intensity ratios can then be used to compare the amounts of each crystal within the sample. Figure 4.69 below is the XRD data for sample A.

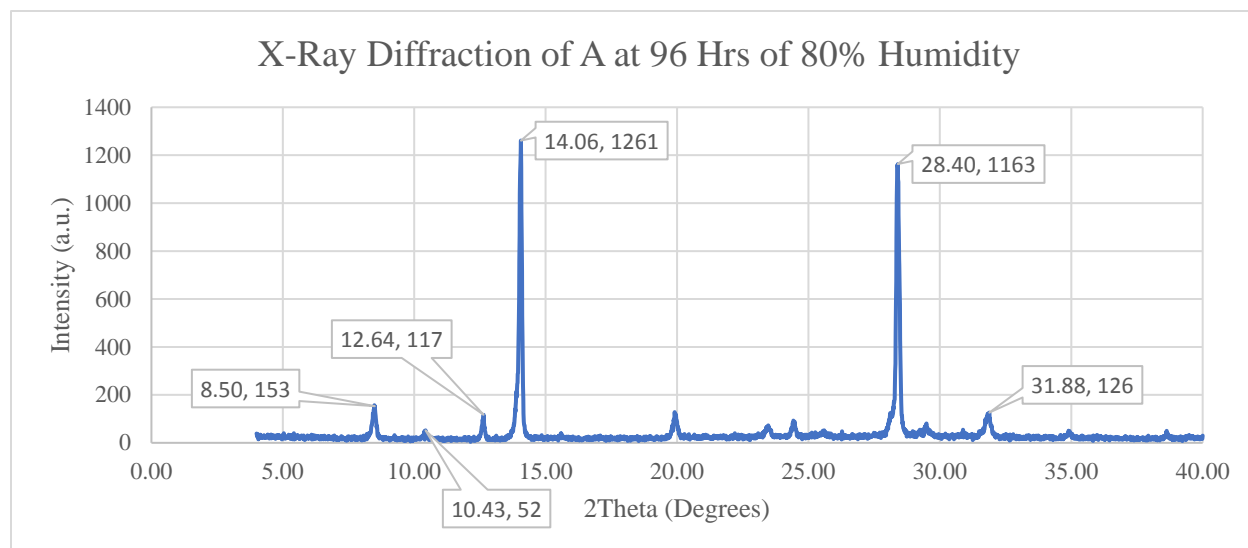


Figure 4.69 XRD Scan of Sample A (MAPbI_3) at 96 Hours of 80% Humidity

Figure 4.69 shows peak intensities typical of MAPbI_3 . The peak at 14.06° is the (110) lattice plane of MAPbI_3 and at 12.64° is PbI_2 . The peak at 8.50° and 10.43° is the (100) and (101) of the monohydrate bond that formed with MAPbI_3 and can be considered a form of degraded MAPbI_3 . The peak at 28.4° is the repeated peak for MAPbI_3 for the (220) crystal lattice plane and 31.88° for the (310) lattice plane. Any other peaks are dismissed. The ratio of intensities of the MAPbI_3 peak and the PbI_2 peak is 10.78:1, and the ratio of MAPbI_3 to the hydrates is 6.15:1. Combined the total degradation ratio is the combination of the 8.50° , 10.43° , and 12.64° peak to the 14.06° peak, which is 3.92:1. In comparison figure 4.4.3.2 below is the XRD scan of sample C at 96 hours of 80% humidity.

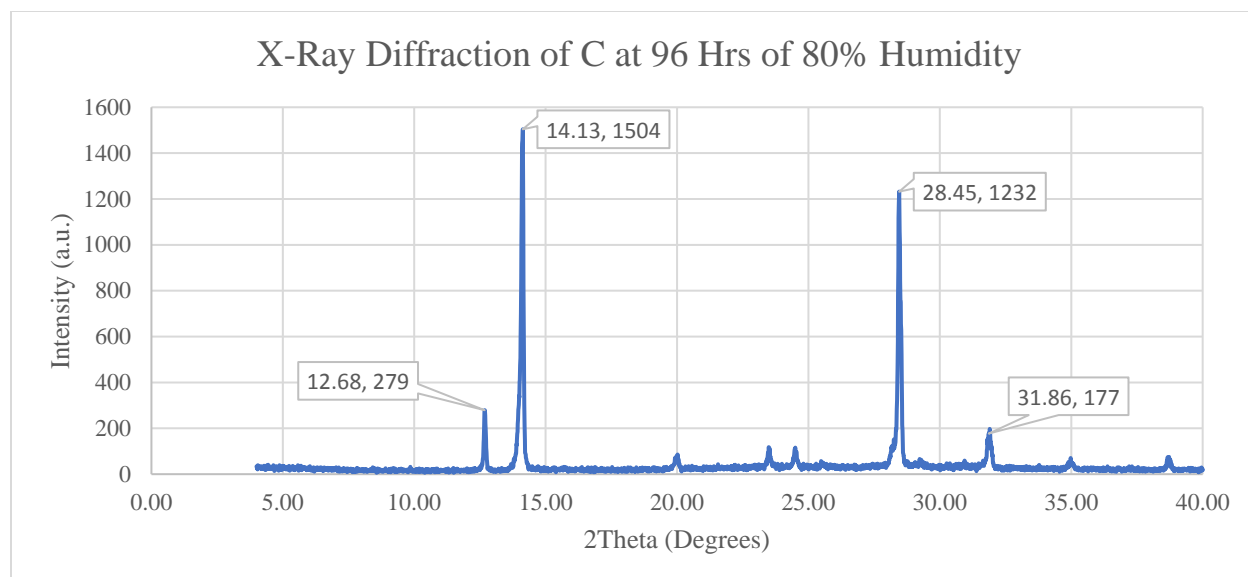


Figure 4.70 XRD Scan of Sample C (MAPbI₃/Graphene) at 96 Hours of 80% Humidity

Figure 4.70 also shows typical peaks of MAPbI₃ at 14.13° for the (110) lattice plane and PbI₂ at 12.68°. The peak at 28.45° is a repeat of MAPbI₃ for the (220) lattice plane and 31.86° for the (310) lattice plane. For sample C the ratio of intensities for the MAPbI₃ peak and the PbI₂ peak is 5.39:1 suggesting that more PbI₂ has formed on sample C than on sample A, however, for sample C there is no peak at 8.50° or 10.43° as there was for sample A. Therefore, the peak ratio for MAPbI₃ to the degraded forms for sample A was 3.92:1 and for sample C was 5.39:1, which suggests that sample C has degraded less than sample A. The XRD scans presented in this study are useful to confirm the crystals in use are in fact MAPbI₃ and are degrading into PbI₂ and hydrates. The XRD scans presented in figures 4.69 and 4.70 are meant to supplement the data already provided and are not the authoritative indicator for degradation in this study.

4.5 Data Analysis and Discussion

While plenty of data has been analyzed and discussed in sections 4.1 through 4.4, section 4.5 will compare data across characterization methods. It may be considered useful to compare results across trials, but the many changes in research procedure in the evolution of the study

makes any comparisons difficult. Preliminary trials 1-3 were used to improve upon the process of creating samples A and B, until sample B was eventually dismissed as an ineffective method for MAPbI₃ encapsulation. Trials 4 and 5 improved and optimized the method of creating sample C. By trial 5 the research methodology had been consistent and only the PMMA dissolution time was increased for trial 6. No accurate comparisons among trials 1 – 4 can be made, because of the many changes that occurred among them. PL measurements varied between trial 5 and 6. For trial 5 PL intensity was not assumed to be at equilibrium for approximately 3 minutes of UV radiation to the sample, which may have caused photobleaching. Trial 6 in comparison quickly took PL measurements with approximately 10 seconds of UV radiation to the surface before taking measurements. Because of this change in PL measurement procedure sample A appears to have a much greater PL intensity for trial 5 than it did in trial 6 but is only an effect of photobleaching. AFM data, however of sample A degradation between trial 5 and 6 can be directly compared, because no change in measurement procedure occurred.

Figure 4.71 below is the direct comparison of figures 4.63 and 4.39, which is the surface roughness graphs for both trials 5 and 6.

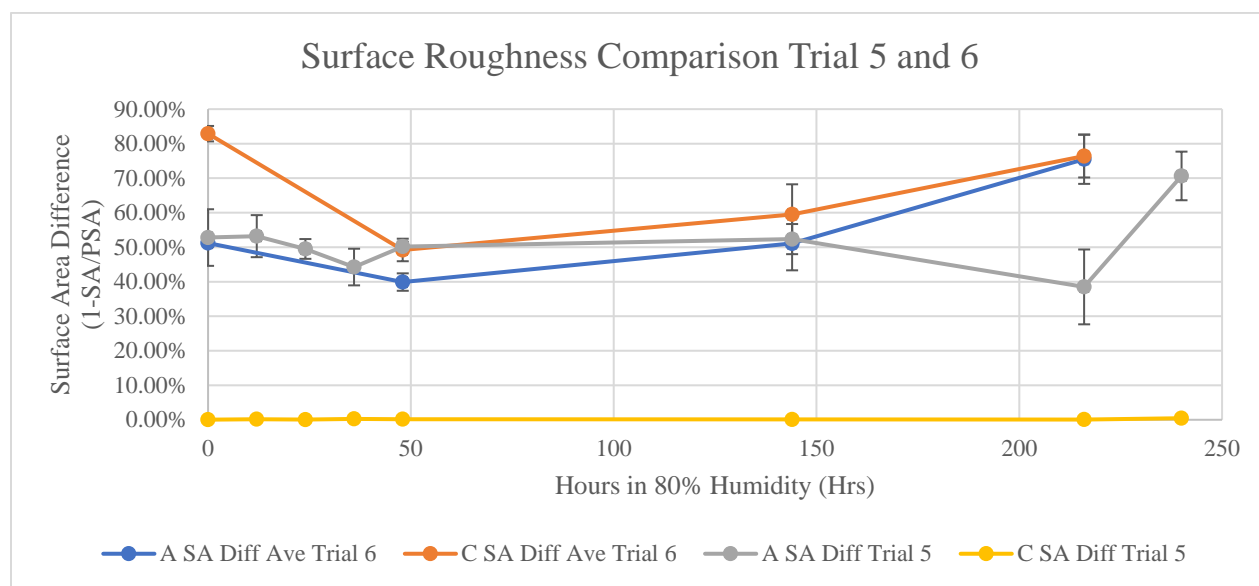


Figure 4.71 Surface Roughness Comparison of Samples A and C for Trials 5 and 6 with error bars of ± 1 std. dev.

Figure 4.71 shows the major change for sample C from trial 5 to trial 6. By fully dissolving the PMMA the surface roughness of sample C was comparable to sample A. Furthermore, the deviations of surface roughness for sample A for trial 5 and trial 6 are minimal. Figure 4.72 below is the combination of the 20 μm x 20 μm number of peaks for trial 5 sample A, trial 6 sample A and trial 6 sample C.

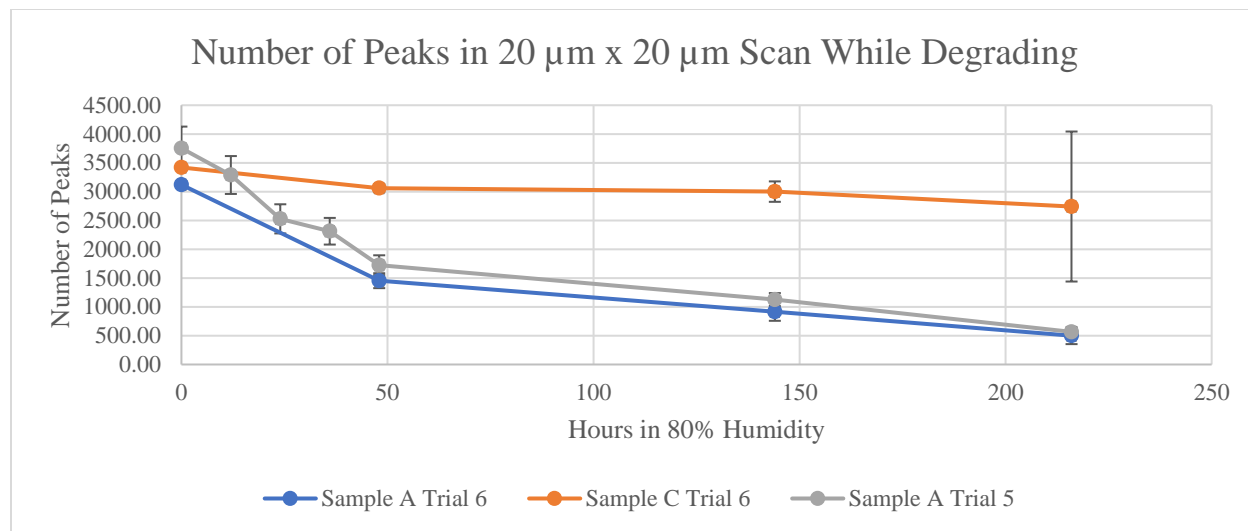


Figure 4.72 Number of Peaks in 20 x 20 AFM Scans for Samples A and C for Trials 5 and 6 with error bars of ± 1 standard deviation

Figure 4.72 again shows that the number of peaks for sample A in trials 5 and 6 are comparable and as the degradation occurs almost the exact same. Sample C begins with a number of peaks between the trial 5 and trial 6 sample A data and the decrease in the number of peaks per 20 μm x 20 μm AFM scan is significantly more gradual than both trial 5 and trial 6 samples of A. Figure 4.73 below is the combination of the scan height range for trial 5 samples A and C, and trial 6 samples A and C.

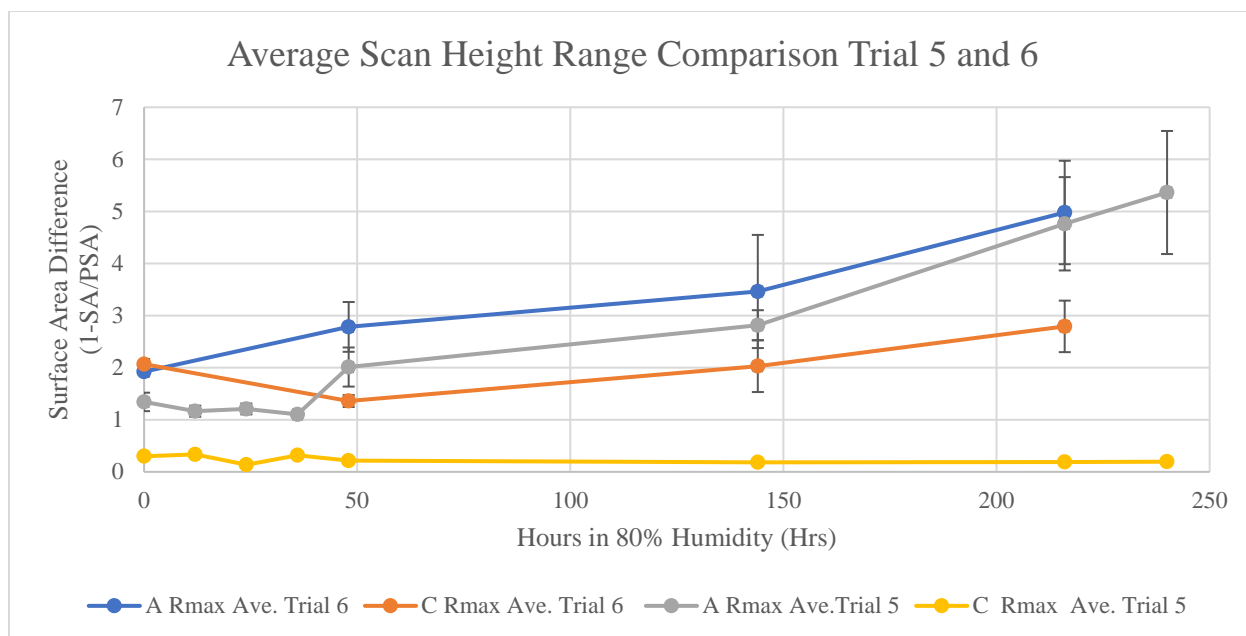


Figure 4.73 Average AFM Scan Height Range for Samples A and C for Trials 5 and 6 with error bars of ± 1 standard deviation

Figure 4.73 shows the comparison between trial 5 and 6 for the average scan height of samples A and C. Again, by dissolving all the PMMA on sample C the scan height increased significantly from trial 5 to trial 6. While sample A for trial 5 had lower initial scan height ranges by 48 hours of 80% humidity exposure both trial 5 and 6 average scan heights were greater than sample C. By 216 hours of 80% humidity exposure sample A for both trial 5 and 6 had comparable scan height ranges near $5 \mu\text{m}$ and significantly greater than sample C for trial 6.

From trial 6 optical images suggested that sample A would begin degrading by 36 hours of 80% humidity exposure, and sample C didn't show first signs until 144 hours. By 336 hours sample A had fully degraded according to PL measurements, and by 528 hours sample C had still not fully degraded. Four estimates were made to compare degradation rates between sample C and sample A in trial 6. The difference in the number of peaks suggested that sample C degraded 501% slower than sample A, the difference in scan height between suggested that sample C degrades 453% slower than sample A, the optical images suggested that sample C

degraded 600% slower than sample A, and PL intensity ratios suggested that sample C degraded 184% slower than sample A. For each of the characterization methods sample C degraded slower than sample A and by weighing each characterization equally sample C degraded 435% slower than sample A on average.

Comparing trial 5 and 6 AFM data certainly defines the differences of how graphene encapsulation of MAPbI₃ reduces degradation effects to the surface topography of MAPbI₃. Another useful comparison is to plot AFM data versus PL data. Figure 4.74 compares the number of peaks in a 20 μm x 20 μm AFM scan to the average peak PL intensity for trial 6 Sample A and C and trial 5 sample A at the same respective times.

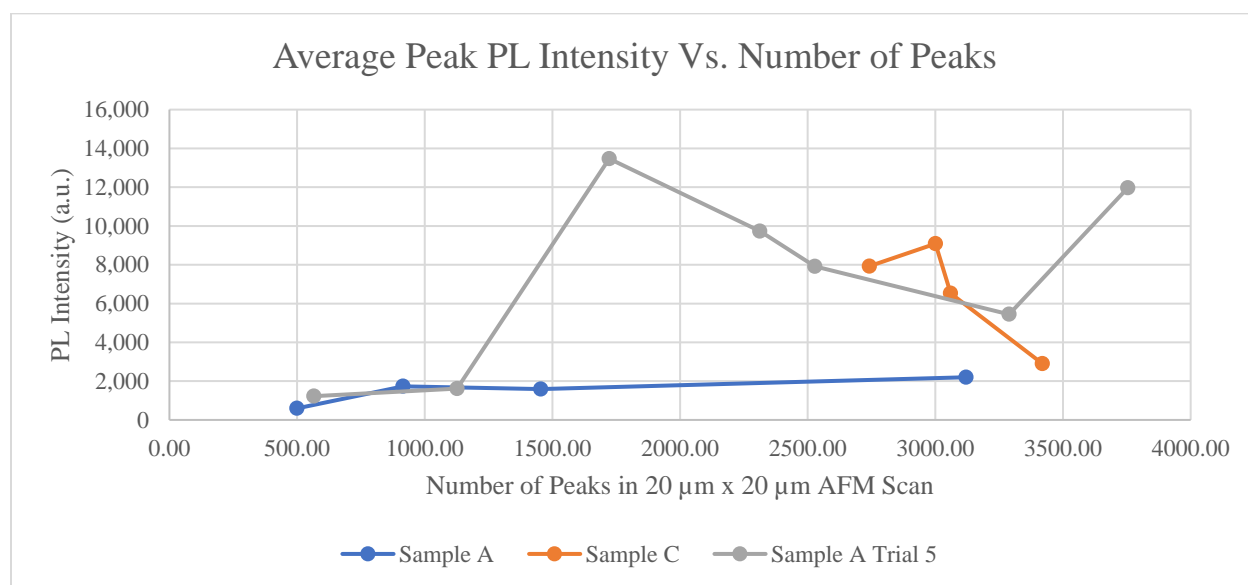


Figure 4.74 Average Peak PL Intensity Vs. Number of Peaks

Figure 4.74 depicts how the relationship between the number of peaks relates with PL intensity. Sample A is more insightful to the relationship of the number of peaks on the surface and the relative PL intensity. Sample A saw a large loss of the number of peaks, whereas sample C did not see a large reduction in the number of peaks. As sample A saw fewer peaks in a 20 μm x 20 μm scan the PL intensity decreased. Sample A in trial 5 did not show as smooth of a

relationship between the number of peaks and the PL intensity. Eventually sample A in trial 5 did have a significant decrease in PL intensity as the number of peaks decreased. However, the spike in PL intensity at approximately 1,700 peaks for trial 5 sample A highlights the threshold between fibers and a “bubbly” film and on the threshold of degradation there is an increase in PL intensity. The relationship of peaks conforming into fibers and reducing the number of peaks is directly correlated with a reduction in PL intensity. Since, sample C did not see a major reduction in peaks that formed into fibers the PL intensity had not yet begun to decrease. The four points in figure 4.5.4 for trial 6 correlate with 0, 48, 144, and 216 hours of 80% humidity exposure from right to left. The seven points for sample A of trial 5 correlates to 0, 12, 24, 36, 48, 144, and 216 hours from right to left. At long term degradation sample A in both trial 5 and 6 converge to a low value of PL intensity and a low number of peaks per 20 μm x 20 μm scan.

Figure 4.75 is another comparison of PL intensity with AFM data that relates average peak PL intensity to the average scan height range at the correlated respective times.

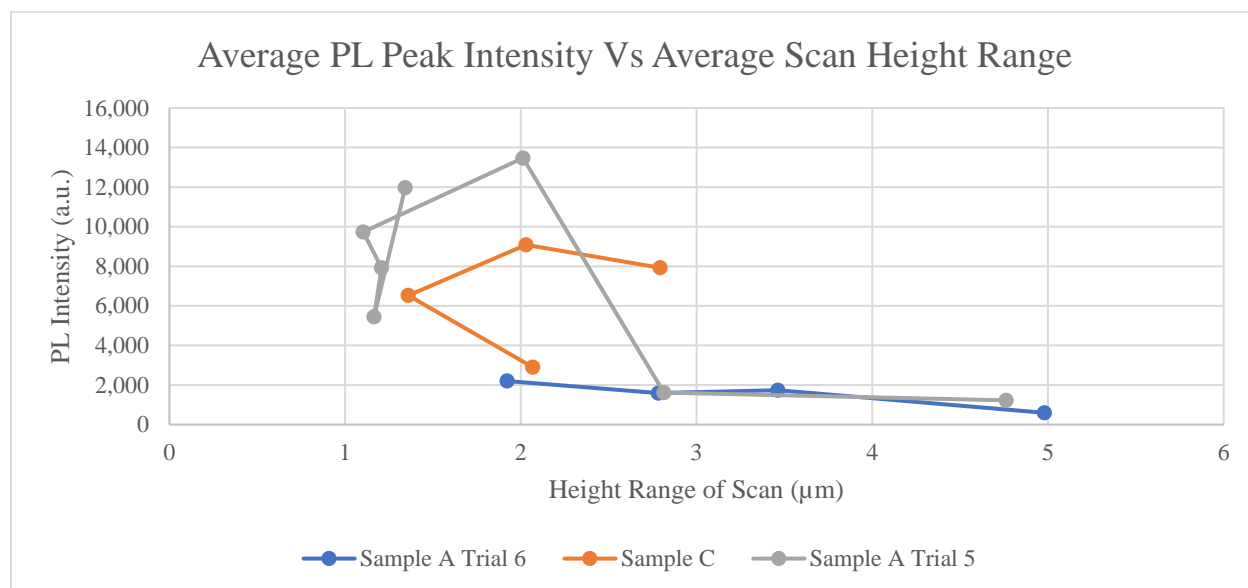


Figure 4.75 Average Peak PL Intensity Vs. Average Scan Height Range

Similar to figure 4.74, sample A in figure 4.75 shows the true relation between average PL peak intensity and scan height range. Sample A for trial 6 saw major degradation from the homogenous film into the fibers and therefore saw a substantial increase in the height of the surface topography. As the film surface topography changes from “bubbles” to fibers the scan range increases, and the PL intensity decreases. Sample C did not see major degradation and had less than a 1 μm difference in the scan height range and thus shows no correlation with the PL intensity. The 4 points for trial 6 data in figure 4.5.5 correlate with 0, 48, 144, and 216 hours of 80% humidity from left to right. Sample A for trial 5 has seven points that correlate with 0, 12, 24, 36, 48, 144, and 216 hours of 80% humidity exposure going from left to right. From 0 to 36 hours the values of the range did not see much change for sample A in trial 5, while PL intensity was bouncing around. At 48 hours sample A for trial 5 reached the threshold where the sample was on the threshold between the fibers and the homogenous film and therefore there is an increase in PL intensity of nearly 14,000 and in the scan height range of 2 μm . Then as major degradation took place at 144 hours the scan height range reached 3 μm and the PL intensity dropped significantly to under 2,000. Lastly, at 216 hours sample A from trial 5 had reached scan height ranges of nearly 5 μm and PL intensities closer to 1,000. Sample A for both trial 5 and 6 converge when reaching full degradation of low values of PL intensity that correlates with high scan height ranges.

Seeing the correlation between the surface topography and the PL intensity give greater insight into the phenomenon of what is happening to the MAPbI_3 and the connection between the mechanical and physical properties of the solar cell. These relations can be useful for understanding degradation properties and how to mitigate them. Most importantly from the entire study is showing through all the measurements and characterizations that the application

of graphene encapsulation around MAPbI₃ has reduced degradation with respect to PL intensities over time, scan height ranges over time, and the number of peaks per scan over time. However, to statistically indicate the confidence of the correlation of these data results to the treatment factor a linear regression analysis was accomplished.

Table 4.10 below indicates the single treatment factor that differed sample A and sample C to accomplish a linear regression model.

Table 4.10 Regression Model Treatment Factor Levels

Factor	Level	
	-1	+1
A: Encapsulation	No Encapsulation	CVD Graphene Encapsulation

The first linear regression model considered compared data results of the PL peak average intensities versus sample A and sample C used from trial 6 for 0 to 528 hours of 80% humidity exposure. Each sample A and C had 19 measurements and therefore is considered a full factorial with 19 replicates. Figure 4.76 below shows the regression plot and table 4.11 the resulting parameter estimates output directly from JMP 13.

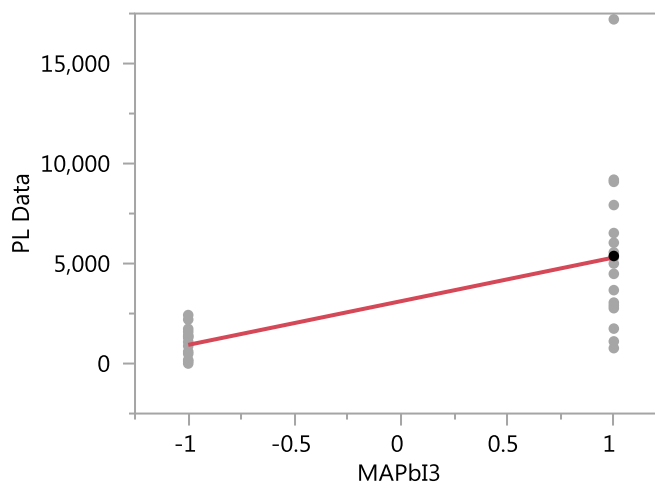


Figure 4.76 PL Regression Plot Trial 6 Data

Table 4.11 Parameter Estimates for Average PL Peak Intensity Regression Model

Term	Estimate	Std Error	t Ratio	Prob> t
Intercept	3118.1579	442.2514	7.05	<.0001*
MAPbI3	2184.2632	442.2514	4.94	<.0001*

From the parameter estimates of the regression model in table 4.11 there is an extremely strong correlation between higher PL values and the treatment factor of graphene encapsulation. The P-value of the PL regression model shows that the treatment level is significant to a 99.99% confidence so that $\alpha < .0001$. The same type of regression models can then be done on the AFM results as well for scan height and the number of peaks using both trial 5 and 6 for sample A and trial 6 for sample C. First, a regression model was also run for the number of peaks correlating to the treatment factor and resulted in the regression plot shown in figure 4.77 with parameter estimates in table 4.12.

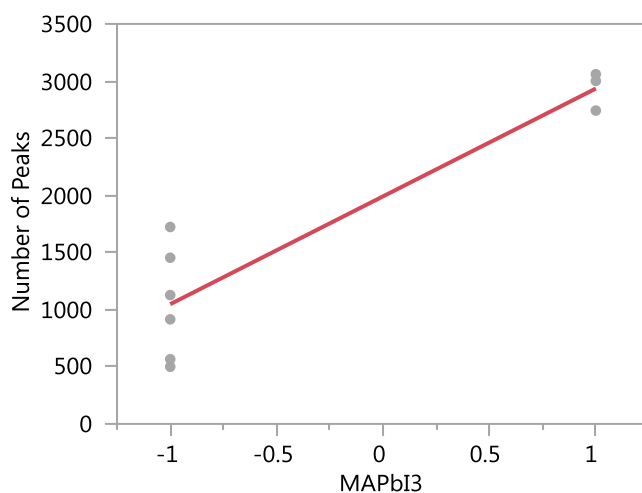


Figure 4.77 AFM Number of Peaks Regression Plot

Table 4.12 Parameter Estimates for Number of Peaks Regression Model

Term	Estimate	Std Error	t Ratio	Prob> t
Intercept	1990.9167	148.4591	13.41	<.0001*
MAPbI3	943.41667	148.4591	6.35	0.0004*

For the number of peaks correlation is also extremely strong between the treatment factor of graphene encapsulation and maintaining a higher number of peaks in a 20 μm x 20 μm scan as shown by the p-value in table 4.12. The confidence of the correlation is 99.96% with $\alpha < .0005$. The scan height data results can also be quantified by a linear regression to understand the confidence of the correlation between graphene encapsulation and scan heights. Both trial 5 and 6 sample A data was used and trial 6 sample C at 216 hours of 80% humidity. Figure 4.78 shows the regression plot below and table 4.13 the resulting parameter estimates.

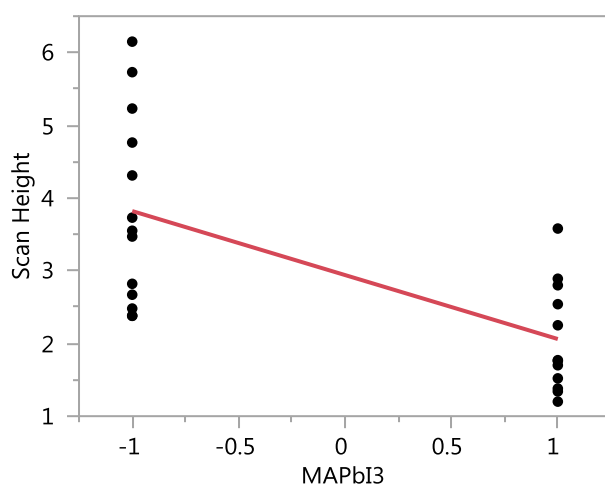


Figure 4.78 AFM Scan Height Regression Plot

Table 4.13 Parameter Estimates for Scan Height Regression Model

Term	Estimate	Std Error	t Ratio	Prob> t
Intercept	2.9405128	0.216029	13.61	<.0001*
MAPbI3	-0.879679	0.216029	-4.07	0.0005*

Comparing the results at 48, 144, and 216 hours on surface height results in a strong negative correlation where adding the graphene encapsulation reduced the scan height. The P-value is .0005 or 99.95% confidence and $\alpha < .05$, which is still a statistically significant correlation. Lastly, the lack of correlation between the treatment factor and the surface roughness can be found for statistical confidence through a linear regression model. Here a high P-value

will show that the surface roughness is not different based on the treatment factor. Sample A and sample C from trial 6 were used to compare the surface roughness regression model. Figure 4.79 below shows the regression model and table 4.14 the resulting parameter estimates.

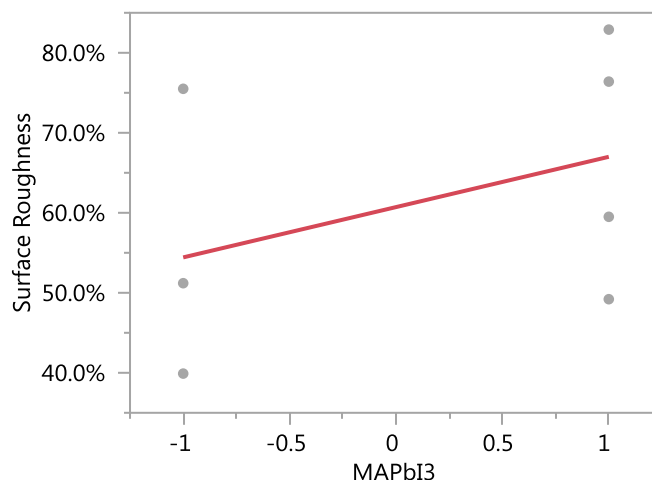


Figure 4.79 AFM Surface Roughness Regression Plot

Table 4.14 Parameter Estimates for Surface Roughness Regression Model

Term	Estimate	Std Error	t Ratio	Prob> t
Intercept	0.607125	0.053829	11.28	<.0001*
MAPbI3	0.062875	0.053829	1.17	0.2871

There is a very low correlation between the treatment factor (graphene encapsulation) and the surface roughness with a p-value of .287. There is still some positive correlation between graphene encapsulation and a rougher surface that shouldn't be fully ignored. However, as expected there is a minimal difference in the surface roughness based on the treatment factor. Having statistically shown the strong correlation of a graphene encapsulation with higher PL intensities, higher number of peaks, and lower scan heights there is a statistically significant correlation that graphene encapsulation reduces degradation of MAPbI₃. Therefore, having analyzed the regression models there is sufficient evidence that fails to reject the hypothesis that graphene encapsulation reduces degradation.

CHAPTER 5. SUMMARY, CONCLUSIONS, AND RECOMMENDATIONS

Chapter five will be an overview of the entire study, what was done, what was learned, the final conclusions from the study, and any future recommendations for the progress and continuation of the research and technology.

5.1 Summary

This study did a thorough analysis of the degradation of MAPbI₃, a material with the potential to change the solar industry and energy generation overall. Chapter one introduced the MAPbI₃ or CH₃NH₃PbI₃ material and how it could be a cheaper, flexible, solution processable material that has photoconversion efficiency rates that compete with its leading solar counterpart silicon. Yet the need for improvement is largely the issue that MAPbI₃ solar cells degrade too quickly to be marketable. Chapter two gave an in-depth background of all the topics that were covered in the study. Current and relevant research on MAPbI₃ was provided to understand what had already been achieved and the quick progress the material was making. Graphene was introduced as a novel material for electronics that is also relatively new to research and is being implemented more and more by major electronic developers. Instrumentation systems that were used to characterize the samples in this study were introduced and explained their relevance and use.

Chapter three explained in detail the entire research methodology for preparing samples A, B, and C, explaining that data results from chapter four consistently affected the preparation methodology. Through trial and error, a succinct procedure for preparing sample A, MAPbI₃, with consistency between samples and within each sample itself was achieved. Sample B, MAPbI₃ with graphene flakes in ethyl alcohol solution spin-coated on top, was easy to create

after sample A had become consistent. Through even more trial and error, the cumbersome procedure to transfer graphene to MAPbI₃ was developed. The state-of-the-art wet PMMA transfer procedure was the first of its kind to be developed as an improvement to dry gel film graphene transfers shown in literature and reduced the number of cracks and contaminants on the graphene film. Lastly, chapter three explained the measuring instruments and their components to be used in the study and the procedures to keep measurements as consistent as possible. The atomic force microscope and photoluminescence measurements were defined as the essential tools to indicate degradation of the samples.

Chapter four contained the data and results from the study and is the most important chapter of the entire study. First, the preliminary trials were introduced and the evolution of creating sample A as well as consistency in measurement procedures. Through trial and error sample A became consistent with minimal variability between samples and within the sample itself. The need for a humidity cabinet presented itself when ambient conditions had low relative humidity and therefore degradation times were becoming long. Trial three was the first attempt of the transfer of CVD graphene to MAPbI₃ but failed because the thin film would crumple and fold on itself leading to a need for more initial PMMA coatings. Trial four was the first successful graphene transfer, but only drops of chlorobenzene (CB) was used to dissolve the PMMA and therefore much of the PMMA was left on the film. Consistency for storage of the samples in a petri dish lid with the lid left on was also realized as a necessity.

Trial five was another successful graphene transfer to MAPbI₃ and led to a five-minute CB bath to dissolve the PMMA, which was then realized was not long enough to fully dissolve the PMMA. The storage method of the samples at this point was consistent and thus led to the

most in depth AFM investigation of the degradation effects on the surface topography of sample A. In trial five Raman spectroscopy was taken leading to the dismissal of sample B, because of the lack of graphene flakes in the solution thus making sample B considered an ineffective encapsulation method of MAPbI₃. The Raman spectroscopy did however indicate that graphene was in fact present on sample C.

Trial six was the most successful trial. Graphene was successfully transferred to MAPbI₃ and a two-hour CB bath fully dissolved the PMMA. Then by measuring surface roughness of sample A and sample C results showed that graphene fully conformed to the MAPbI₃ surface. Subsequent PL and AFM data then indicated that graphene reduced the degradation of MAPbI₃ for each characterization analyzed. Trial six also investigated long term ability for sample C to convert photons into electrons and discovered that even after over 500 hours of exposure to 80% humidity that sample C still had PL intensity. Trial six also made use of a small experiment where a humidity sensor was left in a petri dish with the lid on overnight in the humidity cabinet at 80% humidity and concluded that the humidity inside the petri dish is the same as the humidity outside of the petri dish.

5.2 Conclusions

This study resulted in a set of successful positive conclusions for the initial hypothesis proposed. First, the study concluded that MAPbI₃ does degrade due to humidity. The study also concluded that degradation of MAPbI₃ results in a drop in PL intensity until eventually having no PL intensity at all, indicating that the material is incapable of converting photons into electrons. Optical images concluded that during degradation a homogenous, “bubbly” film will transform into purple fibers. Along with this change in the crystal morphology the number of peaks on a sample will decrease, conforming into larger and taller fibrous features. One negating

conclusion of the study was that pristine graphene flakes in ethyl alcohol spin-coated on MAPbI₃ is an ineffective encapsulation method of MAPbI₃, and therefore sample B was dismissed.

The study did conclude that a wet PMMA transfer method of graphene to a MAPbI₃ solar cell is possible. The most important conclusion of the study was that the application of graphene encapsulation around the MAPbI₃ solar cell reduced all signs of degradation over time exposed to high humidity. Therefore, the study concludes that CVD grown graphene is an effective encapsulation method of MAPbI₃. Reduction in degradation was observed by sample C having PL intensities that outlasted sample A, a lesser reduction in the number of peaks, and a reduction in increases to the surface height range. Four different characterization methods were used to find that sample C degraded slower than sample A. Each of the four characterization methods all concluded that sample C degraded slower than sample C. The average of the four characterization methods concluded that sample C degrades 435% slower than sample A.

Furthermore, AFM surface roughness measurements suggest that graphene conforms to the MAPbI₃ surface, but to be sure force displacement measurements need to be taken. Additionally, PL measurements indicated that the graphene MAPbI₃ heterostructure has the potential to improve PL intensities and therefore photoconversion efficiencies. Lastly, a wet PMMA transfer of graphene to encapsulate MAPbI₃ improved on the results of a dry transfer method presented by Wang et al. (2018).

5.3 Recommendations and Future Work

While this study showed signs of success, there is still substantial amounts of work that needs to be accomplished before MAPbI₃ solar cells, or any perovskite for that matter, is introduced to the marketplace as full photovoltaic (PV) modules. One lesson learned during this study that was not implemented is that marking the graphene surface may have affected the

outcome. By marking the graphene surface with a sharpie, a potential to crack the graphene surface was introduced and may have had detrimental effects on the data results. Instead of marking nine locations in a 3x3 array nine random locations should be measured. Another recommendation is that testing the ability of multiple layers of graphene encapsulation of the MAPbI₃ could further reduce degradation. Additionally, force displacement curves between the graphene and the MAPbI₃ surface would be useful to understand changes in the mechanical properties.

Some future work that still needs to be done before MAPbI₃ can be introduced into the marketplace is the effect of light alone on degradation with graphene. Therefore, graphene encapsulation of MAPbI₃ should also be tested in a dry climate with relative humidity less than 10% to better understand the longevity. Other potential options would be to test MAPbI₃ in space where no humidity is present. Lastly, a vacuum seal of MAPbI₃ could also be tested to see if plastic surrounding the solar cell will reduce long term degradation.

The main purpose of this study and the research on MAPbI₃ is to reduce the cost of solar PV arrays as well as expand their applications. The most important future work is to create MAPbI₃ PV devices and by incorporating graphene encapsulation into the device architecture the photoconversion efficiency may improve as well as the reduction of degradation. Creating flexible, transparent PV modules is the main focus of the future work in the solar community. Laboratories such as the national renewable energy lab (NREL) are working towards creating PV modules from MAPbI₃ to introduce a cheaper solar panel with more applications into the marketplace.

The potential of perovskite technology is substantial and should be considered one of the most paramount materials to be studied of this century. Furthermore, the use of graphene in

electronics also has the capability to create major improvements in mechanical, electrical, and optoelectronic properties. The ability to create cheap solar PV arrays can transform how energy is generated for future generations for a clean energy revolution that is focused on environmental safety and sustainability. Improving the stability of perovskite solar cells is a key step to introducing a revolutionary green technology to the energy generation industry.

LIST OF REFERENCES

- Ahn, N., Son, D., Jang, I., Kang, S., Choi, M., & Park, N. (2015). Highly Reproducible Perovskite Solar Cells with Average Efficiency of 18.3% and Best Efficiency of 19.7% Fabricated via Lewis Base Adduct of Lead(II) Iodide. *Journal of the American Chemical Society*, 137(27), 8696-9.
- Alrefae, M., Kumar, A., Pandita, P., Candadai, A., Billionis, I., & Fisher, T. (2017). Process optimization of graphene growth in a roll-to-roll plasma CVD system. *AIP Advances*, 7(11), 115102-115102-20.
- Aoki, T. (2006). Photoluminescence. In *Optical Properties of Condensed Matter and Applications* (pp. 75-106). Wiley.
- Ayerst, G. (1966). Ferric Chloride as an Etching Material. *Transactions of the IMF*, 44(1), 176-178.
- Bae, S., Kim, H., Lee, Y., Xu, X., Park, J., Zheng, Y., Balakrishnan, J., Lei, T., Kim H.R., Song, Y., Kim, Y., Kim, K.S., Ozyilmaz, B., Ahn, J., Hong, B.H., Iijima, S. (2010). Roll-to-roll production of 30-inch graphene films for transparent electrodes. *Nature Nanotechnology*, 5(8), 574-8.
- Bai, S., Yuan, Z., & Gao, F. (2016). Colloidal metal halide perovskite nanocrystals: Synthesis, characterization, and applications. *Journal of Materials Chemistry C*, 4(18), 3898-3904.
- Banszerus, L., Schmitz, M., Engels, S., Goldsche, M., Watanabe, K., Taniguchi, T., Beschoten, B., Stampfer, C. (2016). Ballistic transport exceeding 28 μm in CVD grown graphene. *ArXiv.org*, 16(2), 1387-1391.
- Binnig, G., Quate, C. F. (1986). Atomic Force Microscope. *Physical Review Letters*, 56(9), 930-933.
- Bischoff, D., Güttinger, Dröscher, Ihn, Ensslin, & Stampfer. (2011). Raman spectroscopy on etched graphene nanoribbons. *Journal of Applied Physics*, 109(7), Journal of Applied Physics, 01 April 2011, Vol.109(7).
- Chang PH. (2017). *Ultrahigh Responsivity and Detectivity Graphene-Perovskite Hybrid Phototransistors by Sequential Vapor Deposition*. (Vol. 7).
- Chen, J., Li, C., Eda, G., Zhang, Y., Lei, W., Chhowalla, M., Milne, W., Deng, W. (2011). Incorporation of graphene in quantum dot sensitized solar cells based on ZnO nanorods. *Chemical Communications*, 47(21), 6084-6086.
- Crosby, G., & Demas, J. (1971). Measurement of photoluminescence quantum yields. Review. *The Journal of Physical Chemistry*, 75(8), 991-1024.

- Dou, L. (2017). Emerging two-dimensional halide perovskite nanomaterials. *Journal of Materials Chemistry C*, 5(43), 11165-11173.
- FLUORESCENCE. (1926). *The Lancet*, 208(5371), 298.
- Geim, A. (2009). Graphene: Status and prospects. *Science (New York, N.Y.)*, 324(5934), 1530-4.
- Graphene and 2D Materials Investment Report 2018 - ResearchAndMarkets.com. (2018). *Business Wire*, p. Business Wire, June 7, 2018.
- Jiang, Qi, Chu, Zema, Wang, Pengyang, Yang, Xiaolei, Liu, Heng, Wang, Ye, Yin, Zhigang, Wu, Jinliang, Zhang, Xingwang, You, Jingbi. (2017). Planar-Structure Perovskite Solar Cells with Efficiency beyond 21%. *Advanced Materials*, 29(46), N/a.
- Jiao, Y., Ma, F., Gao, G., Wang, H., Bell, J., Frauenheim, T., & Du, A. (2015). Graphene-covered perovskites: An effective strategy to enhance light absorption and resist moisture degradation. *RSC Advances*, 5(100), 82346-82350.
- Kim, J., Seo, S., Shin, D., Lee, H., Kim, J., Jang, C., Kim, S., Choi, S., (2017). Ag-nanowires-doped graphene/Si Schottky-junction solar cells encapsulated with another graphene layer. *Current Applied Physics*, 17(8), 1136-1142.
- Kollak, A. and McNally, H., (2013). The Future of Energy: Analyzing the Topography of Solar Cells. Proceedings of ASEE IL IN, 04-2013
- Leguy, A., Hu, Y., Campoy-Quiles, M., Alonso, I., Weber, O. J., Azarhoosh, P., Schilfgaarde, M.V., Weller, M.T., Bein, T., Nelson, J., Docampo, P., Barnes, P. R. F. (2015) Reversible hydration of $\text{CH}_3\text{NH}_3\text{PbI}_3$ in films, single crystals, and solar cells. *Chemistry Materials*, 27, 3397-3407
- Li, X., Zhu, Y., Cai, W., Borysiak, M., Han, B., Chen, D., Piner, R., Columba, L., Ruoff, R. (2009). Transfer of large-area graphene films for high-performance transparent conductive electrodes. *Nano Letters*, 9(12), 4359-63.
- Liang, X., Sperling, B., Calizo, I., Cheng, G., Hacker, C., Zhang, Q., Richter, C. (2011). Toward clean and crackless transfer of graphene. *ACS Nano*, 5(11), 9144-53.
- Lu, J., Wan, M., Wen, Ping, Luo, Fei, Liu, Xin, Wen, Jin, Hu, Chuanyue, and Guo, Jun. "Investigation on the High Pressure Annealing Induced Re-Crystallization Mechanism of $\text{CH}_3\text{NH}_3\text{PbI}_3$ Film." *Journal of Alloys and Compounds* 694 (2017): 1365. Web.
- McNally, H., Rajwa, B., Sturgis, J., & Robinson, J. P. (2005). Comparative three-dimensional imaging of living neurons with confocal and atomic force microscopy. *Journal of Neuroscience Methods*, 142, 177-184

- Messegee, Mamun, Ava, Namkoong, & Abdel-Fattah. (2019). Characterization of perovskite (CH₃NH₃PbI₃) degradation with the integration of different polymers for increased stability. *Materials Letters*, 236, 159-162.
- Mohan, V.B., Lau, K., Hui, D., & Bhattacharyya, D. (2018). Graphene-based materials and their composites: A review on production, applications and product limitations. *Composites Part B*, 142, 200-220.
- Ning, C. Z., Dou, L., & Yang, P. (2017). Bandgap engineering in semiconductor alloy nanomaterials with widely tunable compositions. *Nature Reviews Materials*, 2,
- Nishikawa, S., & Isu, T. (1999). Photoluminescence imaging of phosphor particles using near-field optical microscope with UV light excitation. *Journal of Microscopy*, 194(2-3), 415-420.
- Olympus America Inc. (2010). Instructions BX53M System Microscope. 3500 Corporate Parkway, Center Valley, Pennsylvania 18034-0610 U.S.A.
- Parvez, K., Wu, Z., Li, R., Liu, X., Graf, R., Feng, X., & Müllen, K. (2014). Exfoliation of graphite into graphene in aqueous solutions of inorganic salts. *Journal of the American Chemical Society*, 136(16), 6083-91.
- Polsen, E., McNerny, D., Viswanath, B., Pattinson, S., & Hart, J. (2015). High-speed roll-to-roll manufacturing of graphene using a concentric tube CVD reactor. *Scientific Reports*, 5(1), 10257.
- Ricciardulli, A., Yang, S., Feng, X., & Blom, P. (2017). Solution-Processable High-Quality Graphene for Organic Solar Cells. *ACS Applied Materials & Interfaces*, 9(30), 25412-25417.
- Sasaki, Kitaura, Yuk, Zettl, & Shinohara. (2016). Efficient preparation of graphene liquid cell utilizing direct transfer with large-area well-stitched graphene. *Chemical Physics Letters*, 650(C), 107-112.
- Soufiani, A., Tayebjee, M., Meyer, S., Ho-Baillie, A., Sung Yun, J., McQueen, R., Spiccia, L., Green, M., Hameiri, Z. (2016). Electro- and photoluminescence imaging as fast screening technique of the layer uniformity and device degradation in planar perovskite solar cells. *Journal of Applied Physics*, 120(3), 7
- Sun, Jiawei, Xie, Xiao, Bi, Hengchang, Jia, Haiyang, Zhu, Chongyang, Wan, Neng, Huang, Jianqiu, Nie, Meng, Li, Dan, Sun, Litao. (2017). Solution-assisted ultrafast transfer of graphene-based thin films for solar cells and humidity sensors. *Nanotechnology*, 28(13), 7.

- Tan, Zhenjun, Wu, Yue, Hong, Hao, Yin, Jianbo, Zhang, Jincan, Lin, Li, Wang, Mingzhan, Sun, Xiao, Sun, Luzhao, Huang, Yucheng, Liu, Kaihui, Liu, Zhongfan, Peng, Hailin. (2016). Two-Dimensional (C₄H₉NH₃)₂PbBr₄ Perovskite Crystals for High-Performance Photodetector. *Journal of the American Chemical Society*, 138(51), 16612-16615.
- Wang, B., & Chen, T. (2016). Exceptionally Stable CH₃NH₃PbI₃ Films in Moderate Humid Environmental Condition. *Advanced Science*, 3(2), N/a.
- Wang, Z., Ou, Q., Zhang, Y., Zhang, Q., Hoh, H.Y., & Bao, Q. (2018). Degradation of Two-Dimensional CH₃NH₃PbI₃ Perovskite and CH₃NH₃PbI₃/Graphene Heterostructure. *ACS Applied Materials and Interfaces*, 10(28), 24258-24265.
- Yang, J., Siempelkamp, B., Liu, D., & Kelly, T. (2015). Investigation of CH₃NH₃PbI₃ Degradation Rates and Mechanisms in Controlled Humidity Environments Using in Situ Techniques. *ACS Nano*, 9(2), 1955-1963.
- Yuan, Sijia, Wang, Jiao, Yang, Kunlong, Wang, Pengfei, Zhang, Xin, Zhan, Yiqiang, & Zheng, Lirong. (2018). High efficiency MAPbI_{3-x}Cl_x perovskite solar cell via interfacial passivation. *Nanoscale*, 10(40), 18909-18914.
- Zhou, Y., Yang, M., Wu, W., Vasiliev, A., Zhu, K., & Padture, N. (2015). Room-temperature crystallization of hybrid-perovskite thin films via solventsolvent extraction for high-performance solar cells. *Journal of Materials Chemistry A*, 3(15), 8178-8184.
- Zuo, C., Vak, D., Angmo, D., Ding, L., & Gao, M. (2018). One-step roll-to-roll air processed high efficiency perovskite solar cells. *Nano Energy*, 46, 185-192.